

Rotational Dynamics of Icy Satellites

Tidal response and forced longitudinal librations at the surface of a viscoelastic Europa

Jara Orue, Hermes

DOI

[10.4233/uuid:2e35b789-735a-47a3-ac4f-63dd7651de44](https://doi.org/10.4233/uuid:2e35b789-735a-47a3-ac4f-63dd7651de44)

Publication date

2016

Document Version

Final published version

Citation (APA)

Jara Orue, H. (2016). *Rotational Dynamics of Icy Satellites: Tidal response and forced longitudinal librations at the surface of a viscoelastic Europa*. [Dissertation (TU Delft), Delft University of Technology]. <https://doi.org/10.4233/uuid:2e35b789-735a-47a3-ac4f-63dd7651de44>

Important note

To cite this publication, please use the final published version (if applicable). Please check the document version above.

Copyright

Other than for strictly personal use, it is not permitted to download, forward or distribute the text or part of it, without the consent of the author(s) and/or copyright holder(s), unless the work is under an open content license such as Creative Commons.

Takedown policy

Please contact us and provide details if you believe this document breaches copyrights. We will remove access to the work immediately and investigate your claim.

ROTATIONAL DYNAMICS OF ICY SATELLITES

TIDAL RESPONSE AND FORCED LONGITUDINAL LIBRATIONS AT
THE SURFACE OF A VISCOELASTIC EUROPA

ROTATIONAL DYNAMICS OF ICY SATELLITES

TIDAL RESPONSE AND FORCED LONGITUDINAL LIBRATIONS AT
THE SURFACE OF A VISCOELASTIC EUROPA

Proefschrift

ter verkrijging van de graad van doctor
aan de Technische Universiteit Delft,
op gezag van de Rector Magnificus prof. ir. K.C.A.M. Luyben,
voorzitter van het College voor Promoties,
in het openbaar te verdedigen op dinsdag 15 november 2016 om 15:00 uur

door

Hermes Miguel JARA ORUÉ

ingenieur luchtvaart- en ruimtevaarttechniek,
Technische Universiteit Delft, Delft, Nederland,
geboren te Arequipa, Perú.

Dit proefschrift is goedgekeurd door de

promotor: Prof. dr. L.L.A. Vermeersen

promotor: Prof. dr. ir. P.N.A.M. Visser

Samenstelling promotiecommissie:

Rector Magnificus,	voorzitter
Prof. dr. L.L.A. Vermeersen,	Technische Universiteit Delft
Prof. dr. ir. P.N.A.M. Visser,	Technische Universiteit Delft

Onafhankelijke leden:

Prof. dr. N. Rambaux,	Université Pierre et Marie Curie, Frankrijk
Prof. dr. T. Van Hoolst,	Royal Observatory of Belgium, België
Dr. F. Sohl,	Deutsches Zentrum für Luft- und Raumfahrt, Duitsland
Prof. dr. E.K.A. Gill,	Technische Universiteit Delft
Prof. dr. ir. R.F. Hanssen,	Technische Universiteit Delft
Prof. dr. -ing. Habil R. Klees,	Technische Universiteit Delft, reservelid



Keywords: Icy Moons, Tidal dynamics, Rotational dynamics, Geodynamics, Viscoelasticity, Longitudinal librations

Printed by: Ridderprint BV

Front & Back: Representation of Europa and Ganymede within the Jovian system. Image courtesy: NASA/JPL-Caltech/SET Institute (Europa image), NASA/JPL (Ganymede image), NASA/JPL/University of Arizona (Jupiter image) and ESA/ATG medialab (JUICE model).

Copyright © 2016 by H.M. Jara Orué

ISBN 978-94-6299-466-9

An electronic version of this dissertation is available at
<http://repository.tudelft.nl/>.

CONTENTS

Summary	ix
Samenvatting	xiii
1 Introduction	1
1.1 Evidences for the presence of a subsurface ocean	2
1.2 Research objective and motivation	6
1.3 Thesis outline	8
2 Modeling the Interior of Icy Satellites	11
2.1 Introduction	11
2.2 Structural modeling: definition of internal layers	11
2.2.1 Application to Europa: the case of a liquid water layer in direct contact with a rocky interior	15
2.2.2 Application to Ganymede: the case of a liquid water layer sandwiched between ice layers	18
2.3 Rheological modeling of the internal layers of icy satellites	20
2.3.1 Rheological models	21
2.3.2 Rheology of ice-I	23
2.3.3 Rheological parametrization of the internal layers of icy satellites	26
3 Normal Mode Models for Planetary Bodies with Internal Liquid Layers	29
3.1 Introduction	29
3.2 Conventional normal mode method	31
3.3 Propagation through internal fluid layers	33
3.4 Boundary conditions	35
3.5 Propagator matrix approach for icy moons	37
3.5.1 Individual propagator matrices	37
3.5.2 Connecting the propagator matrices	39
3.5.3 The characteristic equation: normal modes	40
3.5.4 The response at the surface	43
3.5.5 The response at internal interfaces	45
3.6 Love numbers	46
4 Tidal deformations and stresses I: Theory	51
4.1 Introduction	51
4.2 Tidal potential	53
4.3 Tidal deformation	57
4.4 Tidal stresses at the surface of an icy satellite	60
4.4.1 The strain-displacement relations	60

4.4.2	Diurnal stresses	63
4.4.3	NSR stresses	67
5	Tidal deformations and stresses II: Application to icy moons	71
5.1	Tidal Love numbers: Europa	71
5.2	Tidal deformation: application to Europa	81
5.3	Tidal deformation: application to Ganymede	85
5.3.1	Abstract	86
5.3.2	Introduction	86
5.3.3	Interior modeling	88
5.3.4	Tidal response	92
5.3.5	Results	95
5.3.6	Discussion and Conclusions	99
5.4	Tidal and NSR stresses: application to Europa	102
5.4.1	Abstract	102
5.4.2	Introduction	103
5.4.3	The interior of Europa	106
5.4.4	Results	108
5.4.5	Discussion and Conclusions	114
6	Rotational Dynamics of Icy Satellites	119
6.1	Introduction	119
6.2	Basic linearized rotational dynamics for triaxial bodies	120
6.3	Effect of deformation on the rotational dynamics of triaxial bodies	123
6.3.1	Definition of the centrifugal potential for rotational studies	124
6.3.2	Definition of the tidal potential for rotational studies	125
6.3.3	Inertia increments	127
6.3.4	Liouville equations in the oceanless case	129
6.4	Role of the subsurface ocean: differential rotation	133
6.4.1	The coupled Liouville equations	135
6.4.2	Inertia increments	138
7	Longitudinal Libration of Europa	141
7.1	Abstract	141
7.2	Introduction	142
7.3	Rotational dynamics	144
7.3.1	Longitudinal Librations	144
7.3.2	Inertia increments	146
7.3.3	Gravitational coupling	149
7.3.4	Pressure coupling	152
7.3.5	External torques	153
7.3.6	Libration equations for a multi-layered Europa	155
7.4	Interior models of Europa and Love numbers	156
7.5	Results	159
7.6	Discussion and conclusions	165

8	Conclusions and Recommendations	169
8.1	Conclusions	169
8.1.1	Modeling the response to diurnal tides	170
8.1.2	Surface stresses induced by diurnal and NSR tides on Europa	171
8.1.3	Longitudinal librations of Europa's ice shell	173
8.2	Recommendations	175
	References	179
	Acknowledgements	195
	Curriculum Vitæ	197
	List of Publications	199

SUMMARY

The icy satellites of the giant planets Jupiter and Saturn are among the most interesting celestial bodies in our Solar System. Several different observations made by the Voyager flybys (1979-1981), the Galileo mission to Jupiter (1995-2003) and the Cassini-Huygens mission to Saturn (2004-ongoing) strongly suggest that many icy satellites (e.g. Europa, Ganymede, Enceladus and Titan) may harbor a subsurface water ocean underneath the outer ice shell covering the satellites. The availability of water, in combination with the availability of critical chemical elements (C, H, N, O, P, S) and the availability of a source of energy, is considered to be one of the prerequisites for life as we know it. Therefore, the subsurface oceans of the icy satellites of the outer Solar System provide a unique environment in which life may have originated and developed. Among the icy satellites of the Solar System, Jovian moon Europa is thought to possess the most suitable environment for habitability as its presumed geologically stable internal ocean is predicted to be in direct contact with the rocky mantle. This configuration favors the supply of the necessary chemical elements and the availability of an energy source to Europa's ocean through mechanisms comparable to hydrothermal vents on Earth, and hence all known cornerstones for habitability may be well satisfied.

One of the key research objectives within the broader context of the habitability potential of icy moons is the characterization of the physical properties of the putative internal ocean and the overlying ice shell. Spacecraft missions planned to visit the Jovian system and Europa in particular, such as ESA's JUPiter ICy moon Explorer (JUICE) and NASA's Europa Multiple-Flyby Mission (formerly known as the Europa Clipper), may not include a landing segment (NASA's mission may include a surface segment). In the absence of a lander or penetrator, these missions will need to provide the required constraints on the physical properties of Europa's upper layers from remote sensing measurements, such as: 1) the characterization of the magnetic field in the vicinity of the icy satellites, 2) the measurement of radial displacements and gravity perturbations as a result of the acting diurnal tides, and 3) the measurement of the amplitude of the longitudinal librations forced by Jupiter's gravitational torque on the triaxial shape of Europa. Although any of these observations has the potential to confirm the existence of a subsurface ocean on an individual basis (e.g. the possible detection of a subsurface ocean on Europa through the observation of an induced magnetic field by Galileo), the complex way in which the aforementioned observables depend on the physical properties of Europa's interior does not allow for the unambiguous determination of e.g. the thickness of the internal ocean and overlying ice shell.

As a result, the main objective of this thesis is to analyze whether the combined measurement of radial deformations, perturbations in the gravity field and longitudinal librations could be able to provide useful constraints on the physical parameters that characterize Europa's upper layers, especially the thickness of the ice shell. To this end, this thesis strongly focuses on the developing of a self-consistent tidal and rotational

model to determine the tidal and librational response at the surface of a wide variety of radially stratified interior models of Europa. Since most existing rotational models developed to study the forced longitudinal librations of a decoupled ice shell did not take into consideration that the satellite may experience elastic and/or viscoelastic deformation in response to the diurnal tides, the biggest improvement can be achieved by handling the effect of elastic and viscoelastic deformation on the longitudinal librations forced by the gravitational torque of the parent planet on the non-spherical shape of the satellite. Such a description has the advantage of being consistent with the treatment of the viscoelastic response to diurnal tides in earlier studies as well as in this thesis, and therefore it is expected to provide a more complete framework to deduce the physical properties that characterize the interior of an icy satellite from future measurements of radial displacements, gravity perturbations and longitudinal librations.

The numerical model developed in this thesis to determine the viscoelastic tidal response at the surface of a radially stratified Europa (or any other icy satellite) is based on the analytical normal mode approach, in which the viscoelastic response is expressed in terms of the relaxation modes of the interior model upon which the normal mode model is applied. Normal mode methods have been extensively used in the past for the study of solid-Earth geophysical phenomena (e.g. postglacial rebound), mainly because the analytical nature of these methods allows for the gain of physical insight into the mechanisms driving the relaxation process. Nevertheless, due to the likely presence of a subsurface ocean at shallow depths in the interior of icy satellites, conventional normal mode models developed for Earth applications cannot be directly applied to the case of icy moons. Mechanical quantities, such as deformations and stresses, cannot be propagated through a fluid as the governing linear momentum equations degenerate within such a layer. In order to handle this problem, in this thesis the global subsurface ocean is assumed to be in a state of hydrostatic equilibrium in both the undeformed and deformed cases and it is assumed that the deformation of the fluid layer occurs in such a way that its boundaries follow an equipotential surface. This strategy is based on how earlier normal mode models applied to Earth-oriented studies deal with the presence of a fluid core on top of a solid core.

As a first application, the developed analytical method based on the normal mode technique has been used to determine the time-dependent tidal Love numbers h_2 and k_2 at the surface of various multilayer interior models of Europa and Ganymede; all of them built in accordance with the mean moment of inertia condition obtained from the measurement of the degree-2 gravity field under the assumption of hydrostatic equilibrium. As such, it is important to remark that the results and conclusions achieved throughout this thesis only apply to icy satellites whose interior is in hydrostatic equilibrium and for which lateral heterogeneities in the internal structure can be neglected. Furthermore, the modeling in this thesis only applies to linear rheologies for the materials that constitute the interior of the satellite. Under these assumptions, the simulations performed in this thesis indicate that the amplitude of the tidal Love number h_2 at the frequency of the acting diurnal tides is mostly sensitive to uncertainties in the thickness and rheological properties of the ice-I shell. Although the same holds for the tidal Love number k_2 , the amplitude of k_2 is also largely sensitive to uncertainties in the density of the subsurface ocean. As a result, the determination of h_2 and k_2 from future remote

sensing observations has the potential to provide a rather good constraint on the density of the ocean but would fail to constrain the thickness of the ice shell, mainly as a consequence of the poorly known rigidity and viscosity of the ice shell.

As a second application, the developed normal mode model is extended to study the variable tidal stress field acting on Europa's surface by modeling the stresses induced by the small eccentricity of Europa's orbit, the non-zero obliquity of Europa's spin axis (both acting on a diurnal 3.55-days timescale) and the reorientation of the ice shell as a result of non-synchronous rotation (NSR). The simulations in this thesis show that viscoelastic relaxation influences surface stresses in two ways: 1) through viscoelastic relaxation in the lithosphere, and 2) through the viscoelastic tidal response of Europa's interior. The amount of relaxation in the lithosphere is proportional to the ratio between the period of the forcing mechanism and the Maxwell relaxation time of the high-viscous lithosphere. As a result, this effect is only relevant to surface stresses caused by the slow NSR mechanism. On the other hand, the importance of the viscoelastic response on surface stresses is proportional to the ratio between the relaxation time (τ_j) of a given viscoelastic mode j and the period of the forcing function. On a diurnal timescale the fast relaxation of transient modes related to the low viscosity of the asthenosphere can alter the magnitude and phase shift of the diurnal stress field at Europa's surface by as much as 20% in magnitude and 7° in phase for interior models with a thick and highly dissipative asthenosphere. On timescales relevant for NSR ($> 10^4$ years), the magnitude and phase shift of NSR surface stresses can be affected by viscoelastic relaxation of the ocean/ice boundary. This effect, however, becomes only important when the behavior of the lithosphere with respect to NSR approaches the fluid limit, i.e. for strong relaxation in the lithosphere. The combination of NSR and diurnal stresses for different amounts of viscoelastic relaxation of NSR stresses in the lithosphere leads to a large variety of global stress fields that can explain the formation of the large diversity of lineament morphologies observed on Europa's surface. Variation of the amount of relaxation in the lithosphere is likely due to changes in the spin rate of Europa and/or the rheological properties of the surface, mostly driven by heat dissipation in the interior. In addition, the analysis in this thesis shows that a small obliquity (< 1 degree) can have a considerable effect on Europa's diurnal stress field. A non-zero obliquity breaks the symmetric distribution of stress patterns with respect to the equator, thereby affecting the magnitude and orientation of the principal stresses at the surface. As expected, increasing the value of Europa's obliquity leads to larger diurnal stresses at the surface, especially when Europa is located 90° away from the nodes formed by the intersection of its orbital and equatorial planes.

Due to the likely presence of a subsurface ocean, internal solid layers separated by the ocean are expected to experience slightly different rotational variations as a result of mass redistribution in the interior, surface loading and/or external torques. Therefore, the rotational dynamics of icy satellites with a shallow subsurface ocean are best described by differential rotation models, in which the rotational motion of the solid layers separated by the fluid layer is mechanically decoupled but still coupled to some degree due to the effect of internal gravitational and pressure torques. In this thesis, the Love number formalism inherent to the developed normal mode model has been used to introduce the effect of viscoelastic deformation into the rotational dynamics of icy satellites in order to study the longitudinal libration of Europa's shell forced by Jupiter's

gravitational torque on Europa's triaxial shape.

The developed differential rotation model is then applied to determine the amplitude of the shell libration of numerous models of Europa's interior in order to analyze the sensitivity of the computed libration to uncertainties in the value of geophysical parameters that describe the structural and rheological properties of the interior. The simulations indicate that the libration amplitude is most sensitive to the poorly constrained rigidity of the ice-I shell, as the order of magnitude uncertainty in the value of the rigidity of the shell leads to a similar order of magnitude uncertainty in the amplitude of the shell libration. This effect on the libration amplitude is much larger than the one introduced by uncertainties in the shell thickness and/or shell density. Moreover, the dependence of the libration amplitude on the thickness of the ice shell shows a change in behavior depending on the assumed value for the rigidity of the ice-I shell; with the libration amplitude increasing with increasing shell thickness for rigidities larger than ~ 2 GPa and decreasing with increasing shell thickness for rigidities lower than ~ 2 GPa. Furthermore, the unknown viscosity of the lower ductile part of Europa's shell introduces an uncertainty in the libration amplitude that is comparable to the uncertainty introduced by the rigidity, especially for the upper range of tested values for the rigidity of the ice-I shell. As a result, it can be stated that the amplitude of the forced libration of a deformable Europa with a subsurface ocean is mostly sensitive to the poorly constrained rheological properties of the ice-I shell, rather than the thickness of the ice shell.

Regarding the use of libration observations to explore the geophysical properties of Europa's upper layer, the results in this thesis strongly suggest that the measurement of the libration amplitude of Europa's shell with an accuracy of a few meters has the potential to provide a reasonable constraint on the rigidity of the ice-I shell in combination with measurements of the tidal Love numbers h_2 and k_2 . However, the number of interior models analyzed in this dissertation is not large enough to support a strong conclusion regarding whether the ice shell thickness could be inferred from combined measurements of the libration amplitude and tidal Love numbers at the surface of Europa. Therefore, it is strongly recommended to apply the modeling presented in this thesis to determine the libration amplitude and tidal response (i.e. the tidal Love numbers h_2 and k_2 at orbital frequency) of a wide variety of interior models of Europa in order to assess whether the measurement of these physical parameters by future missions such as ESA's JUICE and NASA's Europa Multiple-Flyby Mission could be able to constrain the thickness of the ice-I shell.

SAMENVATTING

De ijsmanen van de reuzenplaneten Jupiter en Saturnus behoren tot de meest intrigerende hemellichamen in ons zonnestelsel. Diverse metingen die uitgevoerd zijn tijdens de Voyager flybys (1979-1981), de Galileo-missie naar Jupiter (1995-2003) en de Cassini-Huygens missie naar Saturnus (2004-heden) wijzen sterk op de aanwezigheid van ondergrondse oceanen van vloeibaar water in het binnenste van ijsmanen zoals Europa, Ganymedes, Enceladus en Titan. De beschikbaarheid van vloeibaar water wordt beschouwd als één van de drie kernvoorwaarden voor het bestaan van leven zoals wij op Aarde kennen. Daarbij zijn de andere twee kernvoorwaarden voor het bestaan van leven noodzakelijk, namelijk de beschikbaarheid van een energiebron en de aanwezigheid van de kritische chemische elementen (C, H, N, O, P, S). Als gevolg hiervan lijkt Europa, van alle ijsmanen in onze zonnestelsel, de meest geschikte omgeving voor bewoonbaarheid te bieden omdat de vloeibare wateroceaan hoogstwaarschijnlijk in direct contact is met de rotsachtige mantel. Een belangrijk voordeel van deze configuratie is dat de benodigde energie en chemische elementen aan het interne oceaan geleverd kunnen worden door middel van mechanismen die vergelijkbaar zijn met hydrothermale bronnen op de bodem van de Aardse oceanen. Daardoor is het goed mogelijk dat alle bekende bouwstenen voor bewoonbaarheid aanwezig zijn in Europa's ondergrondse oceaan.

De karakterisering van de fysische eigenschappen van de interne oceanen en de bovenliggende ijslagen is één van de belangrijkste doelen van het onderzoek naar de potentiële bewoonbaarheid van de ijzige manen. De ruimtevaartmissies die gepland zijn om het Jupiter-systeem, en Europa in het bijzonder, in de nabije toekomst te bezoeken, zoals ESA's Jupiter ICy moon Explorer (JUICE) en NASA's Europa Multiple-Flyby Mission (voorheen Europa Clipper), zullen waarschijnlijk niet voorzien worden van een lander. Als gevolg hiervan zullen remote-sensing waarnemingen noodzakelijk zijn om de fysische eigenschappen van Europa's wateroceaan en ijskorst te kunnen afleiden, bijvoorbeeld: 1) het karakteriseren van het magnetische veld in de nabijheid van de ijzige manen, 2) het meten van de radiale verplaatsing en zwaartekrachtverstoringen als gevolg van de dagelijkse (3.55-dag tijdschaal) getijdenkrachten, en 3) het meten van de amplitude van de longitudinale libraties die aangedreven worden door het koppel dat uitgeoefend wordt door Jupiter's zwaartekracht op de tri-axiale vorm van Europa. Hoewel elk van deze waarnemingen de potentie heeft om het bestaan van een ondergrondse oceaan te bevestigen, zorgt de complexe wijze waarop de te waarnemen grootheden afhankelijk zijn van de fysische eigenschappen van Europa's binnenste ervoor dat het niet mogelijk is om onder andere de dikte van de interne oceaan en bovenliggende ijskorst eenduidig te kunnen bepalen.

De belangrijkste doelstelling van dit proefschrift is om te onderzoeken of de fysische eigenschappen van de buitenste lagen van Europa, en dan met name de dikte van de ijskorst, kunnen worden vastgelegd uit de combinatie van de eerder genoemde remote-sensing metingen (met uitzondering van de magnetisch veld waarnemingen). Binnen

dit kader richt dit proefschrift zich met name op de ontwikkeling van coherente numerieke algoritmes om de respons van Europa's binnenste op getijden en rotatieveranderingen te berekenen. Aangezien de meerderheid van bestaande numerieke modellen die ontwikkeld zijn om de longitudinale libraties van een ontkoppelde ijskorst te bestuderen geen rekening houdt met elastische en/of viscoelastische vervorming door getijdenwerking, is het aannemelijk dat een grote verbetering in de modellering kan worden bereikt door het introduceren van elastische en viscoelastische deformatie. Een dergelijke beschrijving heeft als voordeel dat het in overeenstemming is met de behandeling van de viscoelastische respons van een ijsmaan op de tijdsafhankelijke getijdenwerking in zowel eerdere studies als in dit proefschrift. Het resultaat is dus een numeriek model dat een consistente beschrijving biedt voor het afleiden van de fysische eigenschappen van Europa's binnenste uit de combinatie van waarnemingen van de radiale verplaatsing, zwaartekrachtverstoringen en longitudinale libratie aan het oppervlak.

Het ontwikkelde numerieke model om de viscoelastische getijdenrespons aan het oppervlakte van een gelaagde Europa (of andere ijsmaan) te berekenen is gebaseerd op de analytische normaal-mode analyse, waarin de viscoelastische respons is uitgedrukt in termen van de relaxatie modes van het inwendige model. Normaal-mode methoden zijn in het verleden uitgebreid toegepast voor de studie van geofysische fenomenen op Aarde (bv. postglaciale opheffing), met name omdat de analytische aard van deze methoden het verkrijgen van fysisch inzicht over de mechanismen die het relaxatieproces aandrijven mogelijk maakt. Echter, de mogelijke aanwezigheid van een ondergrondse oceaan in het inwendige van de ijsmanen zorgt ervoor dat conventionele normaal-mode methodes - dus methodes die ontwikkeld zijn voor Aardse toepassingen waarvoor de aanwezigheid van een vaste kern onder de vloeibare kern verwaarloosd kan worden - niet direct toegepast kunnen worden op de inwendige structuur van de ijsmanen. Mechanische grootheden, zoals vervormingen en spanningen, kunnen niet door een vloeibare laag worden gepropageerd omdat de gelineariseerde vergelijking die de wet van behoud van lineaire impuls beschrijft degenerereert binnen een dergelijke laag. Om dit probleem aan te pakken, wordt er hier aangenomen dat de globale ondergrondse oceaan zich in hydrostatisch evenwicht bevindt in zowel de onvervormde als vervormde toestanden. Daarbij wordt er ook aangenomen dat de vervorming van de vloeistoflaag de contouren volgt van een equipotentiaal oppervlak. Deze strategie is gebaseerd op hoe normaal-mode modellen in het verleden toegepast zijn op geofysische studies die zich bezighouden met de dynamische gevolgen van de aanwezigheid van een vloeibare kern bovenop een vaste kern.

Het ontwikkelde numerieke model is als eerst gebruikt om de tijdsafhankelijke getijden Love-getallen h_2 en k_2 aan het oppervlak van verschillende inwendige modellen van zowel Europa en Ganymedes te bepalen. Alle opgestelde inwendige modellen zijn voortgebouwd op het gemiddelde traagheidsmoment dat afgeleid is uit waarnemingen van het zwaartekrachtsveld (graad 2) onder de aanname van hydrostatisch evenwicht. Het is dus belangrijk om hier te vermelden dat de resultaten en conclusies die bereikt zijn in dit proefschrift alleen van toepassing zijn op ijsmanen waarvan het inwendige zich in hydrostatisch evenwicht bevindt en waarvoor laterale heterogeniteiten in de interne structuur kunnen worden verwaarloosd. Daarnaast gelden de resultaten hier uitsluitend voor lineaire rheologiën. Rekening houdend met deze aannames, laat dit on-

derzoek zien dat de amplitude van het Love-getal h_2 op de frequentie van de dagelijkse getijden vooral gevoelig is voor onzekerheden in de dikte en rheologische eigenschappen van de ijs-I schil. Hoewel dezelfde conclusies getrokken kunnen worden voor het Love-getal k_2 , is de amplitude van k_2 ook in hoge mate gevoelig voor onzekerheden in de dichtheid van de ondergrondse oceaan. Als gevolg hiervan heeft de bepaling van de Love-getallen h_2 en k_2 door toekomstige remote-sensing waarnemingen het potentieel om goede randvoorwaarden te verschaffen voor de dichtheid van de ondergrondse oceaan. Echter, hetzelfde kan niet worden gezegd over de dikte van de ijskorst, met name als gevolg van de onzekerheid in de waarden van de stijfheid en viscositeit van het ijs.

Verder is het ontwikkelde normaal-mode model uitgebreid met het modelleren van het tijdsafhankelijk oppervlaktespanningsveld dat ontstaat door: 1) de niet-cirkelvormige omloopbaan van Europa om Jupiter (kleine excentriciteit), 2) de kleine hellingshoek van Europa's equator ten opzichte van het omloopvlak, en 3) de heroriëntatie van de ijskorst als gevolg van niet-synchrone rotatie (NSR). De simulaties in dit onderzoek laten zien dat viscoelastische relaxatie de spanningen aan het oppervlakte van Europa op twee manieren beïnvloedt: 1) door viscoelastische relaxatie in de lithosfeer, en 2) door de viscoelastische respons van Europa's inwendige op de getijdenkrachten. De sterkte van relaxatie in de lithosfeer is evenredig met de verhouding tussen de periode van het aandrijfmechanisme en de Maxwell relaxatietijd van de vrijwel elastische lithosfeer. Vanwege de hoge viscositeit van de lithosfeer is dit effect alleen relevant voor oppervlaktespanningen die veroorzaakt zijn door het trage NSR mechanisme. Daarentegen is het belang van de viscoelastische respons op oppervlaktespanningen evenredig met de verhouding tussen de relaxatietijd (τ_j) van een gegeven viscoelastische mode j en de periode van het aandrijfmechanisme. Voor de 3.55-dagen tijdschaal (d.w.z. voor de dagelijkse tijdschaal), kan de viscoelastische relaxatie van sterke transient modes van inwendige modellen met een dikke en zeer dissipatieve asthenosfeer leiden tot veranderingen van 20% in de grootte van de oppervlaktespanningen en faseverschuivingen van 7° in het spanningsveld. Voor tijdschalen die relevant zijn voor NSR ($> 10^4$ jaar), worden de grootte en de faseverschuiving van NSR oppervlaktespanningen worden beïnvloed door viscoelastische relaxatie van het raakvlak tussen oceaan en ijs. Dit effect is echter alleen van belang als het viscoelastische gedrag van de lithosfeer ten opzichte van NSR de zogenaamde vloeistofflimiet benadert als gevolg van sterke relaxatie in de lithosfeer. De combinatie van NSR en dagelijkse oppervlaktespanningen - voor verschillende mate van viscoelastische relaxatie van NSR spanningen in de lithosfeer - kan leiden tot het ontstaan van globale oppervlaktespanningsvelden die de grote verscheidenheid aan tektonische landschapkenmerken op Europa's oppervlakte mede kunnen verklaren. Veranderingen in de staat van relaxatie in Europa's ijskorst zijn waarschijnlijk te wijten aan variaties in de draaisnelheid van Europa en variaties in de rheologische eigenschappen van de ijskorst. Daarnaast toont dit onderzoek aan dat een kleine obliquiteit (< 1 graad) een aanzienlijke invloed op Europa's dagelijkse oppervlaktespanningsveld kan hebben. De obliquiteit breekt de symmetrie in de verdeling van de oppervlaktespanningspatronen ten opzichte van de evenaar, waardoor de grootte en oriëntatie van de totale dagelijkse hoofdspinningen beïnvloed wordt. Zoals verwacht kan worden, wordt het effect van de obliquiteit op de dagelijkse spanningen groter naarmate de obliquiteit groter wordt.

Vanwege de mogelijke aanwezigheid van een ondergrondse oceaan, kunnen vaste la-

gen in het inwendige die gescheiden zijn door de oceaan naar verwachting verschillende rotatieveranderingen ervaren als gevolg van de herverdeling van massa in het inwendige, oppervlaktebelastingen en externe koppels. Als gevolg hiervan kan de rotatiedynamica van ijsmanen met een ondergrondse oceaan het best beschreven worden door middel van differentiële rotatie modellen, waarin de rotatie van de vaste lagen die gescheiden zijn door de oceaan is mechanische losgekoppeld. Desalniettemin blijft de rotatie aan beide kanten van de oceaan enigszins gekoppeld als gevolg van interne zwaartekrachten en drukkoppels. In dit onderzoek wordt het Love-getal formalisme dat inherent is aan normaal-mode methodes toegepast om het effect van viscoelastische vervorming in de rotatie-dynamica van ijsmanen te introduceren. Het ontwikkelde differentiële rotatie model wordt vervolgens toegepast op een diverse set van modellen van Europa's inwendige om de gevoeligheid van de longitudinale libratie van de ijskorst voor onzekerheden in de waarde van de rheologische en structurele eigenschappen van het inwendige te bestuderen. De resultaten in dit onderzoek geven aan dat de amplitude van de longitudinale libratie het gevoeligst is voor onzekerheden in de waarde van de stijfheid van ijs-I. Deze onzekerheden kunnen leiden tot onzekerheden in de amplitude van de libratie die van vergelijkbare orde van grootte zijn als de onzekerheden in de stijfheid zelf. Dit effect op de amplitude van de longitudinale libraties is veel groter dan het effect dat geïntroduceerd wordt door onzekerheden in de dikte en/of dichtheid van het ijs. Bovendien vertoont de manier waarop de amplitude van de libratie verandert als functie van de ijsdikte verschillende gedragspatronen die sterk beïnvloedt worden door de aangenomen waarde voor de stijfheid van ijs-I. Namelijk, de amplitude van de longitudinale libratie neemt toe met toenemende ijsdikte als de stijfheid van ijs-I groter is dan ~ 2 GPa en neemt af met toenemende ijsdikte als de stijfheid van ijs-I lager is dan ~ 2 GPa. Daarnaast introduceert de onbekende viscositeit van het onderste gedeelte van Europa's ijslaag onzekerheden in de amplitude van de longitudinale libratie die vergelijkbaar zijn met de onzekerheden die door de stijfheid worden geïntroduceerd, met name voor hoge waarden van de stijfheid. Hierdoor kan er worden vastgesteld dat de amplitude van de longitudinale libraties van een vervormbare Europa vooral gevoelig is voor de onbekende reologische eigenschappen van ijs-I.

Met betrekking tot het gebruik van toekomstige waarnemingen van de amplitude van longitudinale libraties voor het afbakenen van de geofysische eigenschappen van Europa's bovenste lagen, wijzen de resultaten in dit onderzoek er op dat het meten van de amplitude van de libratie met een nauwkeurigheid van enkele meters de mogelijkheid biedt om een goede inschatting te geven voor de stijfheid van ijs-I, mits gecombineerd met waarnemingen van de Love-getalen h_2 en k_2 . Daarentegen kan de analyse in dit onderzoek geen duidelijk antwoord geven op de vraag of de ijsdikte afgeleid kan worden uit gecombineerde waarnemingen van de getijden Love-getallen en de libratie-amplitude aan het oppervlakte van Europa, met name omdat de set van gebruikte modellen van Europa's inwendige niet groot en divers genoeg bleek te zijn. Daardoor is het aan te bevelen om de ontwikkelde algoritmes toe te passen op een grotere set van modellen van Europa's inwendige. Dit kan een beter beeld geven van de mogelijkheid om de dikte van Europa's ijskorst te bepalen door waarnemingen van de libratie amplitude en getijde Love-getallen door toekomstige missies zoals ESA's JUICE en NASA's Europa Multiple-Flyby Mission.

1

INTRODUCTION

The icy satellites of the giant planets Jupiter and Saturn are among the most interesting celestial bodies in the Solar System, as revealed by the numerous observations made by the Voyager 1 and 2 flybys (1979-1981), and by the dedicated missions Galileo to the Jupiter system (1995-2003) and Cassini-Huygens to the Saturn system (2004-ongoing). Once thought to be frozen worlds, many icy satellites (e.g. Europa, Ganymede, Enceladus and Titan) exhibit unique geological features on their surfaces that may be linked to the presence of a subsurface water ocean underneath the outer ice shell covering the satellites. The availability of liquid water, as well as the presence of critical chemical elements for building life (C, H, N, O, P, S) and the availability of a source of energy, is considered to be one of the keystones of habitability based on our understanding of life on Earth [e.g. [Pappalardo et al., 1999](#), [Chyba and Phillips, 2002](#), [Hand et al., 2009](#)]. As such, the putative subsurface oceans of the icy satellites of the outer planets may have the potential to harbor a second origin of life in our Solar System. This discovery would lead to a profound transformation in our understanding of life, as it would not only be limited to the conditions available on Earth but it may arise wherever the suitable conditions are available.

Among the icy satellites of the Solar System, the Jovian moon Europa is widely thought to possess the most suitable environment for habitability as its subsurface ocean is predicted to be in direct contact with the rocky mantle [e.g. [Anderson et al., 1998](#), [Sohl et al., 2002](#)]. This configuration may provide the necessary chemical elements and energy source to Europa's ocean through e.g. hydrothermal vents [e.g. [Hand et al., 2009](#), [Vance and Goodman, 2009](#), [Zolotov and Kargel, 2009](#)]. Furthermore, modeling of the heat transfer across Europa's ice shell suggests that Europa's ocean has existed for geological timescales [e.g. [Hussmann et al., 2002](#), [Hussmann and Spohn, 2004](#)], thereby providing a stable environment for possible life to evolve. In contrast to Europa, the putative internal oceans of larger icy satellites such as Ganymede and Titan are expected to be sandwiched between an outer ice shell and a layer of high-pressure (HP) ices underneath, thereby preventing direct contact between the deep interior and the ocean [e.g. [Anderson et al., 1996](#), [Sohl et al., 2002](#), [Jess et al., 2010](#), [Sohl et al., 2014](#)]. Enceladus,

on the other hand, was long expected to have a local subsurface ocean in direct contact with the underlying rock underneath the geologically active South Polar Region [see e.g. [Spencer and Nimmo, 2013](#)]. However, recent measurement of the amplitude of the forced longitudinal librations of Enceladus requires the presence of a thin and laterally heterogeneous global internal ocean [[Thomas et al., 2016](#)]. Independent of the extent of Enceladus' ocean, the observed surface heat flux and high loss of material from the plumes suggest that Enceladus may have a contemporary liquid reservoir that is not stable over geological timescales [e.g. [Roberts and Nimmo, 2008](#), [Tobie et al., 2008](#), [Spencer et al., 2009](#), [O'Neill and Nimmo, 2010](#)].

One of the key research objectives within the broader context of the habitability potential of icy moons is the characterization of the putative internal ocean and the overlying ice shell. Spacecraft missions planned to visit the Jovian system and Europa in particular, such as ESA's JUPITER ICy moon Explorer (JUICE) and NASA's Europa Multiple-Flyby Mission (formerly known as the Europa Clipper), may not include a lander segment mainly due to the technological challenges and risks involved in the design of a reliable landing mission given the limited knowledge of the icy surface at the scale of a lander [[Grasset et al., 2013](#), [Phillips and Pappalardo, 2014](#)]. However, NASA has invited ESA to provide a ~ 250 kg flight element to NASA's Europa Multiple-Flyby Mission [[ESA, 2015](#)]. Vehicle options being considered include a minisat orbiter, a penetrator and a soft lander¹. In the possible case that a landing segment is not included as part of the definitive mission, the physical properties that characterize the upper layers of Europa (or any other icy satellite) will need to be derived from remote sensing measurements of observables such as: 1) the radial deformation of the surface and perturbations in the gravity field due to the eccentricity-driven tides (diurnal tides) exerted by the parent planet on the interior of the satellite, 2) the amplitude of periodic variations in the spin rate (longitudinal librations) caused by the planet's gravitational torque on the non-spherical shape of the satellite, and 3) the induced electromagnetic field caused by the interaction between the planet's rotating magnetic field and the satellite's putative subsurface ocean. This thesis will concentrate on the modeling of radial surface deformations, perturbations on the gravity field and longitudinal librations with the aim of providing improved constraints to the interpretation of future measurements of those observables in terms of the physical properties that characterize the ice shell and underlying ocean. Although important for the realization of this goal, the modeling of the induced magnetic field is beyond the scope of this thesis.

1.1. EVIDENCES FOR THE PRESENCE OF A SUBSURFACE OCEAN

In this Section, a short summary of the observations and theoretical models that support the existence of a subsurface ocean underneath the ice shell of Europa, Ganymede, Callisto, Titan and Enceladus is provided.

¹see e.g. <http://auditore.cab.inta-csic.es/europa-m5initiative/purpose-and-scope/>, last accessed: March 2016.

EUROPA

Several different observations made by Voyager and Galileo strongly suggest the existence of a subsurface ocean below Europa's ice shell. Among these observations, the strongest case is made by Galileo's detection of a time-variable induced magnetic field, which requires the existence of an electrically conductive layer at shallow depth, most probably a salty ocean [Khurana et al., 1998, Kivelson et al., 2000, Hand and Chyba, 2007, Schilling et al., 2007]. The presence of a subsurface ocean is also strongly supported by the observation of tectonic features that resemble a chain of arcuate segments, commonly known as cycloids, which are thought to have formed as tensile cracks in response to the stresses induced by the periodic diurnal tides acting on the satellite [Hoppa et al., 1999b, Lee et al., 2005, Hurford et al., 2007, Rhoden et al., 2010]. To understand why an internal ocean favors the formation of these unique features, one needs to take into consideration that the displacements, and subsequently the stresses, induced by the acting diurnal tides are about two orders of magnitude larger if an ocean is present in Europa's interior. Cracking of Europa's surface ice requires tensile stresses larger than its tensile strength, which may be as low as 40 – 220 kPa for porous and fractured ice [Lee et al., 2005] but still at least one order of magnitude larger than the surface stresses associated with an oceanless interior (see Sections 5.4.4 and 5.4.5).

Although cycloids provide the most convincing geological evidence for the presence of a subsurface ocean, these lineaments are not the only tectonic features on Europa's surface whose formation has been linked to the existence of an internal ocean. The orientation of global-scale lineaments has been so far best explained by the large tensile stresses (~MPa) induced either by non-synchronous rotation (NSR) of a floating ice shell [e.g. Geissler et al., 1998, Greenberg et al., 1998, Harada and Kurita, 2007, Wahr et al., 2009] or by the thickening of the ice shell [Nimmo, 2004]. In addition, NSR has been often invoked as the most likely mechanism to explain the observed systematic longitudinal migration of tectonic features on Europa's surface [e.g. Geissler et al., 1998, Hoppa et al., 2001, Hurford et al., 2007, Rhoden et al., 2010]. Other interesting tectonic features are the so-called small-circle depressions (SCDs), whose location (centered around ~25° from the equator) and morphology are suggested to be the result of the stresses induced by ~80° true polar wander (TPW) of a floating shell [Schenk et al., 2008]. However, the occurrence of TPW on Europa is a topic of scientific debate as the location and orientation of other surface features do not appear to have been affected by such a reorientation mechanism [Leith and McKinnon, 1996, Kattenhorn and Hurford, 2009, Rhoden et al., 2011].

The presence of a subsurface ocean is also strongly supported by theoretical models dealing with the thermal state and evolution of Europa's interior [e.g. Ojakangas and Stevenson, 1989b, Hussmann et al., 2002, Tobie et al., 2003, Hussmann and Spohn, 2004, Mitri and Showman, 2005]. The thermal state of Europa's ice shell depends on the available heat sources and the efficiency of heat transfer within the shell. Taking into account radiogenic heating in Europa's innermost layers and tidal dissipation within the ice shell as heat sources, numerous thermal models of heat transfer by solid state convection predict that an internal liquid water ocean can be maintained over geological timescales [e.g. Hussmann et al., 2002, Tobie et al., 2003, Hussmann and Spohn, 2004, Mitri and Showman, 2005, Nimmo and Manga, 2009]. Furthermore, coupled thermal-orbital evo-

lution models predict oscillations in the thickness of Europa's ice shell as a result of the evolution of Europa's orbital parameters [Hussmann and Spohn, 2004]. However, these models are still in their infancy as they depend on highly uncertain parameters such as the ice rheology and the temperature profile within Europa's silicate mantle, as well as on the tidal interaction between Io and Jupiter [Moore and Hussmann, 2009].

Additional evidence for the presence of a subsurface ocean is given by theoretical models dealing with the morphology of impact craters [Schenk, 2002, Senft and Stewart, 2011]. Of particular interest are the largest impact craters observed on Europa's surface: Tyre and Callanish (diameter > 30 km). These impact basins show a shallow multi-ring structure that is consistent with the presence of a phase change at depth, arguably an ice-liquid interface located at least 19-25 km from the surface [Schenk, 2002]. From a different perspective, the presence of a salty subsurface ocean is also supported by the observed yellow-brown color within geologically young features on Europa's surface, as this coloration may be explained by the presence of endogenous sodium chloride after being exposed to the radiation environment at the surface [Hand and Carlson, 2015]. This evidence is thus indicative of ongoing interaction between the ocean and the silicate mantle underneath, an essential consideration for the assessment of the habitability potential of Europa's ocean.

GANYMEDE AND CALLISTO

In a similar way as for Europa, the strongest evidence for the presence of a liquid water ocean in the interior of Callisto is provided by the detection of an induced magnetic field by Galileo's magnetometer [Khurana et al., 1998, Zimmer et al., 2000]. Unlike the case of Europa's putative ocean, Callisto's ocean is not expected to be in direct contact with an underlying rocky layer as the measured degree two gravity field coefficients suggest a partially differentiated interior [Anderson et al., 2001]. As such, Callisto's internal ocean is most likely sandwiched between an outer ice shell and a region of mixed ice and rock/metal [e.g. Anderson et al., 1997, Nagel et al., 2004].

In the case of Ganymede, the magnetic field observations did not provide a conclusive proof for the presence of an internal ocean as Ganymede's intrinsic magnetic field complicates the unambiguous detection of an induced magnetic field [Kivelson et al., 2002]. Despite the lack of conclusive observational evidences, theoretical models dealing with the thermal profile of Ganymede's ice layers support the presence of a subsurface water ocean sandwiched between an outer ice shell and a layer of high-pressure ices [Spohn and Schubert, 2003, Vance et al., 2014].

TITAN

Several measurements performed by the Cassini-Huygens mission have provided compelling evidence for the presence of a liquid ocean in the interior of Saturn's largest moon Titan. Arguably the strongest case is made by the measurement of the tidal Love number k_2 , which is a representation of the response of Titan's interior to the time-variable tidal field exerted by Saturn. The values for k_2 inferred from the radio science data, i.e. $k_2 = 0.589 \pm 0.150$ and $k_2 = 0.637 \pm 0.224$ [Jess et al., 2012], are actually much larger than the one expected for an oceanless interior, i.e. $k_2 = 0.03$ [Rappaport et al., 2008], and

are thus consistent with the presence of a liquid water ocean in the interior [Rappaport et al., 2008, Iess et al., 2012]. Moreover, interior models of Titan developed to reproduce the measured value(s) of the tidal Love number k_2 show that the large observed values require the presence of a dense liquid ocean and possibly a mushy interior [Baland et al., 2014, Mitri et al., 2014, Sohl et al., 2014].

Additional evidence for the presence of a subsurface ocean is given by the measurement of Titan's obliquity ($\varepsilon = 0.3^\circ$) using synthetic aperture radar (SAR) images obtained by Cassini's RADAR instrument [Stiles et al., 2008]. This measured value is larger than the $\sim 0.12^\circ$ expected for an entirely solid satellite [Bills and Nimmo, 2008], and is consistent with a surface ice shell decoupled from the interior by a liquid ocean [Baland et al., 2012, 2014]. In addition, it has been inferred from the same Cassini SAR images that Titan's spin is slightly faster than synchronous by about 0.02 degrees per year [Stiles et al., 2008, 2010, Meriggiola and Iess, 2012]. This faster spin rate may be the result of seasonal exchange of angular momentum between the surface and the rotating atmosphere, but only in the case that a global internal ocean decouples the rotational motion of the icy crust from the motion of the deep interior [Lorenz et al., 2008, Van Hoolst et al., 2013].

In contrast to the case of the Galilean satellites, the detection of a subsurface ocean through the observation of an induced magnetic field cannot be realized because the measurements performed by Cassini's magnetometer (MAG) cannot reach the required sensitivity. The reasons leading to the insufficient sensitivity of the instrument's measurements are [Béghin et al., 2012]: 1) the weaker Saturnian magnetic field at Titan's orbit, when compared to the case of the Jovian satellites; 2) the large flyby altitude of the spacecraft, which is limited by atmospheric drag; and 3) the shielding effect of Titan's ionosphere. Nevertheless, the presence of a subsurface ocean has been inferred from Huygens' measurement of low frequency electromagnetic waves and the conductivity of Titan's atmosphere after the detection of a Schumann-like resonance trapped within Titan's atmospheric cavity [Béghin et al., 2010, 2012].

ENCELADUS

The presence of liquid water in the interior of Saturn's moon Enceladus was first inferred from the observation of plumes of water vapor and ice being emitted from long fractures located around the south pole, commonly known as the "tiger stripes" [e.g. Porco et al., 2006, Spencer et al., 2006]. Detailed spectral analysis of measurements performed by Cassini's Ion Neutral Mass Spectrometer (INMS) has shown that ammonia, heavy organic materials and ^{40}Ar are present in the plume [Waite Jr et al., 2009, Spencer et al., 2009]. Moreover, observations of the composition of dust particles in Saturn's E-ring (which are derived from the Enceladus plume) by Cassini's Cosmic Dust Analyser (CDA) have identified the presence of grains rich in sodium salts [Postberg et al., 2009]. Both types of observations suggest the presence of a subsurface liquid reservoir as ammonia has the potential to prevent the reservoir from freezing, whereas the presence of ^{40}Ar and sodium salts are indicative of a subsurface ocean in direct contact with an underlying rocky core [Zolotov, 2007, Waite Jr et al., 2009, Spencer et al., 2009, Postberg et al., 2011]. The current location of the geologically active South Polar Terrain (SPT) can be explained by the occurrence of a large ($\sim 90^\circ$) TPW episode around an almost stationary tidal axis either caused by a warm diapir [Nimmo and Pappalardo, 2006] or by the melt-

ing of ice-I in the vicinity of the South Pole [Collins and Goodman, 2007], which would also lead to the remarkable symmetry in the distribution of impact craters and tectonic patterns on the surface of Enceladus [Matsuyama and Nimmo, 2008].

Further evidence for the presence of a subsurface ocean comes from the combined observation of Enceladus' gravity field (second degree and J_3), forced longitudinal librations, topography and surface heat flux [see e.g. Spencer et al., 2006, Nimmo et al., 2011, Iess et al., 2014, Thomas et al., 2016]. In contrast to other icy satellites, the scientific debate regarding Enceladus' subsurface ocean has mainly concentrated on its extent, i.e. whether it is global or localized around the South Pole. A strong case for a global subsurface ocean has arisen from the measurement of the amplitude of the forced longitudinal libration of Enceladus at orbital frequency [Thomas et al., 2016]. The observed value for the libration ($0.120 \pm 0.014^\circ$) is too large to be compatible with a rocky core rigidly connected with the ice shell (libration amplitude $\sim 0.032^\circ - 0.034^\circ$), thereby implying the presence of a thin decoupling global subsurface ocean instead of a regional subsurface sea [Thomas et al., 2016]. This evidence is supported by the reinterpretation of the gravity data of Iess et al. [2014] by McKinnon [2015], in which the effect of the fast rotation of Enceladus on its hydrostatic shape and degree-2 gravity field has been taken into account. Moreover, this global ocean would be thicker beneath the south pole and nearly frozen at the equator [McKinnon, 2015, Thomas et al., 2016]. However, maintaining a global subsurface ocean may be problematic from a thermodynamic perspective, as thermal models suggest that the large heat flux observed at the south pole (15.8 ± 3.1 GW [Howett et al., 2011]) would lead to freezing of a global liquid reservoir [Roberts and Nimmo, 2008, Tobie et al., 2008].

1.2. RESEARCH OBJECTIVE AND MOTIVATION

The discussion in the previous Section shows that the strongest evidences for the presence of global subsurface oceans in the interior of the icy satellites of Jupiter and Saturn have been derived from the measurement of the tidal Love number k_2 at orbital frequency (Titan), the measurement of the amplitude of the forced longitudinal librations at orbital frequency (Enceladus), and the detection of an induced magnetic field (Europa, Callisto). Despite the compelling body of evidence, the presence of a global subsurface ocean in the interior of the Galilean moons and Enceladus has not yet been unambiguously confirmed. The unresolved debate on the extent, depth and composition of these internal oceans has been fundamental for the planning and development of dedicated spacecraft missions, such as NASA's Europa Multiple-Flyby Mission and ESA's Jupiter ICy moon Explorer (JUICE), with the aim of constraining the physical properties that characterize the putative internal ocean of the Galilean satellites as well as the properties of the overlying ice shell. In order to reach this goal, several mission objectives have been proposed, such as (relevant instrument between brackets): 1) the characterization of the magnetic field in the vicinity of the icy satellites (magnetometer), 2) the measurement of radial displacements (laser altimeter) and gravity perturbations (radio science experiment) as a result of the acting diurnal tides, and 3) the determination of the amplitude of forced longitudinal librations (laser altimeter) [Van Hoolst et al., 2008, Baland and Van Hoolst, 2010]. Although the fulfillment of any of these mission objec-

tives has the potential to confirm the existence of a subsurface ocean on an individual basis (see Section 1.1 for the case of Titan), the complex way in which the aforementioned observables depend on the physical properties of the interior does not allow for the unambiguous determination of e.g. the depth and thickness of the internal ocean and overlying ice shell, respectively. Hence, an observation strategy that combines the aforementioned observation techniques is required to constrain the range of possible values for these parameters (see e.g. [Grasset et al., 2013] for the aimed observation strategy for JUICE's characterization of Ganymede's ocean and ice shell).

In contrast to the modeling of radial displacements and gravity perturbations at the surface due to the acting diurnal tides (i.e. the determination of the tidal Love numbers h_2 and k_2 , respectively) [e.g. Moore and Schubert, 2000, Tobie et al., 2005, Rappaport et al., 2008, Wahr et al., 2009, Jara-Oru e and Vermeersen, 2011], most theoretical models developed to study the forced longitudinal librations of a decoupled ice shell did not take into consideration that the satellite may experience elastic and/or viscoelastic deformation in response to the diurnal tides [e.g. Van Hoolst et al., 2008, Baland and Van Hoolst, 2010, Rambaux et al., 2011, Thomas et al., 2016]. Consequently, the results obtained by these simplified models have the tendency of overestimating the amplitude of the forced longitudinal libration at the surface [Goldreich and Mitchell, 2010]. Hence, the main objective of this thesis is to readdress the theoretical framework that describes the rotational dynamics of icy satellites with a shallow subsurface ocean in order to study the effects of elastic and viscoelastic deformation on the longitudinal librations forced by the gravitational torque of the parent planet on the non-spherical shape of the satellite. Such a description will be consistent with the treatment of the viscoelastic response to diurnal tides and will provide a more complete framework to deduce the physical properties that characterize the interior of an icy satellite from future measurements of radial displacements, gravity perturbations and longitudinal librations.

Additional constraints on the structure and physical properties of the ice shell are expected to be provided by the ice-penetrating radar on board of JUICE and Europa Multiple-Flyby Mission, which has the ability of performing subsurface analysis down to ~ 10 km depth and with a vertical resolution of some tens of meters depending on the composition of the ice [Clark et al., 2011, Grasset et al., 2013]. As such, observations by the ice-penetrating radar may have the potential to detect the transition depth from ice to liquid water in the unlikely - but not unrealistic - case that Europa's ice shell is thinner than ~ 10 km [see e.g. Nimmo and Manga, 2009, and references therein], or in the case that shallow pockets of liquid water are present within the ice shell, as suggested by Schmidt et al. [2011]. In the case of Ganymede, radar sounding may not detect the transition depth to liquid water as the thickness of Ganymede's ice shell is expected to be larger than ~ 10 km [Vance et al., 2014]. In addition, observations by the ice-penetrating radar may provide useful constraints on the density and rheology of the upper parts of the ice shell, which in turn can be used to improve the constraints on the thickness of the shell from the indirect measurements discussed in the previous paragraphs.

Furthermore, in this thesis the possibility of long-term variations in the rotational dynamics of icy satellites has been taken into account in the development of the rotational model. Therefore, the model presented in this thesis may be extended to the study of NSR and/or TPW on icy moons as long as the rotational variations remain small. The

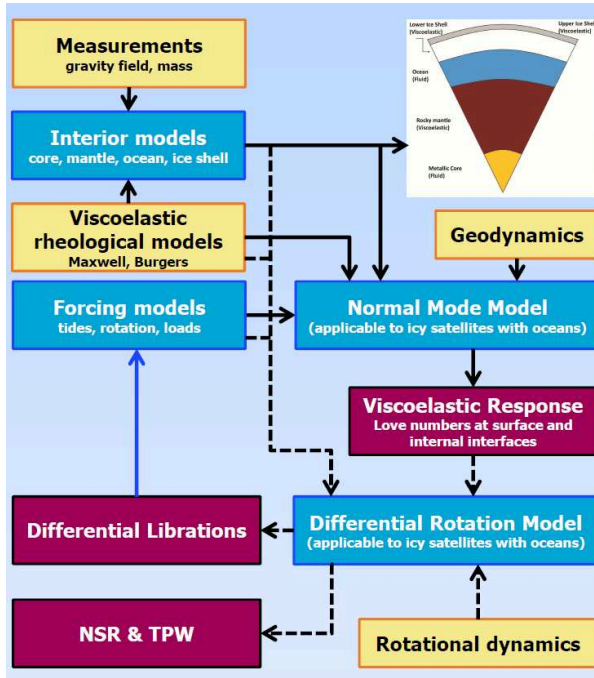


Figure 1.1: Schematic description of the topics involved in the study of the rotational dynamics of icy satellites with a subsurface ocean. In this diagram, the yellow boxes indicate general fields that are required for the development of the rotational model, the blue boxes together represent the structure of the developed model, and the red boxes are the most important output parameters obtained from the modeling process.

analysis of large excursions of the pole, such as the ones suggested for Enceladus and Europa, would therefore require a different approach, most likely based on numerical integration.

1.3. THESIS OUTLINE

This thesis addresses the development of a rotational dynamics model to study the longitudinal librations of deformable icy satellites with a shallow subsurface ocean, as well as providing a framework to analyze long term rotational variations such as true polar wander (TPW) and non-synchronous rotation (NSR). Although the developed model may be applied to any icy satellite with no clear evidence for lateral heterogeneities in its internal structure, the discussion provided in this thesis is focused on the Galilean satellites Europa and Ganymede. The reason for this choice is primarily based on the need for consistent rotational (libration) and tidal models (Love numbers) to improve the constraining of the physical properties that characterize Europa's and Ganymede's ocean and ice shell from future measurements by the instrument packages of NASA's Europa Multiple-Flyby Mission and ESA's JUICE mission, respectively.

The modeling and analysis of the rotational variations of icy satellites with a subsur-

face ocean requires a multidisciplinary approach that includes the application of fields like geophysics, rotational dynamics, continuum mechanics, rheology and tidal dynamics (see Figure 1.1 for an schematic overview of the interaction between these fields). As can be deduced from Figure 1.1, a substantial part of the developed rotational model deals with the determination of the viscoelastic tidal response of the satellite at the surface and internal boundaries. The viscoelastic modeling of the tidal response of an icy satellite is based on three aspects: 1) the definition of interior models that are consistent with the constraints provided by the measurement of the degree-2 gravity field of the satellite and current knowledge on the rheological properties of the materials expected in the interior, 2) the development of a framework to determine how a given interior model responds to the applied tidal forcing, and 3) the definition of the tidal forcing. Chapter 2 concentrates on the definition of several plausible interior models of Europa and Ganymede upon which the tidal and rotational models will be applied. Due to the large uncertainty driven by the limited knowledge of the internal structure and composition of icy satellites, it has been considered to be acceptable for our purposes to model the interior as consisting of a series of concentric spherically symmetric layers with homogeneous properties. Chapter 3 is devoted to the development of a fully analytical method (normal mode method) to determine the viscoelastic response to tidal forces at the surface and internal interfaces of an icy satellite with a global subsurface ocean. This Chapter is an updated version of Appendix A in [Jara-Orué and Vermeersen \[2011\]](#).

Chapters 4 and 5 discuss the effects of tides on icy satellites. Chapter 4 provides the theoretical background required for the determination of the tidal response at the surface (and internal boundaries) of an icy satellite using the normal mode method developed in Chapter 3. This Chapter is subdivided in three parts dealing with: 1) the definition of the tidal forcing field (static, diurnal and NSR) acting on an icy satellite in terms of its potential, 2) the determination of consistent expressions to calculate the tidal deformation at the surface of an icy satellite, and 3) the development of an analytical model based on the normal mode method to determine the surface stresses at the surface due to diurnal tides and NSR tides. Chapter 5 is devoted to the application of the theoretical models presented in Chapter 4 to calculate the tidal deformation at the surface of several interior models of Europa and Ganymede in order to study the relation between the tidal response and the geophysical properties of the interior. In addition, Chapter 5 presents the application of the developed tidal stress model to the case of Europa in order to construct variable patterns of surface stresses that may have led to the formation of the large variety of lineaments on Europa's surface. A detailed analysis of the correlation between the stress field and the observed surface features is beyond the scope of this thesis. However, the model developed in this thesis has been used by [Rhoden et al. \[2013\]](#) with the goal of characterizing the rotation history of Europa's shell from studying such correlation.

The core of the rotational model is discussed in Chapters 6 and 7. Chapter 6 provides a general theoretical description of the model applied to the study of the rotational dynamics of triaxial icy satellites with a subsurface ocean. The rotational model, as presented in this Chapter, extends on existing differential rotational models developed for the study of the rotation of Earth's outer fluid core and solid inner core [e.g. [Sasao et al., 1980](#), [Mathews et al., 1991](#), [Dehant et al., 1993](#), [Szeto and Xu, 1997](#), [Greff-Lefftz et al.,](#)

2000, Dehant and Mathews, 2007, Dumberry, 2009], and emphasizes on the modeling differences that arise from the triaxial hydrostatic figure of icy satellites as well as from the contribution of tides to the rotational dynamics. The description presented in Chapter 6 is, however, not meant to include a detailed discussion about the specific applications of the model (i.e. librations, NSR or TPW). Chapter 7 provides a detailed discussion on the application of the rotational model introduced in Chapter 6 to the study of the forced longitudinal librations driven by Jupiter's gravitational torque on the triaxial shape of a deformable Europa with a subsurface ocean. As part of the main objective of this thesis (see Section 1.2), the main purpose of this Chapter is to analyze the relation between the amplitude of the surface librations and the properties that characterize the upper layers of Europa's interior.

Finally, in Chapter 8, the most important results and conclusions obtained throughout this thesis are presented in a summarized way. In addition, a list of recommendations for further research is provided.

2

MODELING THE INTERIOR OF ICY SATELLITES

2.1. INTRODUCTION

The determination of the tidal response of an icy satellite and the subsequent analysis of its rotational variations require the initial definition of an internal structure upon which the tidal and rotational models will be later applied. Due to the large uncertainty driven by the limited knowledge of the internal structure and composition of icy satellites, it is acceptable to model the interior as consisting of a series of concentric spherically symmetric layers with homogeneous properties. In this Chapter, we provide the geophysical context for the parametrization of those layer properties. First, in Section 2.2, the structural properties (i.e. size and density) are constrained by the measured values for the mass and mean moment of inertia for the particular cases of Europa and Ganymede. The parametrization of the rheological properties (i.e. rigidity and viscosity) follows in Section 2.3, where we also discuss why the Maxwell viscoelastic model is adopted to describe the rheological behavior of the internal solid layers of both Europa and Ganymede.

2.2. STRUCTURAL MODELING: DEFINITION OF INTERNAL LAYERS

Based on the simple constant density model of [Sohl et al. \[2002\]](#), the internal structure of a generic icy satellite is approximated by a series of n concentric spherical material layers of constant density. The size and density characterizing each of these material layers need to be such that the complete interior model of the satellite satisfies the imposed constraints on the radius (R_s), mass (M_s) and mean moment of inertia (I_s) of the satellite, which for a layered planetary body are given by [\[Sohl et al., 2002, Harada and Kurita,](#)

2006]:

$$R_s = \sum_{i=1}^n (r_i - r_{i-1}), \quad (2.1)$$

$$M_s = \frac{4}{3}\pi \sum_{i=1}^n \rho_i (r_i^3 - r_{i-1}^3), \quad (2.2)$$

$$I_s = \frac{8}{15}\pi \sum_{i=1}^n \rho_i (r_i^5 - r_{i-1}^5), \quad (2.3)$$

where r_i and ρ_i refer to the outer radius and density of a layer i (with $i = 1$ being the deepest layer and $i = n$ being the uppermost layer)¹.

The required constraints on the radius, mass and mean moment of inertia have been, so far, only determined for six icy satellites, namely: Europa, Ganymede, Callisto, Enceladus, Rhea and Titan (see Table 2.1). The number of icy satellites for which all constraints are determined is limited by current knowledge about the mean moment of inertia I_s , which is derived from the measured degree-2 gravity field coefficients (i.e. J_2 and C_{22}) of the satellite under the assumption of hydrostatic equilibrium. For synchronously rotating satellites deformed by rotation and tides, such as the regular icy satellites mentioned above, the relation between the mean moment of inertia I_s and the measured value of J_2 is given by Radau's approximation [e.g. Hubbard, 1984, Van Hoolst et al., 2008]:

$$\frac{I_s}{M_s R_s^2} = \frac{2}{3} \left[1 - \frac{2}{5} \left(\frac{25}{4} \frac{q_r}{\frac{3}{2} J_2 + \frac{5}{4} q_r} - 1 \right)^{0.5} \right], \quad (2.4)$$

where the parameter q_r is defined as the ratio of the centrifugal acceleration to the gravitational acceleration, i.e. $q_r = (\omega^2 R_s^3)/(GM_s)$. From a physical perspective, the normalized mean moment of inertia $\frac{I_s}{M_s R_s^2}$ gives an indication of the mass distribution within the interior of a planetary body: a ratio $\frac{I_s}{M_s R_s^2} = 0.4$ corresponds to a uniform density distribution throughout the interior, while $\frac{I_s}{M_s R_s^2} < 0.4$ indicates that the density increases towards the center of the body. The latter is usually the case for planetary bodies, because dense materials tend to sink to deeper parts of the interior - a process commonly known as differentiation - and as a consequence of material compression at higher pressures. As shown by the values of $\frac{I_s}{M_s R_s^2}$ depicted in the last column of Table 2.1, the interiors of most icy satellites show some degree of differentiation, with Ganymede being strongly differentiated and Rhea being nearly homogeneous.

Due to the assumption of hydrostatic equilibrium, Radau's approximation can be alternatively expressed in terms of the gravity coefficient C_{22} after substitution of the hydrostatic condition $J_2 = \frac{10}{3} C_{22}$ into Equation 2.4. The resulting expression for Radau's approximation is more convenient for the determination of the ratio $\frac{I_s}{M_s R_s^2}$ of planetary satellites for which the near-equatorial geometry of the spacecraft encounters did not allow for independent determination of J_2 , which required near-polar encounters. So far,

¹in Equations 2.1 to 2.3, $r_0 = 0$.

Table 2.1: Measured values for the mean radius, mass, J_2 , C_{22} and I of icy satellites Europa, Ganymede, Callisto, Enceladus, Rhea and Titan. Values for the radii are obtained from Archinal et al. [2011]. Values for the masses are taken from JPL's Solar System Dynamics database [NASA, 2014]. Values for the gravity coefficients and normalized mean moment of inertia are from Anderson et al. [1998], Anderson et al. [1996], Anderson et al. [2001], Iess et al. [2014], Anderson and Schubert [2010] and Iess et al. [2010], respectively. In the cases of Europa, Ganymede, Callisto and Rhea, the coefficients J_2 are derived in accordance with the hydrostatic condition $J_2 = \frac{10}{3}C_{22}$.

Satellite	Mean radius [km]	Mass [kg]	J_2 ($\times 10^{-6}$) [-]	C_{22} ($\times 10^{-6}$) [-]	I/MR^2 [-]
Europa	1560.8	4.799844E22	438.3	131.5	0.346
Ganymede	2631.2	1.481859E23	127.3	38.2	0.312
Callisto	2410.3	1.075937E23	32.7	10.2	0.355
Enceladus	252.1	1.079446E20	5435.2	1549.8	0.335
Rhea	763.5	2.307089E21	892.0	267.6	0.391
Titan	2574.7	1.345525E23	31.8	9.98	0.341

independent determination of J_2 has only been possible for Titan and Enceladus [Iess et al., 2010, 2012, 2014], while the determination of J_2 of the Galilean satellites and Rhea has followed by a priori constraining its value to the measured C_{22} through the hydrostatic condition [Anderson et al., 1996, 1998, 2001, Anderson and Schubert, 2010, Iess et al., 2007]. Independent determination of J_2 and C_{22} enables to test the hydrostatic assumption for both Titan and Enceladus, showing that the ratio J_2/C_{22} is consistent with the hydrostatic condition in Titan's case [Iess et al., 2010]. On the other hand, the ratio J_2/C_{22} modestly deviates from the hydrostatic condition (by about $\sim 5\%$) for Enceladus, most likely as a result of strong topographic compensation [Iess et al., 2014].

The interior modeling algorithm described by Equations 2.1 to 2.3 results, however, in an underdetermined system of equations, even for the simple case of a two-layered model. Therefore, additional constraints and/or assumptions on the composition (i.e. density) of certain material layers are required to confine the number of potential solutions for the internal structure. For example, the density of the ice shell and the ocean (if present) are commonly restricted in the modeling to values representative for the density of ice-I² and liquid water, respectively.

In addition, the interface between the subsurface ocean and high-pressure ice layer, if present, is determined in accordance with the phase diagram of water (see Figure 2.1). To that end, first the pressure $p(r)$ at the liquid-solid interfaces is calculated using the hydrostatic relation

$$p(r) = \int_r^{R_s} g(r')\rho(r')dr', \quad (2.5)$$

where $g(r)$ is the acceleration of gravity defined by

$$g(r) = \frac{4\pi G}{r^2} \int_0^r \rho(r')r'^2 dr', \quad (2.6)$$

²Phase of ice at pressures lower than ~ 210 MPa (see Figure 2.1).

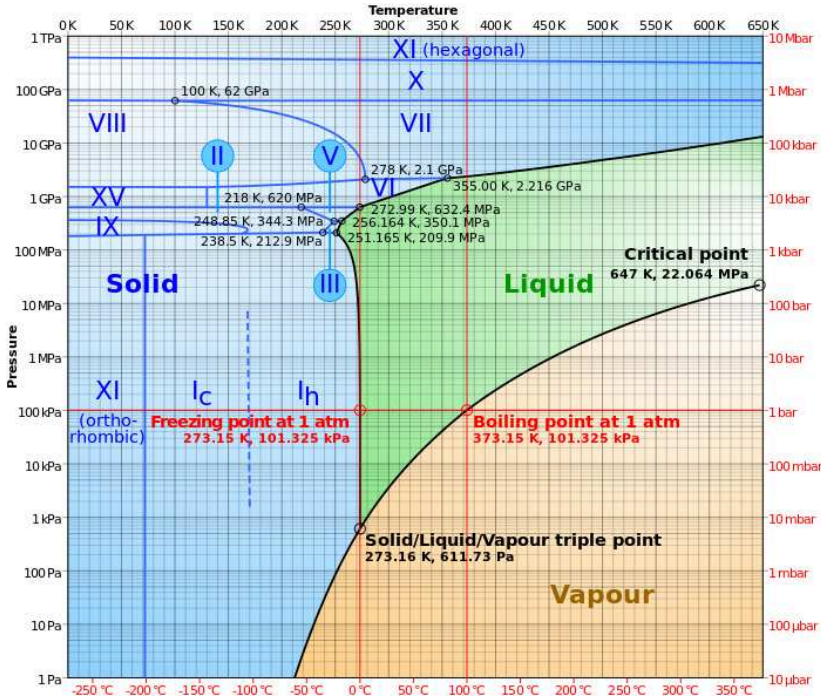


Figure 2.1: Phase diagram of water as a logarithmic-linear chart with pressures from 1 Pa to 1 TPa and temperatures from 0 K to 650 K, based on data in presented in [Chaplin \[2015\]](#) (illustration: Wikipedia).

with G being the universal gravitational constant.

The high-pressure (HP) ice layer may be stratified into ice phases ice-III, ice-V and ice-VI depending on the pressure and temperature conditions in the interior of the satellite. On this regard, thermal models of the density profile of Ganymede's ice layers suggest that the configuration of its HP-ice layer should be largely dominated by ice-V and (especially) ice-VI for different values for the melting temperature of ice-I and the salinity of the putative water ocean [[Vance et al., 2014](#)]. We adopt this result to simplify the interior modeling in this thesis by assuming that the density profile of the HP-ice layer of icy satellites does not include ice-III. As a result, all interior models obtained from Equations 2.1 to 2.3 for which the pressure at the HP-ice/ocean interface is outside the range $350.1 \text{ MPa} \leq p(r) < 2.216 \text{ GPa}$ will be neglected. Also, models for which the temperature at the HP-ice/ocean interface is lower than at the bottom of the ice-I shell will be neglected, as we assume that the temperature within the ocean layer is either constant or increases with depth. The temperature at the interfaces between liquid water and the relevant phases of ice can be determined using the Simon-Glatzel formulation defined by [[Choukroun and Grasset, 2007](#)]

$$T_m = T_{ref} \left(1 + \frac{p_m - p_{ref}}{a} \right)^{1/c}, \quad (2.7)$$

Table 2.2: Empirical parameters for the melting curves of ice-I, ice-V and ice-VI as derived from experimental data [Choukroun and Grasset, 2007].

Ice phase	T_{ref} [K]	p_{ref} [MPa]	a [MPa]	c [-]
Ice-I	273.16	6.11657E-4	-414.5	8.38
Ice-V	256.43	355.0	373.6	8.66
Ice-VI	272.73	618.4	661.4	4.69

where T_m and p_m are the temperature and pressure at the interface with liquid water, T_{ref} and p_{ref} are the temperature and pressure at the triple points³, and a and c are empirical parameters derived from experimental data. Values for these parameters for ice-I, ice-V and ice-VI are shown in Table 2.2.

In the following subsections, the interior modeling algorithm described throughout this Section will be applied to icy satellites Europa and Ganymede to derive a range of interior models that will be used in the following Chapters for the study of the tidal response and rotational dynamics.

2.2.1. APPLICATION TO EUROPA: THE CASE OF A LIQUID WATER LAYER IN DIRECT CONTACT WITH A ROCKY INTERIOR

Europa's measured normalized moment of inertia $\frac{I_s}{M_s R_s^2} = 0.346$ indicates a differentiated interior and suggests the presence of at least three concentric material layers [Anderson et al., 1998]: a metallic core, a silicate mantle and a water layer (ice-I and liquid water). Due to the similar densities of liquid water and ice-I, gravity data cannot be used to distinguish between these two phases of water. Nonetheless, the existence of a subsurface ocean is strongly supported by Galileo's detection of an induced magnetic field [e.g. Khurana et al., 1998, Kivelson et al., 2000], by models built to explain the formation of unique surface features such as cycloids [e.g. Hoppa et al., 1999b, Lee et al., 2005, Hurford et al., 2007, 2009, Rhoden et al., 2010] and chaos terrain [e.g. Greenberg et al., 1999, O'Brien et al., 2002, Sotin et al., 2002, Schmidt et al., 2011], and by theoretical models dealing with the thermal state and evolution of the ice-I shell [e.g. Ojakangas and Stevenson, 1989b, Hussmann et al., 2002, Tobie et al., 2003, Hussmann and Spohn, 2004]. As a result, the ice-I shell and the water ocean will be treated as separate layers in our modeling.

Application of Equations 2.1 to 2.3 to the proposed four-layered interior of Europa results in eight parameters, from which three are assumed to be known: the outer radius and density of the ice-I shell ($r_4 = R_s$, $\rho_4 = \rho_I$), and the density of the subsurface ocean ($\rho_3 = \rho_w$). In addition, in our simplified modeling, the three remaining radii are treated as free parameters. These parameters are allowed to vary within a predetermined range of values (see Table 2.3 for the corresponding values), as long as $r_1 < r_2 < r_3 < R_s$. Then,

³Triple point of ice-I, liquid water and water vapor is the reference temperature-pressure coordinate for ice-I; triple point of ice-III, ice-V and liquid water is the reference for ice-V; and triple point of ice-V, ice-VI and liquid water is the reference for ice-VI.

Table 2.3: (Range of) Values for the radius and density of the four layers considered for the modeling of the internal structure of Europa. ⁽¹⁾ In the modeling, the lower boundary for the outer radius of the water ocean should always be larger than the upper boundary for the outer radius of the mantle, i.e. $r_3 > r_2$ for all cases. ⁽²⁾ Used as compositional constraints only after determination of the solutions of Equation 2.8.

Layer	Index	Outer Radius [km]	Density [kg m ⁻³]
Metallic Core	1	180 - 750	5330 - 7800 ⁽²⁾
Silicate Mantle	2	1392 - 1482 ⁽¹⁾	3222 - 4457 ⁽²⁾
Water Ocean	3	1442 ⁽¹⁾ - 1557	1000
Ice-I Shell	4	1562	937

Equations 2.2 and 2.3 can be conveniently written as a system of equations in terms of the unknown densities of the core (ρ_1) and the mantle (ρ_2), i.e.:

$$\begin{pmatrix} \frac{4}{3}\pi r_1^3 & \frac{4}{3}\pi(r_2^3 - r_1^3) \\ \frac{8}{15}\pi r_1^5 & \frac{8}{15}\pi(r_2^5 - r_1^5) \end{pmatrix} \begin{pmatrix} \rho_1 \\ \rho_2 \end{pmatrix} = \begin{pmatrix} M_s - \frac{4}{3}[\rho_w(r_3^3 - r_2^3) + \rho_I(R_s^3 - r_3^3)] \\ I_s - \frac{8}{15}[\rho_w(r_3^5 - r_2^5) + \rho_I(R_s^5 - r_3^5)] \end{pmatrix}. \quad (2.8)$$

The computed densities ρ_1 and ρ_2 cannot take any possible value, since these densities need to be representative for the expected composition of, respectively, the core and the mantle. Based on the study of Anderson et al. [1998], Europa's metallic core is consistent with a Fe-composition or with a Fe-FeS eutectic composition⁴. As a result, the density of the core may range between $\rho_1 = \rho_{FeS} = 5330 \text{ kg m}^{-3}$ and $\rho_1 = \rho_{Fe} = 7800 \text{ kg m}^{-3}$ [e.g. Sohl et al., 2002]. The existence of a metallic core is not consistent with the presence of a hydrated mantle, as the differentiation of a core requires far larger temperatures than the ones required for the separation of hydrous phases [Anderson et al., 1998, Kuskov and Kronrod, 2005, Schubert et al., 2009]. Hence, the density of Europa's mantle should correspond to the one of olivine, thereby ranging between 3222 kg m^{-3} for a pure forsterite composition and 4447 kg m^{-3} for a pure fayalite composition [e.g. Sohl et al., 2002]. Solutions for the densities ρ_1 and ρ_2 that do not satisfy the previously discussed compositional constraints are thus neglected for further analysis.

In Figure 2.2, the thickness of each material layer is presented against the derived densities of the innermost layers; for all generated four-layered models of Europa's internal structure. Among the various patterns that can be observed in Figure 2.2, we focus primarily on the ones that illustrate the relation between the thickness of Europa's upper layers and the structural properties of the mantle and the core. It can be observed that the total thickness of the water layer is largest for interior models with a large high-density silicate mantle ($r_2 - r_1 \approx 1200 \text{ km}$, $\rho_2 \approx 3800 \text{ kg m}^{-3}$) and a small metallic core ($r_1 \approx 200 \text{ km}$), whereas thin water layers are only possible in combination with a relatively small forsterite mantle ($r_2 - r_1 \approx 800 - 900 \text{ km}$) and a large metallic core ($r_1 > 540 \text{ km}$). Figure 2.2 also shows that the density of the core does not seem to constrain the thickness of the entire water layer, as interior models with either thin or thick water layers are theoretically compatible with the entire range of possible densities for Europa's

⁴A eutectic Fe-FeS composition is defined as a mixture of Fe and FeS at such proportions that the melting temperature of the compound is as low as possible.

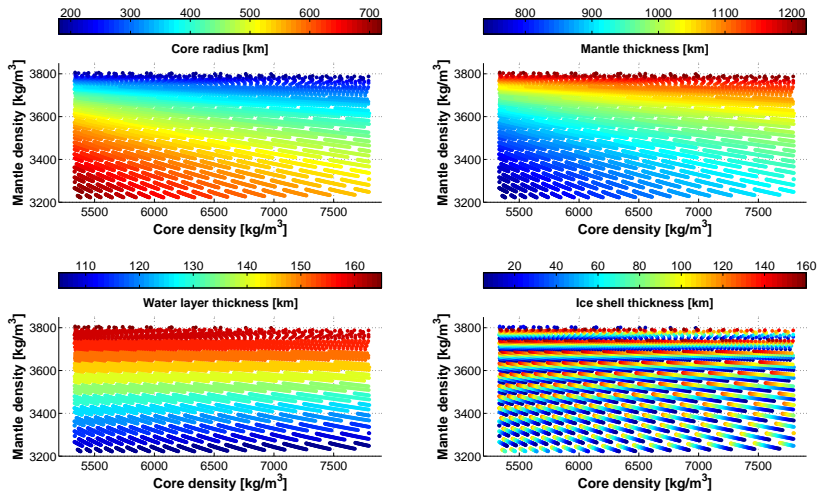


Figure 2.2: Structural properties of the generated interior models of Europa as a function of the derived densities of the core and the mantle. All interior models satisfy the imposed conditions on average density and mean moment of inertia, as well as compositional constraints for both the core and the mantle. (*up left:*) radius of the metallic core; (*up right:*) thickness of the silicate mantle; (*down left:*) thickness of the entire water layer (i.e. water ocean and ice-I shell combined); (*down right:*) thickness of the ice-I shell. All interior models are computed for the densities $\rho_w = 1000 \text{ kg m}^{-3}$ and $\rho_I = 937 \text{ kg m}^{-3}$, in accordance with the range of values presented in Table 2.3.

metallic core.

On the other hand, due to the similar density of liquid water and ice-I, it is less straightforward to observe clear patterns relating the thickness of the ice-I shell to variations of the other parameters that characterize the interior. Nevertheless, Figure 2.2 shows that - for a fixed value for the radius of both the core and the mantle⁵ - the thickness of the ice-I shell increases with increasing mantle density and decreasing core density. This observation is important in the sense that it shows that the densities of the innermost layers (core and mantle) cannot be kept fixed while varying the thickness of the ice-I shell, because the interior models as a whole will no longer satisfy the imposed constraints on average density and mean moment of inertia. The choice to fix the radii of the innermost layers for the construction of a reduced set of model(s) of Europa's interior, which is shown in Table 2.4, is mainly based on the larger effect that variations in the properties of the upper layers have on the tidal and rotational response at the surface of Europa, as will be shown in later Chapters.

⁵In Figure 2.2, interior models with a fixed size for the innermost layers but with a different value for the thickness of the ice-I shell are arranged in diagonals bars.

Table 2.4: Structural parameters defining the reduced set of general 4-layered interior models of Europa. ⁽¹⁾ The densities of the core and the silicate mantle depend on the thickness of the water shell, as the entire model needs to satisfy the imposed conditions on average density and mean moment of inertia.

Layer	Outer Radius [km]	Density [kg·m ⁻³]
Metallic Core	600	(1)
Silicate Mantle	1432	(1)
Water Ocean	1462 – 1557	1000
Ice-I Shell	1562	937

2.2.2. APPLICATION TO GANYMEDE: THE CASE OF A LIQUID WATER LAYER SANDWICHED BETWEEN ICE LAYERS

Ganymede's low normalized mean moment of inertia $\frac{I_s}{M_s R_s^2} = 0.312$ indicates a strongly differentiated interior with a large concentration of mass towards the center of the satellite [Anderson et al., 1996]. In combination with the detection of an intrinsic magnetic field [Kivelson et al., 1996] and the low average density (1936 kg m⁻³), the gravity data suggest that Ganymede's interior is differentiated into at least three material layers: a metallic core, a silicate mantle and a thick water layer on top. In addition, due to the moon's low mean density, Ganymede's water layer (ice and liquid water) is expected to be thick enough such that the pressure within the layer may lead to phase transitions from liquid water to ice-V or ice-VI [e.g. Sohl et al., 2002]. As a result, the basic structural model of Ganymede's interior will consist of five concentric homogeneous material layers: a metallic core, an olivine mantle, a high-pressure ice (HP-ice) layer, a subsurface water ocean and an ice-I shell.

The proposed five-layered models of Ganymede's interior are defined by ten structural parameters, from which four are assumed to be known, i.e.: the outer radius and density of the ice-I shell ($r_5 = R_s$, $\rho_5 = \rho_I$), the density of the subsurface ocean ($\rho_4 = \rho_w$) and the density of the HP-ice layer ($\rho_3 = \rho_{hp}$). Moreover, as in the case of Europa's modeling, the remaining radii are considered as free parameters (see Table 2.5 for the used ranges). The unknown densities of the core and the mantle are then determined using

Table 2.5: (Range of) Values for the radius and density of the five layers considered for the modeling of the internal structure of Ganymede. ⁽¹⁾ Used as compositional constraints only after determination of the solutions of Equation 2.9. ⁽²⁾ Value corresponding to the density of ice-VI [Vance et al., 2014].

Layer	Index	Outer Radius [km]	Density [kg m ⁻³]
Metallic Core	1	340 - 900	5330 - 7800 ⁽¹⁾
Silicate Mantle	2	1400 - 2000	3222 - 4457 ⁽¹⁾
HP-ice Layer	3	2184 - 2434	1346 ⁽²⁾
Water Ocean	4	2484 - 2594	{1000, 1050, ..., 1200}
Ice-I Shell	5	2634	{900, 937, 1000}

the imposed constraints on the mass and mean moment of inertia, which are defined by Equations 2.2 and 2.3. For the particular case of Ganymede's interior modeling, these expressions can be conveniently written as:

$$\begin{pmatrix} \frac{4}{3}\pi r_1^3 & \frac{4}{3}\pi(r_2^3 - r_1^3) \\ \frac{8}{15}\pi r_1^5 & \frac{8}{15}\pi(r_2^5 - r_1^5) \end{pmatrix} \begin{pmatrix} \rho_1 \\ \rho_2 \end{pmatrix} = \mathbf{MI}_s, \quad (2.9)$$

with

$$\mathbf{MI}_s = \begin{pmatrix} M_s - \frac{4}{3}\pi[\rho_{hp}(r_2^3 - r_2^3) + \rho_w(r_4^3 - r_3^3) + \rho_I(R_3^3 - r_4^3)] \\ I_s - \frac{8}{15}\pi[\rho_{hp}(r_3^5 - r_2^5) + \rho_w(r_4^5 - r_3^5) + \rho_I(R_5^5 - r_4^5)] \end{pmatrix}.$$

The numerical values that characterize the properties of the constructed models of Ganymede's interior are depicted in Figure 2.3, where the thickness of some of Ganymede's internal layers (core, mantle, water and ice-I shell) are displayed against the derived values for the densities of the core and the mantle. Despite the addition of a HP-ice layer between the ocean and the silicate mantle, most patterns in Figure 2.3 are roughly similar to the ones encountered in the analysis of Europa's interior modeling (Figure 2.2), i.e. the thickest water layers ($r_5 - r_2 > 900$ km) occur usually in combination with a small metallic core and a large and dense silicate mantle, whereas the thinnest water layers ($r_5 - r_2 < 800$ km) require a large metallic core and a large silicate mantle. The observed patterns are, however, less pronounced than for the case of Europa's interior modeling

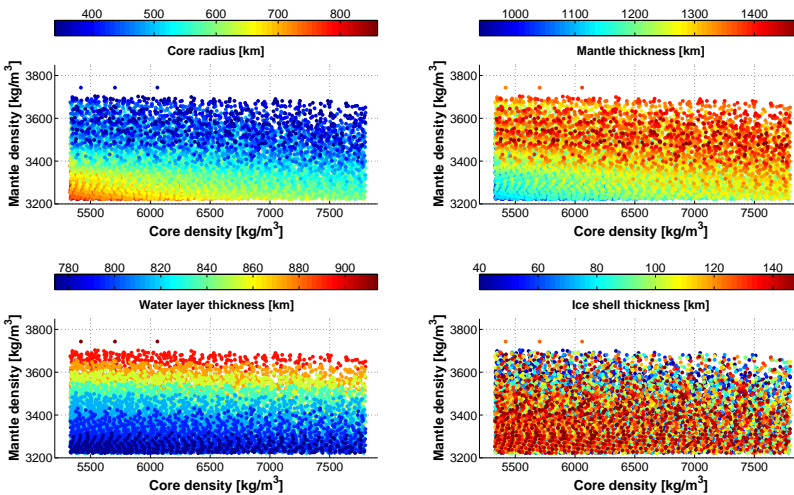


Figure 2.3: Structural properties of the generated interior models of Ganymede as a function of the derived densities of the core and the mantle. All interior models satisfy the imposed conditions on average density and mean moment of inertia, as well as compositional constraints for both the core and the mantle. (*up left:*) radius of the metallic core; (*up right:*) thickness of the silicate mantle; (*down left:*) thickness of the entire water layer (i.e. HP-ice, water ocean and ice-I layers combined); (*down right:*) thickness of the ice-I shell. All interior models are computed for the densities $\rho_w = 1100 \text{ kg m}^{-3}$ and $\rho_I = 937 \text{ kg m}^{-3}$, in accordance with the range of values presented in Table 2.5.

Table 2.6: Structural parameters defining the reduced set of general 5-layered interior models of Ganymede used throughout this thesis. ⁽¹⁾ The densities of the core and the silicate mantle depend on the thickness of the the shell, as the entire model needs to satisfy the imposed conditions on average density and mean moment of inertia. ⁽²⁾ The chosen reference value for the radius of the HP-ice layer is 2284 km; however, this single value does not accommodate to the entire range of values for the radius of the water ocean while still satisfying the imposed constraints on mass and mean moment of inertia.

Layer	Outer Radius [km]	Density [kg·m ⁻³]
Metallic Core	720	⁽¹⁾
Silicate Mantle	1820	⁽¹⁾
HP-ice Layer	{2244, 2284, 2314} ⁽²⁾	1346
Water Ocean	2484 – 2594	1100
Ice-I Shell	2634	937

(compare Figures 2.2 and 2.3).

On the other hand, the presence of a HP-ice layer affects the way the thickness of the ice-I shell is related to the densities of the innermost layers. As shown in the fourth panel (down-right) of Figure 2.3, the thickest ice-I shells are mostly concentrated in the lower part of the plot, which corresponds to models with the smallest values for the combined thickness of the water layer. This is opposite to the pattern observed for the generated models of Europa's interior, in which the thickest shells are mostly related to the largest values for the combined thickness of the water layer.

The large amount of generated interior models of Ganymede is, however, unpractical for the study of the tidal and rotational response that will be presented in later chapters. Therefore, it is convenient to reduce the amount of interior models by fixing the values of structural parameters that are known to have a small effect on the response at the surface, such as the size of the innermost layers (mantle and silicate core) and the density of the HP-ice layer [e.g. Moore and Schubert, 2003]. Note that the densities of the core and silicate mantle are not kept fixed to a value, as their values are the result of the application of the constraints on mass and moment applied to the model. The resulting set of reference models of Ganymede's interior is shown in Table 2.6.

2.3. RHEOLOGICAL MODELING OF THE INTERNAL LAYERS OF ICY SATELLITES

Each internal layer is characterized, in addition to their structural properties, by rheological parameters that give a representation of the layer's response to internal and/or external excitations. At short timescales, such as the timescale of the satellite's orbital revolution around its parent planet, the response of the internal layers is most likely to be rather elastic, whereas at long timescales the response is most likely to reach a state of hydrostatic equilibrium. In order to describe the rheological behavior of the satellite's interior at any timescale, we assume that internal solid layers (silicate mantle, ice layers) behave as incompressible viscoelastic bodies while liquid layers (metallic core, water ocean) are treated as incompressible inviscid fluids.

2.3.1. RHEOLOGICAL MODELS

The simplest and most commonly used viscoelastic model in geophysical applications is the Maxwell model, which can be schematically represented by a spring (elastic element) and a dashpot (viscous element) connected in series (see Figure 2.4). According to the definition of this model, the rheology of each internal solid layer is fully described by only two macroscopic parameters, namely the rigidity μ and the steady-state viscosity η . The ratio of these two parameters, the so-called Maxwell time $\tau_M = \frac{\eta}{\mu}$, gives an indication of the timescale at which the material under deformation shows a transition from elastic to viscous behavior. Hence, a Maxwell viscoelastic layer will behave as elastically at timescales much smaller than the Maxwell time (i.e. for $t \ll \tau_M$), whereas it will behave as a fluid body at timescales much larger than the Maxwell time (i.e. for $t \gg \tau_M$). In the Laplace domain, the stress-strain relation that characterizes the linear Maxwell rheology can be written as [Sabadini and Vermeersen, 2004]:

$$\tilde{\sigma}_{ij}(s) = 2\tilde{\mu}(s)\tilde{\varepsilon}_{ij}(s) + \tilde{\lambda}(s) \sum_{k=1}^3 \tilde{\varepsilon}_{kk}(s)\delta_{ij}, \quad (2.10)$$

where σ_{ij} is the deviatoric stress, ε_{ij} is the deviatoric strain, δ_{ij} is the Kronecker delta and s is the Laplace variable. The tilde on top of the elements of the stress and strain tensors denotes the Laplace transform of the original quantities. Furthermore, the compliances $\tilde{\mu}(s)$ and $\tilde{\lambda}(s)$ are given by

$$\tilde{\mu}(s) = \frac{\mu s}{s + \frac{\mu}{\eta}}, \quad (2.11)$$

and

$$\tilde{\lambda}(s) = \frac{(\kappa - \frac{2}{3}\mu)s + \frac{\mu}{\eta}\kappa}{s + \frac{\mu}{\eta}}, \quad (2.12)$$

where κ is the bulk modulus, which in the case of incompressible bodies theoretically approaches infinity.

Another often used linear rheological model is the Burgers model, which is schematically represented by a serial connection of a Kelvin element (spring and dashpot in parallel) and a Maxwell element (spring and dashpot in series), as shown in Figure 2.4. An important property of the Burgers rheological model is that it takes into account the effect of transient creep, due to the incorporation of a Kelvin element, in addition to the steady-state creep already introduced by the Maxwell element [e.g. Ranalli, 1995, McCarthy and Castillo-Rogez, 2013]. As such, a Burgers body experiences instantaneous elastic behavior, followed by transient creep over short timescales, and linear viscous behavior over long timescales. Similar to the Maxwell model, the stress-strain relation that applies to a Burgers body is mathematically defined by Equation 2.10, with the compliances given by [e.g. Yuen and Peltier, 1982, Yuen et al., 1986]

$$\tilde{\mu}(s) = \frac{s \left(s + \frac{\mu_k}{\eta_k} \right) \mu}{s^2 + s \left(\frac{\mu + \mu_k}{\eta_k} + \frac{\mu}{\eta} \right) + \frac{\mu \mu_k}{\eta \eta_k}}, \quad (2.13)$$

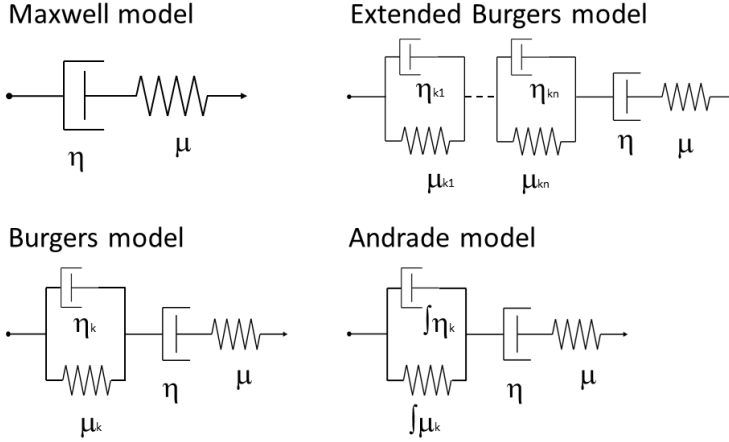


Figure 2.4: Mechanical analogs of linear rheological models, where the spring represents the elastic response and the dashpot controls the viscous relaxation. Based on [McCarthy and Castillo-Rogez \[2013\]](#).

and

$$\tilde{\lambda}(s) = \frac{(\kappa - \frac{2}{3}\mu) s^2 + s \left(\left(\frac{\mu + \mu_k}{\eta_k} + \frac{\mu}{\eta} \right) \kappa - \frac{2}{3} \frac{\mu \mu_k}{\eta_k} \right) + \frac{\mu \mu_k}{\eta \eta_k} \kappa}{s^2 + s \left(\frac{\mu + \mu_k}{\eta_k} + \frac{\mu}{\eta} \right) + \frac{\mu \mu_k}{\eta \eta_k}}, \quad (2.14)$$

where μ_k and η_k are the short-term rigidity and viscosity associated with the Kelvin element.

Other linear rheological models that incorporate transient creep into the material response are the extended Burgers model, in which a series of n Kelvin elements are put in series with a Maxwell element (see Figure 2.4), and the Andrade model, which may be represented by infinite Kelvin elements in series with a Maxwell element [[McCarthy and Castillo-Rogez, 2013](#)]. The main advantage of these more elaborate linear rheological models is that they are able to incorporate a spectrum of characteristic times into the material response, thereby leading to a more realistic frequency-dependent description of the rheology; especially at the short timescales at which the tidal forces act on the icy satellites [[Ranalli, 1995](#), [Castillo-Rogez et al., 2011](#), [McCarthy and Castillo-Rogez, 2013](#)]. On the other hand, the main disadvantage of these models is the added complexity, which either requires the introduction of several poorly constrained parameters to characterize the rheological behavior of the material (extended Burgers) or the introduction of poorly known empirical constants for which their dependence on the material properties is not yet fully understood (Andrade model).

In addition to recoverable anelastic effects, transient creep may include a non-recoverable component due to plastic deformation of the material. The strain due to this plastic transient component usually has a nonlinear dependence on the stress, which is often described through a power-law rheological relation in which the creep parameters are derived from experimental data [[Ranalli, 1995](#)]. In addition, the steady-state creep

part of the response is the result of various interrelated creep mechanisms that - on an individual basis - may be characterized by a linear dependence on the stress (e.g. diffusion creep) or by a nonlinear power-law dependence on the stress (e.g. dislocation creep), with the corresponding creep parameters being derived from experimental data as well [e.g. Ranalli, 1995, Durham et al., 1997, Goldsby and Kohlstedt, 2001]. As in the case of the previously discussed anelastic models, nonlinear power-law rheologies have the advantage to describe the creep processes experienced by geophysical materials in a more realistic way. However, their inherent nonlinear definition precludes their application in combination with established analytical methods to determine the response of a viscoelastic planetary body (see Chapter 3).

2.3.2. RHEOLOGY OF ICE-I

In accordance with the structural modeling of the interior of icy satellites discussed in Section 2.2, all the models considered in this thesis simulate the presence of a subsurface ocean between the ice-I outer shell and the deep interior of the satellite (silicates and/or high-pressure ices). As a result, the response of the satellite to forces acting at timescales comparable to the satellite's orbital period is expected to be dominated by the properties of the upper material layers, e.g. the rheological properties of the ice-I shell. In this Section, the properties that characterize the transient and steady-state creep regimes of the rheological response of ice-I at conditions relevant to icy satellites will be presented in some detail. This description is considered necessary in order to understand the reasoning behind the selection of a Maxwell (or Burgers) linear rheology to model the rheological behavior of ice-I at all regimes, as well as the limitations introduced by such a choice.

TRANSIENT CREEP REGIME

The transient creep regime of the rheological response of ice-I at conditions relevant for icy satellites has been usually modeled through the use of either the Burgers model [Robuchon et al., 2010] or the Andrade model [Rambaux et al., 2010, Castillo-Rogez et al., 2011, Mitri et al., 2014]. Although both models introduce anelastic transient creep into the rheological response, it is the Andrade description that provides a better fit to experimental data due to its ability to incorporate a frequency-dependent distribution of retardation times within the transient regime [e.g. Ranalli, 1995, Castillo-Rogez et al., 2011]. The creep compliance $J(t)$, which describes the viscoelastic behavior of an Andrade body as a function of time, is commonly defined by [e.g. McCarthy and Castillo-Rogez, 2013]

$$J(t) = \frac{1}{\mu} + \beta t^m + \frac{t}{\eta}, \quad (2.15)$$

where $J(t)$ is the inverse Laplace transform of the compliance $\tilde{J}(s)$, which in turn is defined as the inverse of the compliance $\tilde{\mu}(s)$ applicable to an Andrade body (see e.g. McCarthy and Castillo-Rogez [2013] for an explicit expression for $\tilde{J}(s)$ in the case $s = i\omega$). The effect of anelastic transient creep is introduced by the term βt^m , in which β and m are empirical parameters with measured values in the range $\beta = 10^{-11} - 10^{-13}$ and

$m = 0.3 - 0.4$ at conditions applicable to icy satellites [Rambaux et al., 2010, McCarthy and Castillo-Rogez, 2013]. The parameter β , which from a physical viewpoint is expected to be related to e.g. the mobility and density of dislocations driving transient retardation, determines the amplitude of the anelastic transient effect. As such, for very small values of β ($\sim 10^{-13}$), the contribution of anelasticity to the rheological response of the material becomes negligibly small and the Andrade model starts to approach the Maxwell model [McCarthy and Castillo-Rogez, 2013]. On the other hand, the empirical parameter m does not have a clear dependence on the material properties, although it has been suggested that its value may be linked to the presence of impurities and non-uniform grain sizes within the material [McCarthy and Castillo-Rogez, 2013].

Despite its more realistic description of the rheological behavior of ice-I at short timescales, the Andrade rheological model has been nearly exclusively applied in research that involves the determination of tidal heat dissipation within the ice-I shell [e.g. Castillo-Rogez et al., 2011, Shoji et al., 2013], while the simpler Maxwell model still remains the most used in research dealing with tidal deformation and/or stresses at the surface of icy satellites [e.g. Moore and Schubert, 2000, Wahr et al., 2009, Jara-Oru e and Vermeersen, 2011, Sohl et al., 2014]. This seemingly contradictory use of rheological models is largely based on the relation between the studied tidal phenomena and the properties of the interior. The tidal dissipation rate, which is defined as the amount of tidal strain energy that can be converted into heat by viscous friction within the ice-I shell, is directly proportional to the contribution of attenuation to the tidal response [e.g. Ojakangas and Stevenson, 1989b, Hussmann et al., 2002, Hussmann and Spohn, 2004, Tobie et al., 2005, Roberts and Nimmo, 2008, Sotin et al., 2009, Beuthe, 2013]. As a result, the inclusion of anelasticity into the rheological response of the material can substantially improve the modeling of tidal dissipation in the ice-I shell of icy satellites [Castillo-Rogez et al., 2011, Shoji et al., 2013]. On the other hand, tidal deformation and stresses are directly proportional to the amplitude of the tidal response, which at the short timescales of diurnal tides is dominated by its elastic part [e.g. Wahr et al., 2009, Jara-Oru e and Vermeersen, 2011, Sohl et al., 2014, Mitri et al., 2014]. Hence, the addition of anelasticity is not expected to lead to significant improvements in the modeling of tidal deformations and stresses, as shown by Mitri et al. [2014] for the case of Titan's tidal deformation and Rambaux et al. [2010] for the case of the amplitude of forced librations on Enceladus.

STEADY-STATE CREEP REGIME

The steady-state creep regime of the rheological response of ice-I has been studied through several deformation experiments on polycrystalline ice-I at temperature and pressure conditions relevant to icy satellites. Based on these laboratory experiments, the behavior of planetary ice-I can be described by the combination of four deformation mechanisms, i.e. [Durham et al., 1997, 2001, Goldsby and Kohlstedt, 2001, Barr and Showman, 2009]:

- *Dislocation creep*: in the high stress regime ($\sigma > 1$ MPa), creep in ice is governed by the movement of dislocations. The mechanism of dislocation creep is characterized by a high exponential dependence on the applied stress ($n = 4$) and by being

independent from the grain size d .

- *Basal slip*: in the intermediate stress regime ($0.01\text{MPa} < \sigma < 1\text{MPa}$), creep is governed by grain-size-sensitive (GSS) mechanisms. Basal slip, which is the deformation of ice grains along the basal planes of their crystals, is characterized by a modest exponential dependence on the applied stress ($n = 2.4$) and by being insensitive to the grain size.
- *Grain boundary sliding (GBS)*: also in the intermediate stress regime, GBS creep occurs in conjunction with basal slip in order to accommodate deformation in crystals with planes which are not appropriately aligned for basal slip to occur. This deformation mechanism is characterized by a weakly exponential dependence on the applied stress ($n = 1.8$) and by being sensitive to the grain size. As such, the properties of the deformation mechanisms that characterize the intermediate stress regime (GBS and basal slip) lead to weakly non-Newtonian deformation of the material within this stress regime.
- *Diffusion creep*: ice-I is expected to deform by diffusion creep at low stresses ($\sigma < 0.1$), at temperatures larger than 180 K and for small grain sizes ($d < 1$ mm). Diffusion is a deformation process in which the strain rate is linearly dependent on the applied stress ($n = 1$) and is sensitive to the grain size.

With the notable exception of diffusion creep, which has not yet been observed in laboratory experiments [Barr and Showman, 2009], the stress-strain rate relation of any creep mechanism of ice-I is commonly defined by⁶

$$\dot{\epsilon} = Ad^{-p'} \sigma^n \exp\left(\frac{-(E^* + pV^*)}{RT}\right), \quad (2.16)$$

where p , d , T and R are the pressure, grain size, temperature and gas constant, respectively. Furthermore, the parameters A , p' , n , E^* and V^* are empirically-derived flow parameters, which respectively stand for a factor associated with the material properties, the grain size exponent, the stress exponent, the activation energy and the activation volume [e.g. Ranalli, 1995].

Since a set of different creep mechanisms independently dominates at a given stress regime, the rheological behavior of ice-I over a broad range of conditions can be described by a composite flow law, i.e. [Goldsby and Kohlstedt, 2001]

$$\dot{\epsilon} = \dot{\epsilon}_{diff} + \left(\frac{1}{\dot{\epsilon}_{gbs}} + \frac{1}{\dot{\epsilon}_{bs}}\right)^{-1} + \dot{\epsilon}_{dis}, \quad (2.17)$$

where the subscripts *diff*, *gbs*, *bs* and *disl* refer to diffusion creep, grain boundary sliding, basal slip and dislocation creep, respectively.

Since the stresses and strain rates acting within the ice-I shells of icy moons are expected to be in the low stress regime, the rheological behavior of ice-I at all grain sizes is most likely dominated by (volume) diffusion creep [Moore, 2006]. An important advantage of a rheology dominated by diffusion creep is that it can be largely described by

⁶For an expression relevant for diffusion creep, the reader is referred to e.g. Goldsby and Kohlstedt [2001].

a Newtonian rheological model, as diffusion creep depends linearly on the stress. However, in such models, the viscosity would still depend on the unknown grain size and other relevant diffusion parameters which are yet to be measured for ice-I at planetary conditions [Nimmo and Manga, 2009]. As a result of these uncertainties, it is reasonable to adopt a simple Maxwell rheological model, with Newtonian viscosity η , in order to give a first order description of the steady-state creep of ice-I.

2.3.3. RHEOLOGICAL PARAMETRIZATION OF THE INTERNAL LAYERS OF ICY SATELLITES

Even under the assumption of a Maxwell rheology, the rheological parameters that characterize the internal layers of icy satellites are largely uncertain or even unknown. Therefore, in this thesis, we consider all previously defined internal layers to be homogeneous in terms of their rheology. An exception is made for the ice-I shell, which is subdivided into two layers of different viscosity, but equal rigidity [Wahr et al., 2006], in order to simulate the effect of an effectively elastic icy crust on top of a more ductile and convective lower part of the shell. The introduction of a viscosity contrast within the ice-I shell is consistent with thermal models dealing with stagnant-lid convection in ice-I shells [e.g. Kirk and Stevenson, 1987, Showman et al., 1997, Showman and Han, 2004, Hussmann et al., 2002, Ruiz and Tejero, 2003, Tobie et al., 2003, 2005, McKinnon, 2006, Moore, 2006, Bland et al., 2009, Nimmo and Manga, 2009] and with numerical models dealing with the morphology of impact craters on the surface of icy satellites [e.g. Schenk, 2002, Senft and Stewart, 2011].

Since the properties of the upper layers of an icy satellite are expected to dominate the tidal response, most variations in the rheological parameters in this thesis are introduced in the definition of the rigidity and viscosity of the layers that simulate the ice-I shell. The value of the rigidity of ice-I (μ_I) at planetary conditions is uncertain by about one order of magnitude, with values as low as ~ 0.3 GPa [Vaughan, 1995, Schmeltz et al., 2002, Wahr et al., 2006] and as high as ~ 10 GPa [Moore and Schubert, 2000, Harada and Kurita, 2006] being suggested as appropriate for research on icy satellites. Nevertheless, in the vast majority of research cases, the reference value for the rigidity of ice-I has been taken between 2 GPa and 4 GPa, which is a range that includes the value $\mu_I \approx 2$ GPa obtained from laboratory experiments involving periodic loading (2.5 – 3 hours) of unfractured saline ice at -30°C [Cole and Durell, 1995] and the value $\mu_I \approx 3.5$ GPa obtained from laboratory experiments on several samples of natural and artificial ice [Gammon et al., 1983, Helgerud et al., 2009]. The latter will be used as the reference value for the rigidity of the ice-I shell in our modeling, as it has been widely used as reference value in previous research on tidal problems involving icy satellites [e.g. Tobie et al., 2005, Rappaport et al., 2008, Sotin et al., 2009, Wahr et al., 2009, Jara-Oru e and Vermeersen, 2011, Beuthe, 2013, Shoji et al., 2013, Van Hoolst et al., 2013].

The viscosities of the layers that constitute the ice-I shell are among the least known rheological parameters in the modeling of icy satellites. The viscosity of the upper part of the shell (η_{Ic}), which is assumed to be an effectively elastic layer, may range from 1.0×10^{19} Pa s to 1.0×10^{22} Pa s in accordance with previous research on stresses due to non-synchronous rotation (NSR) [e.g. Harada and Kurita, 2007, Wahr et al., 2009, Jara-

Table 2.7: Range of values for the rheological parameters that characterize the internal layers of icy satellites.

Layer	Parameter	Value	Unit
Silicate Mantle	Rigidity (μ_m)	40 – 100	GPa
	Viscosity (η_m)	$1.0 \times 10^{19} - 1.0 \times 10^{21}$	Pa s
HP-ice layer	Rigidity (μ_{hp})	4.6 – 7.5	GPa
	Viscosity (η_{hp})	$1.0 \times 10^{13} - 1.0 \times 10^{17}$	Pa s
Ductile Ice-I layer	Rigidity (μ_I)	0.3 – 10	GPa
	Viscosity (η_{Id})	$1.0 \times 10^{13} - 1.0 \times 10^{17}$	Pa s
Ice-I crust	Rigidity (μ_I)	0.3 – 10	GPa
	Viscosity (η_{Ic})	$1.0 \times 10^{19} - 1.0 \times 10^{22}$	Pa s

Oru e and Vermeersen, 2011], although larger values are physically possible. On the other hand, the viscosity of the ductile and plausibly convective lower part of the ice shell (η_{Id}) may range from 1.0×10^{13} Pa s to 1.0×10^{17} Pa s, in accordance with the parameter space commonly used in stagnant-lid convection models that assume an Arrhenius relation for the temperature dependence of the viscosity of ice-I [e.g. Deschamps and Sotin, 2001, Hussmann et al., 2002, Showman and Han, 2004, Barr and Showman, 2009].

The rheological parameters of the remaining internal viscoelastic layers are also poorly constrained, as the exact composition of these layers remains unknown. Commonly used values for the rigidity of a HP-ice layer (μ_{hp}) usually range between 4.6 GPa (ice-III) and 7.5 GPa (ice-VI) [Sohl et al., 2002], while the corresponding values for the rigidity of the silicate mantle (μ_m) may range between 40 GPa and 100 GPa [e.g. Moore and Schubert, 2000, Sohl et al., 2002, Harada and Kurita, 2006, Rappaport et al., 2008, Sotin et al., 2009, Beuthe, 2013, Sohl et al., 2014]. As reference values, we adopt $\mu_{hp} = 6.5$ GPa for the high-pressure ice layer and $\mu_m = 65$ GPa for the silicate mantle, because these are values representative for the rigidity of ice-V and olivine, respectively [Sohl et al., 2002]. Moreover, for the unknown viscosity of the silicate mantle (η_m) we adopt values in the range $\eta_m = 1.0 \times 10^{19} - 1.0 \times 10^{21}$ Pa s, whereas for the viscosity of the HP-ice layer (η_{hp}) we assume the same range as for the ductile ice-I layer. The range of values for the rheological parameters that characterize each of the viscoelastic internal layers of icy satellites is summarized in Table 2.7.

Table 2.8: Reference 5-layer model of Europa’s interior.

Layer	Outer Radius [km]	Density [kg m ⁻³]	Rigidity [GPa]	Viscosity [Pa s]
Metallic Core	600	5565.8	0	0
Silicate Mantle	1432	3453.6	65.0	1.0×10^{19}
Water Ocean	1532	1000.0	0	0
Ductile Ice-I Layer	1557	937.0	3.5	1.0×10^{14}
Ice-I Crust	1562	937.0	3.5	1.0×10^{21}

Table 2.9: Reference 6-layer model of Ganymede's interior.

Layer	Outer Radius [km]	Density [kg m ⁻³]	Rigidity [GPa]	Viscosity [Pa s]
Metallic Core	720	5777.9	0	0
Silicate Mantle	1820	3291.5	65.0	1.0×10^{20}
HP-ice Layer	2284	1346.0	6.6	1.0×10^{17}
Water Ocean	2534	1100.0	0	0
Ductile Ice-I Layer	2614	937.0	3.5	1.0×10^{17}
Ice-I Crust	2634	937.0	3.5	1.0×10^{21}

Similar to the rheological parameters of the silicate mantle and HP-ice layer, the state of the metallic core of icy satellites remains unknown. In the case of Ganymede, the observation of an intrinsic magnetic field by Galileo's magnetometer provides a strong evidence for the presence of a molten iron core [Kivelson et al., 1996, Hauck et al., 2006]. However, due to the unknown composition and temperature profile within the core, it is currently not possible to state whether the entire metallic core is fluid. Therefore, the existence of a solid metallic inner core as Ganymede's innermost layer cannot be precluded. In the case of Europa, Galileo's magnetometer did not observe an intrinsic magnetic field [Khurana et al., 1998, Kivelson et al., 2000], meaning that dynamo action does not take place in the core. However, the absence of a dynamo does not constrain the state of the metallic core, as a completely fluid core, a fully solid core and a partially molten core are all consistent with the lack of an intrinsic magnetic field [Schubert et al., 2009]. In this thesis, for simplicity, we assume that the entire core is fluid in order to reduce the number of unconstrained rheological parameters in the modeling.

As a final step, we combine the reference values for the structural and rheological parameters of each internal layer to define the reference interior models of both Europa and Ganymede. These reference models are shown in Tables 2.8 and 2.9, respectively.

3

NORMAL MODE MODELS FOR PLANETARY BODIES WITH INTERNAL LIQUID LAYERS

The content in this Chapter is largely based on the description provided in Section 4 and Appendix A of [Jara-Orué and Vermeersen \[2011\]](#). Nevertheless, the discussion starting in Sections 3.4 deviates from [Jara-Orué and Vermeersen \[2011\]](#) as a result of the introduction of internal boundary conditions at fluid-solid interfaces that take into consideration the effect of differential rotation, which adapts the approach outlined in [Greff-Lefftz et al. \[2000\]](#) for the case of Earth's fluid core to the propagator matrix method discussed in this Chapter.

3.1. INTRODUCTION

As for terrestrial planets, the study of the rotational variations experienced by a deformable icy satellite requires previous knowledge of the viscoelastic response of the interior to the acting excitations. A powerful method to determine the viscoelastic response of a planetary body is based on the use of the correspondence principle [[Peltier, 1974](#)], which states that the response of a spherical, self-gravitating and radially stratified viscoelastic planetary body can be retrieved from the solution of the equivalent elastic problem in either the Fourier or Laplace domain. Although both the Fourier and Laplace descriptions are similar in their representation of the physical laws necessary to compute the response, methods based on a Fourier description often make use of numerical integration techniques to provide a constant complex-valued solution at the frequency of the acting (periodic) forcing [e.g. [Moore and Schubert, 2000](#), [Tobie et al., 2005](#), [Harada and Kurita, 2007](#), [Rappaport et al., 2008](#), [Roberts and Nimmo, 2008](#), [Wahr et al., 2009](#)], whereas methods based on the Laplace description often employ the normal mode approach to provide a time-dependent solution in terms of the relaxation modes of the

interior model [e.g. Sabadini et al., 1982, Wu and Peltier, 1982, Spada et al., 1992, Vermeersen et al., 1996, Mitrović and Milne, 1998, Sabadini and Vermeersen, 2004, Jara-Orué and Vermeersen, 2011]. Due to this methodological difference, the Laplace approach has an advantage in the sense that it leads to a deeper insight into the mechanisms governing the relaxation process. On the other hand, the Fourier approach has the advantage of dealing in a rather straightforward way with compressible rheological models when the response at a single frequency is required.

Throughout this thesis, the normal mode approach will be applied to determine the viscoelastic response of an icy satellite to the acting external and internal excitations. This choice is mainly based on three reasons: 1) to analyze the characteristics of the relaxation process, 2) to study rotational variations at different timescales including the effect of relaxation of the bulges, 3) to take into account the viscoelastic response to non-periodic excitations (e.g. a Heaviside surface loading). Although normal mode models that can deal with compressible rheologies have been developed in the past [e.g. Sabadini and Vermeersen, 2004], the approach followed in this thesis will not take into account the effect of compressibility on the response of the interior. This decision is a trade-off between the added value that can be obtained from including compressibility in the modeling (< 20% influence on the response and hence less than the uncertainty introduced by the poorly known rheology) and the subsequent increase in complexity [e.g. Sabadini and Vermeersen, 2004, Jara-Orué and Vermeersen, 2011].

Furthermore, due to the presence of a subsurface ocean at shallow depths in the interior of icy satellites, conventional normal mode models that make use of the propagator matrix technique (i.e. normal mode models developed for Earth applications) cannot be directly applied to the case of icy moons. This is because mechanical quantities, such as deformations and stresses, cannot be propagated through a fluid as the governing linear momentum equations degenerate within such a layer [Saito, 1974, Chinnery, 1975]. Therefore, a different strategy needs to be applied in which the solution within the fluid is fully described by the Poisson equation [Saito, 1974, Chinnery, 1975] and where boundary conditions are used to connect the fluid solution to the solid solution at liquid-solid interfaces [Chinnery, 1975, Greff-Lefftz and Legros, 1997, Greff-Lefftz et al., 2000]. This strategy is based on previous studies on the response of Earth's fluid core [e.g. Saito, 1974, Chinnery, 1975, Dehant et al., 1993, Greff-Lefftz et al., 2000] and that have been applied to icy satellites harboring an internal ocean using numerical integration techniques [Harada and Kurita, 2006, 2007].

In this Chapter, the complete development of the propagator matrix technique for icy satellites harboring internal oceans will be presented. Section 3.2 provides a brief discussion of the most relevant aspects of the conventional propagator matrix approach used for the determination of the response of solid viscoelastic layers. Propagation through inviscid fluid layers is then introduced in Section 3.3. The required sets of boundary conditions at internal interfaces are then presented in some detail in Section 3.4. Thereafter, in Section 3.5, the theoretical discussion introduced in the aforementioned Sections is used to build the required propagator matrix algorithm applicable to icy satellites with internal oceans. In addition to Jara-Orué and Vermeersen [2011], the description provided here takes into account different types of internal and external excitations and does not only focus on tidal forces. Then, the response at internal interfaces and at the

surface is expressed in terms of Love numbers in Section 3.6.

3.2. CONVENTIONAL NORMAL MODE METHOD

The response of a spherical, self-gravitating and radially stratified viscoelastic planetary body to e.g. tides or surface loads is usually expressed in terms of the so-called radial functions \tilde{y}_1 to \tilde{y}_6 , which define the six components of the spheroidal solution vector $\tilde{\mathbf{y}}(r, s)$. These radial functions are formally defined as [e.g. Peltier, 1974, Sabadini et al., 1982, Wu and Peltier, 1982, Sabadini and Vermeersen, 2004]

$$\tilde{y}_1 = \tilde{U}_l, \quad (3.1)$$

$$\tilde{y}_2 = \tilde{V}_l, \quad (3.2)$$

$$\tilde{y}_3 = 2\tilde{\mu} \frac{\partial \tilde{U}_l}{\partial r} + \tilde{\lambda} \tilde{\chi}_l = \tilde{\sigma}_{rrl}, \quad (3.3)$$

$$\tilde{y}_4 = \tilde{\mu} \left(\frac{\partial \tilde{V}_l}{\partial r} - \frac{\tilde{V}_l}{r} + \frac{\tilde{U}_l}{r} \right) = \tilde{\sigma}_{r\theta l}, \quad (3.4)$$

$$\tilde{y}_5 = -\tilde{\Phi}_l, \quad (3.5)$$

$$\tilde{y}_6 = -\frac{\partial \tilde{\Phi}_l}{\partial r} - \frac{l+1}{r} \tilde{\Phi}_l + 4\pi G \rho_0 \tilde{U}_l = \tilde{Q}_l, \quad (3.6)$$

where \tilde{U}_l is the radial deformation, \tilde{V}_l is the tangential or lateral deformation, $\tilde{\sigma}_{rrl}$ is the radial stress, $\tilde{\sigma}_{r\theta l}$ is the tangential stress, $-\tilde{\Phi}_l$ is the perturbed gravitational potential and \tilde{Q}_l is a function related to the radial derivative of the perturbed potential. Furthermore, the radial functions depend on the radial distance r , the Laplace parameter s and the degree l of the spherical harmonic expansion. The parameters G , ρ_0 and $\tilde{\chi}_l$ are defined as the universal gravitational constant, the unperturbed density of the material and the divergence of the displacement field or dilatation, respectively. The Laplace-transformed compliances $\tilde{\mu}$ and $\tilde{\lambda}$ relevant for a Maxwell rheology are given by Equations 2.11 and 2.12, respectively. These expressions are repeated below for convenience:

$$\tilde{\mu} = \frac{\mu s}{s + \frac{\mu}{\eta}},$$

and

$$\tilde{\lambda} = \frac{(\kappa - \frac{2}{3}\mu) s + \frac{\mu}{\eta} \kappa}{s + \frac{\mu}{\eta}},$$

where κ represents the bulk modulus. In the incompressible case, the bulk modulus κ of the material (and hence also the compliance $\tilde{\lambda}$) approaches infinity whereas the dilatation $\tilde{\chi}_l$ goes to zero. Mathematically, the product $\tilde{\lambda} \tilde{\chi}_l$ in Equation 3.3 remains finite in the incompressible limit and thus needs to be defined for the calculation of stresses (see Section 4.4.2). From a physical viewpoint, the product $\tilde{\lambda} \tilde{\chi}_l$ has the meaning of a mean normal stress [Wu and Peltier, 1982].

An important property of the six radial functions, as defined by Equations 3.1 to 3.6, is

that they are continuous at every internal boundary. Our definition of the radial function \tilde{y}_6 differs from the widely used and also radially continuous definition given in [Alterman et al. \[1959\]](#), which does not include a term proportional to the perturbed potential $\tilde{\Phi}_l$. The reason to include this additional term in our definition of \tilde{y}_6 is to obtain a boundary condition at the surface that directly relates \tilde{y}_6 to the acting forcing. This trait is convenient from a methodological perspective as it allows to split the solution vector at the surface into a constrained set of parameters (\tilde{y}_3 , \tilde{y}_4 and \tilde{y}_6) and an unconstrained set (\tilde{y}_1 , \tilde{y}_2 and \tilde{y}_5) that needs to be solved for [[Sabadini and Vermeersen, 2004](#)].

In the conventional normal mode method, the relevant equations of motion that describe the response of an incompressible viscoelastic body - i.e. conservation of linear momentum and Poisson's equation for the perturbed gravitational potential - are simplified to a set of six coupled first-order ordinary differential equations in terms of the radial functions, i.e. [[Sabadini and Vermeersen, 2004](#)]

$$\frac{d\tilde{y}_1}{dr} = -\frac{2}{r}\tilde{y}_1 + \frac{l(l+1)}{r}\tilde{y}_2, \quad (3.7)$$

$$\frac{d\tilde{y}_2}{dr} = -\frac{1}{r}\tilde{y}_1 + \frac{1}{r}\tilde{y}_2 + \frac{1}{\tilde{\mu}}\tilde{y}_4, \quad (3.8)$$

$$\begin{aligned} \frac{d\tilde{y}_3}{dr} = & \frac{4}{r} \left(\frac{3\tilde{\mu}}{r} - \rho_0 g \right) \tilde{y}_1 - \frac{l(l+1)}{r} \left(\frac{6\tilde{\mu}}{r} - \rho_0 g \right) \tilde{y}_2 + \frac{l(l+1)}{r} \tilde{y}_4 \\ & - \frac{\rho_0(l+1)}{r} \tilde{y}_5 + \rho_0 \tilde{y}_6, \end{aligned} \quad (3.9)$$

$$\frac{d\tilde{y}_4}{dr} = -\frac{1}{r} \left(\frac{6\tilde{\mu}}{r} - \rho_0 g \right) \tilde{y}_1 + \frac{2(2l^2 + 2l - 1)\tilde{\mu}}{r^2} \tilde{y}_2 - \frac{1}{r} \tilde{y}_3 - \frac{3}{r} \tilde{y}_4 + \frac{\rho_0}{r} \tilde{y}_5, \quad (3.10)$$

$$\frac{d\tilde{y}_5}{dr} = -4\pi G \rho_0 \tilde{y}_1 - \frac{l+1}{r} \tilde{y}_5 + \tilde{y}_6, \quad (3.11)$$

$$\frac{d\tilde{y}_6}{dr} = -\frac{4\pi G \rho_0(l+1)}{r} \tilde{y}_1 + \frac{4\pi G \rho_0 l(l+1)}{r} \tilde{y}_2 + \frac{l-1}{r} \tilde{y}_6, \quad (3.12)$$

where $g = 4\pi G \rho_0 r/3$ is the gravity at radial distance r .

This system of ordinary differential equations can be alternatively written in terms of the independent solutions of the system, such that the spheroidal solution vector $\tilde{\mathbf{y}}(r, s)$ can be defined as

$$\tilde{\mathbf{y}}_l(r, s) = \tilde{\mathbf{Y}}_l(r, s) \tilde{\mathbf{c}}_l(r), \quad (3.13)$$

where $\tilde{\mathbf{c}}_l$ is a 6×1 vector of integration constants and $\tilde{\mathbf{Y}}_l$ is the fundamental matrix defined by [[Sabadini et al., 1982](#), [Spada et al., 1992](#), [Sabadini and Vermeersen, 2004](#)]

$$\tilde{\mathbf{Y}}_l = \begin{pmatrix} \frac{l r^{l+1}}{2(2l+3)} & r^{l-1} & 0 \\ \frac{(l+3)r^{l+1}}{2(2l+3)(l+1)} & \frac{r^{l-1}}{l} & 0 \\ \frac{(l\rho_0 g r + 2(l^2 - l - 3)\tilde{\mu})r^l}{2(2l+3)} & (\rho_0 g r + 2(l-1)\tilde{\mu})r^{l-2} & -\rho_0 r^l \\ \frac{l(l+2)\tilde{\mu}r^l}{(2l+3)(l+1)} & \frac{2(l-1)\tilde{\mu}r^{l-2}}{l} & 0 \\ 0 & 0 & -r^l \\ \frac{2\pi G \rho_0 l r^{l+1}}{2l+3} & 4\pi G \rho_0 r^{l-1} & -(2l+1)r^{l-1} \end{pmatrix} \dots$$

$$\dots \left(\begin{array}{ccc} \frac{(l+1)r^{-l}}{2(2l-1)} & r^{-l-2} & 0 \\ \frac{(2-l)r^{-l}}{2l(2l-1)} & -\frac{r^{-l-2}}{l+1} & 0 \\ \frac{(l+1)\rho_0 g r^{-2}(l^2+3l-1)\bar{\mu}}{2(2l-1)r^{l+1}} & \frac{\rho_0 g r^{-2}(l+2)\bar{\mu}}{r^{l+3}} & -\frac{\rho_0}{r^{l+1}} \\ \frac{(l^2-1)\bar{\mu}}{l(2l-1)r^{l+1}} & \frac{2(l+2)\bar{\mu}}{(l+1)r^{l+3}} & 0 \\ 0 & 0 & -\frac{1}{r^{l+1}} \\ \frac{2\pi G\rho_0(l+1)}{(2l-1)r^l} & \frac{4\pi G\rho_0}{r^{l+2}} & 0 \end{array} \right), \quad (3.14)$$

with its inverse explicitly given in [Sabadini and Vermeersen \[2004\]](#).

Since the radial functions are assumed to be continuous at every internal boundary between two viscoelastic layers, the unknown vector of integration constants $\tilde{\mathbf{c}}_l^{(i)}$ of a material layer i can be expressed in terms of the also unknown vector $\tilde{\mathbf{c}}_l^{(i+1)}$ that belongs to the layer immediately below it, i.e.

$$\begin{aligned} \tilde{\mathbf{c}}_l^{(i)} &= \left(\tilde{\mathbf{Y}}_l^{(i)}(r_{i+1}, s) \right)^{-1} \tilde{\mathbf{y}}_l^{(i+1)}(r_{i+1}) \\ \tilde{\mathbf{c}}_l^{(i)} &= \left(\tilde{\mathbf{Y}}_l^{(i)}(r_{i+1}, s) \right)^{-1} \tilde{\mathbf{Y}}_l^{(i+1)}(r_{i+1}, s) \tilde{\mathbf{c}}_l^{(i+1)}. \end{aligned} \quad (3.15)$$

Subsequent application of the continuity condition shown above to every internal boundary between viscoelastic layers leads then to an analytical expression that allows us to propagate the solution vector from the base of a group of viscoelastic layers to the top of the same group of layers. As an example, the solution vector at the surface ($r = r_s$) is related to the solution vector at the Core-Mantle Boundary or CMB ($r = r_N$) by

$$\tilde{\mathbf{y}}_l^{(1)}(r_s, s) = \left(\prod_{i=1}^{N-1} \tilde{\mathbf{Y}}_l^{(i)}(r_i, s) \left(\tilde{\mathbf{Y}}_l^{(i)}(r_{i+1}, s) \right)^{-1} \right) \tilde{\mathbf{y}}_l^{(N-1)}(r_N). \quad (3.16)$$

Further detailed information applying exclusively to the determination of the response of a viscoelastic planetary body without subsurface liquid layers other than the core using the propagator matrix technique is given in [Sabadini and Vermeersen \[2004\]](#). However, in the case of icy moons, the presence of an internal ocean breaks the propagation from the CMB to the surface as mechanical quantities cannot be propagated through fluid layers. Therefore, Equation 3.16 cannot be directly applied to calculate the response of an icy satellite to internal and/or external excitations and the propagator matrix technique needs to be modified in order to cope with the presence of a shallow internal ocean.

3.3. PROPAGATION THROUGH INTERNAL FLUID LAYERS

The classical propagator matrix method inherently implies propagation of the radial functions \tilde{y}_1 to \tilde{y}_6 from the core-mantle boundary (CMB) to the surface through exclusively solid material layers. However, as suggested in Chapter 2, our models of the interior of icy satellites include at least one material layer with zero rigidity sandwiched between two viscoelastic layers: the subsurface ocean. The presence of a liquid ocean between the mantle and the ice shell changes the dynamics of the interior response as

fluid layers are not able to propagate mechanical quantities, such as deformations and stresses, from the top of the solid mantle layers to the base of the ice-I shell.

The presence of a liquid inviscid ocean in the interior of Europa introduces a challenge to the application of the propagator matrix method. As can be observed from Equation 3.8, an internal fluid material layer (with $\tilde{\mu} = 0$) introduces a singularity in the radial propagation of the tangential displacement \tilde{y}_2 . This singularity disrupts the propagation of the remaining mechanical quantities (\tilde{y}_1 , \tilde{y}_3 and \tilde{y}_4) and the potential flux \tilde{y}_6 through the liquid ocean using the conventional technique introduced in Section 3.2. In order to circumvent this problem, we assume that the global subsurface ocean is in a state of hydrostatic equilibrium in both the undeformed and deformed cases and that the deformation of the fluid layer occurs in such a way that its boundaries follow an equipotential surface [Chinnery, 1975]. In this way, the physical behavior of Europa's putative subsurface ocean is fully determined by Poisson's equation. If we further assume that every ocean layer is homogeneous and incompressible, Poisson's equation reduces to Laplace's equation because $\tilde{\chi}_l$ and $\frac{\partial \rho_0}{\partial r}$ become equal to zero. Then, the relevant set of differential equations can be written as [Saito, 1974, Harada and Kurita, 2006]

$$\frac{d\tilde{z}_5}{dr} = \left(\frac{4\pi G\rho_0}{g} - \frac{l+1}{r} \right) \tilde{z}_5 + \tilde{z}_6, \quad (3.17)$$

$$\frac{d\tilde{z}_6}{dr} = \frac{2(l-1)}{r} \frac{4\pi G\rho_0}{g} \tilde{z}_5 - \left(\frac{4\pi G\rho_0}{g} - \frac{l+1}{r} \right) \tilde{z}_6, \quad (3.18)$$

where \tilde{z}_5 represents the perturbed gravitational potential and \tilde{z}_6 is defined by

$$\tilde{z}_6 = -\frac{\partial \tilde{\Phi}_l}{\partial r} - \left(\frac{l+1}{r} - \frac{4\pi G\rho_0}{g} \right) \tilde{\Phi}_l = \tilde{Q}_l^*, \quad (3.19)$$

which already takes into account that the radial deformation of fluid layers follows the shape of an equipotential surface. Note that the notation used here to describe the radial functions (\tilde{z} instead of \tilde{y}) only has the purpose of emphasizing the kind of material layer to which they apply (i.e. \tilde{y} for solid layers and \tilde{z} for liquid layers).

In a similar way as for solid viscoelastic layers, the system of two first-order ordinary differential equations defined by Equations 3.17 and 3.18 can be conveniently expressed in terms of its independent solutions, i.e. $\tilde{\mathbf{z}}_l(r, s) = \tilde{\mathbf{Z}}_l(r, s)\tilde{\mathbf{c}}_l(r)$. In the case of fluid layers, however, the relevant vector of integration constants contains only two elements and the fundamental matrix $\tilde{\mathbf{Z}}_l$ is defined by

$$\tilde{\mathbf{Z}}_l = \begin{pmatrix} r^l & r^{-l-1} \\ (2l+1)r^{l-1} - \frac{4\pi G\rho_0}{g}r^l & -\frac{4\pi G\rho_0}{g}r^{-l-1} \end{pmatrix}. \quad (3.20)$$

As both \tilde{z}_5 and \tilde{z}_6 are continuous at interfaces between fluid layers, the response at the top of a group of fluid layers can be related to the response at its bottom in a similar way as it has been done for solid viscoelastic layers in Equations 3.15 and 3.16. At interfaces between fluid and viscoelastic layers, boundary conditions are required to express the response vector at the upper side of the interface in terms of the response at the lower side. In this way, the response at the surface can be related to the response at the lowermost internal boundary through the use of an adapted propagator matrix.

3.4. BOUNDARY CONDITIONS

As briefly mentioned in the previous Sections, a proper set of boundary conditions is required to constrain the radial functions \tilde{y}_3 , \tilde{y}_4 and \tilde{y}_6 at the surface and to express the solution vector at the upper side of an internal fluid-solid interface in terms of the solution at the lower side of the interface. In addition, the boundary conditions introduce the effect of internal and external excitations on the response of the planetary body. In this thesis, in which we will deal with the case of differential rotation of the interior of icy satellites, we consider the following excitations: 1) tidal potential (W_l), 2) centrifugal potential of the icy moon (V_l^e), 3) centrifugal potential due to the differential rotation of the subsurface ocean (δV_l^o), 4) centrifugal potential due to the differential rotation of the deep interior (δV_l^m), 5) surface loading potential (S_l^s), and 6) internal loading potential at the mantle-ocean boundary (S_l^m). Then, the relevant boundary conditions that apply to the general models for the interior of an icy satellite (see Figure 3.1) may be written as:

At the surface: Deformations and perturbed potential (\tilde{y}_1 , \tilde{y}_2 and \tilde{y}_5) are unknown, as these are the parameters we need to solve for. The boundary conditions for the remaining three radial functions at the surface ($r = r_s$) may be written as [Sabadini and Vermeersen, 2004]:

$$\tilde{y}_3(r_s) = -\frac{G}{r_s} \frac{2l+1}{3} \bar{\rho} \hat{S}_l^s, \quad (3.21)$$

$$\tilde{y}_4(r_s) = 0, \quad (3.22)$$

$$\tilde{y}_6(r_s) = -\frac{2l+1}{r_s} (\hat{V}_l^e + \hat{W}_l) - \frac{G}{r_s} \frac{2l+1}{r_s} \hat{S}_l^s, \quad (3.23)$$

where $\bar{\rho}$ is the mean density of the icy moon. In addition, the hats on top of the different excitations denote that a unit impulse excitation has been implied. This is convenient in order to separate the contribution of each excitation source to the response.

At the CMB: As the CMB is the lowermost internal interface in our modeling, the boundary conditions at this interface can be directly related to the unknown integration constants K_1 , K_2 and K_3 of the underlying fluid core¹. Assuming that no additional internal excitations act at this interface and that the fluid metallic core follows the rotation of the overlying mantle, the boundary conditions at the CMB ($r = r_f$) may be written as [Sabadini and Vermeersen, 2004]:

$$\tilde{y}_1(r_f^+) = -\frac{1}{A_f} r_f^{l-1} K_1 + K_3, \quad (3.24)$$

$$\tilde{y}_2(r_f^+) = K_2, \quad (3.25)$$

$$\tilde{y}_3(r_f^+) = \rho(r_f^-) A_f r_f K_3, \quad (3.26)$$

¹Aside the notable exception of Ganymede for which a molten iron core provides the best explanation for the observed intrinsic magnetic field of this icy satellite [Kivelson et al., 1996], the state of the metallic core of icy satellites is rather unknown. A theoretical description including a fluid core allows to easily integrate a solid core into the developed framework by introducing a small dummy fluid core at the bottom of the solid core. The opposite is not the case.

$$\tilde{y}_4(r_f^+) = 0, \quad (3.27)$$

$$\tilde{y}_5(r_f^+) = r_f^l K_1, \quad (3.28)$$

$$\tilde{y}_6(r_f^+) = 2(l-1)r_f^{l-1}K_1 + 3A_f K_3, \quad (3.29)$$

where $\rho(r_f^-)$ is the homogeneous density of the fluid core and $A_f = \frac{4}{3}\pi G\rho(r_f^-)$. The superscripts + and – refer to the upper side and lower side of the interface, respectively. Moreover, using Equations 3.24 to 3.29, the solution vector at the base of the mantle can be conveniently written as $\tilde{\mathbf{y}}(r_f^+, s) = \tilde{\mathbf{I}}_l^f \tilde{\mathbf{c}}_l^f$, with

$$\tilde{\mathbf{I}}_l^f = \begin{pmatrix} -\frac{r_f^{l-1}}{A_f} & 0 & 1 \\ 0 & 1 & 0 \\ 0 & 0 & \rho(r_f^-)A_f r_f \\ 0 & 0 & 0 \\ r_f^l & 0 & 0 \\ 2(l-1)r_f^{l-1} & 0 & 3A_f \end{pmatrix}, \quad (3.30)$$

and $\tilde{\mathbf{c}}_l^f = (K_1, K_2, K_3)^T$.

At the ocean-ice interface: The radial deformation of the ocean $\tilde{y}_1(r_w^-)$ at the ocean-ice interface ($r = r_w$) cannot follow an equipotential surface as the icy shell prevents such a radial displacement. An unknown parameter K_4 takes into account the difference between the shape of the ideal equipotential surface at the top of the ocean layer and the shape of the icy shell at its base. Furthermore, the pressure induced by this parameter K_4 defines the radial stress at the top of the ocean. Furthermore, the tangential deformation at the base of the icy shell is assumed to be decoupled from the motion of the ocean underneath and equal to a constant K_5 . The tangential stress at the interface is zero in the absence of acting tangential traction². Then, the set of boundary conditions at the ocean-ice interface can be written as [Chinnery, 1975, Greff-Lefftz et al., 2000]:

$$\tilde{y}_1(r_w^+) = -\frac{\tilde{z}_5(r_w^-)}{g(r_w)} + K_4, \quad (3.31)$$

$$\tilde{y}_2(r_w^+) = K_5, \quad (3.32)$$

$$\tilde{y}_3(r_w^+) = \rho(r_w^-)g(r_w)K_4, \quad (3.33)$$

$$\tilde{y}_4(r_w^+) = 0, \quad (3.34)$$

$$\tilde{y}_5(r_w^+) = \tilde{z}_5(r_w^-) + \delta \hat{V}_l^o, \quad (3.35)$$

$$\tilde{y}_6(r_w^+) = \tilde{z}_6(r_w^-) + 4\pi G\rho(r_w^-)K_4 + \frac{2l+1}{r_w} \delta \hat{V}_l^o, \quad (3.36)$$

where r_w^+ refers to the upper (solid) side of the boundary and r_w^- to the lower (fluid) side.

²Recall that the water ocean is assumed to be an inviscid fluid.

At the mantle-ocean interface: The boundary conditions at this interface are similar to the ones that apply to the Inner Core Boundary (ICB) on Earth [see e.g. Greff-Lefftz et al., 2000]. As for the ocean-ice interface, an unknown parameter K_6 needs to be introduced in order to take into account the difference between the radial deformation experienced by the solid mantle and the equipotential deformation of the overlying ocean. The tangential displacement is undetermined as in the previous case and set to be equal to a constant K_7 and the tangential stress is zero due to the absence of tangential traction. Then, the set of boundary conditions at the mantle-ocean interface ($r = r_m$) can be written as [Greff-Lefftz et al., 2000]:

$$\tilde{y}_1(r_m^-) = -\frac{\tilde{z}_5(r_m^+)}{g(r_m)} - K_6, \quad (3.37)$$

$$\tilde{y}_2(r_m^-) = K_7, \quad (3.38)$$

$$\tilde{y}_3(r_m^-) = -\rho(r_m^+)g(r_m)K_6 - \frac{2l+1}{3}\bar{\rho}^I\hat{S}_l^m, \quad (3.39)$$

$$\tilde{y}_4(r_m^-) = 0, \quad (3.40)$$

$$\tilde{y}_5(r_m^-) = \tilde{z}_5(r_m^+) + \left(\frac{r_m}{r_w}\right)^l \delta\hat{V}_l^o - \delta\hat{V}_l^m, \quad (3.41)$$

$$\tilde{y}_6(r_m^-) = \tilde{z}_6(r_m^+) - 4\pi G\rho(r_m^+)K_6 + \frac{2l+1}{r_m} \left[\left(\frac{r_m}{r_w}\right)^l \delta\hat{V}_l^o - \delta\hat{V}_l^m - \hat{S}_l^m \right], \quad (3.42)$$

where $\bar{\rho}^I$ is the average density of a sphere containing all material layers located below the mantle-ocean interface. Furthermore, r_m^- refers to the lower (solid) side of the interface, whereas r_m^+ refers to the upper (liquid) side.

3.5. PROPAGATOR MATRIX APPROACH FOR ICY MOONS

The presence of an internal ocean separates the propagation of the solution vector $\tilde{\mathbf{y}}(r, s)$ from the CMB to the surface in three parts: 1) propagation through the solid deep interior (i.e. silicate and high pressure ice mantle layers and eventually a solid core), 2) propagation through the liquid ocean, and 3) propagation through the ice shell. For each of these regions, a propagator matrix can be defined that allows to express the conditions at the top of the region to the conditions at its bottom. At the interfaces between the aforementioned regions, the boundary conditions defined in Section 3.4 are then applied in order to connect the individual propagators, thereby allowing for a single propagator from the CMB to the surface.

3.5.1. INDIVIDUAL PROPAGATOR MATRICES

We consider here that the interior of a general icy satellite consists of N concentric spherical and homogeneous material layers (see Figure 3.1), from which layers 1 to $n-1$ represent the ice shell; layer n is the subsurface water ocean; layers $n+1$ to $N-1$ represent the mantle layers and eventually a solid core; and layer N is the fluid core (or a dummy fluid

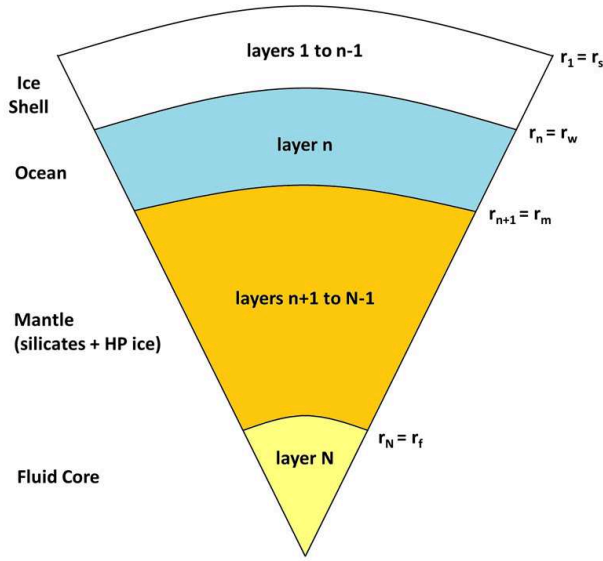


Figure 3.1: Nomenclature used to describe the internal layers of an icy moon. Layers $1 \leq i \leq n-1$ represent the ice shell, layer $i = n$ is the subsurface ocean, layers $n-1 \leq i \leq N-1$ include the mantle layers (silicate and high pressure ice) and eventually a solid core, and layer $i = N$ is the fluid core (or a dummy core if the core is treated as solid).

core³). Using the continuity condition given by Equation 3.15 for layers within one of the aforementioned regions and the definition of the fundamental matrices $\tilde{\mathbf{Y}}_l$ (for viscoelastic layers) and $\tilde{\mathbf{Z}}_l$ (for liquid layers), the three relevant propagators may be defined as follows:

Mantle propagator: The conditions at the top of the mantle ($r = r_{n+1} = r_m^-$) can be expressed in terms of the conditions at the bottom of the mantle ($r = r_N = r_f^+$) by

$$\tilde{\mathbf{y}}_l^{(n+1)}(r_m^-, s) = \tilde{\mathbf{B}}_l^m \tilde{\mathbf{y}}_l^{(N-1)}(r_N), \quad (3.43)$$

where $\tilde{\mathbf{B}}_l^m$ is the mantle propagator matrix defined by

$$\tilde{\mathbf{B}}_l^m = \prod_{i=n+1}^{N-1} \tilde{\mathbf{Y}}_l^{(i)}(r_i, s) \left(\tilde{\mathbf{Y}}_l^{(i)}(r_{i+1}, s) \right)^{-1}. \quad (3.44)$$

Ocean propagator: Similarly, the response at the top of the ocean ($r = r_n = r_w^-$) is related to the response at its bottom ($r = r_{n+1} = r_m^+$) through

$$\tilde{\mathbf{z}}_l^{(n)}(r_w^-, s) = \tilde{\mathbf{B}}_l^w \tilde{\mathbf{z}}_l^{(n)}(r_{n+1}, s), \quad (3.45)$$

³A solid metallic core could alternatively be introduced by propagation of the three regular solutions at the center of the planetary body. In that case the matrix $\tilde{\mathbf{I}}_l^f$ is not defined by Equation 3.30 and the continuity condition holds at the CMB. Both methods yield the same results.

where $\tilde{\mathbf{B}}_l^w$ is the ocean propagator matrix defined by

$$\tilde{\mathbf{B}}_l^w = \tilde{\mathbf{Z}}_l^{(n)}(r_n) \left(\tilde{\mathbf{Z}}_l^{(n)}(r_{n+1}) \right)^{-1}. \quad (3.46)$$

Ice shell propagator: Finally, the response at the surface ($r = r_1 = r_s$) is related to the response at the bottom of the ice shell ($r = r_n = r_w^+$) through

$$\tilde{\mathbf{y}}_l^{(1)}(r_s, s) = \tilde{\mathbf{B}}_l^s \tilde{\mathbf{y}}_l^{(n-1)}(r_n), \quad (3.47)$$

where $\tilde{\mathbf{B}}_l^s$ is the shell propagator matrix defined by

$$\tilde{\mathbf{B}}_l^s = \prod_{i=1}^{n-1} \tilde{\mathbf{Y}}_l^{(i)}(r_i, s) \left(\tilde{\mathbf{Y}}_l^{(i)}(r_{i+1}, s) \right)^{-1}. \quad (3.48)$$

3.5.2. CONNECTING THE PROPAGATOR MATRICES

In this subsection the boundary conditions at the ocean-ice and mantle-ocean interfaces are applied in order to derive a single propagator that connects the response at the surface to the conditions at the lowermost internal boundary, in this case the CMB. As a first step, the set of boundary conditions at the ocean-ice boundary (Equations 3.31 - 3.36) and the definition of the shell propagator (Equation 3.48) are used to express the solution vector at the surface $\tilde{\mathbf{y}}_l(r_s, s)$, which is defined by Equation 3.47, in terms of the conditions at the top of the ocean $\tilde{\mathbf{z}}_l(r_w^-, s)$. The resulting expression can then be written as

$$\tilde{\mathbf{y}}_l(r_s, s) = \tilde{\mathbf{B}}_l^s \left(\tilde{\mathbf{H}}_l^w \tilde{\mathbf{z}}_l(r_w^-, s) + \tilde{\mathbf{K}}_l^w \tilde{\mathbf{c}}_l^w + \tilde{\mathbf{b}}_{l,w}^{Vo} \delta \hat{V}_l^o \right), \quad (3.49)$$

where

$$\tilde{\mathbf{H}}_l^w = \begin{pmatrix} -\frac{1}{g(r_w)} & 0 \\ 0 & 0 \\ 0 & 0 \\ 0 & 0 \\ 1 & 0 \\ 0 & 1 \end{pmatrix}, \quad \tilde{\mathbf{K}}_l^w = \begin{pmatrix} 1 & 0 \\ 0 & 1 \\ \rho(r_w^-)g(r_w) & 0 \\ 0 & 0 \\ 0 & 0 \\ 4\pi G\rho(r_w^-) & 0 \end{pmatrix}, \quad \tilde{\mathbf{b}}_{l,w}^{Vo} = \begin{pmatrix} 0 \\ 0 \\ 0 \\ 0 \\ 1 \\ \frac{2l+1}{r_w} \end{pmatrix},$$

and $\tilde{\mathbf{c}}_l^f = (K_4, K_5)^T$ is the vector of constants introduced by the boundary conditions at the ocean-ice interface.

As a next step in the derivation, the solution vector at the top of the ocean $\tilde{\mathbf{z}}_l(r_w^-, s)$ is expressed in terms of the conditions at the top of the mantle $\tilde{\mathbf{y}}_l(r_m^-, s)$ by using the definition of the fluid propagator matrix (Equation 3.46) and the boundary conditions for the radial functions \tilde{y}_5 and \tilde{y}_6 at the mantle-ocean interface (Equations 3.41 - 3.42). Then, Equation 3.45 can be written as

$$\tilde{\mathbf{z}}_l(r_w^-, s) = \tilde{\mathbf{B}}_l^w \left[\begin{pmatrix} \tilde{y}_5(r_m^-) \\ \tilde{y}_6(r_m^-) \end{pmatrix} + \begin{pmatrix} 0 \\ 4\pi G\rho(r_m^+)K_6 \end{pmatrix} \right]$$

$$+ \left(\frac{1}{\frac{2l+1}{r_m}} \right) \left[\delta \hat{V}_l^m - \left(\frac{r_m}{r_w} \right)^l \delta \hat{V}_l^o + \hat{S}_l^m \right]. \quad (3.50)$$

Thereafter, the unknown constant K_6 in Equation 3.50 is expressed in terms of the radial stress \tilde{y}_3 at the top of the mantle in accordance with the boundary condition given by Equation 3.41. Then, Equation 3.50 can be simplified to

$$\tilde{z}_l(r_w^-, s) = \tilde{\mathbf{B}}_l^w \left[\tilde{\mathbf{H}}_l^m \tilde{\mathbf{y}}_l(r_m^-, s) + \left(\frac{1}{\frac{2l+1}{r_m}} \right) \left(\delta \hat{V}_l^m - \left(\frac{r_m}{r_w} \right)^l \delta \hat{V}_l^o \right) \right], \quad (3.51)$$

where

$$\tilde{\mathbf{H}}_l^m = \begin{pmatrix} 0 & 0 & 0 & 0 & 1 & 0 \\ 0 & 0 & -\frac{4\pi G}{g(r_m)} & 0 & 0 & 1 \end{pmatrix}.$$

Furthermore, the solution vector at the top of the mantle $\tilde{\mathbf{y}}_l(r_m^-, s)$ can be easily expressed in terms of the integration constants of the fluid core through the use of the definition of the mantle propagator (Equation 3.44) and the set of boundary conditions at the CMB (Equations 3.24 - 3.29). The resulting expression becomes

$$\tilde{\mathbf{y}}_l(r_m^-, s) = \tilde{\mathbf{B}}_l^m \tilde{\mathbf{y}}_l(r_f^+, s) = \tilde{\mathbf{B}}_l^m \tilde{\mathbf{I}}_l^f \tilde{\mathbf{c}}_l^f. \quad (3.52)$$

The desired expression that relates the conditions at the surface to the integration constants of the fluid core can then be obtained by substituting Equations 3.51 and 3.52 into Equation 3.49, i.e.

$$\tilde{\mathbf{y}}_l(r_s, s) = \tilde{\mathbf{B}}_l^I \tilde{\mathbf{c}}_l^f + \tilde{\mathbf{B}}_l^s \tilde{\mathbf{K}}_l^w \tilde{\mathbf{c}}_l^w + \tilde{\mathbf{b}}_l^I, \quad (3.53)$$

where the 6×3 icy moon propagator matrix $\tilde{\mathbf{B}}_l^I$ is defined as the product

$$\tilde{\mathbf{B}}_l^I = \tilde{\mathbf{B}}_l^s \tilde{\mathbf{H}}_l^w \tilde{\mathbf{B}}_l^w \tilde{\mathbf{H}}_l^m \tilde{\mathbf{B}}_l^m \tilde{\mathbf{I}}_l^f, \quad (3.54)$$

and the vector of internal excitations $\tilde{\mathbf{b}}_l^I$ is given by

$$\tilde{\mathbf{b}}_l^I = \tilde{\mathbf{B}}_l^s \left[\tilde{\mathbf{b}}_{l,w}^{Vo} - \tilde{\mathbf{H}}_l^w \tilde{\mathbf{B}}_l^w \left(\frac{1}{\frac{2l+1}{r_m}} \right) \left(\frac{r_m}{r_w} \right)^l \right] \delta \hat{V}_l^o + \tilde{\mathbf{B}}_l^s \tilde{\mathbf{H}}_l^w \tilde{\mathbf{B}}_l^w \left(\frac{1}{\frac{2l+1}{r_m}} \right) \delta \hat{V}_l^m. \quad (3.55)$$

3.5.3. THE CHARACTERISTIC EQUATION: NORMAL MODES

As previously stated in Section 3.4, the solution vector $\tilde{\mathbf{y}}_l(r_s, s)$ at the surface can be split into two parts: one containing the parameters we need to solve for, i.e. $(\tilde{y}_1, \tilde{y}_2, \tilde{y}_5) = \tilde{\mathbf{P}}_2 \tilde{\mathbf{y}}_l(r_s, s)$, and the other containing the ones constrained by the boundary conditions at the surface, i.e. $(\tilde{y}_3, \tilde{y}_4, \tilde{y}_6) = \tilde{\mathbf{P}}_1 \tilde{\mathbf{y}}_l(r_s, s)$ ⁴. In contrast to the conventional case, the three imposed constraints at the surface are not sufficient to provide a unique solution

⁴ \mathbf{P}_1 and \mathbf{P}_2 are the 3×6 projection matrices that remove, respectively, the unconstrained parameters and the constrained parameters from the 6×1 solution vector at the surface.

to the five unknown constants (i.e. K_1 to K_5) in Equation 3.53. As a result, two additional constraints need to be introduced:

$$0 = \mathbf{F}_1 \tilde{\mathbf{B}}_l^m \tilde{\mathbf{I}}_l^f \tilde{\mathbf{c}}_l^f, \quad (3.56)$$

$$0 = \mathbf{F}_2 \tilde{\mathbf{B}}_l^m \tilde{\mathbf{I}}_l^f \tilde{\mathbf{c}}_l^f - \frac{1}{g(r_m)} \left(\left(\frac{r_m}{r_w} \right)^l \delta \hat{V}_l^o - \delta \hat{V}_l^m \right) + \frac{2l+1}{4\pi G r_m \rho(r_m^+)} \hat{S}_l^m, \quad (3.57)$$

which are the boundary conditions for the radial functions \tilde{y}_4 and \tilde{y}_1 at the mantle-ocean interface, respectively. The row vectors \mathbf{F}_1 and \mathbf{F}_2 in the equations above are defined as

$$\mathbf{F}_1 = (0 \ 0 \ 0 \ 1 \ 0 \ 0), \quad (3.58)$$

$$\mathbf{F}_2 = \left(1 \ 0 \ -\frac{1}{\rho(r_m^+)g(r_m)} \ 0 \ \frac{1}{g(r_m)} \ 0 \right). \quad (3.59)$$

The required system of constrained equations can be obtained by combining the constrained part of Equation 3.54 with the additional constraints given by Equations 3.56 and 3.57. The resulting expression can then be compactly written as

$$\tilde{\mathbf{b}}_l^V (\hat{V}_l^e + \hat{W}_l) + \tilde{\mathbf{b}}_l^S \hat{S}_l^s = \tilde{\mathbf{W}}_1 \tilde{\mathbf{c}}_l + \tilde{\mathbf{b}}_l^{Vo} \delta \hat{V}_l^o + \tilde{\mathbf{b}}_l^{Vm} \delta \hat{V}_l^m + \tilde{\mathbf{b}}_l^{Sm} \hat{S}_l^m, \quad (3.60)$$

where the elements of the 5×5 matrix $\tilde{\mathbf{W}}_1$ are given by

$$\tilde{\mathbf{W}}_1 = \begin{pmatrix} 0 & 0 & \left(\mathbf{F}_1 \tilde{\mathbf{B}}_l^m \tilde{\mathbf{I}}_l^f \right)_{1,1} & \left(\mathbf{F}_1 \tilde{\mathbf{B}}_l^m \tilde{\mathbf{I}}_l^f \right)_{1,2} & \left(\mathbf{F}_1 \tilde{\mathbf{B}}_l^m \tilde{\mathbf{I}}_l^f \right)_{1,3} \\ 0 & 0 & \left(\mathbf{F}_2 \tilde{\mathbf{B}}_l^m \tilde{\mathbf{I}}_l^f \right)_{1,1} & \left(\mathbf{F}_2 \tilde{\mathbf{B}}_l^m \tilde{\mathbf{I}}_l^f \right)_{1,2} & \left(\mathbf{F}_2 \tilde{\mathbf{B}}_l^m \tilde{\mathbf{I}}_l^f \right)_{1,3} \\ \left(\mathbf{P}_1 \tilde{\mathbf{B}}_l^s \tilde{\mathbf{K}}_l^w \right)_{1,1} & \left(\mathbf{P}_1 \tilde{\mathbf{B}}_l^s \tilde{\mathbf{K}}_l^w \right)_{1,2} & \left(\mathbf{P}_1 \tilde{\mathbf{B}}_l^I \right)_{1,1} & \left(\mathbf{P}_1 \tilde{\mathbf{B}}_l^I \right)_{1,2} & \left(\mathbf{P}_1 \tilde{\mathbf{B}}_l^I \right)_{1,3} \\ \left(\mathbf{P}_1 \tilde{\mathbf{B}}_l^s \tilde{\mathbf{K}}_l^w \right)_{2,1} & \left(\mathbf{P}_1 \tilde{\mathbf{B}}_l^s \tilde{\mathbf{K}}_l^w \right)_{2,2} & \left(\mathbf{P}_1 \tilde{\mathbf{B}}_l^I \right)_{2,1} & \left(\mathbf{P}_1 \tilde{\mathbf{B}}_l^I \right)_{2,2} & \left(\mathbf{P}_1 \tilde{\mathbf{B}}_l^I \right)_{2,3} \\ \left(\mathbf{P}_1 \tilde{\mathbf{B}}_l^s \tilde{\mathbf{K}}_l^w \right)_{3,1} & \left(\mathbf{P}_1 \tilde{\mathbf{B}}_l^s \tilde{\mathbf{K}}_l^w \right)_{3,2} & \left(\mathbf{P}_1 \tilde{\mathbf{B}}_l^I \right)_{3,1} & \left(\mathbf{P}_1 \tilde{\mathbf{B}}_l^I \right)_{3,2} & \left(\mathbf{P}_1 \tilde{\mathbf{B}}_l^I \right)_{3,3} \end{pmatrix}, \quad (3.61)$$

in which the notation $(\tilde{\mathbf{M}})_{i,j}$ has been used to denote the element at row i and column j of the corresponding matrix $\tilde{\mathbf{M}}$.

Moreover, the 5×1 internal excitation vectors $\tilde{\mathbf{b}}_l^{Vo}$, $\tilde{\mathbf{b}}_l^{Vm}$ and $\tilde{\mathbf{b}}_l^{Sm}$ on the right-hand side of Equation 3.60 are defined by

$$\tilde{\mathbf{b}}_l^{Vo} = \begin{pmatrix} 0 \\ -\frac{1}{g(r_m)} \left(\frac{r_m}{r_w} \right)^l \\ \left(\mathbf{P}_1 \tilde{\mathbf{B}}_l^s \left[\tilde{\mathbf{b}}_{l,w}^{Vo} - \tilde{\mathbf{H}}_l^w \tilde{\mathbf{B}}_l^w \begin{pmatrix} 1 \\ \frac{2l+1}{r_m} \end{pmatrix} \left(\frac{r_m}{r_w} \right)^l \right] \right)_{1,1} \\ \left(\mathbf{P}_1 \tilde{\mathbf{B}}_l^s \left[\tilde{\mathbf{b}}_{l,w}^{Vo} - \tilde{\mathbf{H}}_l^w \tilde{\mathbf{B}}_l^w \begin{pmatrix} 1 \\ \frac{2l+1}{r_m} \end{pmatrix} \left(\frac{r_m}{r_w} \right)^l \right] \right)_{2,1} \\ \left(\mathbf{P}_1 \tilde{\mathbf{B}}_l^s \left[\tilde{\mathbf{b}}_{l,w}^{Vo} - \tilde{\mathbf{H}}_l^w \tilde{\mathbf{B}}_l^w \begin{pmatrix} 1 \\ \frac{2l+1}{r_m} \end{pmatrix} \left(\frac{r_m}{r_w} \right)^l \right] \right)_{3,1} \end{pmatrix}, \quad (3.62)$$

$$\tilde{\mathbf{b}}_l^{Vm} = \begin{pmatrix} 0 \\ \frac{1}{g(r_m)} \\ \left(\mathbf{P}_1 \tilde{\mathbf{B}}_l^s \tilde{\mathbf{H}}_l^w \tilde{\mathbf{B}}_l^w \left(\frac{1}{r_m} \right) \right)_{1,1} \\ \left(\mathbf{P}_1 \tilde{\mathbf{B}}_l^s \tilde{\mathbf{H}}_l^w \tilde{\mathbf{B}}_l^w \left(\frac{2l+1}{r_m} \right) \right)_{2,1} \\ \left(\mathbf{P}_1 \tilde{\mathbf{B}}_l^s \tilde{\mathbf{H}}_l^w \tilde{\mathbf{B}}_l^w \left(\frac{1}{r_m} \right) \right)_{3,1} \end{pmatrix}, \quad (3.63)$$

and

$$\tilde{\mathbf{b}}_l^{Sm} = \begin{pmatrix} 0 \\ \frac{2l+1}{4\pi G r_m \rho(r_m^*)} \\ 0 \\ 0 \\ 0 \end{pmatrix}. \quad (3.64)$$

Furthermore, the surface excitation vectors $\tilde{\mathbf{b}}_l^V$ and $\tilde{\mathbf{b}}_l^S$ on the left-hand side of Equation 3.60 are fully defined by the boundary conditions at the surface (i.e. Equations 3.21 - 3.23) as the two additional constraints given by Equations 3.56 and 3.57 do not depend on conditions at the surface. The resulting expressions are then given by

$$\tilde{\mathbf{b}}_l^V = \begin{pmatrix} 0 \\ 0 \\ 0 \\ 0 \\ -\frac{2l+1}{r_s} \end{pmatrix}, \quad (3.65)$$

and

$$\tilde{\mathbf{b}}_l^S = \begin{pmatrix} 0 \\ 0 \\ -\frac{G}{r_s} \frac{2l+1}{3} \bar{\rho} \\ 0 \\ -\frac{G}{r_s} \frac{2l+1}{r_s} \end{pmatrix}. \quad (3.66)$$

Each one of the applied internal and external boundary conditions defined by Equations 3.62 - 3.66 fully constrains Equation 3.60 such that a unique solution for the unknown vector of constants $\tilde{\mathbf{c}}_l$ can be found from an alternative version of Equation 3.60, written as

$$\tilde{\mathbf{c}}_l = \tilde{\mathbf{W}}_1^{-1} \tilde{\mathbf{b}}_l = \frac{\tilde{\mathbf{W}}_1^\dagger}{\det(\tilde{\mathbf{W}}_1)} \tilde{\mathbf{b}}_l, \quad (3.67)$$

where $\tilde{\mathbf{W}}_1^\dagger$ is the matrix of complementary minors and $\tilde{\mathbf{b}}_l$ being a short notation for

$$\tilde{\mathbf{b}}_l = \tilde{\mathbf{b}}_l^V (\hat{V}_l^e + \hat{W}_l) + \tilde{\mathbf{b}}_l^S \hat{S}_l^s - \tilde{\mathbf{b}}_l^{Vo} \delta \hat{V}_l^o - \tilde{\mathbf{b}}_l^{Vm} \delta \hat{V}_l^m - \tilde{\mathbf{b}}_l^{Sm} \hat{S}_l^m, \quad (3.68)$$

As can be observed from Equations 3.60 or 3.67, the vector of constants $\tilde{\mathbf{c}}_l$ remains undetermined if no excitations act on the interior model. In that particular case, the solutions of the resulting equation (i.e. $\tilde{\mathbf{W}}_1 \tilde{\mathbf{c}}_l = \mathbf{0}$) is given by the non-zero M roots $s = s_j$ ($j = 1, 2, 3, \dots, M$) of the secular equation $\det(\tilde{\mathbf{W}}_1) = 0$. From a physical viewpoint, the solutions $s = s_j$ represent the inverse relaxation times of the M relaxation modes of the interior model.

The number of modes or free oscillations of a model depends on the chosen internal layering and rheology. For an icy satellite consisting of Maxwell viscoelastic solid layers and an internal ocean, the following relaxation modes are expected [Sabadini and Vermeersen, 2004]:

- The surface contributes one mode, labeled S_0 .
- At the boundary between the mantle (rocky and HP-ice layers) and the fluid ocean, the buoyancy mode M_0 is triggered if the boundary marks a density contrast.
- At the top of the ocean, i.e. at the boundary between the ocean and the ice-I shell, the buoyancy mode L_0 is triggered if the boundary marks a density contrast.
- At the boundary between two viscoelastic layers within the mantle, one buoyancy mode M_i ($i = 1, 2, 3, \dots$) is triggered if the density on both sides of the boundary is different. The same applies when a density contrast is introduced within the ice-I shell. In that case, however, the corresponding buoyancy modes are labeled as S_i .
- At the boundary between two viscoelastic layers, two additional modes T_i ($i = 1, 2, 3, \dots$) are triggered if the Maxwell time $\tau_M = \frac{\eta}{\mu}$ on both sides of the boundary is different. These paired modes are called transient modes as they have relatively short relaxation times.
- The core-mantle boundary (CMB) contributes one mode, labeled C_0 .

As an example, the response corresponding to the reference model of Europa defined in Chapter 2 (Table 2.8) will consist of six relaxation modes: S_0 at the surface, L_0 at the ocean-ice interface, M_0 at the mantle-ocean interface, C_0 at the CMB, and the transient pair of modes T_1 and T_2 at the interface between the ice sublayers.

3.5.4. THE RESPONSE AT THE SURFACE

The response at the surface, which consists of the radial functions $\tilde{y}_1(r_s)$, $\tilde{y}_2(r_s)$ and $\tilde{y}_5(r_s)$, is fully defined by the unconstrained part of Equation 3.53. Using the definition of the projection matrix \mathbf{P}_2 and the vector of constants $\tilde{\mathbf{c}}_l$ (Equation 3.67), the unconstrained part of Equation 3.53 can be written as

$$\begin{pmatrix} \tilde{y}_1(r_s) \\ \tilde{y}_2(r_s) \\ \tilde{y}_5(r_s) \end{pmatrix} = \tilde{\mathbf{W}}_2 \frac{\tilde{\mathbf{W}}_1^\dagger}{\det(\tilde{\mathbf{W}}_1)} \tilde{\mathbf{b}}_l + \tilde{\mathbf{d}}_l^{Vo} + \tilde{\mathbf{d}}_l^{Vm}, \quad (3.69)$$

where $\tilde{\mathbf{W}}_2$ and $\tilde{\mathbf{b}}_l$ are defined by Equations 3.61 and 3.68, respectively. In addition, the 3×5 matrix $\tilde{\mathbf{W}}_2$ is defined by

$$\tilde{\mathbf{W}}_2 = \begin{pmatrix} (\mathbf{P}_2 \tilde{\mathbf{B}}_l^s \tilde{\mathbf{K}}_l^w)_{1,1} & (\mathbf{P}_2 \tilde{\mathbf{B}}_l^s \tilde{\mathbf{K}}_l^w)_{1,2} & (\mathbf{P}_2 \tilde{\mathbf{B}}_l^f)_{1,1} & (\mathbf{P}_2 \tilde{\mathbf{B}}_l^f)_{1,2} & (\mathbf{P}_2 \tilde{\mathbf{B}}_l^f)_{1,3} \\ (\mathbf{P}_2 \tilde{\mathbf{B}}_l^s \tilde{\mathbf{K}}_l^w)_{2,1} & (\mathbf{P}_2 \tilde{\mathbf{B}}_l^s \tilde{\mathbf{K}}_l^w)_{2,2} & (\mathbf{P}_2 \tilde{\mathbf{B}}_l^f)_{2,1} & (\mathbf{P}_2 \tilde{\mathbf{B}}_l^f)_{2,2} & (\mathbf{P}_2 \tilde{\mathbf{B}}_l^f)_{2,3} \\ (\mathbf{P}_2 \tilde{\mathbf{B}}_l^s \tilde{\mathbf{K}}_l^w)_{3,1} & (\mathbf{P}_2 \tilde{\mathbf{B}}_l^s \tilde{\mathbf{K}}_l^w)_{3,2} & (\mathbf{P}_2 \tilde{\mathbf{B}}_l^f)_{3,1} & (\mathbf{P}_2 \tilde{\mathbf{B}}_l^f)_{3,2} & (\mathbf{P}_2 \tilde{\mathbf{B}}_l^f)_{3,3} \end{pmatrix}, \quad (3.70)$$

and the excitation vectors $\tilde{\mathbf{d}}_l^{Vo}$ and $\tilde{\mathbf{d}}_l^{Vm}$ are given by

$$\tilde{\mathbf{d}}_l^{Vo} = \mathbf{P}_2 \tilde{\mathbf{B}}_l^s \left[\tilde{\mathbf{b}}_{l,w}^{Vo} - \tilde{\mathbf{H}}_l^w \tilde{\mathbf{B}}_l^w \left(\frac{1}{r_m} \right) \left(\frac{r_m}{r_w} \right)^l \right] \delta \hat{V}_l^o, \quad (3.71)$$

$$\tilde{\mathbf{d}}_l^{Vm} = \mathbf{P}_2 \tilde{\mathbf{B}}_l^s \tilde{\mathbf{H}}_l^w \tilde{\mathbf{B}}_l^w \left(\frac{1}{r_m} \right) \delta \hat{V}_l^m. \quad (3.72)$$

Furthermore, as all terms on the right-hand side of Equation 3.69 can be written as linear functions of the acting external and internal excitations, the response at the surface can be conveniently expressed as

$$\begin{pmatrix} \tilde{y}_1(r_s) \\ \tilde{y}_2(r_s) \\ \tilde{y}_5(r_s) \end{pmatrix} = \tilde{\mathbf{X}}_{l,s}^V (\hat{V}_l^e + \hat{W}_l) + \tilde{\mathbf{X}}_{l,s}^S \hat{S}_l^s + \tilde{\mathbf{X}}_{l,s}^{Vo} \delta \hat{V}_l^o + \tilde{\mathbf{X}}_{l,s}^{Vm} \delta \hat{V}_l^m + \tilde{\mathbf{X}}_{l,s}^{Sm} \hat{S}_l^m, \quad (3.73)$$

where $\tilde{\mathbf{X}}_{l,s}^V$, $\tilde{\mathbf{X}}_{l,s}^S$, $\tilde{\mathbf{X}}_{l,s}^{Vo}$, $\tilde{\mathbf{X}}_{l,s}^{Vm}$ and $\tilde{\mathbf{X}}_{l,s}^{Sm}$ are a representation of the unit impulse response at the surface due to the acting centrifugal (tidal) potential, surface loading, differential rotation of the ocean, differential rotation of the mantle and internal loading at the mantle-ocean interface, respectively. An important property of the unit impulse response of a planetary body to a given excitation is that it only depends on the structural and rheological properties of the interior and thus not on the excitation itself. The actual response to an excitation E is then defined by the product between the unit impulse response $\tilde{\mathbf{X}}_{l,s}^E$ and the corresponding excitation; both expressed in the Laplace domain in accordance with the correspondence principle. The equivalent response in the time domain can then be determined by applying the inverse Laplace transform to the outcome of the aforementioned product.

In the Laplace domain, the unit response vector $\tilde{\mathbf{X}}_{l,s}^E$ due to any forcing E can be expressed as a partial fraction expansion of the form

$$\tilde{\mathbf{X}}_{l,s}^E(r_s) = \mathbf{K}_{l,s}^{E,e}(r_s) + \sum_{j=1}^M \frac{\mathbf{K}_{l,s}^{E,j}(r_s)}{s - s_j}, \quad (3.74)$$

where the s_j are the M inverse relaxation times discussed at the end of subsection 3.5.3, $\mathbf{K}_{l,s}^{E,e}(r_s)$ is a 3×1 vector of coefficients containing the elastic part of the response, and the $\mathbf{K}_{l,s}^{E,j}(r_s)$ are 3×1 vectors of coefficients carrying the contribution of every normal mode j to the response at the surface due to the applied forcing E . In this thesis, both $\mathbf{K}_{l,s}^{E,e}(r_s)$

and $\mathbf{K}_{l,s}^{E,j}(r_s)$ are derived from the partial fraction expansion executed by means of an algebraic software package like MAPLE. Alternatively, both vectors of coefficients could be obtained through the use of complex contour integration, as shown in e.g. [Sabadini and Vermeersen \[2004\]](#) and [Jara-Orué and Vermeersen \[2011\]](#) for the case of a surface load and a tidal potential, respectively.

3.5.5. THE RESPONSE AT INTERNAL INTERFACES

As will be shown in Chapter 7, the study of rotational variations experienced by icy satellites with subsurface oceans requires knowledge about the response of individual internal layers to the excitations acting on them. Taking into account the layering of internal models discussed in Chapter 2 and the definition of propagators and excitation vectors discussed earlier in this Chapter, the response at the ocean-ice interface, mantle-ocean interface and CMB can be defined as:

Ocean-ice interface: The response (deformations and gravitational changes) at the bottom of the ice shell ($r = r_w^+$) can be derived straightforwardly from the definition of the response at the surface (Equation 3.69), as it is equivalent to it before the propagation through the ice shell. Hence, the response at the bottom of the shell can be written as

$$\begin{pmatrix} \tilde{y}_1(r_w^+) \\ \tilde{y}_2(r_w^+) \\ \tilde{y}_5(r_w^+) \end{pmatrix} = \tilde{\mathbf{W}}_3 \frac{\tilde{\mathbf{W}}_1^\dagger}{\det(\tilde{\mathbf{W}}_1)} \tilde{\mathbf{b}}_l + \tilde{\mathbf{d}}_{l,o}^{Vo} + \tilde{\mathbf{d}}_{l,o}^{Vm}, \quad (3.75)$$

where the propagator matrix $\tilde{\mathbf{W}}_3$ is defined by

$$\tilde{\mathbf{W}}_3 = \begin{pmatrix} (\mathbf{P}_2 \tilde{\mathbf{K}}_l^w)_{1,1} & (\mathbf{P}_2 \tilde{\mathbf{K}}_l^w)_{1,2} & (\mathbf{P}_2 \tilde{\mathbf{B}}_l^{Io})_{1,1} & (\mathbf{P}_2 \tilde{\mathbf{B}}_l^{Io})_{1,2} & (\mathbf{P}_2 \tilde{\mathbf{B}}_l^{Io})_{1,3} \\ (\mathbf{P}_2 \tilde{\mathbf{K}}_l^w)_{2,1} & (\mathbf{P}_2 \tilde{\mathbf{K}}_l^w)_{2,2} & (\mathbf{P}_2 \tilde{\mathbf{B}}_l^{Io})_{2,1} & (\mathbf{P}_2 \tilde{\mathbf{B}}_l^{Io})_{2,2} & (\mathbf{P}_2 \tilde{\mathbf{B}}_l^{Io})_{2,3} \\ (\mathbf{P}_2 \tilde{\mathbf{K}}_l^w)_{3,1} & (\mathbf{P}_2 \tilde{\mathbf{K}}_l^w)_{3,2} & (\mathbf{P}_2 \tilde{\mathbf{B}}_l^{Io})_{3,1} & (\mathbf{P}_2 \tilde{\mathbf{B}}_l^{Io})_{3,2} & (\mathbf{P}_2 \tilde{\mathbf{B}}_l^{Io})_{3,3} \end{pmatrix}, \quad (3.76)$$

in which $\tilde{\mathbf{B}}_l^{Io}$ is the 6×3 propagator matrix that propagates the solution vector from the CMB to the bottom of the shell and is defined by

$$\tilde{\mathbf{B}}_l^{Io} = \tilde{\mathbf{H}}_l^w \tilde{\mathbf{B}}_l^w \tilde{\mathbf{H}}_l^m \tilde{\mathbf{B}}_l^m \tilde{\mathbf{I}}_l^f. \quad (3.77)$$

Furthermore, the excitation vectors $\tilde{\mathbf{d}}_{l,o}^{Vo}$ and $\tilde{\mathbf{d}}_{l,o}^{Vm}$ in Equation 3.75 are given by

$$\tilde{\mathbf{d}}_{l,o}^{Vo} = \mathbf{P}_2 \left[\tilde{\mathbf{b}}_{l,w}^{Vo} - \tilde{\mathbf{H}}_l^w \tilde{\mathbf{B}}_l^w \left(\frac{1}{r_m} \right) \left(\frac{r_m}{r_w} \right)^l \right] \delta \hat{V}_l^o, \quad (3.78)$$

$$\tilde{\mathbf{d}}_{l,o}^{Vm} = \mathbf{P}_2 \tilde{\mathbf{H}}_l^w \tilde{\mathbf{B}}_l^w \left(\frac{1}{r_m} \right) \delta \hat{V}_l^m. \quad (3.79)$$

Mantle-ocean interface: The response at the top of the mantle ($r = r_m^-$) is defined by the first, second and fifth element of Equation 3.52, which can alternatively be written

as

$$\begin{pmatrix} \tilde{y}_1(r_m^-) \\ \tilde{y}_2(r_m^-) \\ \tilde{y}_5(r_m^-) \end{pmatrix} = \mathbf{P}_2 \tilde{\mathbf{B}}_l^m \tilde{\mathbf{I}}_l^f \mathbf{P}_3 \frac{\tilde{\mathbf{W}}_1^\dagger}{\det(\tilde{\mathbf{W}}_1)} \tilde{\mathbf{b}}_l, \quad (3.80)$$

where \mathbf{P}_3 is a 3×5 projection matrix that removes the two first elements of the vector of constants $\tilde{\mathbf{c}}_l$, such that $\mathbf{P}_3 \tilde{\mathbf{W}}_1^{-1} \tilde{\mathbf{b}}_l = \tilde{\mathbf{c}}_l^f$.

CMB: The response at the bottom of the mantle ($r = r_f^+$) is equivalent to Equation 3.80 but without the propagation through the mantle layers, i.e.

$$\begin{pmatrix} \tilde{y}_1(r_f^+) \\ \tilde{y}_2(r_f^+) \\ \tilde{y}_5(r_f^+) \end{pmatrix} = \mathbf{P}_2 \tilde{\mathbf{I}}_l^f \mathbf{P}_3 \frac{\tilde{\mathbf{W}}_1^\dagger}{\det(\tilde{\mathbf{W}}_1)} \tilde{\mathbf{b}}_l. \quad (3.81)$$

The response $\mathbf{P}_2 \tilde{\mathbf{y}}_l(r)$ at any of the aforementioned internal interfaces can be conveniently expressed in terms of the individual contributions to the response that are induced by the different excitation sources E applied to the surface of the satellite and its interior. This decomposition is similar to the one performed to the response at the surface, given explicitly by Equation 3.73. As such, every single term of the decomposition is defined as the product of the unit impulse response $\tilde{\mathbf{X}}_{l,k}^E(r_k)$ to an excitation E at interface k and the excitation itself.

Similar to the case of the response at the surface, the unit impulse response $\tilde{\mathbf{X}}_{l,k}^E(r_k)$ at internal interfaces is a partial fraction expansion that can be written as

$$\tilde{\mathbf{X}}_{l,k}^E(r_k) = \mathbf{K}_{l,k}^{E,e}(r_k) + \sum_{j=1}^M \frac{\mathbf{K}_{l,k}^{E,j}(r_k)}{s - s_j}, \quad (3.82)$$

where $\mathbf{K}_{l,k}^{E,e}(r_k)$ and $\mathbf{K}_{l,k}^{E,j}(r_k)$ are coefficient vectors that are found from the partial fraction expansion performed by means of an algebraic software package.

3.6. LOVE NUMBERS

At any given internal interface or at the surface, the viscoelastic response of the interior of a planetary body to external and/or internal excitations is usually expressed in terms of the dimensionless Love numbers $\tilde{h}_l(r_k)$, $\tilde{l}_l(r_k)$ and $\tilde{k}_l(r_k)$ [Love, 1909]. As a result of the different types of excitations acting on the interior in our modeling, different sets of Love numbers need to be defined in order to give a representation of the individual effect of each excitation source on the response at a given (internal) interface. Then, the three elements of the response at a given surface r_k can be expressed as [e.g. Hinderer and Legros, 1989, Dehant et al., 1993, Greff-Lefftz and Legros, 1997, Greff-Lefftz et al., 2000, Sabadini and Vermeersen, 2004]

$$\tilde{y}_1(r_k) = \tilde{U}_l(r_k) = \tilde{h}_l(r_k) \frac{\hat{V}_l^e + \hat{W}_l}{g_0} + \frac{G}{r_s} \tilde{h}'_l(r_k) \frac{\hat{S}_l^s}{g_0} + \tilde{h}_l^o(r_k) \frac{\delta \hat{V}_l^o}{g_0}$$

$$+ \tilde{h}_l^m(r_k) \frac{\delta \hat{V}_l^m}{g_0} + \tilde{h}_l^L(r_k) \frac{\hat{S}_l^m}{g_0}, \quad (3.83)$$

$$\begin{aligned} \tilde{y}_2(r_k) = \tilde{V}_l(r_k) = & \tilde{l}_l(r_k) \frac{\hat{V}_l^e + \hat{W}_l}{g_0} + \frac{G}{r_s} \tilde{l}'_l(r_k) \frac{\hat{S}_l^s}{g_0} + \tilde{l}_l^o(r_k) \frac{\delta \hat{V}_l^o}{g_0} \\ & + \tilde{l}_l^m(r_k) \frac{\delta \hat{V}_l^m}{g_0} + \tilde{l}_l^L(r_k) \frac{\hat{S}_l^m}{g_0}, \end{aligned} \quad (3.84)$$

and

$$\begin{aligned} \tilde{y}_5(r_k) = -\tilde{\Phi}_l(r_k) = & \left[\left(\frac{r_k}{r_s} \right)^l + \tilde{k}_l(r_k) \right] (\hat{V}_l^e + \hat{W}_l) + \frac{G}{r_s} \left[\left(\frac{r_k}{r_s} \right)^l + \tilde{k}'_l(r_k) \right] \hat{S}_l^s \\ & + \tilde{k}_l^o(r_k) \delta \hat{V}_l^o + \tilde{k}_l^m(r_k) \delta \hat{V}_l^m + \tilde{k}_l^L(r_k) \hat{S}_l^m, \end{aligned} \quad (3.85)$$

where $\tilde{h}_l(r_k)$, $\tilde{l}_l(r_k)$ and $\tilde{k}_l(r_k)$ are the tidal Love numbers; $\tilde{h}'_l(r_k)$, $\tilde{l}'_l(r_k)$ and $\tilde{k}'_l(r_k)$ are the load Love numbers; $\tilde{h}_l^o(r_k)$, $\tilde{l}_l^o(r_k)$ and $\tilde{k}_l^o(r_k)$ are the Love numbers related to the differential rotation of the ocean; $\tilde{h}_l^m(r_k)$, $\tilde{l}_l^m(r_k)$ and $\tilde{k}_l^m(r_k)$ are the Love numbers due to the differential rotation of the deep interior; $\tilde{h}_l^L(r_k)$, $\tilde{l}_l^L(r_k)$ and $\tilde{k}_l^L(r_k)$ are the Love numbers due to an internal load at the mantle-ocean interface; and g_0 is the acceleration of gravity at the surface.

The generalized Love numbers defined by Equations 3.83 to 3.85 are by definition frequency-dependent (or time-dependent after transformation to the time domain). This can be observed by comparing the structure of the aforementioned expressions to the structure of Equation 3.73, which gives the response at the surface in terms of the unit response, and the definition of the unit response vector due to a forcing E , which is given by Equation 3.82. Hence, every single Love number in Equations 3.83 to 3.85 is proportional to the partial fraction expansion of their corresponding unit impulse response (e.g. Equation 3.74 for the surface, or Equation 3.82 for internal interfaces). For example, the set of tidal Love numbers at the surface can be written as:

$$\begin{pmatrix} \tilde{h}_l(r_s) g_0^{-1} \\ \tilde{l}_l(r_s) g_0^{-1} \\ 1 + \tilde{k}_l(r_s) \end{pmatrix} = \mathbf{K}_{l,s}^{V,e}(r_s) + \sum_{j=1}^M \frac{\mathbf{K}_{l,s}^{V,j}(r_s)}{s - s_j}, \quad (3.86)$$

where the superscript V refers to the excitation source, in this case a centrifugal or tidal potential. Following this example, comparable expressions can be written for the remaining sets of generalized Love numbers defined by Equations 3.83 to 3.85.

Besides the frequency-dependent Love numbers, convenient sets of constant Love numbers can be defined in the limits $s \rightarrow -\infty$ and $s \rightarrow 0$. In the first limit, which corresponds to the case in which the interior behaves as a purely elastic body, the contribution of the relaxation modes to the response vanishes. Hence, the set of e.g. tidal Love numbers at the surface reduces to

$$\begin{pmatrix} h_{l,e}(r_s) g_0^{-1} \\ l_{l,e}(r_s) g_0^{-1} \\ 1 + k_{l,e}(r_s) \end{pmatrix} = \mathbf{K}_{l,s}^{V,e}(r_s), \quad (3.87)$$

where $h_{l,e}(r_s)$, $l_{l,e}(r_s)$ and $k_{l,e}(r_s)$ are usually referred to as the elastic Love numbers.

On the other hand, in the limit $s \rightarrow 0$ the interior behaves as a fluid body, since all normal modes composing the viscoelastic response have completely relaxed. Then, the aforementioned set of tidal Love numbers at the surface would become:

$$\begin{pmatrix} h_{l,f}(r_s)g_0^{-1} \\ l_{l,f}(r_s)g_0^{-1} \\ k_{l,f}(r_s) \end{pmatrix} = \begin{pmatrix} h_{l,e}(r_s)g_0^{-1} \\ l_{l,e}(r_s)g_0^{-1} \\ k_{l,e}(r_s) \end{pmatrix} + \sum_{j=1}^M \frac{\mathbf{K}_{l,s}^{V,j}(r_s)}{-s_j}, \quad (3.88)$$

where $h_{l,f}(r_s)$, $l_{l,f}(r_s)$ and $k_{l,f}(r_s)$ are the so-called fluid Love numbers. Furthermore, for each normal mode j in the viscoelastic solution, the quotients $\frac{\mathbf{K}_{l,s}^{V,j}(r_s)}{-s_j}$ in Equation 3.88 can alternatively be written as

$$\begin{pmatrix} h_{l,j}(r_s)g_0^{-1} \\ l_{l,j}(r_s)g_0^{-1} \\ k_{l,j}(r_s) \end{pmatrix} = \frac{\mathbf{K}_{l,s}^{V,j}(r_s)}{-s_j}, \quad (3.89)$$

where $h_{l,j}(r_s)$, $l_{l,j}(r_s)$ and $k_{l,j}(r_s)$ are the so-called modal strengths of a normal mode j .

At this point, it is important to keep in mind that the description provided throughout this Chapter is a general one. As such, the developed normal mode approach can be used for the study of a diverse range of geodynamic problems relevant to icy satellites harboring an internal ocean. In this thesis, however, we will concentrate on the study of rotational variations and tidal deformations, for which only the degree two harmonic ($l = 2$) component of the response is relevant to our interests, as the centrifugal and tidal potential acting on the satellite are fully described by their second degree harmonic term (see Sections 4.2 and 6.3).

The representation of the tidal Love numbers in terms of its normal modes is not widely used for applications involving a periodic forcing, such as the diurnal tides acting on the icy satellites of e.g. Jupiter and Saturn. In that case, the tidal Love numbers \tilde{h}_l , \tilde{l}_l and \tilde{k}_l are usually expressed as complex functions of the forcing frequency ω , with the real part referring to the part of the response in-phase with the forcing and the imaginary part referring to the part of the response out-of-phase with the forcing. The complex tidal Love numbers are thus defined as:

$$\tilde{h}_l(\omega) = h_{l,re}(\omega) + i h_{l,im}(\omega), \quad (3.90)$$

$$\tilde{l}_l(\omega) = l_{l,re}(\omega) + i l_{l,im}(\omega), \quad (3.91)$$

$$\tilde{k}_l(\omega) = k_{l,re}(\omega) + i k_{l,im}(\omega), \quad (3.92)$$

where $h_{l,re}$, $l_{l,re}$ and $k_{l,re}$ denote the real part of the Love numbers, whereas $h_{l,im}$, $l_{l,im}$ and $k_{l,im}$ denote the imaginary part. These complex Love numbers can be easily obtained from our normal mode framework by substituting $s = i\omega$ in Equation 3.86.

One of the convenient properties of the complex Love numbers is that they can be written in terms of their amplitude and phase, i.e. (for the radial deformation Love number \tilde{h}_l):

$$\tilde{h}_l(\omega) = |\tilde{h}_l(\omega)| e^{-i\epsilon_l(\omega)}, \quad (3.93)$$

where

$$|\tilde{h}_l(\omega)| = \sqrt{h_{l,re}^2(\omega) + h_{l,im}^2(\omega)} \quad (3.94)$$

is the amplitude of the Love number at frequency ω , and

$$\epsilon_l(\omega) = \arctan\left(\frac{-h_{l,im}(\omega)}{h_{l,re}(\omega)}\right) = \arcsin\left(\frac{-h_{l,im}(\omega)}{|\tilde{h}_l(\omega)|}\right) \quad (3.95)$$

is its corresponding phase lag.

4

TIDAL DEFORMATIONS AND STRESSES I: THEORY

4.1. INTRODUCTION

Due to the physical dimensions of planetary satellites, the gravitational force exerted by their parent planet varies in both magnitude and direction across the interior of the satellite. These variations lead to a differential forcing field, the so-called tidal forcing field, that attempts to elongate the shape of the satellite in the direction of the tide-raising planet, thereby leading to the formation of the tidal bulge as the materials composing the interior of the satellite are not rigid. The shape and orientation of this tidal bulge would have remained fixed to the satellite's figure if the satellite had always shown exactly the same face to the tide-raising planet. This particular configuration will take place if: 1) the spin rate of the satellite is synchronous to its orbital motion (synchronous rotation), 2) the satellite's orbit around the planet is circular (zero eccentricity), and 3) the spin axis of the satellite is perpendicular to its orbital plane (zero obliquity). In reality, however, none of these requirements are fulfilled for the regular satellites of the solar system and hence reshaping of the tidal bulge may take place at different timescales. In order to illustrate this statement, we discuss in the following the case of Jupiter's moon Europa in more detail.

First of all, the 1:2:4 Laplace resonance between the orbital motions of Io, Europa and Ganymede prevents the orbit of Europa to become circular. As a result of the slightly elliptical shape of Europa's orbit around Jupiter (with eccentricity $e = 0.0094$), the tidal force field acting on Europa's surface varies periodically on a diurnal timescale (≈ 3.55 days), thereby leading to continuous stretching and squeezing of the tidal bulge. On the other hand, diurnal changes in the orientation of the tidal field with respect to the surface, which are caused by differences between Europa's spin rate and the instantaneous orbital rate, lead to periodic longitudinal migrations of the tidal bulge. In both cases, the materials composing the interior of Europa will continuously try to deform in response to the acting diurnal tidal field. This periodic reshaping of Europa's interior leads to the

generation of frictional heat in the interior and stresses in the order of 100 kPa at the surface [e.g. Harada and Kurita, 2006, Wahr et al., 2009, Jara-Oru  and Vermeersen, 2011].

In addition, the obliquity of Europa's spin axis is expected to be small but different from zero as a consequence of precession of Europa's orbital plane [Bills, 2005, Baland et al., 2012]. As a result, the tidal force field acting on Europa's surface experiences additional diurnal periodic variations, which introduce an additional source of heat dissipation in the interior and stresses at the surface of Europa. As such, Europa's non-zero obliquity may have played a substantial role in the formation of cycloidal cracks crossing the equator [Hurford et al., 2009] and the global distribution of strike-slip fault orientations on the surface [Rhoden et al., 2010, 2011, 2012, Rhoden and Hurford, 2013].

On timescales much longer than one European orbital revolution, the tidal forcing field acting on the surface of Europa may experience (periodic) variations due to spin pole precession, non-synchronous rotation and/or true polar wander [e.g. Rhoden et al., 2010]. Here we will address the case of non-synchronous rotation (NSR), since it is the long-term mechanism usually favored as an explanation for the orientation and location of tectonic features on Europa's surface [e.g. Greenberg et al., 1998, Hoppa et al., 2001, Kattenhorn, 2002, Greenberg et al., 2003, Hurford et al., 2007, Rhoden et al., 2010]. Since NSR has not been observed from Voyager and Galileo measurements of the surface, it has been hypothesized that a complete revolution of the tidal bulge with respect to Europa's surface (i.e. the period of NSR) would take more than 12000 years [Hoppa et al., 1999a]. If present, NSR of Europa's shell could be a very important process in the analysis of surface stresses for two reasons: 1) it could be a source of large \sim MPa stresses that may be related to the formation of global lineaments on Europa's surface [e.g. Greenberg et al., 1998, Harada and Kurita, 2007, Hurford et al., 2007, Wahr et al., 2009, Jara-Oru  and Vermeersen, 2011] and 2) it would be a mechanism that may change the location of tectonic features on the surface [e.g. Hoppa et al., 2001, Hurford et al., 2007, Kattenhorn and Hurford, 2009, Rhoden et al., 2010].

However, more recent tectonic models on the global distribution of strike-slip faults [e.g. Rhoden et al., 2012, Rhoden and Hurford, 2013] and studies on the dynamics of NSR [e.g. Bills et al., 2009, Goldreich and Mitchell, 2010] have weakened the evidence for NSR occurring on Europa. From a perspective of rotational dynamics, NSR of Europa's ice shell has been hypothesized to be the result of the decoupling effect of a global sub-surface ocean. In such a scenario, the positive average tidal torque¹ experienced by the satellite tends to drive the spin rate of the decoupled ice shell to a rotation state slightly faster than synchronous whereas the rocky interior remains tidally locked [e.g. Greenberg and Weidenschilling, 1984, Ojakangas and Stevenson, 1989b]. However, the torque caused by Jupiter's gravitational pull on permanent asymmetries in Europa's mass distribution² is expected to offset the net tidal torque and maintain synchronicity of the spin rate [Greenberg and Weidenschilling, 1984, Bills et al., 2009, Goldreich and Mitchell, 2010]. Despite the strong theoretical case against NSR of Europa's shell, steady-state NSR may still occur if the decoupled shell shows lateral variations in thickness and/or com-

¹This torque arises from the gravitational pull of Jupiter on the lagged tidally deformed figure of Europa

²The contribution of the permanent asymmetries to the evolution of the spin rate depends on the difference between the two principal equatorial moments of inertia (i.e. $B - A$) and the orientation of the longest axis (related to moment of inertia A) with respect to the direction of the planet [e.g. Goldreich and Peale, 1966].

position. A plausible scenario, which is described in [Ojakangas and Stevenson \[1989b\]](#), suggests that Europa's shell may rotate slightly faster than synchronous as a result of variations in the thickness of the shell if the shell is conductive. In this scenario, the torque on the asymmetric shell rotates the shell to a state in which it is no longer in thermal equilibrium, thereby leading to changes in the spatial distribution of the shell thickness and thereby maintaining NSR.

The aim of this Chapter and Chapter 5, which are largely based on the work presented in [Jara-Oru  and Vermeersen \[2011\]](#), is two-fold: 1) to provide the necessary theoretical background for the determination of tidal deformations and stresses at the surface of icy satellites within the framework of the normal mode approach discussed in Chapter 3 (this Chapter), and 2) to apply this theoretical background to the computation of tidal deformations and stresses at the surface of Europa and Ganymede (only deformations) using the interior models presented in Section 2.3.3 (Chapter 5).

4.2. TIDAL POTENTIAL

Tidal forces are usually expressed as the gradient of a scalar field, the tidal potential V^T , which can be expressed as a series of spherical harmonics, i.e.

$$V^T = GM^T \frac{1}{d} \sum_{l=2}^{\infty} \left(\frac{R}{d}\right)^l P_l(\cos \Psi), \quad (4.1)$$

where G is the universal gravitational constant, M^T is the mass of the tide-raising body, R is the mean radius of the tidally deformed satellite, and d is the distance between the centers of mass of both bodies. In addition, the function P_l is defined as the Legendre polynomial of spherical harmonic degree l . The angle Ψ is the angular distance, measured from the center of mass of the tidally perturbed body, between the position vector of the tide-raising body and the position vector of a point at the surface of the perturbed body at which the potential is evaluated.

The series of spherical harmonics given by Equation 4.1 converges rapidly as the term $(R/d)^l$ decreases exponentially as the harmonic degree l increases. Therefore, the tidal potential exerted by a planet on one of its satellites can be adequately expressed by the second degree term of Equation 4.1. For example, in the case of Jupiter's tide on Europa, the contribution of the second degree term is already about 430 times larger than the contribution of the third degree term. Hence, the tidal potential exerted by Jupiter on Europa can safely be represented by its second degree contribution.

The expression given by Equation 4.1, which implicitly depends on time, can be conveniently expressed in terms of the Keplerian elements that describe the orbital motion of the tide-raising body with respect to a reference frame centered at the center of mass of the perturbed body and attached to its rotating surface. This frame is defined in such a way that the z -axis coincides with the orientation of the spin axis of the perturbed body, whereas the x -axis points towards the point at the surface of the perturbed body that is intersected by the position vector of the tide-raising body at pericenter; the y -axis completes the right-handed reference frame. Then, the relevant second degree term of the

tidal potential can be written as [Kaula, 1964]

$$V^T = \frac{GM^T R^2}{a^3} \sum_{m=0}^2 (2 - \delta_{0,m}) \frac{(2-m)!}{(2+m)!} P_{2,m}(\cos\theta) \sum_{p=0}^2 F_{2,m,p}(i) \times \sum_{q=-\infty}^{\infty} G_{2,p,q}(e) S_{2,m,p,q}^T(\varpi, M, \Omega, \zeta), \quad (4.2)$$

where a , e and i denote the semi-major axis, eccentricity and inclination of the orbit of the tide-raising body around the perturbed body, respectively. Furthermore, θ is the colatitude of a point on the surface at which the potential is evaluated and the functions $P_{2,m}(\cos\theta)$ are the associated Legendre polynomials of degree $l = 2$ and order m , the $F_{2,m,p}(i)$ are the inclination functions, the $G_{2,p,q}(e)$ are the eccentricity functions, and the $S_{2,m,p,q}^T(\varpi, M, \Omega, \zeta)$ are given by [Kaula, 1964]

$$S_{2,m,p,q}^T = \begin{bmatrix} \cos(m\phi) \\ -\sin(m\phi) \end{bmatrix}_{2-m \text{ odd}}^{2-m \text{ even}} \cos[(2-2p)\varpi + (2-2p+q)M + m(\Omega - \zeta)] + \begin{bmatrix} \sin(m\phi) \\ \cos(m\phi) \end{bmatrix}_{2-m \text{ odd}}^{2-m \text{ even}} \sin[(2-2p)\varpi + (2-2p+q)M + m(\Omega - \zeta)] \quad (4.3)$$

where ϖ , Ω and M are defined as the argument of pericenter, the right ascension of the ascending node, and the mean anomaly of the orbit of the tide-raising body around the perturbed body, respectively. Moreover, ϕ is the longitude of a point on the surface at which the potential is evaluated, and the parameter ζ is a reference longitude fixed to the surface of the perturbed body; which in our case is the longitude of the meridian that intersects the x -axis.

In the particular case of the tides exerted by a planet on one of its satellites, Equation 4.2 can be simplified by taking into account that the eccentricity and obliquity³ of the satellites are small. Then, to first order in the obliquity (inclination), the only non-zero inclination functions $F_{2,m,p}(i)$ in Equation 4.2 are [Kaula, 1964]:

$$\begin{aligned} F_{2,0,1}(i) &= -\frac{1}{2}, \\ F_{2,1,0}(i) &= \frac{3}{2} \sin(i) = \frac{3}{2} \sin(\varepsilon), \\ F_{2,1,1}(i) &= -\frac{3}{2} \sin(i) = -\frac{3}{2} \sin(\varepsilon), \\ F_{2,2,0}(i) &= 3. \end{aligned}$$

Since only terms with $p = 0$ and $p = 1$ result in non-zero inclination functions, the relevant set of eccentricity functions $G_{2,p,q}(e)$ is given by [Kaula, 1964]:

$$\begin{aligned} G_{2,0,-1}(e) &= -\frac{1}{2}e, \\ G_{2,0,0}(e) &= 1, \end{aligned}$$

³acts as inclination of the tide-raising body w.r.t. the perturbed body

$$\begin{aligned}
 G_{2,0,1}(e) &= \frac{7}{2}e, \\
 G_{2,1,-1}(e) &= \frac{3}{2}e, \\
 G_{2,1,0}(e) &= \frac{3}{2}e, \\
 G_{2,1,1}(e) &= 1,
 \end{aligned}$$

where only terms up to first order in the eccentricity have been considered.

Introduction of Equation 4.3 and the inclination and eccentricity functions listed above into Equation 4.2 leads then to:

$$\begin{aligned}
 V^T = \frac{GM^T R^2}{a^3} \left\{ -\frac{1}{2}P_{2,0}(\cos\theta) (1 + 3e \cos(M)) \right. \\
 + \frac{1}{4}P_{2,2}(\cos\theta) \times \left(\cos(2\phi) \cos[2\varpi + 2M + 2(\Omega - \zeta)] \right. \\
 + \sin(2\phi) \sin[2\varpi + 2M + 2(\Omega - \zeta)] \\
 - \frac{1}{2}e \cos(2\phi) \cos[2\varpi + M + 2(\Omega - \zeta)] \\
 - \frac{1}{2}e \sin(2\phi) \sin[2\varpi + M + 2(\Omega - \zeta)] \\
 + \frac{7}{2}e \cos(2\phi) \cos[2\varpi + 3M + 2(\Omega - \zeta)] \\
 + \left. \frac{7}{2}e \sin(2\phi) \sin[2\varpi + 3M + 2(\Omega - \zeta)] \right) \\
 + \frac{1}{2}P_{2,1}(\cos\theta) \sin(\varepsilon) \times \left(-\sin(\phi) \cos[2\varpi + 2M + (\Omega - \zeta)] \right. \\
 + \cos(\phi) \sin[2\varpi + 2M + (\Omega - \zeta)] \\
 + \left. \sin(\phi) \cos[\Omega - \zeta] - \cos(\phi) \sin[\Omega - \zeta] \right) \left. \right\}, \quad (4.4)
 \end{aligned}$$

where we neglected all cross terms of the eccentricity and obliquity. Furthermore, as long as the obliquity can be considered to be small, the reference longitude ζ can be defined as

$$\zeta = \Omega + \varpi + (n + \Omega_{ns})t, \quad (4.5)$$

where n is the mean motion of the satellite's orbit, which is equal to the spin rate of the satellite for synchronously rotating bodies, and Ω_{ns} describes the constant angular rate of NSR, i.e. the difference between the actual spin rate and the mean orbital rate. Furthermore, the angle ϖ represents the angular distance of the pericenter measured with respect to the ascending node where the satellite's orbital plane crosses its equatorial plane.

As a final step, we neglect the effect of NSR on the eccentricity tide and obliquity tide because these terms are approximately two orders of magnitude smaller than the effect of NSR on the main "static" tide (see Equation 4.4). Then, substitution of Equation 4.5

Table 4.1: Physical parameters used to describe the tidal potential acting on Europa

Parameter	Value	Unit	Reference
Mean radius (R)	1562	km	[Seidelmann et al., 2007]
Mean motion (n)	101.37472	deg./day	[e.g. Bills, 2005]
Eccentricity (e)	0.0094	-	[e.g. Wahr et al., 2009]
Obliquity (ε)	< 0.1	deg.	[Baland et al., 2012]
Argument of pericenter (ϖ)	345	deg.	[Hurford et al., 2009]
Angular rate of NSR (Ω_{ns})	< 0.03	deg./year	[Hoppa et al., 1999a]
Period of NSR (T_{ns})	> 12,000	year	[Hoppa et al., 1999a]

leads to the desired expression for the tidal potential exerted by a planet on the surface of one of its satellites, i.e.

$$V^T = (nR)^2 \{V_0^T + V_{ns}^T + V_{e1}^T + V_{e2}^T + V_{o1}^T\}, \quad (4.6)$$

where

$$V_0^T = -\frac{1}{2}P_{2,0}(\cos\theta) + \frac{1}{4}P_{2,2}(\cos\theta) \cos(2\phi), \quad (4.7)$$

$$V_{ns}^T = -\frac{1}{2}P_{2,2}(\cos\theta) \sin(2\phi + \Omega_{ns}t) \sin(\Omega_{ns}t), \quad (4.8)$$

$$V_{e1}^T = -\frac{3e}{2}P_{2,0}(\cos\theta) \cos(nt), \quad (4.9)$$

$$V_{e2}^T = \frac{e}{4}P_{2,2}(\cos\theta) [3\cos(2\phi) \cos(nt) + 4\sin(2\phi) \sin(nt)], \quad (4.10)$$

$$V_{o1}^T = P_{2,1}(\cos\theta) \sin(\varepsilon) \cos(\phi) \sin(\varpi + nt), \quad (4.11)$$

were we took into consideration that $M = nt$ and $n^2 = \frac{GM^T}{a^3}$. Furthermore, the associated Legendre polynomials $P_{2,0}(\cos\theta)$, $P_{2,1}(\cos\theta)$ and $P_{2,2}(\cos\theta)$ are defined by

$$P_{2,0}(\cos\theta) = \frac{3\cos^2(\theta) - 1}{2}, \quad (4.12)$$

$$P_{2,1}(\cos\theta) = 3\sin(\theta) \cos(\theta), \quad (4.13)$$

$$P_{2,2}(\cos\theta) = 3\sin^2(\theta). \quad (4.14)$$

The numerical values corresponding to the aforementioned parameters are listed in Table 4.1.

Equations 4.6 to 4.11 show that the tidal potential acting on an icy satellite consists of a static component and several time-dependent components. The term V_0^T represents the time invariant potential, although the second term of Equation 4.7 would contain a time variable component if physical librations (forced periodic variations of the spin rate) of the ice shell would be taken into account [Van Hoolst et al., 2008, Baland and Van Hoolst, 2010, Van Hoolst et al., 2013, Beuthe, 2015]. The term V_0^T would completely define the tidal potential acting on a satellite's surface if the satellite's orbit had

been circular, its rotation synchronous and its obliquity zero. In that particular case, the stresses induced by the formation of the bulge would have had sufficient time to relax completely and tidal heat would not be dissipated in the interior of the satellite. The term V_{ns}^T describes the contribution of NSR to the tidal potential. This term is only non-zero and time dependent if the ice shell rotates non-synchronously with respect to the orbital motion, i.e. when $\Omega_{ns} \neq 0$. Finally, the terms V_{e1}^T , V_{e2}^T and V_{o1}^T represent the diurnal tidal potential resulting from the non-zero eccentricity of the satellite's orbit (first two terms) and the non-zero obliquity of Europa's spin axis (last term). As a matter of convenience we will denote the combination of these three components as the diurnal tidal potential V_d^T , i.e. $V_d^T = V_{e1}^T + V_{e2}^T + V_{o1}^T$.

4.3. TIDAL DEFORMATION

At any point on the surface of an icy satellite, the deformation induced by the continuously acting diurnal tides can be subdivided into three orthogonal components: radial deformation u_r , tangential deformation along meridians u_θ and tangential deformation along circles of latitude u_ϕ . Under the previously imposed condition of spherical symmetry, the spheroidal components of the deformation vector at the surface can be retrieved from the definition of the Laplace-transformed displacement vector $\tilde{\mathbf{u}}(r, \theta, \phi, s)$, which is given by [Alterman et al., 1959]

$$\tilde{\mathbf{u}}(r, \theta, \phi, s) = \sum_{l=0}^{\infty} \left(\tilde{U}_l(r, s) Y_l(\theta, \phi) \mathbf{e}_r + \tilde{V}_l(r, s) \frac{\partial Y_l(\theta, \phi)}{\partial \theta} \mathbf{e}_\theta + \frac{\tilde{V}_l(r, s)}{\sin \theta} \frac{\partial Y_l(\theta, \phi)}{\partial \phi} \mathbf{e}_\phi \right), \quad (4.15)$$

where the spherical harmonics $Y_l(\theta, \phi)$ satisfy the differential equation given by [e.g. Heiskanen and Moritz, 1984]

$$0 = l(l+1) Y_l(\theta, \phi) + \frac{1}{\sin \theta} \frac{\partial}{\partial \theta} \left(\sin \theta \frac{\partial Y_l(\theta, \phi)}{\partial \theta} \right) + \frac{1}{\sin^2 \theta} \frac{\partial^2 Y_l(\theta, \phi)}{\partial \phi^2}. \quad (4.16)$$

Thereafter, using the definition of the second-degree tidal Love numbers \tilde{h}_2 and \tilde{l}_2 , given by 3.83 and 3.84, the spheroidal components of the displacement vector at the surface as a result of the acting diurnal tides can be written as:

$$u_r(R, \theta, \phi, t) = \mathcal{L}^{-1} \left(\frac{\tilde{h}_2}{g_0} \tilde{V}_d^T \right), \quad (4.17)$$

$$u_\theta(R, \theta, \phi, t) = \mathcal{L}^{-1} \left(\frac{\tilde{l}_2}{g_0} \frac{\partial \tilde{V}_d^T}{\partial \theta} \right), \quad (4.18)$$

$$u_\phi(R, \theta, \phi, t) = \mathcal{L}^{-1} \left(\frac{\tilde{l}_2}{g_0 \sin(\theta)} \frac{\partial \tilde{V}_d^T}{\partial \phi} \right), \quad (4.19)$$

where the symbol \mathcal{L}^{-1} represents the inverse Laplace transform required to convert the expressions to the time domain.

Although all three components of the displacement are required for the definition of strains and stresses at the surface (see Section 4.4), in this Section we will only focus

on the radial component of the deformation (u_r) caused by the diurnal tide, as future spacecraft missions carrying an altimeter are expected to determine the existence of a subsurface ocean and characterize both the putative ocean and the overlying ice-I shell from direct measurements of the radial component of the tidal deformation at the surface [e.g. Moore and Schubert, 2000, Wahr et al., 2006, Rappaport et al., 2008, Clark et al., 2011, Grasset et al., 2013]. Therefore, we expand Equation 4.17 using analytical expressions for the Love number \tilde{h}_2 (Equation 3.86 for harmonic degree $l = 2$) and the diurnal potential $\tilde{V}_d^T(R, \theta, \phi, s)$ (Laplace transform of diurnal components of Equation 4.6). After some analytical manipulation, the radial deformation u_r at a given time t can be defined as the sum of an elastic component u_r^e and a viscous component u_r^v , which are given by

$$\begin{aligned} u_r^e = & \frac{1}{4}(nR)^2 \frac{h_{2,e}}{g_0} \left(-6eP_{2,0}(\cos\theta) \cos(nt) \right. \\ & + 4P_{2,1}(\cos\theta) \sin(\varepsilon) \left[\cos(\phi) \sin(\varpi + nt) \right] \\ & \left. + eP_{2,2}(\cos\theta) \left[4 \sin(2\phi) \sin(nt) + 3 \cos(2\phi) \cos(nt) \right] \right), \end{aligned} \quad (4.20)$$

$$\begin{aligned} u_r^v = & \frac{1}{4}(nR)^2 \sum_{j=1}^M \frac{h_{2,j}}{g_0} \frac{1}{\sqrt{1+\Gamma_j^2}} \left(-6eP_{2,0}(\cos\theta) \cos(nt - \angle\Gamma_j) \right. \\ & + 4P_{2,1}(\cos\theta) \sin(\varepsilon) \left[\cos(\phi) \sin(\varpi + nt - \angle\Gamma_j) \right] \\ & \left. + eP_{2,2}(\cos\theta) \left[4 \sin(2\phi) \sin(nt - \angle\Gamma_j) + 3 \cos(2\phi) \cos(nt - \angle\Gamma_j) \right] \right), \end{aligned} \quad (4.21)$$

where the dimensionless ratio Γ_j is defined as

$$\Gamma_j = \frac{n}{-s_j} = \frac{2\pi\tau_j}{T}, \quad (4.22)$$

with τ_j being the relaxation time of the j -th relaxation mode and T the orbital period. Furthermore, the angular variable $\angle\Gamma_j$ in Equation 4.21 represents the phase delay in the response, and is given by

$$\angle\Gamma_j = \arctan(\Gamma_j). \quad (4.23)$$

Although every relaxation mode j contributes in a characteristic way to the radial deformation at the surface, not all modal contributions are large enough to introduce an observable viscoelastic effect on the total radial deformation. In order to analyze which relaxation modes dominate the viscoelastic response, we present in Figure 4.1 a graphical representation of the influence of the ratio Γ_j on the attenuation of the modal strength $h_{2,j}$ and consequently on the amplitude of the radial deformation. If one takes into consideration that complete attenuation is represented by a value of zero in Figure 4.1 and no attenuation is represented by a value of one, we observe:

1. the contribution of a relaxation mode j to the radial deformation at diurnal frequency does not experience attenuation for values of Γ_j smaller than 0.1 (i.e. for

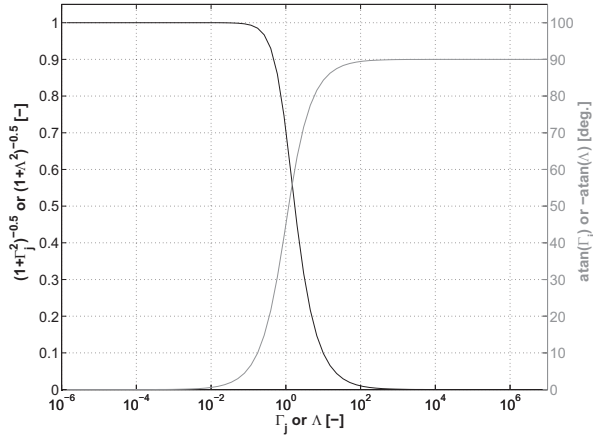


Figure 4.1: Theoretical effect of the ratio $\Gamma_j = \frac{n}{-s_j}$ on the contribution of a relaxation mode j to the amplitude of the tidal deformation (or diurnal stress) at the surface, and effect of the ratio $\Lambda = \frac{\mu/\eta}{n}$ on the relaxation state of diurnal stresses at the surface. Regarding the ratio Γ_j , the dark curve represents the attenuation of the corresponding modal strength h_{2j}^v (1 is no attenuation and 0 is complete attenuation, see e.g. Equation 4.21) and the light curve shows the phase-lag of the contribution of a mode j to the tidal deformation (or diurnal stress field). Regarding the ratio Λ , the dark curve presents the importance of viscous relaxation on the magnitude of diurnal stresses at the surface (1 means that stresses are elastically stored, whereas 0 means complete relaxation of the stresses, see Equations 4.53 to 4.58) and the light curve gives the phase-lead caused by relaxation.

relaxation times τ_j shorter than 1.36 hours in Europa's case). In other words, the relaxation of a mode j is so fast that its contribution to the tidal response is fluid-like.

2. the contribution of a relaxation mode j to the radial deformation at diurnal frequency is (nearly) completely attenuated for values of Γ_j larger than 100 (i.e. for relaxation times τ_j larger than 52.5 days in Europa's case). In other words, the relaxation of a mode j is so slow that it does not contribute to the tidal response.
3. For the range in between, i.e. $0.1 < \Gamma_j < 100$, the contribution of a relaxation mode j to the radial deformation at diurnal frequency experiences some degree of attenuation. In this range the contribution of a mode j to the tidal response is viscoelastic.

Consequently, only relaxation modes with a strong modal strength $h_{2,j}$ and a short relaxation time ($\tau_j < 52.5$ days) will have a non-negligible effect on the magnitude of the radial deformation. In a similar way, Figure 4.1 clearly shows that relaxation modes with a very short relaxation time ($\Gamma_j < 0.01$ or $\tau_j < 8$ minutes in Europa's case) contribute in a practically elastic way to the radial deformation, as their corresponding phase-lag becomes negligibly small. The phase-lag of the contribution of a given relaxation mode to the radial deformation increases significantly for larger relaxation times, becoming 90° for values of Γ_j larger than 100. However, such slow relaxation modes do not affect the

phase of the deformation field due to the strong attenuation they experience.

4.4. TIDAL STRESSES AT THE SURFACE OF AN ICY SATELLITE

In this Section we develop a method to derive the diurnal and NSR stress field at the surface of an icy satellite from the tidal viscoelastic response given by Equation 3.74 (for harmonic degree $l = 2$ and only for an external tidal excitation, i.e. $E = V$). Although the method developed here is roughly similar to the one presented by Wahr et al. [2009], there are some important differences that arise from the way the tidal Love numbers are calculated by the normal modes (or “our”) method and numerical integration methods: 1) our method enables a deeper insight into the physics of relaxation, as the non-elastic part of the response is described in terms of the contribution of each relaxation mode to the tidal response; 2) due to its purely analytical definition our method remains stable in the fluid limit, thereby making it possible to determine the tidal response and subsequent stresses of interior models containing viscoelastic layers with a very small Maxwell time (e.g. a low viscous bottom part of the ice-I shell with viscosities $\eta_{ast} < 10^{13}$ Pa s); 3) in its current definition, our method does allow for the treatment of compressibility.

The structure of this Section is as follows. In Section 4.4.1, the spheroidal elements of strain tensor at the surface are defined in terms of the tidal Love numbers. Thereafter, in Sections 4.4.2 and 4.4.3, the derived expressions for the surface strain are substituted into the stress-strain relation for a Maxwell body (Equation 2.10) to find analytical expressions for the spheroidal components of the diurnal stress tensor and NSR stress tensor at the surface. Due to the use of Love numbers computed with the normal mode method, the derived expressions for the surface strains and stresses are presented here in terms of the relaxation modes of the response in order to gain a deeper insight into the relaxation processes that may influence the response at the timescale of the applied forcing.

4.4.1. THE STRAIN-DISPLACEMENT RELATIONS

As shown by Equation 2.10, the elements of the stress tensor depend linearly on the strain for either a Maxwell or Burgers rheology. A first step in the derivation of analytical expressions to describe the surface stresses induced by tides requires then a consistent definition of the spheroidal elements of the strain tensor in terms of the surface displacements u_r , u_θ and u_ϕ through the use of the so-called strain-displacement relations. Even though this step in the derivation of tidal stresses has not been explicitly shown in Jara-Oru e and Vermeersen [2011], its omission on that article has been the source of several discussions regarding the correctness of our model after its publication. As the involving derivation appeared to be non-obvious, this subsection will concentrate on how the spheroidal elements of the surface strain tensor are obtained from general strain-displacement relations in continuum mechanics after transformation of the strain tensor to spherical coordinates. In the Laplace domain, in which the tidal Love numbers have been previously defined, the strain-displacement relations are given

by [e.g. McConnell, 1957]

$$\tilde{\epsilon}_{rr} = \frac{\partial \tilde{u}_r}{\partial r}, \quad (4.24)$$

$$\tilde{\epsilon}_{\theta\theta} = \frac{1}{r} \left(\frac{\partial \tilde{u}_\theta}{\partial \theta} + \tilde{u}_r \right), \quad (4.25)$$

$$\tilde{\epsilon}_{\phi\phi} = \frac{1}{r \sin \theta} \frac{\partial \tilde{u}_\phi}{\partial \phi} + \frac{\tilde{u}_r}{r} + \frac{\tilde{u}_\theta}{r} \cot \theta, \quad (4.26)$$

$$\tilde{\epsilon}_{r\theta} = \frac{1}{2} \left(\frac{\partial \tilde{u}_\theta}{\partial r} + \frac{1}{r} \frac{\partial \tilde{u}_r}{\partial \theta} - \frac{\tilde{u}_\theta}{r} \right), \quad (4.27)$$

$$\tilde{\epsilon}_{r\phi} = \frac{1}{2} \left(\frac{\partial \tilde{u}_\phi}{\partial r} + \frac{1}{r \sin \theta} \frac{\partial \tilde{u}_r}{\partial \phi} - \frac{\tilde{u}_\phi}{r} \right), \quad (4.28)$$

$$\tilde{\epsilon}_{\theta\phi} = \frac{1}{2} \left(\frac{1}{r} \frac{\partial \tilde{u}_\phi}{\partial \theta} + \frac{1}{r \sin \theta} \frac{\partial \tilde{u}_\theta}{\partial \phi} - \frac{\tilde{u}_\phi}{r \sin \theta} \cos \theta \right). \quad (4.29)$$

Then, substitution of the definition of the spheroidal components of the displacement vector $\tilde{\mathbf{u}}$, given by Equation 4.15, into the aforementioned strain-stress relations yields

$$\tilde{\epsilon}_{rr} = \sum_l \frac{\partial \tilde{U}_l(r, s)}{\partial r} Y_l(\theta, \phi), \quad (4.30)$$

$$\tilde{\epsilon}_{\theta\theta} = \sum_l \frac{1}{r} \left(\tilde{V}_l(r, s) \frac{\partial^2 Y_l(\theta, \phi)}{\partial \theta^2} + \tilde{U}_l(r, s) Y_l(\theta, \phi) \right), \quad (4.31)$$

$$\begin{aligned} \tilde{\epsilon}_{\phi\phi} = \sum_l \left(\frac{1}{r \sin^2 \theta} \tilde{V}_l(r, s) \frac{\partial^2 Y_l(\theta, \phi)}{\partial \phi^2} + \frac{1}{r} \tilde{U}_l(r, s) Y_l(\theta, \phi) \right. \\ \left. + \frac{\cot \theta}{r} \tilde{V}_l(r, s) \frac{\partial Y_l(\theta, \phi)}{\partial \theta} \right), \end{aligned} \quad (4.32)$$

$$\tilde{\epsilon}_{r\theta} = \frac{1}{2} \sum_l \left(\frac{\partial \tilde{V}_l(r, s)}{\partial r} + \frac{1}{r} \tilde{U}_l(r, s) - \frac{1}{r} \tilde{V}_l(r, s) \right) \frac{\partial Y_l(\theta, \phi)}{\partial \theta}, \quad (4.33)$$

$$\tilde{\epsilon}_{r\phi} = \frac{1}{2} \sum_l \frac{1}{\sin \theta} \left(\frac{\partial \tilde{V}_l(r, s)}{\partial r} + \frac{1}{r} \tilde{U}_l(r, s) - \frac{1}{r} \tilde{V}_l(r, s) \right) \frac{\partial Y_l(\theta, \phi)}{\partial \phi}, \quad (4.34)$$

$$\tilde{\epsilon}_{\theta\phi} = \sum_l \left(\frac{1}{r \sin\theta} \tilde{V}_l(r, s) \frac{\partial^2 Y_l(\theta, \phi)}{\partial\theta\partial\phi} - \frac{1}{r \sin^2\theta} \tilde{V}_l(r, s) \frac{\partial Y_l(\theta, \phi)}{\partial\phi} \right). \quad (4.35)$$

The expressions listed above give a general representation of the strain-displacement relations applicable to the interior and surface of planetary bodies. With the exception of the expression for the $\tilde{\epsilon}_{\phi\phi}$ -term, given by Equation 4.32, the relations above are already defined in a convenient way for further derivation steps. The second derivative of the spherical harmonic $\partial Y_l(\theta, \phi)$ with respect to the longitude ϕ in Equation 4.32 can be conveniently rewritten in terms of other partial derivatives using the differential equation given by Equation 4.16 such that the resulting expression resembles the structure of the $\tilde{\epsilon}_{\theta\theta}$ -term; i.e.

$$\tilde{\epsilon}_{\phi\phi} = \sum_l \left\{ \left(\frac{1}{r} \tilde{U}_l(r, s) - \frac{l(l+1)}{r} \tilde{V}_l(r, s) \right) Y_l(\theta, \phi) - \frac{1}{r} \tilde{V}_l(r, s) \frac{\partial^2 Y_l(\theta, \phi)}{\partial\theta^2} \right\}. \quad (4.36)$$

At the surface, however, some of the general strain-displacement relations presented above can be simplified by the use of the boundary condition for the tangential stress at the surface, i.e. Equation 3.22, and the differential equation for the radial deformation, i.e. Equation 3.7. Then, at the surface of a planetary satellite, the following holds:

$$\begin{aligned} \frac{\partial \tilde{V}_l(R, s)}{\partial r} + \frac{1}{R} \tilde{U}_l(R, s) - \frac{1}{R} \tilde{V}_l(R, s) &= 0, \\ \frac{\partial \tilde{U}_l(R, s)}{\partial r} &= -\frac{2}{R} \tilde{U}_l(R, s) + \frac{l(l+1)}{R} \tilde{V}_l(R, s), \end{aligned}$$

where the first expression is valid as long as the viscoelastic compliance $\tilde{\mu}(s)$ for the uppermost layer does not become equal to zero. This condition, although important for the definition of the strains, does not have an effect on the derivation of expressions for the shear stresses because the boundary condition for the tangential stress at the surface (Equation 3.22) forces the product $\tilde{\mu}(s) \left(\frac{\partial \tilde{V}_l(R, s)}{\partial r} + \frac{1}{R} \tilde{U}_l(R, s) - \frac{1}{R} \tilde{V}_l(R, s) \right)$ to be equal to zero at the surface.

Substitution of the expressions above into the relevant strain-displacement relations (i.e. Equations 4.33 and 4.34) and using the definition of the tidal Love numbers \tilde{h}_2 and \tilde{l}_2 , given by 3.83 and 3.84, leads then to the desired expressions for the second degree strain-displacement relations at the surface of an icy satellite forced by tides, i.e.

$$\tilde{\epsilon}_{rr} = \frac{2}{Rg_0} (-\tilde{h}_2(R, s) + 3\tilde{l}_2(R, s)) \tilde{V}^T, \quad (4.37)$$

$$\tilde{\epsilon}_{\theta\theta} = \frac{1}{Rg_0} \left(\tilde{l}_2(R, s) \frac{\partial^2 \tilde{V}^T}{\partial\theta^2} + \tilde{h}_2(R, s) \tilde{V}^T \right), \quad (4.38)$$

$$\tilde{\epsilon}_{\phi\phi} = \frac{1}{Rg_0} \left((\tilde{h}_2(R, s) - 6\tilde{l}_2(R, s)) \tilde{V}^T - \tilde{l}_2(R, s) \frac{\partial^2 \tilde{V}^T}{\partial\theta^2} \right), \quad (4.39)$$

$$\tilde{\epsilon}_{r\theta} = 0, \quad (4.40)$$

$$\tilde{\epsilon}_{r\phi} = 0, \quad (4.41)$$

$$\tilde{\epsilon}_{\theta\phi} = \frac{1}{Rg_0} \tilde{l}_2(R, s) \left(\frac{1}{\sin\theta} \frac{\partial^2 \tilde{V}^T}{\partial\theta\partial\phi} - \frac{\cos\theta}{\sin^2\theta} \frac{\partial \tilde{V}^T}{\partial\phi} \right), \quad (4.42)$$

where \tilde{V}^T is the Laplace-transform of the tidal potential defined by Equation 4.6, which can either refer to the diurnal part (terms V_{e1}^T , V_{e2}^T and V_{o1}^T) or the NSR part (V_{ns}^T) of the potential, depending on the timescale at which the surface stresses need to be modeled.

4.4.2. DIURNAL STRESSES

As discussed in the introduction to this Chapter, at the timescale of one orbital revolution (diurnal timescale) the interior of an icy satellite experiences tides that are driven, among others, by the orbit's non-zero eccentricity and the non-zero obliquity of the satellite's spin axis. These so-called diurnal tides trigger stresses at the surface that could be responsible for the formation of some of the tectonic features observed at the surface of the Jovian moon Europa. Here we will present a derivation of the diurnal stresses at the surface that is consistent with the normal mode approach introduced in Chapter 3. Therefore, the analytical expressions for the diurnal stresses in this Section differ in their structure from the ones given in Wahr et al. [2009], although both sets of equations lead to the same results in the incompressible limit.

Irrespective of the timescale at which the applied forcing acts and within the framework of linear viscoelasticity (see Section 2.3.1), the stress tensor at the surface of an icy satellite can be defined as

$$\sigma_{ij} = \mathcal{L}^{-1} (\tilde{\Pi} \delta_{ij} + 2\tilde{\mu}(s) \tilde{\epsilon}_{ij}(s)), \quad (4.43)$$

where δ_{ij} is the Kronecker delta, $\tilde{\epsilon}_{ij}(s)$ is the strain tensor at the surface (Equations 4.37 to 4.42) and $\tilde{\Pi}$ denotes the mean normal stress, which is defined as the product between the compliance $\tilde{\lambda}(s)$ and the dilatation $\nabla \cdot \tilde{\mathbf{u}}$. The latter can be expanded as [e.g. Sabadini and Vermeersen, 2004]

$$\nabla \cdot \tilde{\mathbf{u}} = \sum_{l=0}^{\infty} \tilde{\chi}_l Y_l(\theta, \phi). \quad (4.44)$$

Based on the spherical harmonic expansion of the dilatation given above, the definition of the radial stress for an incompressible Maxwell body (Equation 3.3), and the boundary condition on the radial stress at the surface given by Equation 3.21 (i.e. $\tilde{\sigma}_{rrl}(R, s) = 0$ in the absence of surface loading), the second degree harmonic of the mean normal stress $\tilde{\Pi}$ at the surface can be defined as

$$\tilde{\Pi} = \frac{4\tilde{\mu}(s)}{Rg_0} (\tilde{h}_2(R, s) - 3\tilde{l}_2(R, s)) \tilde{V}^T. \quad (4.45)$$

Thereafter, the non-zero elements of the stress tensor acting on the surface of an incompressible Maxwell planetary body can be retrieved by substituting Equations 4.37-4.42 and 4.45 into Equation 4.43. The resulting expressions are listed below:

$$\sigma_{\theta\theta} = \mathcal{L}^{-1} \left(2\tilde{\mu}(s) \frac{1}{Rg_0} \left\{ \tilde{l}_2(R, s) \frac{\partial^2 \tilde{V}^T}{\partial \theta^2} + 3(\tilde{h}_2(R, s) - 2\tilde{l}_2(R, s)) \tilde{V}^T \right\} \right), \quad (4.46)$$

$$\sigma_{\phi\phi} = \mathcal{L}^{-1} \left(2\tilde{\mu}(s) \frac{1}{Rg_0} \left\{ 3(\tilde{h}_2(R, s) - 4\tilde{l}_2(R, s)) \tilde{V}^T - \tilde{l}_2(R, s) \frac{\partial^2 \tilde{V}^T}{\partial \theta^2} \right\} \right), \quad (4.47)$$

$$\sigma_{\theta\phi} = \mathcal{L}^{-1} \left(2\tilde{\mu}(s) \frac{\tilde{l}_2(R, s)}{Rg_0} \left\{ \frac{1}{\sin \theta} \frac{\partial^2 \tilde{V}^T}{\partial \theta \partial \phi} - \frac{\cos \theta}{\sin^2 \theta} \frac{\partial \tilde{V}^T}{\partial \phi} \right\} \right). \quad (4.48)$$

Equations 4.46 to 4.48 show that viscoelasticity influences the state of stresses at the surface in two ways: 1) through the compliance $\tilde{\mu}(s)$, which is related to the rheological properties of the lithosphere, and 2) by the viscoelastic response itself, which is represented by the Love numbers $\tilde{h}_2(R, s)$ and $\tilde{l}_2(R, s)$. Assuming the lithosphere behaves as a Maxwell viscoelastic body, we can redefine the relevant compliance $\tilde{\mu}(s)$ as

$$\tilde{\mu}(s) = \mu \left(1 - \frac{1}{1 + s\tau_M} \right) = \mu (1 - \nu(s, \tau_M)), \quad (4.49)$$

where $\tau_M = \eta/\mu$, which is defined as the characteristic Maxwell time of the lithosphere, gives an indication of the time scale at which the rheological behavior of a material shows a transition from elastic to viscous. Moreover, the term $\nu(s, \tau_M)$ represents the relaxation of the elastic shear modulus as a function of s and the Maxwell time τ_M . As a result, the compliance $\tilde{\mu}(s)$ can be interpreted as being the effective shear modulus of the lithosphere.

Explicit analytical expressions for the diurnal stresses $\sigma_{\theta\theta}$, $\sigma_{\phi\phi}$ and $\sigma_{\theta\phi}$ at the surface can then be derived by substituting the Laplace transform of Equation 4.6 (only the diurnal terms V_{e1}^T , V_{e2}^T and V_{o1}^T), Equations 3.86 to 3.89 (for harmonic degree $l = 2$) and 4.49 into Equations 4.46 to 4.48. After some analytical manipulation, the resulting expressions for the surface stresses can be written as

$$\sigma_{\theta\theta} = \sigma_{\theta\theta}^e + \sigma_{\theta\theta}^v, \quad (4.50)$$

$$\sigma_{\phi\phi} = \sigma_{\phi\phi}^e + \sigma_{\phi\phi}^v, \quad (4.51)$$

$$\sigma_{\theta\phi} = \sigma_{\theta\phi}^e + \sigma_{\theta\phi}^v, \quad (4.52)$$

where the contribution of the elastic response (superscript e) and relaxation modes (superscript v) to the elements of the diurnal stress tensor are given by

$$\sigma_{\theta\theta}^e = \frac{1}{2} \frac{n^2 R \mu}{g_0} \frac{1}{\sqrt{1 + \Lambda^2}} \left\{ -6e\beta_{2,0}^{\theta\theta}(\theta) \cos(nt + \angle\Lambda) \right\}$$

$$\begin{aligned}
& + e\beta_{2,2}^{\theta\theta}(\theta) \left[4 \sin(2\phi) \sin(nt + \angle\Lambda) + 3 \cos(2\phi) \cos(nt + \angle\Lambda) \right] \\
& + 4 \sin(\varepsilon) \beta_{2,1}^{\theta\theta}(\theta) \left[\cos(\phi) \sin(\varpi + nt + \angle\Lambda) \right] \Big\}, \tag{4.53}
\end{aligned}$$

$$\begin{aligned}
\sigma_{\theta\theta}^v &= \frac{1}{2} \frac{n^2 R \mu}{g_0} \frac{1}{\sqrt{1 + \Lambda^2}} \sum_{j=1}^M \left(\frac{1}{\sqrt{1 + \Gamma_j^2}} \left\{ -6e\beta_{2,0}^{\theta\theta,j}(\theta) \cos(nt - \angle\Gamma_j + \angle\Lambda) \right. \right. \\
& + 4e\beta_{2,2}^{\theta\theta,j}(\theta) \sin(2\phi) \sin(nt - \angle\Gamma_j + \angle\Lambda) \\
& + 3e\beta_{2,2}^{\theta\theta,j}(\theta) \cos(2\phi) \cos(nt - \angle\Gamma_j + \angle\Lambda) \\
& \left. \left. + 4 \sin(\varepsilon) \beta_{2,1}^{\theta\theta,j}(\theta) \left[\cos(\phi) \sin(\varpi + nt - \angle\Gamma_j + \angle\Lambda) \right] \right\} \right), \tag{4.54}
\end{aligned}$$

$$\begin{aligned}
\sigma_{\phi\phi}^e &= \frac{1}{2} \frac{n^2 R \mu}{g_0} \frac{1}{\sqrt{1 + \Lambda^2}} \left\{ -6e\beta_{2,0}^{\phi\phi}(\theta) \cos(nt + \angle\Lambda) \right. \\
& + e\beta_{2,2}^{\phi\phi}(\theta) \left[4 \sin(2\phi) \sin(nt + \angle\Lambda) + 3 \cos(2\phi) \cos(nt + \angle\Lambda) \right. \\
& \left. \left. + 4 \sin(\varepsilon) \beta_{2,1}^{\phi\phi}(\theta) \left[\cos(\phi) \sin(\varpi + nt + \angle\Lambda) \right] \right\}, \tag{4.55}
\end{aligned}$$

$$\begin{aligned}
\sigma_{\phi\phi}^v &= \frac{1}{2} \frac{n^2 R \mu}{g_0} \frac{1}{\sqrt{1 + \Lambda^2}} \sum_{j=1}^M \left(\frac{1}{\sqrt{1 + \Gamma_j^2}} \left\{ -6e\beta_{2,0}^{\phi\phi,j}(\theta) \cos(nt - \angle\Gamma_j + \angle\Lambda) \right. \right. \\
& + 4e\beta_{2,2}^{\phi\phi,j}(\theta) \sin(2\phi) \sin(nt - \angle\Gamma_j + \angle\Lambda) \\
& + 3e\beta_{2,2}^{\phi\phi,j}(\theta) \cos(2\phi) \cos(nt - \angle\Gamma_j + \angle\Lambda) \\
& \left. \left. + 4 \sin(\varepsilon) \beta_{2,1}^{\phi\phi,j}(\theta) \left[\cos(\phi) \sin(\varpi + nt - \angle\Gamma_j + \angle\Lambda) \right] \right\} \right), \tag{4.56}
\end{aligned}$$

$$\begin{aligned}
\sigma_{\theta\phi}^e &= \frac{1}{2} \frac{n^2 R \mu}{g_0} \frac{1}{\sqrt{1 + \Lambda^2}} \\
& \times \left\{ 2e\beta_{2,2}^{\theta\phi}(\theta) \left[4 \cos(2\phi) \sin(nt + \angle\Lambda) - 3 \sin(2\phi) \cos(nt + \angle\Lambda) \right] \right. \\
& \left. + 4 \sin(\varepsilon) \beta_{2,1}^{\theta\phi}(\theta) \left[\sin(\phi) \sin(\varpi + nt + \angle\Lambda) \right] \right\}, \tag{4.57}
\end{aligned}$$

$$\begin{aligned}
\sigma_{\theta\phi}^v &= \frac{1}{2} \frac{n^2 R \mu}{g_0} \frac{1}{\sqrt{1 + \Lambda^2}} \sum_{j=1}^M \left(\frac{1}{\sqrt{1 + \Gamma_j^2}} \right. \\
& \times \left. \left\{ 8e\beta_{2,2}^{\theta\phi,j}(\theta) \cos(2\phi) \sin(nt - \angle\Gamma_j + \angle\Lambda) \right\} \right)
\end{aligned}$$

Table 4.2: Auxiliary Beta-functions relevant for the definition of the elements of the diurnal stress tensor, which are given by Equations 4.53 to 4.58.

Beta-function	Definition
$\beta_{2,0}^{\theta\theta}(\theta)$	$\frac{3}{4}(3h_{2,e} - 10l_{2,e})\cos(2\theta) + \frac{3}{4}(h_{2,e} - 2l_{2,e})$
$\beta_{2,0}^{\theta\theta,j}(\theta)$	$\frac{3}{4}(3h_{2,j} - 10l_{2,j})\cos(2\theta) + \frac{3}{4}(h_{2,j} - 2l_{2,j})$
$\beta_{2,1}^{\theta\theta}(\theta)$	$\frac{3}{2}(3h_{2,e} - 10l_{2,e})\sin(2\theta)$
$\beta_{2,1}^{\theta\theta,j}(\theta)$	$\frac{3}{2}(3h_{2,j} - 10l_{2,j})\sin(2\theta)$
$\beta_{2,2}^{\theta\theta,j}(\theta)$	$-\frac{3}{2}(3h_{2,j} - 10l_{2,j})\cos(2\theta) + \frac{9}{2}(h_{2,j} - 2l_{2,j})$
$\beta_{2,0}^{\theta\phi}(\theta)$	$\frac{3}{4}(3h_{2,e} - 8l_{2,e})\cos(2\theta) + \frac{3}{4}(h_{2,e} - 4l_{2,e})$
$\beta_{2,0}^{\theta\phi,j}(\theta)$	$\frac{3}{4}(3h_{2,j} - 8l_{2,j})\cos(2\theta) + \frac{3}{4}(h_{2,j} - 4l_{2,j})$
$\beta_{2,1}^{\theta\phi}(\theta)$	$\frac{3}{2}(3h_{2,e} - 8l_{2,e})\sin(2\theta)$
$\beta_{2,1}^{\theta\phi,j}(\theta)$	$\frac{3}{2}(3h_{2,j} - 8l_{2,j})\sin(2\theta)$
$\beta_{2,2}^{\theta\phi}(\theta)$	$-\frac{3}{2}(3h_{2,e} - 8l_{2,e})\cos(2\theta) + \frac{9}{2}(h_{2,e} - 4l_{2,e})$
$\beta_{2,2}^{\theta\phi,j}(\theta)$	$-\frac{3}{2}(3h_{2,j} - 8l_{2,j})\cos(2\theta) + \frac{9}{2}(h_{2,j} - 4l_{2,j})$
$\beta_{2,1}^{\theta\phi}(\theta)$	$3l_{2,e}\sin(\theta)$
$\beta_{2,1}^{\theta\phi,j}(\theta)$	$3l_{2,j}\sin(\theta)$
$\beta_{2,2}^{\theta\phi}(\theta)$	$3l_{2,e}\cos(\theta)$
$\beta_{2,2}^{\theta\phi,j}(\theta)$	$3l_{2,j}\cos(\theta)$

$$\begin{aligned}
& -6e\beta_{2,2}^{\theta\phi,j}(\theta)\sin(2\phi)\cos(nt - \angle\Gamma_j + \angle\Lambda) \\
& + 4\sin(\varepsilon)\beta_{2,1}^{\theta\phi,j}(\theta)\left[\sin(\phi)\sin(\varpi + nt - \angle\Gamma_j + \angle\Lambda)\right]\Bigg\}, \quad (4.58)
\end{aligned}$$

where the auxiliary Beta-functions in the equations listed above are short notations that include the dependence of the diurnal stress on the elastic Love numbers $h_{2,e}$ and $l_{2,e}$ (or the modal strengths $h_{2,j}$ and $l_{2,j}$) and the co-latitude θ . Explicit expressions for these functions are listed separately in Table 4.2. Furthermore, the dimensionless ratio Λ and its corresponding angular variable $\angle\Lambda$ are defined by⁴

$$\Lambda = \frac{\mu/\eta}{n} = \frac{T}{2\pi\tau_M}, \quad (4.59)$$

$$\angle\Lambda = \arctan(\Lambda), \quad (4.60)$$

From a theoretical point of view, the dimensionless ratio Λ describes the relaxation state of diurnal stresses at the surface. As can be observed from Figure 4.1, relaxation at the surface starts to become important for values of Λ larger than 0.1. In the case of Europa's lithosphere, $\Lambda > 0.1$ corresponds to viscosities smaller than 1.7×10^{15} Pa s for a rigidity $\mu = 3.5$ GPa, or to viscosities smaller than 4.9×10^{14} Pa s for a rigidity $\mu = 1$ GPa. Such low viscosities are, however, more representative for the lower portion of the

⁴ Γ_j and $\angle\Gamma_j$ were previously defined in Section 4.3, by Equations 4.22 and 4.23, respectively

icy shell and are several orders of magnitude smaller than the plausible values expected for the viscosity of a cold, conducting lithosphere [Husmann et al., 2002, Nimmo and Manga, 2009]. For this reason, it can be stated that diurnal stresses are elastically stored in the lithosphere due to the high viscosity of the upper ice layer and/or the high frequency of the forcing function. This statement is in agreement with [Wahr et al., 2009].

On the other hand, viscoelasticity may have an important effect on the magnitude and geographical distribution of surface diurnal stresses. As shown by Equations 4.54, 4.56 and 4.58, every relaxation mode j that is part of the viscoelastic response contributes to the surface diurnal stress. However, often only a few modes are strong enough to introduce a noticeable viscoelastic effect to the diurnal stress field at the surface. Similar to the discussion on the effect of relaxation modes on the radial deformation at the surface, the curves in Figure 4.1 suggest that only the relaxation modes with strong modal strengths ($h_{2,j}$ and $l_{2,j}$) and short relaxation time τ_j will have a non-negligible effect on the magnitude of the diurnal stresses at the surface, whereas modes with a value for Γ_j around 1.0 have the largest potential to induce a phase-lag in the stress field. Despite their large phase-lag, the contribution of relaxation modes with Γ_j larger than 100 (i.e. τ_j larger than 52.5 days in Europa's case) can be safely neglected, since their corresponding modal strengths are reduced by more than two orders of magnitude.

4.4.3. NSR STRESSES

Based on studies on the formation of global scale tectonic features on Europa's surface, non synchronous rotation (NSR) of Europa's ice shell has been widely suggested as an important mechanism to generate large stresses (\sim MPa) at the surface [Leith and McKinnon, 1996, Greenberg et al., 1998, Gleeson et al., 2005, Harada and Kurita, 2007, Hurford et al., 2007, Kattenhorn and Hurford, 2009, Sotin et al., 2009, Wahr et al., 2009]. From the perspective of rotational dynamics, NSR would take place if tidal torques acting on the decoupled shell have driven the rotation of the shell to a slightly faster than synchronous state [Greenberg and Weidenschilling, 1984]. However, as shown by Bills et al. [2009], the tidal torque acting on Europa cannot be large enough to overcome the counteracting gravitational torque exerted by Jupiter on permanent asymmetries in the figure of Europa (represented by the difference between the equatorial moments of inertia, i.e. $B - A$). In addition, recent research by [Goldreich and Mitchell, 2010] points out that the tidal torque is counteracted by an elastic torque resulting from the rotation of the ice-I shell with respect to the equilibrium figure of the ocean. Even though the occurrence of NSR cannot be precluded from this study, the resulting stresses on the surface would be too small to create a crack [Goldreich and Mitchell, 2010]. Although non synchronous rotation (NSR) of Europa's ice shell is strongly opposed by the dynamical considerations discussed above, NSR is still possible if driven by mass displacements in the interior of the body [Ojakangas and Stevenson, 1989b, Bills et al., 2009].

Here, we compute the NSR stress field at Europa's surface from the Maxwell viscoelastic response (Equation 3.74 for harmonic degree $l = 2$ and only for an external tidal excitation, i.e. $E = V$) and the NSR forcing function (term V_T^{ns} in Equation 4.6) by applying the methodology introduced in Section 4.4.2. As a result, we are allowed to write each non-zero element of the NSR stress tensor in the form given by Equations

4.46 to 4.48. Before using these equations to compute NSR surface stresses, we need to remark that the Love numbers \tilde{h}_2 and \tilde{l}_2 required for NSR calculations differ from the Love numbers used to derive the diurnal response (see Tables in Section 5.4). The different set of tidal Love numbers results from our assumption to keep the rocky interior synchronously locked while the ice shell experiences NSR. As the rocky mantle remains tidally locked, the stresses induced by the formation of the mantle's bulge had sufficient time to relax completely and, therefore, the response of the rocky interior to the NSR forcing function can be described as being purely fluid. From a modeling perspective, we can describe this physical behavior by decreasing the rigidity of the mantle μ to values relevant for near-fluid materials, i.e. $\mu \approx 0$ [e.g. Wahr et al., 2009]. After taking these observations into account, we can proceed to express the NSR stress field at Europa's surface ($\hat{\sigma}_{ij}$) as a combination of a purely elastic part (superscript e) and the contribution from the relaxation modes (superscript v), i.e.:

$$\hat{\sigma}_{\theta\theta} = \hat{\sigma}_{\theta\theta}^e + \hat{\sigma}_{\theta\theta}^v, \quad (4.61)$$

$$\hat{\sigma}_{\phi\phi} = \hat{\sigma}_{\phi\phi}^e + \hat{\sigma}_{\phi\phi}^v, \quad (4.62)$$

$$\hat{\sigma}_{\theta\phi} = \hat{\sigma}_{\theta\phi}^e + \hat{\sigma}_{\theta\phi}^v, \quad (4.63)$$

where the individual stress components in Equations 4.61 to 4.63 are obtained after substitution of the Laplace transform of Equation 4.6 (only the NSR term V_{ns}^T), Equations 3.86 to 3.89 (for harmonic degree $l = 2$) and 4.49 into Equations 4.46 to 4.48. After some analytical manipulation, the resulting expressions for the surface stresses can be written as

$$\hat{\sigma}_{\theta\theta}^e = \frac{1}{2} \frac{n^2 R \mu}{g_0} \frac{1}{\sqrt{\Delta^2 + 1}} \alpha_{2,2}^{\theta\theta}(\theta) \cos(2\phi + 2\Omega_{ns}t + \angle\Delta), \quad (4.64)$$

$$\begin{aligned} \hat{\sigma}_{\theta\theta}^v &= \frac{1}{2} \frac{n^2 R \mu}{g_0} \frac{1}{\sqrt{\Delta^2 + 1}} \\ &\times \sum_{j=1}^M \left\{ \frac{1}{\sqrt{1 + \gamma_j^2}} \alpha_{2,2}^{\theta\theta,j}(\theta) \cos(2\phi + 2\Omega_{ns}t + \angle\Delta - \angle\gamma_j) \right\}, \end{aligned} \quad (4.65)$$

$$\hat{\sigma}_{\phi\phi}^e = \frac{1}{2} \frac{n^2 R \mu}{g_0} \frac{1}{\sqrt{\Delta^2 + 1}} \alpha_{2,2}^{\phi\phi}(\theta) \cos(2\phi + 2\Omega_{ns}t + \angle\Delta), \quad (4.66)$$

$$\hat{\sigma}_{\phi\phi}^v = \frac{1}{2} \frac{n^2 R \mu}{g_0} \frac{1}{\sqrt{\Delta^2 + 1}}$$

$$\times \sum_{j=1}^M \left\{ \frac{1}{\sqrt{1+\gamma_j^2}} \alpha_{2,2}^{\phi\phi,j}(\theta) \cos(2\phi + 2\Omega_{ns}t + \angle\Delta - \angle\gamma_j) \right\}, \quad (4.67)$$

$$\hat{\sigma}_{\theta\phi}^e = -\frac{n^2 R\mu}{g_0} \frac{1}{\sqrt{\Delta^2+1}} \alpha_{2,2}^{\theta\phi}(\theta) \sin(2\phi + 2\Omega_{ns}t + \angle\Delta), \quad (4.68)$$

$$\begin{aligned} \hat{\sigma}_{\theta\phi}^v = & -\frac{n^2 R\mu}{g_0} \frac{1}{\sqrt{\Delta^2+1}} \\ & \times \sum_{j=1}^M \left\{ \frac{1}{\sqrt{1+\gamma_j^2}} \alpha_{2,2}^{\theta\phi,j}(\theta) \sin(2\phi + 2\Omega_{ns}t + \angle\Delta - \angle\gamma_j) \right\}, \end{aligned} \quad (4.69)$$

where the Alpha-functions are similar to the previously defined Beta-functions in the sense that they provide a description of the dependence of NSR stresses on the interior's response (Love numbers) and the co-latitude. Explicit expressions for these functions are listed in Table 4.3.

Furthermore, the dimensionless ratio Δ , which describes the relaxation state of NSR stresses at Europa's surface, is defined by

$$\Delta = \frac{\mu/\eta}{2\Omega_{ns}} = \frac{T_{ns}}{4\pi\tau_M}, \quad (4.70)$$

and the ratio γ_j , which describes the influence of a relaxation mode to NSR stresses, is defined by

$$\gamma_j = \frac{2\Omega_{ns}}{-s_j} = \frac{4\pi\tau_j}{T_{ns}}. \quad (4.71)$$

In Equations 4.70 and 4.71, the frequency of the NSR forcing function is defined as twice the constant angular rate of NSR, i.e. $2\Omega_{ns}$. This definition is motivated by the fact

Table 4.3: Auxiliary Alpha-functions relevant for the definition of the elements of the NSR stress tensor, which are given by Equations 4.64 to 4.69. The elastic Love numbers $\hat{h}_{2,e}$ and $\hat{l}_{2,e}$, and modal strengths $\hat{h}_{2,j}$ and $\hat{l}_{2,j}$ refer to the tidal response of interior models in which the silicate mantle has been assumed to behave as a fluid with respect to NSR.

Alpha-function	Definition
$\alpha_{2,2}^{\theta\theta}(\theta)$	$-\frac{3}{2}(3\hat{h}_{2,e} - 10\hat{l}_{2,e}) \cos(2\theta) + \frac{9}{2}(\hat{h}_{2,e} - 2\hat{l}_{2,e})$
$\alpha_{2,2}^{\theta\theta,j}(\theta)$	$-\frac{3}{2}(3\hat{h}_{2,j} - 10\hat{l}_{2,j}) \cos(2\theta) + \frac{9}{2}(\hat{h}_{2,j} - 2\hat{l}_{2,j})$
$\alpha_{2,2}^{\phi\phi}(\theta)$	$-\frac{3}{2}(3\hat{h}_{2,e} - 8\hat{l}_{2,e}) \cos(2\theta) + \frac{9}{2}(\hat{h}_{2,e} - 4\hat{l}_{2,e})$
$\alpha_{2,2}^{\phi\phi,j}(\theta)$	$-\frac{3}{2}(3\hat{h}_{2,j} - 8\hat{l}_{2,j}) \cos(2\theta) + \frac{9}{2}(\hat{h}_{2,j} - 4\hat{l}_{2,j})$
$\alpha_{2,2}^{\theta\phi}(\theta)$	$3\hat{l}_{2,e} \cos(\theta)$
$\alpha_{2,2}^{\theta\phi,j}(\theta)$	$3\hat{l}_{2,j} \cos(\theta)$

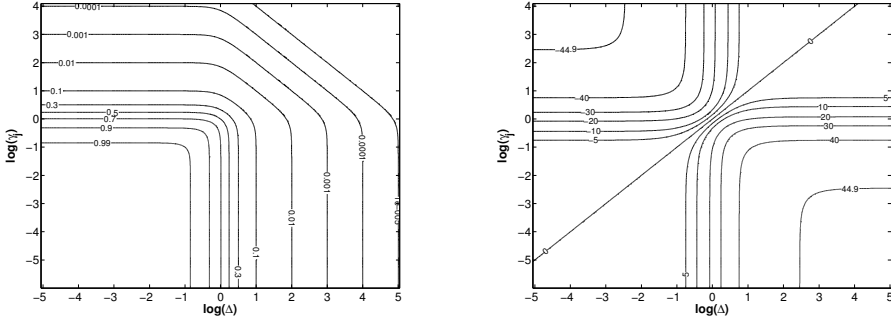


Figure 4.2: (Left:) Viscoelastic relaxation state (1 is no relaxation and 0 is complete relaxation) of the contribution of a normal mode j to NSR stresses as a function of the dimensionless parameters $\Delta = \frac{\mu/\eta}{2\Omega_{ns}}$ and $\gamma_j = \frac{2\Omega_{ns}}{-s_j}$. (Right:) Westward longitudinal shift of NSR stress patterns at the surface as a function of the dimensionless parameters $\Delta = \frac{\mu/\eta}{2\Omega_{ns}}$ and $\gamma_j = \frac{2\Omega_{ns}}{-s_j}$.

that a fixed point on the surface of Europa's rotating shell crosses the tidal bulge twice during one period of NSR, under the assumption that the angular rate Ω_{ns} remains constant.

The combined effect of Δ and γ_j on the various components of the NSR stress field can be analyzed with support of Figure 4.2, in which the relaxation behavior of very fast relaxation modes (i.e. $\gamma_j \ll 0.1$) provides a good approximation to the behavior of the purely elastic contribution to NSR stresses. Both figures show that viscoelastic relaxation in the lithospheric ice shell starts to strongly influence the behavior of NSR stresses when Δ becomes larger than ~ 0.1 . However, as shown by the left panel of Figure 4.2, viscoelastic relaxation has a relatively larger effect on nearly-elastic contributions to NSR stresses ($\gamma_j < 0.1$) than on contributions from slow relaxation modes. This behavior is logical, as stresses related to slow relaxation modes are already attenuated by the viscoelastic character of the response itself. Besides attenuation of the magnitude, viscoelastic relaxation also introduces a westward shift on the spatial distribution of stress patterns at the surface. The right panel of Figure 4.2 shows that the longitudinal shift in westward direction can become as large as 45 degrees for $\Delta > 100$ and $\gamma_j < 0.1$, i.e. in a regime where NSR stresses are being severely relaxed away.

5

TIDAL DEFORMATIONS AND STRESSES II: APPLICATION TO ICY MOONS

As briefly mentioned in Chapter 4, this Chapter concentrates on the application of the theoretical background presented throughout Chapter 4 to the determination of tidal deformations and stresses at the surface of the Jovian icy satellites Europa and Ganymede. In Sections 5.2 and 5.3, the relation between deformation due to the acting diurnal tides and the parameters that define the interiors of Europa and Ganymede, respectively, is analyzed. In Section 5.4, the combined diurnal and NSR tidal stress field at Europa's surface is determined in order to analyze whether the resulting global stress field could provide an explanation for the formation of the large diversity of lineament morphologies observed at Europa's surface.

5.1. TIDAL LOVE NUMBERS: EUROPA

Application of the normal mode approach to a range of plausible 5-layered interior models of Europa, which are constructed by combining the values shown in Tables 2.4 and 2.7, shows that the viscoelastic response of Europa's interior to the applied tidal forces consists of six relaxation modes and the elastic response. The triggered normal modes are: C_0 at the core-mantle boundary, M_0 at the mantle-ocean boundary, L_0 at the ocean-ice boundary, T_1 and T_2 at the introduced viscosity contrast within the ice-I shell, and S_0 at the surface. The corresponding inverse relaxation times s_j (in kyr^{-1} , with kyr being a kiloyear or one thousand years) and modal strengths $h_{2,j}$ and $l_{2,j}$ are listed in Table 5.1 for the reference interior model of Europa defined in Table 2.8. Similar tables could be generated for other interior models, however the general properties of the response to diurnal tides would remain largely unchanged as most variations are introduced by the redefinition of the properties of the layers that describe Europa's ice-I shell as will be

Table 5.1: Tidal response of the reference model of Europa's interior to diurnal tidal forces.

Mode	s_j [kyr ⁻¹]	Γ_j [-]	$h_{2,e}$ or $h_{2,j}$ [-]	$l_{2,e}$ or $l_{2,j}$ [-]
elastic	–	–	1.15071×10^0	3.07919×10^{-1}
C_0	-4.49845×10^{-1}	1.43652×10^6	5.17450×10^{-2}	1.40281×10^{-2}
M_0	-3.44861×10^0	1.87383×10^5	7.16873×10^{-1}	1.94708×10^{-1}
L_0	-3.23712×10^{-1}	1.99625×10^6	1.36834×10^{-3}	2.33756×10^{-4}
S_0	-1.08495×10^{-1}	5.95614×10^6	3.70745×10^{-2}	1.00821×10^{-2}
T_1	-1.82721×10^5	3.53661×10^0	7.19756×10^{-5}	5.99921×10^{-3}
T_2	-1.02845×10^6	6.28334×10^{-1}	8.51979×10^{-2}	2.27102×10^{-2}

discussed later.

A close inspection of the values listed in Table 5.1 shows that the slow-relaxing buoyancy modes C_0 , M_0 , L_0 and S_0 do not contribute to the diurnal response as their corresponding values for the ratio $\Gamma_j = \frac{n}{-s_j}$ are several orders of magnitude larger than 100. Only the fast-relaxing transient modes T_1 and T_2 remain as potential candidates, with the mode T_2 having by far the largest contribution to the diurnal response due to its larger modal strength and its faster relaxation time. Note, however, that the contribution of the transient mode T_1 to the tidal Love number l_2 may be non-negligible, especially when its own ratio Γ_j is around 1. In order to illustrate how large the contribution of the transient modes to the tidal response is, Figures 5.1 and 5.2 display the dependence of the magnitude and phase-lag of the tidal Love number h_2 on the frequency of the applied forcing for interior models based on the reference model but with a varying value for the viscosity of the ductile lower part of the ice-I shell (or asthenosphere). In Figure 5.1 it can be observed that only interior models with a low-viscous asthenosphere contribute to the diurnal response in radial direction at the surface, whereas models with a high-viscous asthenosphere will only experience viscous relaxation if the frequency of the forcing would be much smaller than the orbital frequency. This pattern is the result of the relation between the Γ_j (or the relaxation time) of the transient mode T_2 and the viscosity of the asthenosphere, with Γ_j decreasing/increasing by one order of magnitude when the viscosity decreases/increases by the same order. Therefore, for the models depicted in Figure 5.1, the viscoelastic behavior of the asthenosphere at the frequency of the acting diurnal tides ranges from nearly fluid for $\eta_{ast} = 1.0 \times 10^{13}$ Pa s (nearly complete relaxation of the T_2 -mode) to effectively elastic for $\eta_{ast} \geq 1.0 \times 10^{15}$ Pa s (no relaxation of the T_2 -mode). In between, for values around $\eta_{ast} = 1.0 \times 10^{14}$ Pa s the strong transient mode T_2 experiences viscous relaxation, thereby leading to a phase-lag in the response, as can be observed from the peak in Figure 5.2 for the curve corresponding to $\eta_{ast} = 1.0 \times 10^{14}$ Pa s. As such, the results depicted in Figures 5.1 and 5.2 are in complete agreement with the theoretical expectations based on the curves displayed in Figure 4.1.

Besides the viscosity of the lower ductile part of the ice-I shell, other geophysical parameters may have an important effect on the magnitude and phase-lag of the tidal Love numbers at the surface at the frequency of the acting diurnal tides. Of special interest are the parameters that characterize the upper layers of the internal structure, especially the

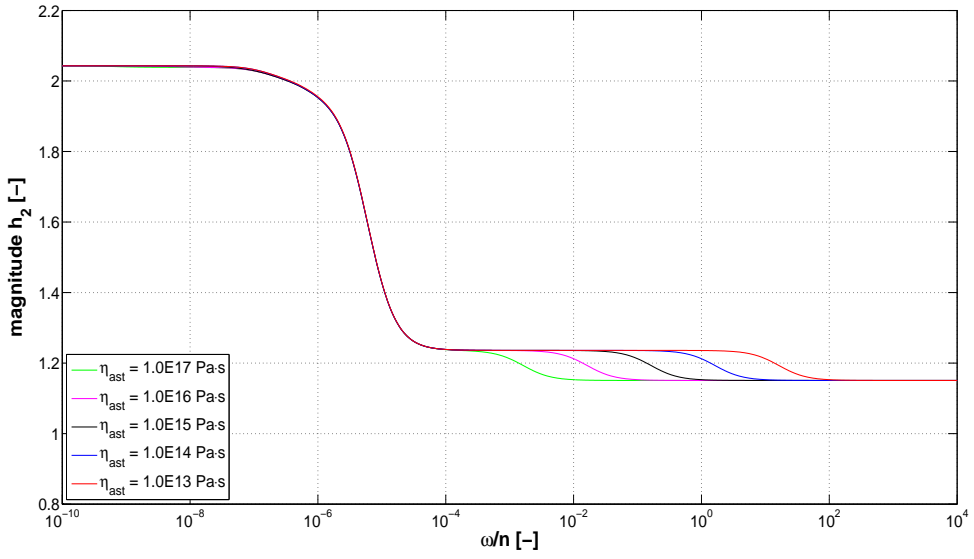


Figure 5.1: Magnitude of the complex tidal Love number h_2 as a function of the normalized frequency ω/n for interior models based on the reference model shown in Table 2.8, in which the viscosity of the lower ductile part of the ice-I shell (or asthenosphere) ranges from 1.0×10^{13} Pa s to 1.0×10^{17} Pa s.

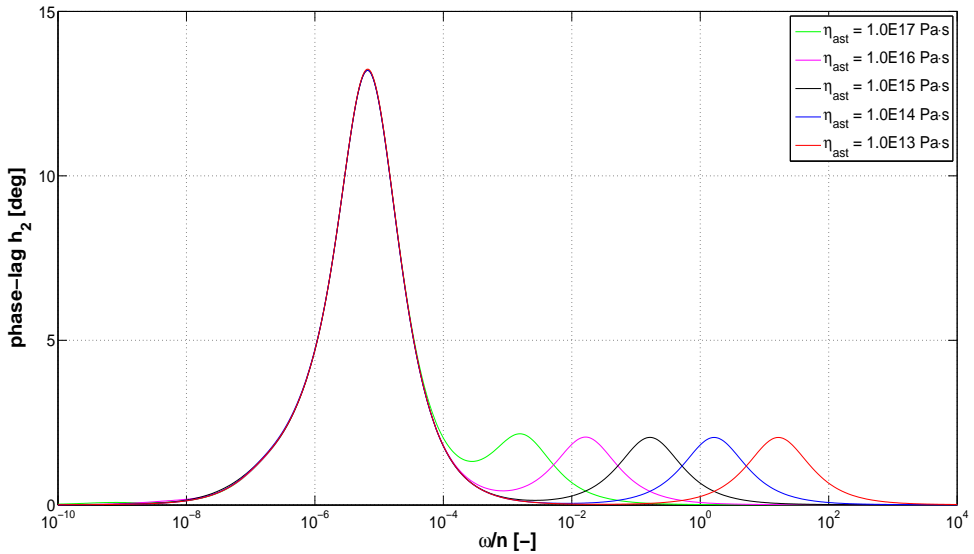


Figure 5.2: Phase-lag of the complex tidal Love number h_2 as a function of the normalized frequency ω/n for interior models based on the reference model shown in Table 2.8, in which the viscosity of the lower ductile part of the ice-I shell (or asthenosphere) ranges from 1.0×10^{13} Pa s to 1.0×10^{17} Pa s.

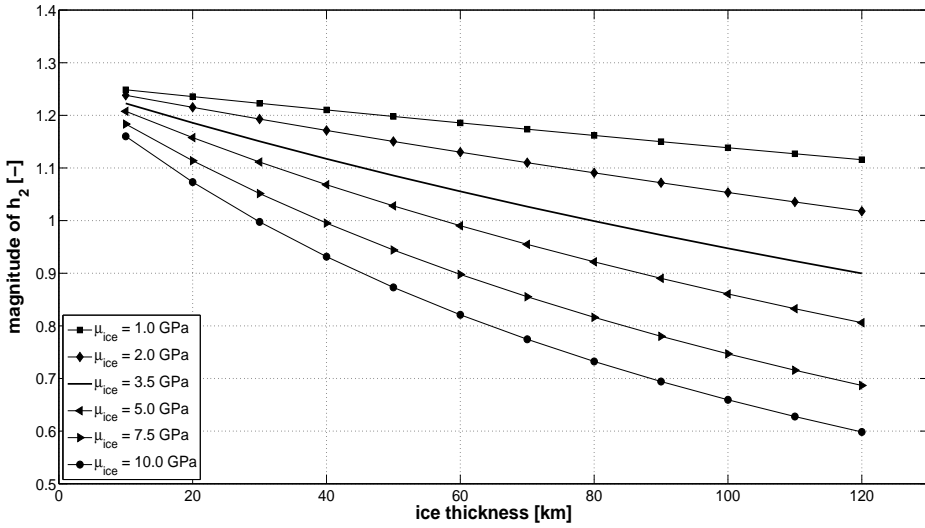


Figure 5.3: Magnitude of the complex tidal Love number h_2 as a function of the ice-I shell thickness for values of the rigidity of ice ranging from 1 GPa to 10 GPa. In all cases, the viscosity of the lower ductile part of the ice-I shell (or asthenosphere) is set at 1.0×10^{17} Pa s, the bottom of the ocean is at 130 km depth and the density of the ocean and shell are 1000 kg m^{-3} and 937 kg m^{-3} , respectively.

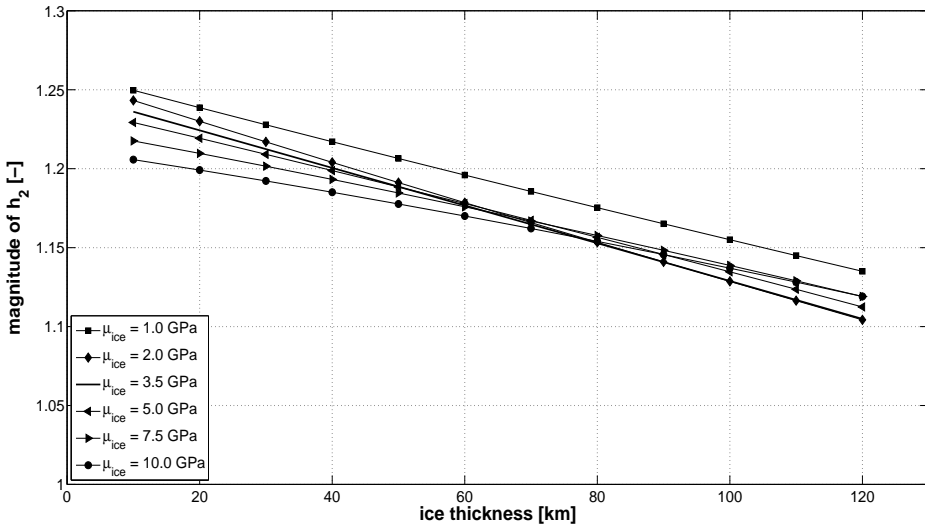


Figure 5.4: Magnitude of the complex tidal Love number h_2 as a function of the ice-I shell thickness for values of the rigidity of ice ranging from 1 GPa to 10 GPa. In all cases, the viscosity of the lower ductile part of the ice-I shell (or asthenosphere) is set at 1.0×10^{14} Pa s, the bottom of the ocean is at 130 km depth and the density of the ocean and shell are 1000 kg m^{-3} and 937 kg m^{-3} , respectively.

thickness and rigidity of the ice-I shell and the density of the subsurface ocean. Figure 5.3 shows the sensitivity of the magnitude of the tidal Love number h_2 to the aforementioned properties of the shell for models of Europa's interior that are further defined by the parameters that characterize the reference model¹ and a value for the viscosity of the lower part of the ice-I shell that leads to an effectively elastic response at the surface (i.e. $\eta_{ast} = 1.0 \times 10^{17}$ Pa s). As can be observed from the patterns shown in Figure 5.3, the magnitude of the tidal Love number h_2 decreases with increasing thickness of the ice-I shell as well as with increasing rigidity. In addition, it can be observed that the variations in the magnitude of h_2 as a result of the rigidity become more pronounced as the thickness of the shell increases. As a result, the lowest values for the Love number h_2 in the case of an effectively elastic shell correspond to a thick and rigid shell. This statement is somewhat expected since thicker and more rigid shells will offer more resistance to deformation at the surface.

The previous discussion does not hold, however, if the viscosity of the lower portion of the shell is more representative of a convective interior. In that scenario, viscoelastic relaxation in the lower portion of the ice-I shell would lead to an increase of the magnitude of the Love numbers at the surface and a phase-lag in the response as long as the response of the shell does not approach the fluid limit (see e.g. Figures 5.1 and 5.2), with the effects of viscoelastic relaxation on the Love numbers being more pronounced for thick shells with a large value for the rigidity of ice-I due to presence of a stronger transient mode T_2 in the viscoelastic response. As such, the magnitude of the tidal Love numbers is expected to become less sensitive on the assumed values for the thickness and rigidity of the ice-I shell, as can be observed from the patterns shown in Figure 5.4 for the same interior models as in Figure 5.3 but with a viscosity $\eta_{ast} = 1.0 \times 10^{14}$ Pa s for the lower part of the ice-I shell (be aware of the different scale for the y-axis). Figure

¹Recall that the densities of the core and mantle vary as the thickness of the shell changes.

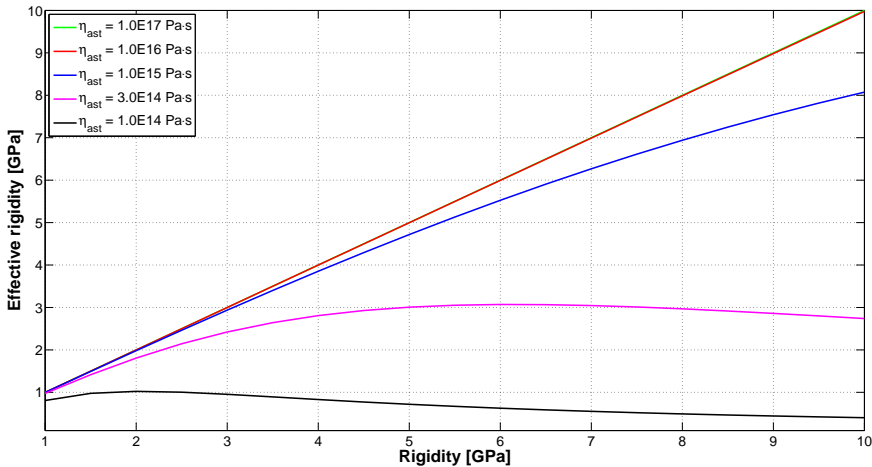


Figure 5.5: Effective rigidity of the asthenosphere (real part of $\bar{\mu}$) at the frequency of the diurnal tides as a function of the rigidity of ice for different values for the viscosity of the asthenosphere.

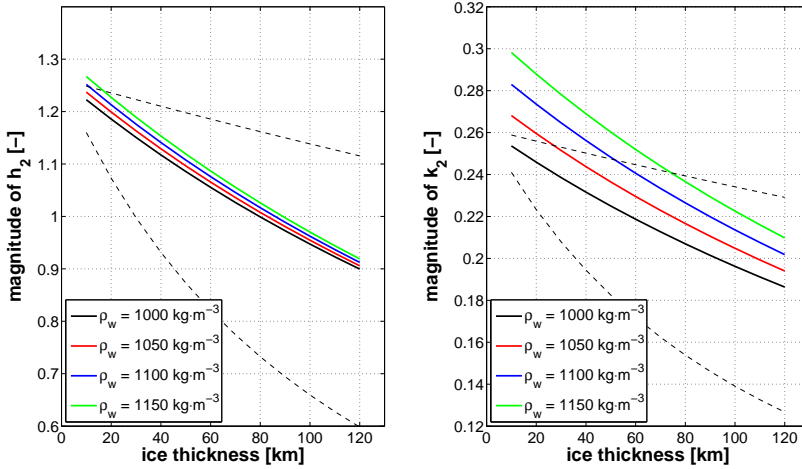


Figure 5.6: Magnitude of the tidal Love numbers h_2 (left) and k_2 (right) as a function of the ice shell thickness for values for the density of the ocean ranging from $\rho_w = 1000 \text{ kg m}^{-3}$ to $\rho_w = 1150 \text{ kg m}^{-3}$. The other parameters are taken from the reference interior model in the effectively elastic limit for the viscosity of the lower part of the ice shell. The broken lines represent a rigidity of 1 GPa (upper curve) and 10 GPa (lower curve) for the ice-I shell and are shown in the figure as a representation of the variations induced by the thickness and rigidity of the ice-I shell.

5.4 shows that the magnitude of the tidal Love number h_2 still decreases with increasing thickness, albeit in a less pronounced way relative to the effectively elastic case discussed before (compare to Figure 5.3). The dependence of the Love numbers on the rigidity of the ice shell is less straightforward because the viscosity of the asthenosphere lowers the value of the effective shear modulus of the lower ductile part of the ice-I shell for viscosities lower than $\eta_{ast} \sim 1.0 \times 10^{16} \text{ Pa s}$ (see Figure 5.5). For the assumed value for the viscosity of the icy asthenosphere ($\eta_{ast} = 1.0 \times 10^{14} \text{ Pa s}$), Figure 5.5 also shows that the effective rigidity of the asthenosphere increases slightly as the rigidity increases towards $\sim 2 \text{ GPa}$ while it decreases for larger values for the rigidity. This behavior explains why the dependence of the magnitude of the Love number h_2 on the shell thickness becomes weaker for the larger values of the rigidity of ice depicted in Figure 5.4.

In addition, uncertainties in the densities of Europa's upper layers may also lead to variations in the magnitude of the tidal Love numbers at the surface. However, as can be observed from Figures 5.6 (for the density of the ocean) and 5.7 (for the density of the shell), these variations are relatively small (only a few percent) when compared to the ones introduced by the poorly constrained thickness and rheological parameters of the ice-I shell. The only significant exception is given by the strong increase in the magnitude of the tidal Love number k_2 with increasing ocean density ($\sim 12 - 18\%$ for the explored range of densities), which is shown in the right panel of Figure 5.6. As such, the sensitivity of the tidal Love number k_2 on the density of the subsurface ocean is nearly of a similar order as its sensitivity on the thickness and rheological parameters of the ice-I shell. Therefore, the role of the poorly constrained density of the internal ocean needs to

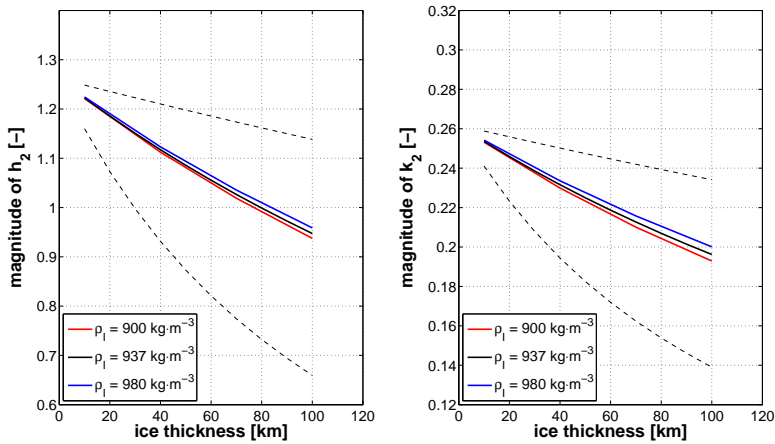


Figure 5.7: Magnitude of the tidal Love numbers h_2 (left) and k_2 (right) as a function of the ice shell thickness for values for the density of the ice-I shell ranging from $\rho_I = 900 \text{ kg m}^{-3}$ to $\rho_I = 980 \text{ kg m}^{-3}$. The other parameters are taken from the reference interior model in the effectively elastic limit for the viscosity of the lower part of the ice shell. The broken lines represent a rigidity of 1 GPa (upper curve) and 10 GPa (lower curve) for the ice-I shell and are shown in the figure as a representation of the variations induced by the thickness and rigidity of the ice-I shell.

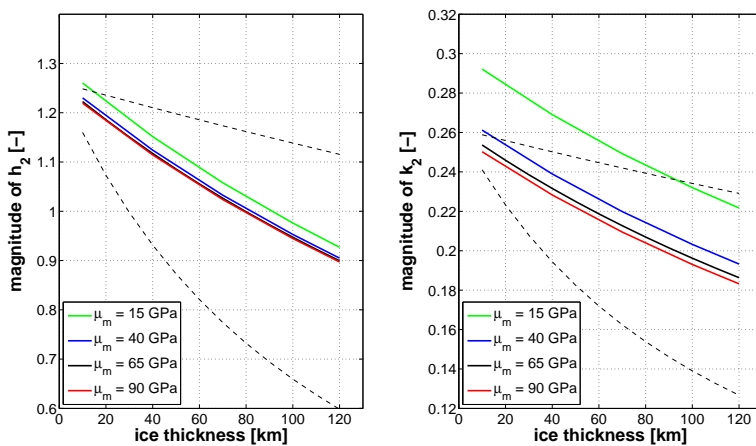


Figure 5.8: Magnitude of the tidal Love numbers h_2 (left) and k_2 (right) as a function of the ice shell thickness for values for the rigidity of the silicate mantle ranging from $\mu_m = 12 \text{ GPa}$ to $\mu_m = 90 \text{ GPa}$. The other parameters are taken from the reference interior model in the effectively elastic limit for the viscosity of the lower part of the ice shell. The broken lines represent a rigidity of 1 GPa (upper curve) and 10 GPa (lower curve) for the ice-I shell and are shown in the figure as a representation of the variations induced by the thickness and rigidity of the ice-I shell.

be taken into account when analyzing the implications of a measured value of k_2 on the characterization of the geophysical parameters of Europa's upper layers. In addition, the tidal Love numbers are only weakly dependent (or nearly independent) on the density of the shell and, in the case of the deformation Love numbers h_2 and l_2 , on the density of the ocean.

The parameters that characterize the deeper layers of Europa's internal structure usually have a negligibly small effect on the tidal Love numbers at the frequency of the diurnal tides. Nevertheless, deviations from the assumed value for the rigidity of the rocky mantle may lead to considerable variations in the magnitude of the tidal Love numbers at the surface. As can be observed from Figure 5.8, these variations are largest for the tidal Love number k_2 in the case that the rigidity of the mantle is only a fraction of the reference value. On the other hand, changes in the tidal Love number h_2 remain limited to a few percent unless the rigidity of the mantle would be as low as 15 GPa. Such low values are, however, significantly smaller than typical values for the rigidity of rocky materials, unless Europa's mantle contains a few percent of melt [e.g. Fischer and Spohn, 1990, Moore, 2003, Moore and Hussmann, 2009].

Based on the discussion presented so far in this Section, the dependence of the tidal Love numbers at the surface on the geophysical parameters that characterize Europa's interior may be summarized, for practical purposes, as follows:

- In case that the lower portion of the ice-I shell behaves in an effectively elastic way at the frequency of the diurnal tides, i.e. when the relaxation time of the dominant relaxation mode T_2 is much larger than the orbital period (or alternatively when $\Gamma_j \gg 1$ for the T_2 -mode), the tidal response at the surface will be largely controlled by the thickness and rigidity of the ice-I shell. Since the magnitude of the tidal Love numbers decreases with increasing thickness and/or increasing rigidity, the largest values for the Love numbers most likely correspond to interior models with a thin ice shell and a low value for the rigidity of ice. On the other hand, the smallest values for the Love numbers suggest interior models with a thick shell and a large value for the rigidity of ice. For most values for the tidal Love numbers, however, many different combinations of thickness and rigidity are possible as the contribution of both parameters on the tidal response is difficult to separate.
- Viscoelastic relaxation in the lower portion of the ice-I shell (or asthenosphere) lowers the effective rigidity of that layer, thereby leading to an increase in the magnitude of the tidal response at the surface. The tidal response becomes less sensitive to the thickness and rigidity of the ice-I shell. The effect of viscoelastic relaxation on the magnitude of the tidal Love numbers is largest for values for the viscosity of the asthenosphere close to the reference value at melting point ($\sim 10^{13}$ Pa s), as the behavior of the lower portion of the ice-I shell as a response to the acting diurnal tides starts to approach the fluid limit (i.e. $\Gamma_j \ll 1$ for the dominant relaxation mode T_2).
- In addition, viscoelastic relaxation may lead to a phase-lag in the response as long as the inverse relaxation time s_j of the dominant T_2 transient mode of the viscoelastic response is of the order of the orbital frequency (i.e. $0.01 < \Gamma_j < 100$). This statement can be rephrased in a simpler way by taking into account that the

inverse relaxation time of the T_2 -mode, which is related to the rheological properties of the icy asthenosphere, and the inverse Maxwell time ($\tau_M^{-1} = \mu/\eta$) of the icy asthenosphere are of the same order of magnitude. Hence, it can be alternatively stated that the tidal response at the surface will show a phase-lag if the inverse Maxwell time of the icy asthenosphere is of similar order of magnitude as the orbital frequency.

- Although the tidal Love numbers h_2 and l_2 barely depend on the density of the subsurface ocean, the magnitude of the tidal Love number k_2 can experience variations in the order 15 – 18% as a result of uncertainties in the density of the ocean. These variations are nearly of a similar order as the ones induced by uncertainties in the thickness and/or rigidity of the ice-I shell on the magnitude of the k_2 tidal Love number at the surface.
- The tidal Love numbers h_2 , l_2 and k_2 barely depend on the density of the ice-I shell.
- The tidal Love numbers at the surface are largely independent of parameters that characterize the deeper layers of Europa's internal structure. However, a softer silicate mantle, due e.g. the presence of melt, may lead to larger tidal Love numbers at the surface of Europa, especially in the case of the Love number k_2 .

At this point, it is interesting to discuss the implications of the previous statements on future measurements of Europa's tidal Love numbers. Due to the complex dependence of Europa's tidal Love numbers on the geophysical properties of the ice-I shell and ocean, it can be stated that future measurements of Europa's tidal Love numbers h_2 and k_2 will most likely not allow for the unambiguous determination of the shell thickness. As can be observed from Figure 5.9, in which the relation between the thickness of Europa's shell and the tidal Love numbers h_2 and k_2 at the surface is depicted for a plausible set of interior models of Europa, it is mostly the combination of the unknown thickness and rigidity of the shell that makes it difficult to interpret the Love numbers in terms of the shell thickness, whereas the density of the ocean could in principle be constrained due to its larger effect on the Love number k_2 . This is in agreement with previous results presented in e.g. Moore and Schubert [2000].

As an example, we assume that Europa's tidal Love numbers h_2 and k_2 at the frequency of the acting diurnal tides have a magnitude equal to $h_2 = 1.12 \pm 0.01$ and $k_2 = 0.23 \pm 0.0014$, where the uncertainties are a first guess taken from the ones expected for future measurements by ESA's JUpiter ICy moons Explorer (JUICE) mission for the case of Ganymede's tidal Love numbers [e.g. Parisi et al., 2014]. This hypothetical measurement of Europa's tidal Love numbers is shown in Figure 5.9, in which the intersection region between the assumed measurements encompasses the plausible interior models that would fit the hypothetical measurements. In that sense, Figure 5.9 shows that the assumed values for the tidal Love numbers h_2 and k_2 would provide a rather good constraint on the density of the ocean (i.e. $\rho_w \sim 1000 \text{ kgm}^{-3}$) but would fail to constrain the thickness of the ice-I shell, mainly as a consequence of the poorly known rigidity of ice-I because interior models with a shell thickness ranging from $\sim 30 \text{ km}$ to $\sim 120 \text{ km}$

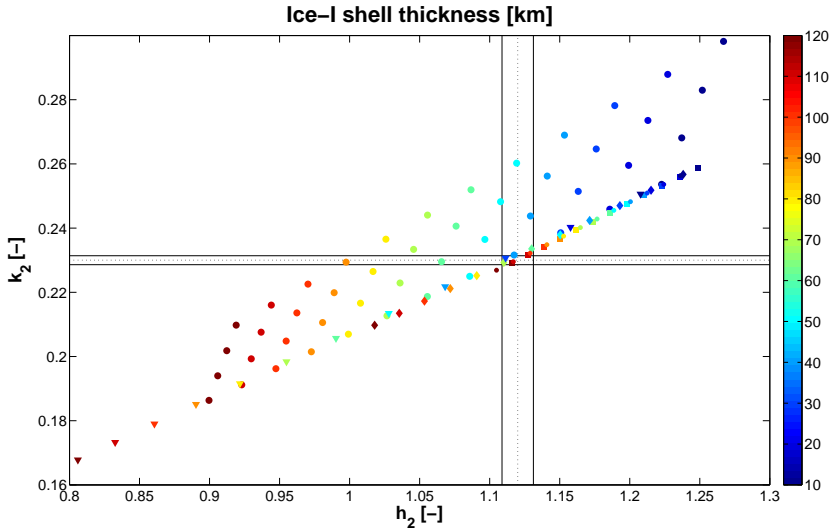


Figure 5.9: Total thickness of Europa's ice-I shell for different combinations of the tidal Love numbers h_2 and k_2 . The large circles in the plot represent interior models with a rigidity $\mu_I = 3.5$ GPa (reference value) for the ice-I shell and a viscosity $\eta_{ast} = 1.0 \times 10^{17}$ Pa s for the lower part of the ice-I shell (effectively elastic shell). The lowest diagonal corresponds to models with an ocean density $\rho_w = 1000 \text{ kgm}^{-3}$; the density of the ocean increases by 50 kgm^{-3} for every diagonal in the plot. Furthermore, the small circles correspond to interior models for which $\mu_I = 3.5$ GPa and $\rho_w = 1000 \text{ kgm}^{-3}$, but with a low-viscous icy asthenosphere ($\eta_{ast} = 1.0 \times 10^{14}$ Pa s). The squares, diamonds and triangles correspond to interior models with a rigidity $\mu_I = 1$ GPa, $\mu_I = 2$ GPa and $\mu_I = 5$ GPa for the ice-I shell, respectively. In all those cases, the density of the ocean is fixed at $\rho_w = 1000 \text{ kgm}^{-3}$ and the viscosity of the asthenosphere at $\eta_{ast} = 1.0 \times 10^{17}$ Pa s. The colors represent the corresponding thickness of the ice-I shell. In addition, random but plausible values for the magnitude of the tidal Love numbers h_2 and k_2 are included in the plot ($h_2 = 1.12 \pm 0.01$ and $k_2 = 0.23 \pm 0.0014$) in order to simulate the implication a possible future measurement of these values for the determination of the ice shell thickness.

5

would fit the assumed values. Additional measurements, such as of longitudinal librations, would then be necessary to discriminate between the rigidity and thickness of the shell. The same conclusions hold for other combinations of values for h_2 and k_2 , with the exception of the left part of the plot as only interior models with a thick and very rigid ice-I shell fit the assumed values for the tidal Love numbers.

Furthermore, as can be observed from the data points depicted by the small solid colored circles in Figure 5.9, the introduction of a dissipative viscoelastic ice layer in the modeling ($\eta_{ast} = 1.0 \times 10^{14}$ Pa s in this case) leads to a similar effect in the interpretation of the tidal Love numbers as the lowering of the rigidity of the shell. However, as shown in Figure 5.2, the presence of a dissipative ice layer also leads to a phase lag in the response. Since the phase lag depends strongly on the imaginary part of the Love numbers², future observations of this phase lag may have the potential to provide some insight into the rheological properties that characterize the bottom part of the ice shell.

²In contrast, the magnitude of the tidal Love numbers at diurnal frequency depends stronger on the real part of the Love numbers.

The interpretation of the phase lag of the tidal Love numbers in terms of the geophysical parameters of the ice shell remains challenging though, as the rheological behavior of the icy asthenosphere does not need to obey the linear Maxwell model implemented here (see Section 2.3).

5.2. TIDAL DEFORMATION: APPLICATION TO EUROPA

The actual surface deformation experienced by Europa due to the acting diurnal tides exerted by Jupiter can easily be retrieved by substituting the relevant Love numbers (elastic Love number $h_{2,e}$, modal strengths $h_{2,j}$ and inverse relaxation times s_j) into Equations 4.20 and 4.21. For the case of the reference model of Europa's interior (see Table 2.8 for its definition and Table 5.1 for the corresponding tidal response at the diurnal frequency), the maximum radial displacement at the surface is displayed in Figure 5.10 for the case in which only the eccentricity tides are taken into account (i.e. zero obliquity). It can be observed that the largest radial displacement at the surface is about 27 meters and takes place at the equator about 33° eastwards and westwards from the 0° and 180° meridians. Another interesting feature in Figure 5.10 can be observed at latitudes $\sim 54.5^\circ\text{N}$ and $\sim 54.5^\circ\text{S}$ along the 0° and 180° meridians, where the tidal deformation experienced by Europa's surface is close to zero. This may be important to take into consideration for the design of future spacecraft missions to Europa, as altimeter crossover analysis at these locations can be used to detect errors in the spacecraft orbit and/or errors in the instrument itself [Wu et al., 2001, Wahr et al., 2006].

Since the surface displacement due to diurnal tides depends on the geophysical parameters that characterize Europa's interior only through the tidal Love number h_2 , the dependence of the tidal deformation on parameters such as the ice thickness, ice rigidity and density of the ocean will follow the same patterns as the ones previously discussed for the tidal Love number h_2 . As a result, the maximum surface displacement may range

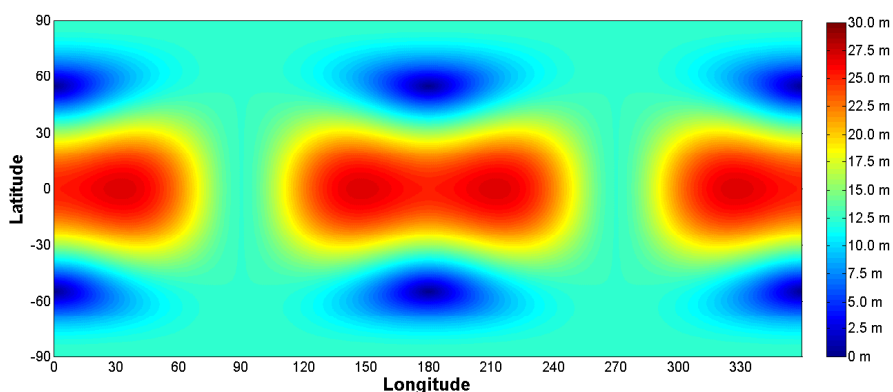


Figure 5.10: Maximum radial displacement at the surface of the reference model of Europa's interior as a result of the acting diurnal tides. The obliquity of Europa's spin axis is assumed to be zero.

between ~ 14 m, for the case of an interior with a very rigid and thick ice-I shell, and ~ 30 m, for the case of an interior with a dense subsurface ocean and a thin ice-I shell (see Figure 5.6).

The patterns shown in Figure 5.10 do not hold if the obliquity of Europa's spin axis is taken into account in the analysis. Although not yet measured, the obliquity of Europa's spin axis is expected to be small based on the outcome of dynamical models dealing with the precessional motion of the spin pole about the orbit pole [Bills, 2005, Bills et al., 2009, Baland et al., 2012]. Figure 5.11 shows the deformation patterns corresponding to three possible scenarios: 1) one in which the obliquity is assumed to take the theoretical value $\varepsilon = 0.04^\circ$ corresponding to the case in which the dynamical model has been extended to deal with the presence of an internal liquid layer [Baland et al., 2012], 2) one in which the obliquity takes the value $\varepsilon = 0.1^\circ$ corresponding to the case in which the dynamical model has been applied to a completely solid interior [Bills, 2005, Bills et al., 2009]³, and 3) one in which the obliquity is assumed to be $\varepsilon = 0.3^\circ$, which corresponds to the lowest estimates resulting from the fitting of cycloid features with tidal stress patterns [Rhoden et al., 2010]. In all three cases, it can be observed that a non-zero obliquity breaks the symmetric deformation pattern along Europa's equator, with the shifts in the patterns becoming more pronounced as the obliquity increases. Moreover, in Figure 5.11 a non-zero obliquity also leads to anti-symmetric deformation patterns at the surface along the 0° and 180° meridians. These anti-symmetric patterns, however, are an artifact of the assumed value for the unknown argument of pericenter ϖ ($\varpi = 0^\circ$ in the plots shown in Figure 5.11). Alternative values for the argument of pericenter ϖ would therefore lead to different deformation patterns at the surface, as can be observed from Figure 5.12 for $\varpi = 90^\circ$.

An alternative way to provide a graphical representation of the tidal deformation experienced by Europa is by illustrating how the surface deformation patterns evolve as Europa moves along its orbit; i.e. as a function of time. In Figure 5.13, the diurnal deformation experienced by Europa at times $t = 0$, $t = 1/4T$, $t = 1/2T$ and $t = 3/4T$ is shown for two similar models of Europa's interior⁴ for an obliquity $\varepsilon = 0.1^\circ$. Aside from the visualization of the expected change from deformation patterns dominated by stretching (positive deformation) in the vicinity of the orbit's pericenter to patterns dominated by squeezing (negative deformation) around the orbit's apocenter, Figure 5.13 shows that the presence of a dissipative ice-I layer in Europa's interior leads to a westward shift of the deformation patterns at the surface relative to the case in which the behavior of the ice shell is effectively elastic (compare the patterns in the bottom plot to the ones in the top plot). The resulting westward shift of the deformation patterns can be regarded as the surface expression of the phase lag that characterizes the tidal response of a viscoelastic Europa, which by definition should be understood as a time delay in the re-

³The same case has been studied by Baland et al. [2012], leading to a value $\varepsilon = 0.055^\circ$. This value differs from the one in Bills [2005] mainly due to the omission of a coefficient term for the harmonic $C_{2,2}$ in the definition of the spin precession rate parameter in Bills [2005].

⁴Both interior models are characterized by the values corresponding to the reference model but with an ice thickness of 90 km instead of 30 km (and the subsequent changes in the density of the core and the silicate mantle). The only difference between the models is the value for the viscosity of the ductile part of the ice-I shell, which in the case of the top plot is $\eta_{ast} = 1.0 \times 10^{17}$ Pa s and in the case of the bottom plot $\eta_{ast} = 1.0 \times 10^{14}$ Pa s.

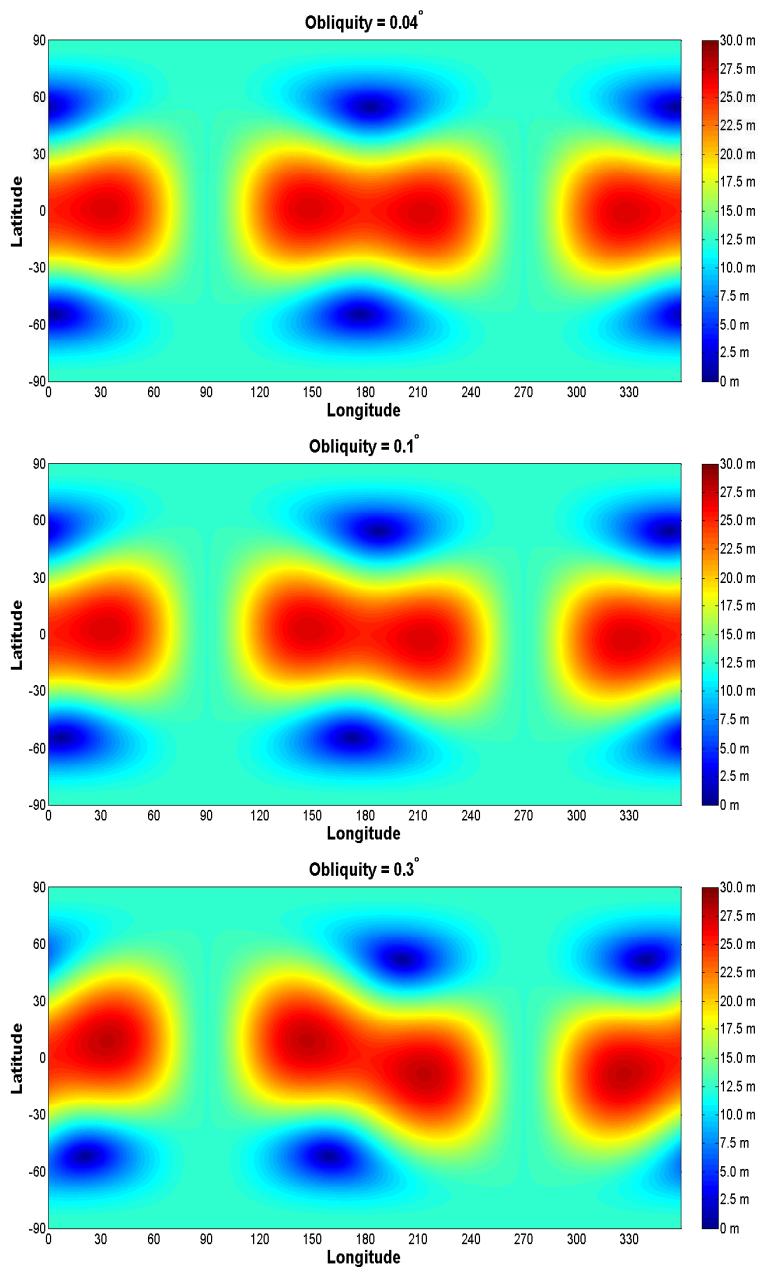
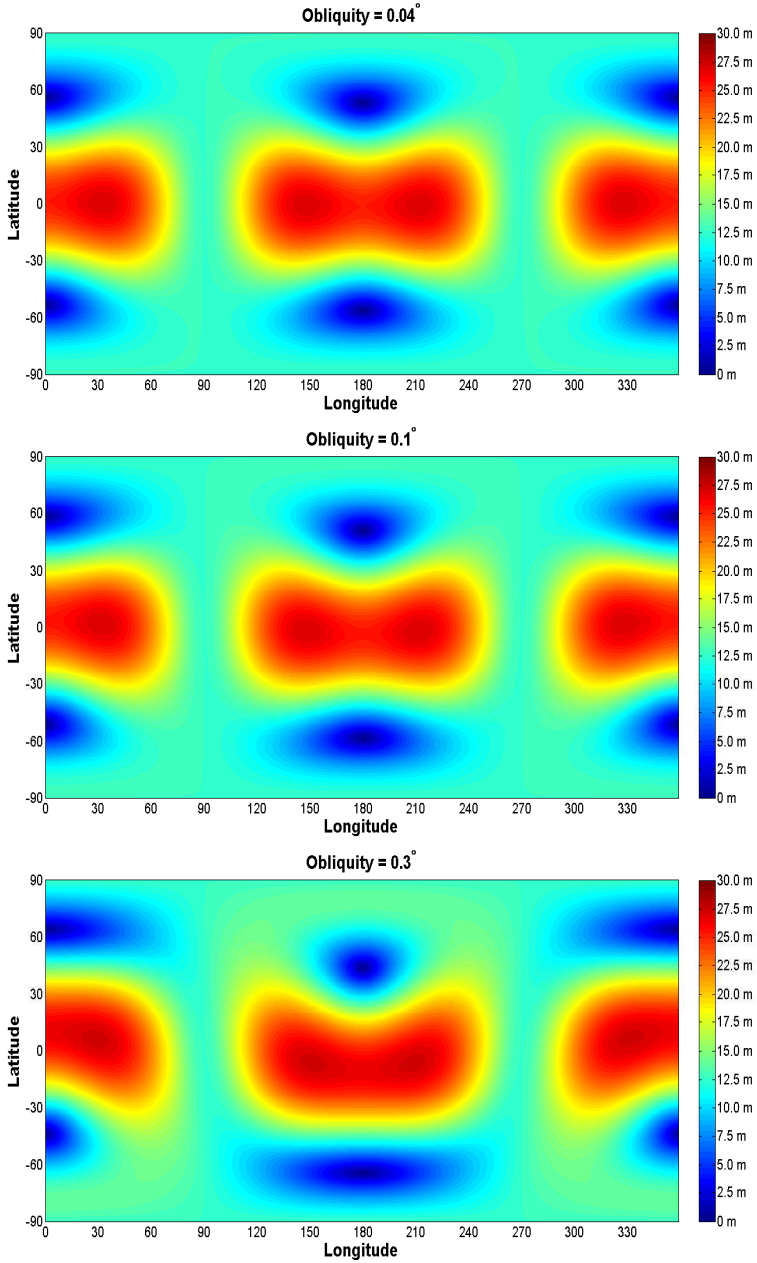


Figure 5.11: Maximum radial displacement at the surface of the reference model of Europa's interior as a result of the acting diurnal tides. The obliquity of Europa's spin axis is assumed to be $\varepsilon = 0.04^\circ$ (top), $\varepsilon = 0.1^\circ$ (middle) and $\varepsilon = 0.3^\circ$ (bottom). In all cases the unknown argument of pericenter ϖ is assumed to be $\varpi = 0^\circ$.



5

Figure 5.12: Maximum radial displacement at the surface of the reference model of Europa's interior as a result of the acting diurnal tides. The obliquity of Europa's spin axis is assumed to be $\epsilon = 0.04^\circ$ (top), $\epsilon = 0.1^\circ$ (middle) and $\epsilon = 0.3^\circ$ (bottom). In all cases the unknown argument of pericenter ω is assumed to be $\omega = 90^\circ$.

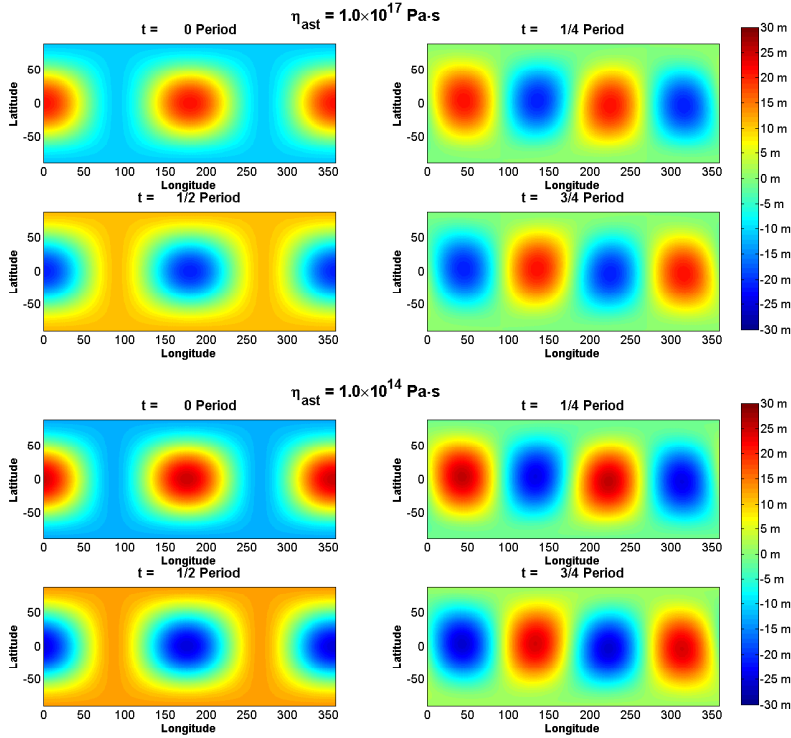


Figure 5.13: Radial displacement at Europa's surface due to the acting diurnal tides as a function of Europa's position along its orbit ($t = 0$, $t = 1/4T$, $t = 1/2T$ and $t = 3/4T$, where T is Europa's orbital period around Jupiter). The parameters that characterize the interior of Europa are defined by the values corresponding to the reference model (Table 2.8) but with an ice thickness of 90 km instead of 30 km and different values for the viscosity of the asthenosphere. (Top:) viscosity of the icy asthenosphere is $\eta_{ast} = 1.0 \times 10^{17}$ Pa s. (Bottom:) viscosity of the icy asthenosphere is $\eta_{ast} = 1.0 \times 10^{14}$ Pa s. In both cases, the obliquity of Europa's spin axis is assumed to be $\varepsilon = 0.1^\circ$ and the unknown argument of pericenter is assumed to be $\omega = 0^\circ$.

sponse and not as a longitudinal shift itself. As an example, the phase lag corresponding to tidal response shown in the bottom half of Figure 5.13 is about 6 degrees for the assumed Maxwell rheology. On the other hand, as can be deduced from the modeling used to produce Figure 5.13, the westward shift oscillates around half of that value depending on the position of Europa along its orbit.

5.3. TIDAL DEFORMATION: APPLICATION TO GANYMEDE

The content of this Section has been entirely taken from the article *Tides on Jupiter's moon Ganymede and their relation to its internal structure* [Jara-Oru e and Vermeersen, 2016] that has been accepted for publication in the special issue for *Dutch Planetary Geosciences* of the *Netherlands Journal of Geosciences*. As such, the content in this Section may contain some topics that have been already discussed earlier in this thesis. Further-

more, the notation and interior models used for the generation of results in this Section are only valid for this Section and, hence, they do not apply to other Sections of this thesis.

5.3.1. ABSTRACT

One of the major scientific objectives of ESA's JUICE (Jupiter ICy moons Explorer) mission, which is scheduled for launch in 2022 and planned to arrive at the Jovian system in 2030, is to characterize the internal water ocean and overlying ice shell of Jupiter's largest moon Ganymede. As part of the strategy developed to realize this objective, the tidal response of Ganymede's interior will be constrained by JUICE's measurements of surface displacements - by the Ganymede Laser Altimeter (GALA) instrument - and variations in the gravitational potential - by the 3GM radio science package - due to the acting diurnal tides. Here we calculate the tidal response at the surface of Ganymede for several plausible internal configurations in order to analyze the relation between the tidal response and the geophysical parameters that characterize Ganymede's interior. Similarly to the case of Jupiter's smallest icy satellite Europa, the tidal response of Ganymede in the presence of a subsurface ocean - which could be as large as about 3.5 meters in terms of the induced radial deformation - mostly depends on the structural (thickness, density) and rheological (rigidity, viscosity) properties of the ice-I shell. Nevertheless, the dependence of the tidal response on several geophysical parameters of the interior, in particular on the thickness and rigidity of the ice-I shell, does not allow for the unambiguous determination of the shell thickness from tidal measurements alone. Additional constraints could be provided by the measurement of forced longitudinal librations at the surface, as their amplitude is more sensitive to the rigidity than to the thickness of the shell.

5.3.2. INTRODUCTION

Jupiter's moon Ganymede, the largest icy satellite in our solar system and the only one with an own magnetic field [Kivelson et al., 1996], may harbor a subsurface water ocean underneath its icy crust. The expected presence of a subsurface ocean in Ganymede's interior is based on evidences provided by thermal evolution models [e.g. Showman et al., 1997, Spohn and Schubert, 2003, Bland et al., 2009], as well as models dealing with the morphology of impact craters [Schenk, 2002, Senft and Stewart, 2011] and the possible detection of an induced magnetic field from Galileo's observation of Ganymede's internal magnetic moments [Kivelson et al., 2002]. However, despite this body of evidences, the existence of a subsurface ocean has not yet been unambiguously confirmed and remains, therefore, one of the most important scientific objectives of future dedicated missions such as ESA's Jupiter ICy moons Explorer (JUICE) mission [Grasset et al., 2013].

If a subsurface ocean is present, the properties of both the ocean and the overlying ice-I shell need to be characterized in order to assess its potential habitability. In order to reach this goal, the JUICE mission carries instruments able to measure the tidally-induced displacements at the surface, the variations in the gravitational potential due to tides, the amplitude of forced longitudinal librations and the properties of the induced

magnetic field. The main goal of the Ganymede Laser Altimeter (GALA) is the determination of the surface topography and tidally-induced vertical displacements. The development of the GALA instrument is based on the heritage of BELA, the laser altimeter for the BepiColombo mission to Mercury [Thomas et al., 2007]; though the design of GALA is expected to be very different as a result of different mission constraints and the specific environment at Jupiter. The gravity field of Ganymede will be derived from the Gravity and Geophysics of Jupiter and Galilean Moons (3GM) radio science package instrument. The main observable here is the spacecraft (S/C) velocity along the Earth-to-S/C line-of-sight (the so-called range-rate) reconstructed by means of precise measurements of the Doppler shift of a highly stable microwave radio link at Ka-band between the S/C and the ground station antennas. Furthermore, JUICE's magnetometer (MAG) will detect the magnetic induction response at multiple frequencies of likely subsurface oceans in Ganymede's interior. MAG will consist of two boom-mounted sensors. Although the separate measurements provided by any of these instruments have the potential to identify the putative subsurface ocean, the characterization of the geophysical properties of the ocean and the shell would require an observation strategy that combines all the aforementioned measurements [Grasset et al., 2013].

In this paper we will focus on analyzing the sensitivity of the tidally-induced deformations at Ganymede's surface and variations in Ganymede's gravitational potential (i.e. the tidal Love numbers h_2 and k_2 , respectively) on the geophysical parameters that characterize the internal structure of the satellite. In our analysis we will assume that an ocean is present in the interior, as the clear difference in the tidal response between models with an ocean and those without has been already extensively discussed in Moore and Schubert [2003]. Although Moore and Schubert [2003] also discussed the dependence of the Love numbers on the rheology and thickness of the shell, their models considered a constant density for all present phases of water in the interior under the assumption that variations in density are small compared to uncertainties in their interior modeling. However, as shown by Baland et al. [2014] for the case of Saturn's moon Titan, the tidal Love number k_2 is mostly sensitive to uncertainties in the density of the subsurface ocean and to a lesser extent to the thickness and rheology of the shell. Therefore, it seems necessary to include the effect of density variations caused by phase transitions of water in the interior in order to provide a more robust analysis of the sensitivity of the tidal response on the parameters that characterize Ganymede's interior. In addition, in accordance with stagnant-lid convection models [e.g. Kirk and Stevenson, 1987, Showman et al., 1997, Spohn and Schubert, 2003, Tobie et al., 2005, Bland et al., 2009] and impact cratering models [Schenk, 2002, Senft and Stewart, 2011], we subdivide the ice-I shell into an effectively elastic upper layer (stagnant-lid) and a ductile convective lower layer by introducing a viscosity contrast within the shell at 20 km depth [Schenk, 2002].

This paper is organized as follows. In Section 5.3.3 we provide a short description of our approach to model the internal structure of Ganymede. Thereafter, in Section 5.3.4 we shortly describe the applied normal mode methodology to determine the tidal response of the derived interior models of Ganymede. Thereafter, in Section 5.3.5 we present our analysis of the sensitivity of the tidal response on the parameters that characterize the interior, thereby focusing on the rheological and structural parameters of the ocean and ice-I shell. Finally, in Section 5.3.6 we discuss the implications that our

results may have on the interpretation of future measurements by JUICE's instruments.

5.3.3. INTERIOR MODELING

An essential parameter in the modeling of the radial distribution of mass in Ganymede's interior is the so-called normalized mean moment of inertia $\frac{I}{MR^2}$, which can be derived from the degree-2 gravitational coefficients J_2 and C_{22} observed by Galileo. Under the a priori assumption that Ganymede's interior is in hydrostatic equilibrium (i.e. $J_2 = \frac{10}{3}C_{22}$), the observed quadrupole coefficients J_2 and C_{22} yield a low value for the normalized mean moment of inertia ($\frac{I}{MR^2} = 0.312$), which strongly suggests that Ganymede's interior is strongly differentiated with a large concentration of mass towards its center [Anderson et al., 1996]. The assumed hydrostatic equilibrium constraint does not need to hold for Ganymede's interior, but Galileo's observations of the quadrupole coefficients were highly correlated [Anderson et al., 1996]. Using the orbit phases at Ganymede, it is expected that JUICE observations will improve the degree-2 gravitational field without relying on the assumption of hydrostatic equilibrium [Grasset et al., 2013].

In addition, the detection of an intrinsic magnetic field suggests the presence of a metallic core [Kivelson et al., 1996], whereas Ganymede's low average density ($\bar{\rho} = 1936 \text{ kg m}^{-3}$) requires a large water-ice component [Anderson et al., 1996]. Therefore, combination of the constraints given by the gravity data, magnetic data and average density favors three-layer models of Ganymede's interior, consisting of a metallic core, a silicate mantle and a thick water-ice layer on top [Anderson et al., 1996].

Moreover, mainly due to the moon's low average density, Ganymede's water-ice layer is expected to be sufficiently thick ($\sim 800 - 900 \text{ km}$) to experience pressure-driven phase transitions into high-pressure ices, such as ice-V and ice-VI [e.g. Sohl et al., 2002]. From this point of view, a global water ocean would be sandwiched between an ice-I shell on top and a high-pressure ice (HP-ice) layer on the bottom. Unfortunately, the gravitational data does not provide any information about differentiation within the water-ice layer due the small density differences between liquid water and the relevant ice phases. However, the presence of a subsurface water ocean in Ganymede's interior is supported by studies on the morphology of impact craters on Ganymede's surface [Schenk, 2002] and the recent observation by Hubble Space Telescope (HST) of the weak oscillation amplitude of auroral ovals due to the presence of an electrically conducting layer [Saur et al., 2015].

Since our research is focused on the tidal response of Ganymede in the presence of a subsurface ocean, our modeling of Ganymede's interior needs to take into account the previously discussed phase transitions within the water layer. As such, the basic structural models of Ganymede's interior in this paper will consist of five homogeneous layers: a metallic core, a rocky mantle, a HP-ice layer, a subsurface water ocean and an ice-I shell. The radius r and density ρ of each of these layers need to be such that the entire model satisfies the constraints on average density and normalized mean moment of inertia, as well as additional compositional constraints on the densities of the two innermost layers: a) for the metallic core, we assume that the density ranges between $\rho_c = 5330 \text{ kg m}^{-3}$ (density of Fe-FeS) and $\rho_c = 7800 \text{ kg m}^{-3}$ (density of Fe) [e.g. Sohl et al., 2002]; and b) for the silicate mantle, we assume values between $\rho_m = 3222 \text{ kg m}^{-3}$

and $\rho_m = 3800 \text{ kg m}^{-3}$, where the first value is consistent with the presence of modest amounts of hydrated materials [Bland et al., 2009, Vance et al., 2014] while the latter is consistent with low concentrations of iron in the rock as a result of the differentiation of the metallic core [e.g. Anderson et al., 1996, Vance et al., 2014]. Through the use of these constraints plausible values for the radii of Ganymede's internal layers can be determined following the constant density approach for interior modeling outlined in Sohl et al. [2002], in which the densities of the three water-ice layers are also assumed to be known. Reference values for these densities are $\rho_{hp} = 1346 \text{ kg m}^{-3}$, $\rho_w = 1100 \text{ kg m}^{-3}$ and $\rho_I = 937 \text{ kg m}^{-3}$, for respectively the HP-ice layer, the subsurface ocean and the ice-I shell [e.g. Sohl et al., 2002, Vance et al., 2014]. Furthermore, in order to analyze the effect of the density of the upper layers on the tidal response, we allow the density of Ganymede's ocean to vary between $\rho_w = 1000 \text{ kg m}^{-3}$ and $\rho_w = 1200 \text{ kg m}^{-3}$, which are plausible values depending on the salinity of the ocean [Vance et al., 2014]. Similarly, for the density of the ice-I shell the range $\rho_w = 900 - 1000 \text{ kg m}^{-3}$ is assumed to take into account the possible effect of porosity and impurities.

In addition, each internal layer is characterized by rheological parameters that give a representation of the layer's response to internal and/or external excitations. In this paper, we have chosen to adopt the linear Maxwell viscoelastic model to describe the rheological behavior of internal solid layers, mainly due to its simplicity and the large uncertainty in the knowledge of the rheological properties of materials at conditions relevant for icy satellites. According to the definition of the Maxwell model, the rheology of each internal solid layer is fully described by only two macroscopic parameters, namely the rigidity μ and the viscosity η . The ratio of these two parameters, the so-called Maxwell time $\tau_M = \frac{\eta}{\mu}$, gives an indication of the timescale at which the material under deformation shows a transition from elastic to viscous behavior. Hence, a Maxwell viscoelastic layer will behave as an elastic layer at timescales much smaller than the Maxwell time (i.e. for $t \ll \tau_M$), whereas it will behave as a fluid body at timescales much larger than the Maxwell time (i.e. for $t \gg \tau_M$). On the other hand, internal liquid layers, such as the core and the water ocean, are treated as inviscid fluids (i.e. rigidity and viscosity are by definition equal to zero).

Even under the assumption of a Maxwell rheology, the rheological parameters that characterize the internal layers of icy satellites are largely uncertain or even unknown. Therefore, here we consider all previously defined internal layers to be homogeneous in terms of their rheology. Nevertheless, an exception is made for the ice-I shell, which is subdivided into two layers of different viscosity, but equal rigidity [Wahr et al., 2006], in order to simulate the effect of an effectively elastic icy crust on top of a more ductile lower part of the shell. The introduction of a viscosity contrast within the ice-I shell is consistent with thermal models dealing with solid-state convection in ice-I shells [e.g. Kirk and Stevenson, 1987, Showman et al., 1997, Barr and Pappalardo, 2005, Tobie et al., 2005, McKinnon, 2006, Bland et al., 2009, Hammond and Barr, 2014] and with numerical models dealing with the morphology of impact craters on the surface of icy satellites [e.g. Schenk, 2002, Senft and Stewart, 2011]. However, it needs to be pointed out that thermal models have been mostly applied to the study of the formation of grooved terrain in Ganymede's surface, which is thought to be the result of a period of global surface expansion due to either satellite differentiation or partial melting of the ice-I shell when

Ganymede entered a possible Laplace-like resonance with Europa and Io [e.g. [Showman et al., 1997](#), [Bland et al., 2009](#), [Hammond and Barr, 2014](#)]. As a result, the chosen subdivision of the ice shell into a nearly elastic top layer and a ductile lower layer at the bottom may be more representative for the conditions in Ganymede's past and thus may not be a good description of the current thermal state of Ganymede's ice-I shell [e.g. [Barr and Pappalardo, 2005](#)].

Since the properties of the upper layers of an icy satellite are expected to dominate the tidal response, most variations in the rheological parameters are introduced in the definition of the rigidity and viscosity of the layers that simulate the ice-I shell. The value of the rigidity of ice-I (μ_I) at planetary conditions is uncertain by about one order of magnitude, with values as low as ~ 0.3 GPa [[Vaughan, 1995](#), [Schmeltz et al., 2002](#), [Wahr et al., 2006](#)] and as high as ~ 10 GPa [[Moore and Schubert, 2000](#), [Harada and Kurita, 2006](#)] being suggested as appropriate for research on icy satellites. Nevertheless, in the vast majority of research cases, the reference value for the rigidity of ice-I is most likely between 2 GPa and 4 GPa, which is a range that includes the value $\mu_I \approx 2$ GPa obtained from laboratory experiments involving periodic loading (2.5 – 3 hours) of unfractured saline ice at -30°C [[Cole and Durell, 1995](#)] and the value $\mu_I \approx 3.5$ GPa obtained from laboratory experiments on several samples of natural and artificial ice [[Gammon et al., 1983](#), [Helgerud et al., 2009](#)]. The latter will be used as the reference value for the rigidity of the ice-I shell in our modeling, as it has been widely used as reference value in previous research on tidal problems involving icy satellites [e.g. [Tobie et al., 2005](#), [Rappaport et al., 2008](#), [Wahr et al., 2009](#), [Jara-Oru e and Vermeersen, 2011](#), [Beuthe, 2013](#), [Shoji et al., 2013](#), [Van Hoolst et al., 2013](#)].

The viscosities of the layers that constitute the ice-I shell are the less-known rheological parameters in the modeling of icy satellites. The upper part of the shell, which is assumed to be 20 km thick in our modeling [e.g. [Schenk, 2002](#)], is considered to be cold enough to behave in an effectively elastic way [[Moore and Schubert, 2003](#)], and hence its viscosity is assumed to be 1.0×10^{21} Pa s (larger values are plausible but will not influence the results). The lower part of the shell is considered to be more ductile as a result of either the increase in temperature with depth (if the shell is in conductive equilibrium) or the presence of a nearly isothermal convective layer (stagnant-lid/sluggish-lid convection case). To take both possible scenarios into account, we allow the viscosity of the lower part of the shell (η_{ast}) to range between 1.0×10^{14} Pa s (around the value for the

Table 5.2: Reference 6-layer model of Ganymede's interior. See text for explanation on the values.

Layer	Outer Radius [km]	Density [kg m^{-3}]	Rigidity [GPa]	Viscosity [Pa s]
Metallic Core	720	5777.9	0	0
Silicate Mantle	1820	3291.5	65.0	1.0×10^{20}
HP-ice Layer	2284	1346.0	6.6	1.0×10^{17}
Water Ocean	2534	1100.0	0	0
Ductile Ice-I Layer	2614	937.0	3.5	1.0×10^{17}
Ice-I Crust	2634	937.0	3.5	1.0×10^{21}

Table 5.3: Range of values for the size and density that characterize the internal structure of Ganymede's proposed 6-layered models. See text for explanation on the values. (a) The density of the core and the mantle are such that the entire interior models satisfies the imposed conditions on average density and mean moment of inertia. (b) The value $r_m = 1840$ km is only used for cases in which the density of the ocean is assumed to be lower than the reference value. (c) Values within the given range are equally spaced.

Layer	Outer Radius [km]	Density [kg m ⁻³]
Metallic Core	{450, 720}	5334.6 – 7479.5 ^(a)
Silicate Mantle	{1740, 1820, 1840} ^(b)	3223.5 – 3656.6 ^(a)
HP-ice Layer	2184 – 2394	1346
Water Ocean	{2484, 2494, ..., 2594} ^(c)	{1000, 1050, ..., 1200} ^(c)
Ductile Ice-I Layer	2614	{900, 937, 1000}
Ice-I Crust	2634	{900, 937, 1000}

viscosity at melting temperature) and 1.0×10^{17} Pa s (effectively elastic response). Since the onset of convection is uncertain [e.g. [Barr and Pappalardo, 2005](#)], the latter will be used as reference value for the viscosity of the lower part of the shell.

The rheological parameters of the remaining internal viscoelastic layers are also poorly constrained, as the exact composition of these layers remains unknown. Commonly used values for the rigidity of a HP-ice layer (μ_{hp}) usually range between 4.6 GPa (ice-III) and 7.5 GPa (ice-VI) [[Sohl et al., 2002](#)], while the corresponding values for the rigidity of the silicate mantle (μ_m) may range between 40 GPa and 100 GPa [e.g. [Moore and Schubert, 2000](#), [Sohl et al., 2002](#), [Rappaport et al., 2008](#), [Sohl et al., 2014](#)]. As reference values, we adopt $\mu_{hp} = 6.6$ GPa for the HP-ice layer [[Sohl et al., 2014](#)] and $\mu_m = 65$ GPa for the silicate mantle [e.g. [Turcotte and Schubert, 2014](#)]. Furthermore, to preclude viscoelastic relaxation to take place in the deeper layers of Ganymede, we assume $\eta_m = 1.0 \times 10^{20}$ Pa s for the viscosity of the silicate mantle and $\eta_m = 1.0 \times 10^{17}$ Pa s for the viscosity of the HP-ice layer.

As an overview of the discussion in this Section, we have listed the reference values for each interior parameter in Table 5.2 (reference model) as well as the explored range of values for the interior parameters in Tables 5.3 and 5.4.

Table 5.4: Range of values for the rheological parameters that characterize the internal structure of Ganymede's proposed 6-layered models. See text for explanation on the values.

Layer	Rigidity [GPa]	Viscosity [Pa s]
Metallic Core	0	0
Silicate Mantle	65.0	1.0×10^{20}
HP-ice Layer	6.6	1.0×10^{17}
Water Ocean	0	0
Ductile Ice-I Layer	{1, 3.5, 10}	$1.0 \times 10^{14} - 1.0 \times 10^{17}$
Ice-I Crust	{1, 3.5, 10}	1.0×10^{21}

5.3.4. TIDAL RESPONSE

The tidal potential exerted by Jupiter on Ganymede experiences periodic variations on the timescale of the orbital motion - or diurnal timescale (period $T \approx 7.155$ days, mean motion $n = 1.016 \times 10^{-5}$ rad/s) - as a result of Ganymede's slightly elliptical orbit (eccentricity $e = 0.0013$) and its likely non-zero but small obliquity [Bills, 2005, Baland et al., 2012]. Ganymede's eccentric orbit around Jupiter leads on one hand to stretching and squeezing of the tidal bulge, as a result of periodic changes in the distance Ganymede-Jupiter. On the other hand, Ganymede's instantaneous orbital motion is usually not equal to its spin rate as a result of its eccentric orbit, thereby leading to periodic longitudinal librations of the tidal bulge. Similarly, a non-zero obliquity leads to changes in the latitudinal orientation of the tidal bulge. To first order in eccentricity and obliquity, the diurnal tidal potential exerted by Jupiter at Ganymede's surface, can be defined as [Kaula, 1964, Wahr et al., 2009, Jara-Oru  and Vermeersen, 2011]

$$\Phi_T = (nR)^2 \left\{ -\frac{3e}{2} P_{2,0}^\theta \cos(nt) + \frac{e}{4} P_{2,2}^\theta [3 \cos(2\phi) \cos(nt) + 4 \sin(2\phi) \sin(nt)] + P_{2,1}^\theta \sin(\varepsilon) \cos(\phi) \sin(\varpi + nt) \right\}, \quad (5.1)$$

where R is the mean radius of Ganymede, ε is the obliquity of Ganymede's spin axis, and ϖ is the argument of pericenter measured with respect to the ascending node where Ganymede's orbital plane crosses its equatorial plane. Values for these parameters are listed in Table 5.5. Moreover, the angles θ and ϕ are, respectively, the colatitude and the longitude of a point on Ganymede's surface. Finally, the associated Legendre polynomials $P_{2,0}^\theta$, $P_{2,1}^\theta$ and $P_{2,2}^\theta$ are defined by

$$P_{2,0}^\theta = \frac{3 \cos^2(\theta) - 1}{2}, \quad (5.2)$$

$$P_{2,1}^\theta = 3 \sin(\theta) \cos(\theta), \quad (5.3)$$

Table 5.5: Radius, orbital parameters and rotational parameters of Ganymede. (a) The current value for Ganymede's mean radius is $R = 2631.2$ km [Archinal et al., 2011]. Although this value may lead to Love numbers slightly different than for $R = 2634$ km, the differences are small enough (less than 0.5%) that they will not affect the results and conclusions in this paper. (b) Assumed value for the argument of pericenter for modeling purposes (not measured).

Parameter	Symbol	Value	Unit	Reference
Mean radius	R	2634	km	[Anderson et al., 1996] ^(a)
Mean motion	n	1.016×10^{-5}	rad/s	[Bills, 2005]
Orbital period	T	7.155	days	[Bills, 2005]
Eccentricity	e	0.0013	-	[Baland and Van Hoolst, 2010]
Obliquity	ε	{0, 0.032, 0.155}	deg.	[Bills, 2005, Baland et al., 2012]
Arg. of pericenter	ϖ	0	deg.	^(b)

$$P_{2,2}^{\theta} = 3 \sin^2(\theta). \quad (5.4)$$

Since Ganymede's interior is not rigid, the materials composing the interior will continuously deform in response to the acting diurnal tide Φ_T . In geophysics, the response of a planetary body to forces like tides is usually expressed in terms of dimensionless numbers, the so-called tidal Love numbers h_2 , l_2 and k_2 [Love, 1911], where h_2 and l_2 refer to the tidally-driven radial and lateral deformation experienced by the interior and k_2 refers to the gravitational potential due to the tidally-induced mass redistribution. Here, we make use of the analytical method outlined in Jara-Oru  and Vermeersen [2011] to determine the tidal Love numbers at the surface of several plausible geophysical models of Ganymede's interior. This method is largely based on the viscoelastic normal mode approach of Sabadini and Vermeersen [2004], with some modifications in order to handle the presence of a subsurface ocean layer at shallow depth from the surface.

Since the JUICE mission is expected to measure Ganymede's surface displacements and variations of the gravitational potential due to diurnal tides [Grasset et al., 2013], our modeling in this paper will concentrate on the determination of the tidal Love numbers h_2 and k_2 . Within the framework of the normal mode approach, these two Love numbers can be conveniently written as [Sabadini and Vermeersen, 2004, Jara-Oru  and Vermeersen, 2011]:

$$\tilde{h}_2(s) = h_2^e + \sum_{j=1}^M \frac{h_2^j \cdot (-s_j)}{s - s_j}, \quad (5.5)$$

$$\tilde{k}_2(s) = k_2^e + \sum_{j=1}^M \frac{k_2^j \cdot (-s_j)}{s - s_j}, \quad (5.6)$$

where h_2^e and k_2^e are defined as the elastic Love numbers, the s_j 's are the inverse relaxation times of the M relaxation modes of the interior, the h_2^j 's and k_2^j 's are the corresponding modal strengths, and s is the Laplace variable. The tilde on top of h_2 and k_2 indicates that the Love numbers are defined in the Laplace domain.

In the case of a periodic forcing, such as the diurnal tides, it is common to express the tidal Love numbers \tilde{h}_2 and \tilde{k}_2 as functions of frequency (with $s = i\omega$ in Equations 5.5 and 5.6). The resulting frequency-dependent Love numbers are complex, in which the real part denotes the part of the response in-phase with the forcing whereas the imaginary part refers to the part of the response out-of-phase with the forcing. This set of complex Love numbers are characterized by a magnitude $|\tilde{h}_2(\omega)| = (\text{Re}(\tilde{h}_2(\omega))^2 + \text{Im}(\tilde{h}_2(\omega))^2)^{0.5}$ and a phase-lag $\epsilon_2(\omega) = \arctan\left(-\frac{\text{Im}(\tilde{h}_2(\omega))}{\text{Re}(\tilde{h}_2(\omega))}\right)$.

Then, using the definition of the Love numbers [e.g. Love, 1911, Sabadini and Vermeersen, 2004], the actual radial deformation u_r and perturbation potential ϕ_1 experienced by Ganymede at its surface due to the acting diurnal tides can be expressed in the time domain as

$$u_r(t) = \frac{h_2(t)}{g_0} * \Phi_T(t), \quad (5.7)$$

$$-\phi_1(t) = k_2(t) * \Phi_T(t), \quad (5.8)$$

where g_0 is the acceleration of gravity at Ganymede's surface ($g_0 = 1.425 \text{ m s}^{-2}$) and the symbol $*$ denotes time convolution. Explicit expressions for the tidal deformation u_r and potential perturbation ϕ_1 are commonly derived after transformation of Equations 5.7 and 5.8 to the Laplace domain (or alternatively to the Fourier domain) and subsequent substitution of Equations 5.5, 5.6 and the Laplace transform of Equation 5.1. After some analytical manipulation, the radial deformation u_r at the surface may be written as

$$u_r(t) = u_r^e(t) + u_r^v(t), \quad (5.9)$$

where the elastic component of the radial deformation (u_r^e) is defined by

$$u_r^e(t) = \frac{1}{4}(nR)^2 \frac{h_2^e}{g_0} \left(-6eP_{2,0}^\theta \cos(nt) + eP_{2,2}^\theta \left[4 \sin(2\phi) \sin(nt) + 3 \cos(2\phi) \cos(nt) \right] + 4 \sin(\varepsilon) P_{2,1}^\theta \left[\cos(\phi) \sin(\varpi + nt) \right] \right) \quad (5.10)$$

and the deformation due to viscoelastic relaxation (u_r^v) is given by

$$u_r^v(t) = \frac{1}{4}(nR)^2 \sum_{j=1}^M \left\{ \frac{h_2^j}{g_0} \frac{1}{\sqrt{1+\Gamma_j^2}} \left(-6eP_{2,0}^\theta \cos(nt - \arctan(\Gamma_j)) + eP_{2,2}^\theta \left[4 \sin(2\phi) \sin(nt - \arctan(\Gamma_j)) + 3 \cos(2\phi) \cos(nt - \arctan(\Gamma_j)) \right] + 4 \sin(\varepsilon) P_{2,1}^\theta \left[\cos(\phi) \sin(\varpi + nt - \arctan(\Gamma_j)) \right] \right) \right\}. \quad (5.11)$$

An important parameter in the definition of the contribution of an individual relaxation mode j to the experienced tidal deformation is the ratio Γ_j , which is defined as the ratio between the mean angular velocity of Ganymede's orbit (n) and the inverse relaxation time ($-s_j$) of the j -th relaxation mode, i.e.

$$\Gamma_j = \frac{n}{-s_j} = \frac{2\pi\tau_j}{T}, \quad (5.12)$$

where τ_j is the relaxation time of the normal mode j . Similar expressions can be derived for the potential perturbation.

As can be seen from Equation 5.11, the dimensionless ratio Γ_j has two important effects on the contribution of a relaxation mode j to the radial deformation at the surface: 1) it attenuates the magnitude of the modal strength h_2^j , and 2) it causes a phase-lag in the corresponding response. As discussed in [Jara-Oru e and Vermeersen \[2011\]](#) for the case of the viscoelastic response of the Jovian moon Europa, most relaxation modes have relaxation times that are several orders of magnitude larger than the orbital period; and hence their contribution to the radial deformation may be considered as being negligibly small. However, some of the so-called transient modes (see [e.g. [Sabadini and Vermeersen, 2004](#)] for their definition) may have relaxation times that are sufficiently short to have a theoretical contribution to the experienced radial deformation at the surface.

Transient modes are generally weak, with the notable exception of the ones due to the viscosity contrast introduced within the ice-I shell. Therefore, the non-elastic part of Ganymede's tidal response is expected to be dominated by the rheological properties of the lower part of the ice-I shell, similar to the case of Europa [Jara-Oru e and Vermeersen, 2011].

5.3.5. RESULTS

Application of the normal mode approach to a diverse range of plausible interior models of Ganymede allows us to study how the tidal response at the surface depends on the geophysical parameters that characterize its internal structure. As a first step, several interior models of Ganymede are constructed using the range of values presented in Table 5.3, thereby taking into consideration that all generated models satisfy the constraints introduced in Section 5.3.3. As can be observed in Tables 5.3 and 5.4, most of the variations are introduced in the parameters that characterize the upper layers, as these layers are expected to have a dominant influence on the tidal response at the surface [e.g. Moore and Schubert, 2003].

As a next step, we determine the frequency-dependent complex tidal Love numbers \tilde{h}_2 and \tilde{k}_2 by applying the methodology described in Section 5.3.4 to the generated interior models of Ganymede. Since the normal mode model is inherently viscoelastic, the non-elastic part of the response includes the contribution of nine normal modes: the core mode C_0 ; the buoyancy modes M_0 and M_1 at the ocean-HP-ice boundary and HP-ice-mantle boundary, respectively; the L_0 buoyancy mode at the ocean-ice-I boundary; the surface mode S_0 ; the transient modes TM_1 and TM_2 at the boundary between the HP-ice mantle and the silicate mantle; and the transient modes TS_1 and TS_2 at the introduced viscosity contrast within the ice-I shell [e.g. Sabadini and Vermeersen, 2004]. Although many of these relaxation modes are strong enough to influence the properties of the tidal response at lower frequencies ($\omega \ll n$), only the fastest and strongest of the transient modes at the introduced viscosity contrast within the ice-I shell (here TS_1) may have a non-negligible contribution to the tidal response at the high frequency of the acting diurnal tides. To illustrate this statement, we first express the contribution of the TS_1 -mode to e.g. the tidal Love number \tilde{h}_2 at the frequency of the acting forcing ($\omega = n$) in terms of the ratio Γ_j through the use of Equations 5.5 and 5.12, i.e.

$$\frac{h_2^j \cdot (-s_j)}{i n - s_j} = \frac{h_2^j}{1 + \Gamma_j^2} - i \frac{h_2^j \Gamma_j}{1 + \Gamma_j^2}, \quad (5.13)$$

for $j = TS_1$.

If the viscosity of the ductile ice layer is too small, such that the inverse relaxation time of the strong transient mode TS_1 is much larger than the orbital frequency (i.e. $-s_j \gg n$ or $\Gamma_j \ll 1$), viscous relaxation in the lower part of the ice-I shell takes place rapidly and hence the layer will show a fluid-like behavior at the forcing frequency. This behavior can be deduced from Equation 5.13, as the imaginary part goes to zero for $\Gamma_j \ll 1$ whereas the real part approaches the fluid behavior $h_2^e + h_2^j$. On the other hand, if the viscosity in the lower part of the ice-I shell is too large (i.e. for $-s_j \ll n$ or $\Gamma_j \gg 1$),

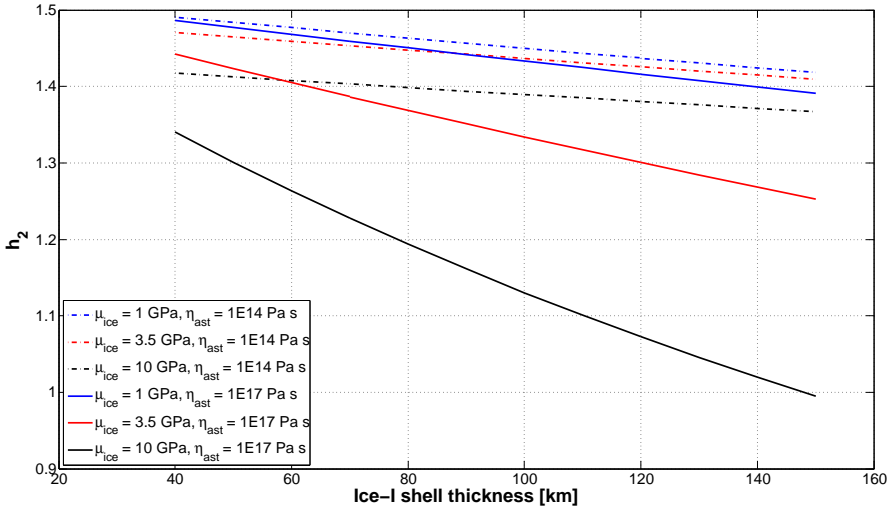


Figure 5.14: Radial deformation tidal Love number h_2 as a function of the thickness of the ice-I shell for models with ice-I rigidities $\mu_I = 1$ GPa, $\mu_I = 3.5$ GPa (reference models) and $\mu_I = 10$ GPa. The curves are shown for two different values for the viscosity of the ductile part of ice-I layer: (1) for a low viscosity at which viscoelastic relaxation affects the diurnal response to the acting tides, and (2) for a high viscosity at which the diurnal response is effectively elastic.

viscous relaxation does not take place in the lower part of the ice-I shell and hence the response of the layer will be effectively elastic. In this case, both the real and imaginary parts of the contribution of the transient mode TS_1 approach zero and therefore the tidal response is effectively dominated by the elastic response. A different behavior takes place when the viscosity of the lower part of the ice-I shell is such (e.g. $\eta_{ast} = 5.0 \times 10^{14}$ Pa s) that a strong transient mode with inverse relaxation time $-s_j \approx n$ (i.e. $\Gamma_j \approx 1$) is present in the tidal response. In this scenario viscoelastic relaxation within the lower part of the ice-I shell would lead to an increase in the magnitude of the deformation compared to the effectively elastic case (non-negligible real part in Equation 5.13) and would introduce a phase-lag of some degrees in the tidal response (non-negligible imaginary part in Equation 5.13).

A more concrete analysis of the dependence of the tidal response at the surface on the parameters that characterize Ganymede's ice-I shell can be obtained from the curves shown in Figures 5.14 and 5.15, where the magnitude of the complex Love numbers h_2 and k_2 at frequency $\omega = n$ is depicted as a function of the ice-I shell thickness for a range of plausible values for the rigidity and viscosity of the shell. We clearly observe in Figures 5.14 and 5.15 that the magnitude of the Love numbers decreases nearly linearly with increasing thickness of the ice-I shell, with the rate of decrease being strongest for effectively elastic shells with a large value for the rigidity ($\sim 35\%$ for h_2 and $\sim 37\%$ for k_2 in the thickness range 40-150 km). In addition, we observe that larger values for the rigidity of ice-I (μ_I) lead in all depicted cases to smaller values for the Love numbers, with the effect being largest for effectively elastic shells as well.

Furthermore, as shown by the dash-dotted curves in Figures 5.14 and 5.15, lowering

the viscosity of the ductile part of the shell from $\eta_{ast} = 1.0 \times 10^{17}$ Pa s to $\eta_{ast} = 1.0 \times 10^{14}$ Pa s would reduce the sensitivity that the magnitude of the Love numbers has to variations in the thickness and rigidity of the ice-I shell. As expected, the changes in the magnitude of the Love numbers as a result of the lower viscosity are largest for thick and very rigid shells, with changes up to $\sim 37\%$ for both h_2 and k_2 within the given viscosity range.

Although the densities of Ganymede's upper layers are not as poorly constrained as the thickness and rheological parameters of the ice-I shell, uncertainty in their values may also lead to non-negligible effects on the magnitude of the Love numbers h_2 and k_2 . In particular, the effect of the density of the ocean may be large and nearly comparable in magnitude to the effect of the thickness and/or rigidity of the ice-I shell, especially for the Love number k_2 . As can be deduced from the curves shown in Figure 5.16, the magnitude of both Love numbers decreases with decreasing density of the ocean by as much as 6% for h_2 and 23% for k_2 within the explored range of ocean densities (1000-1200 kg m³). The sensitivity of the amplitude of the Love numbers on the density of the ice-I shell is smaller. As shown in Figure 5.17, the amplitude of both Love numbers decreases with decreasing ice-I density by at most $\sim 3\%$ for h_2 and $\sim 4.5\%$ for k_2 within the explored range of values for the density of the ice-I shell (900-1000 kg m³).

Other parameters that characterize the internal structure of Ganymede have a much smaller effect on the magnitude of the tidal Love numbers at the surface. For example, the sensitivity of the Love numbers on the size of the HP-ice layer is so small that it can not be noticed from Figures 5.14 to 5.17 that the depicted curves are obtained by combining the tidal response of models with different values for the size of the HP-ice layer.

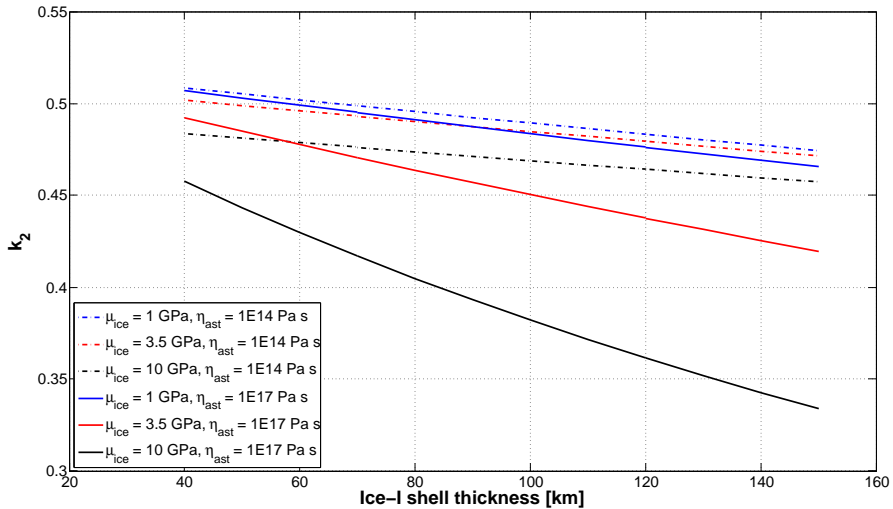


Figure 5.15: Gravitational perturbation tidal Love number k_2 as a function of the thickness of the ice-I shell for models with ice-I rigidities $\mu_I = 1$ GPa, $\mu_I = 3.5$ GPa (reference models) and $\mu_I = 10$ GPa. The curves are shown for two different values for the viscosity of the ductile part of ice-I layer: (1) for a low viscosity at which viscoelastic relaxation affects the diurnal response to the acting tides, and (2) for a high viscosity at which the diurnal response is effectively elastic.

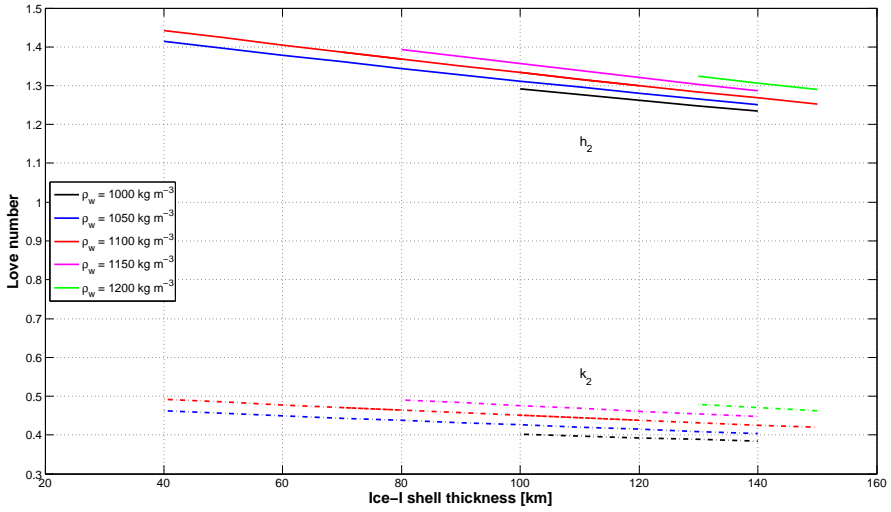


Figure 5.16: Tidal Love numbers h_2 and k_2 as a function of the thickness of the ice-I shell for models with ocean density $\rho_w = 1000 \text{ kg m}^{-3}$, $\rho_w = 1050 \text{ kg m}^{-3}$, $\rho_w = 1100 \text{ kg m}^{-3}$ (reference models), $\rho_w = 1150 \text{ kg m}^{-3}$ and $\rho_w = 1200 \text{ kg m}^{-3}$. The upper cluster of curves refers to the radial deformation tidal Love number h_2 , whereas the lower cluster (dash-dotted curves) refers to the Love number k_2 . In all cases the density of the ice-I shell is taken at $\rho_I = 937 \text{ kg m}^{-3}$ and the rigidity at $\mu_I = 3.5 \text{ GPa}$.

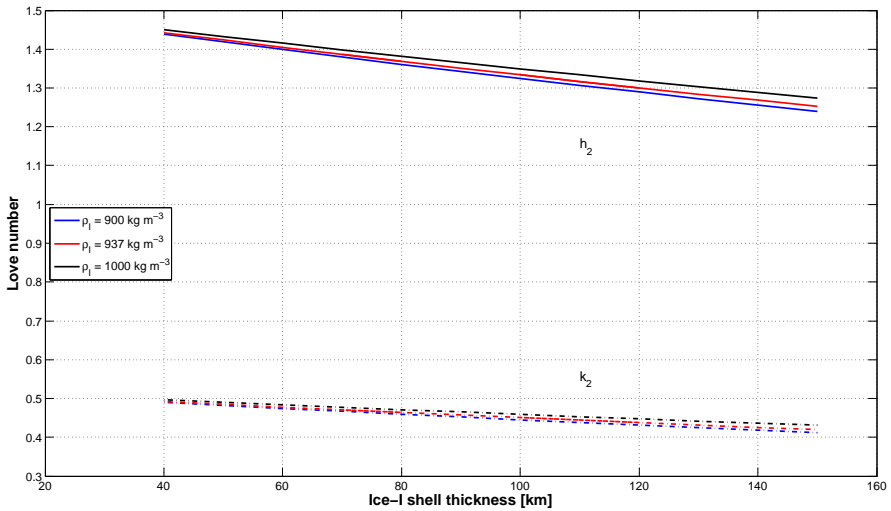


Figure 5.17: Tidal Love numbers h_2 and k_2 as a function of the thickness of the ice-I shell for models with ice-I density $\rho_I = 900 \text{ kg m}^{-3}$, $\rho_I = 937 \text{ kg m}^{-3}$ (reference models) and $\rho_I = 1000 \text{ kg m}^{-3}$. The upper cluster of curves refers to the radial deformation tidal Love number h_2 , whereas the lower cluster (dash-dotted curves) refers to the Love number k_2 . In all cases the density of the ocean is taken at $\rho_w = 1100 \text{ kg m}^{-3}$ and the rigidity of the ice-I shell at $\mu_I = 3.5 \text{ GPa}$.

5

In a similar way, the size and density of the deepest internal layers have a negligibly effect on the magnitude of the tidal Love numbers (e.g. less than 0.1% for h_2 and around 0.2% for k_2 if a smaller core is used for the modeling). The rheological parameters of the silicate mantle and HP-ice layer may have a larger effect on the tidal Love numbers if the layers would be soft, as the inverse relaxation times of their corresponding normal modes M_1 and M_0 will shift towards the orbital frequency, thereby increasing the amplitude and phase-lag of the Love numbers.

So far, we have shown our results in terms of the Love numbers which give a representation of the tidal response experienced by Ganymede. The actual tidal deformation is obtained from substitution of the calculated Love numbers into Equations 5.9 to 5.11. For our reference interior model of Ganymede (see Table 5.2), the maximum radial displacement at the surface due to the acting diurnal tides during one orbital revolution is displayed in Figure 5.18a for the case in which the obliquity is assumed to be equal to zero. The shown (single) amplitude of the largest surface displacements (~ 3 meters) is slightly lower than in previous research, mainly due to our choice for the geophysical parameters that characterize the reference model. However, our results are within the uncertainty range in those models and their values (~ 4 meters) could be replicated by choosing either a thinner shell, a less rigid shell or a less viscous ductile part of the shell.

In contrast to e.g. Europa or Titan, even small obliquities - such as the ones proposed in the study by Baland et al. [2012] - can have a noticeable effect on the tidal deformation patterns at the surface (see Figure 5.18b). The relatively large effect of the contribution of Ganymede's small obliquity to the deformation is mainly a consequence of the small eccentricity of its orbit relative to the assumed value for the obliquity (e.g. compare the relative difference between $e = 0.0013$ and $\sin(\varepsilon) = 0.00059$ for $\varepsilon = 0.032^\circ$ in the case of Ganymede with $e = 0.0094$ and $\sin(\varepsilon) = 0.00077$ for $\varepsilon = 0.044^\circ$ in the case of Europa, with both values for the obliquity being taken from Baland et al. [2012]). As a result, larger values for the unknown obliquity, such as the $\varepsilon = 0.155^\circ$ proposed by Bills [2005], will lead to a large contribution to the surface displacement due to the acting diurnal tides. Then, as shown in Figure 5.18c, the obliquity tide will start to dominate the deformation patterns at the surface and the amplitude of the deformation will increase with respect to the eccentricity-only case. Although not shown here, changing the value of the unknown argument of pericenter ϖ will also lead to different deformation patterns at the surface.

On the other hand, the contribution of forced longitudinal librations (not shown here) will remain small, because the libration amplitude is usually several orders of magnitude smaller than the amplitude of the optical libration ($2e$) that is part of the eccentricity tide [Van Hoolst et al., 2013].

5.3.6. DISCUSSION AND CONCLUSIONS

In this paper we have presented a normal mode based method to determine the time-dependent tidal Love numbers h_2 and k_2 at the surface of a viscoelastic Ganymede in the case that a subsurface ocean is assumed to be present in the interior. If the tidal response of Ganymede's interior at the diurnal frequency is considered to be effectively elastic, i.e. no relaxation in the ice-I shell, the amplitude of the radial displacement Love number h_2

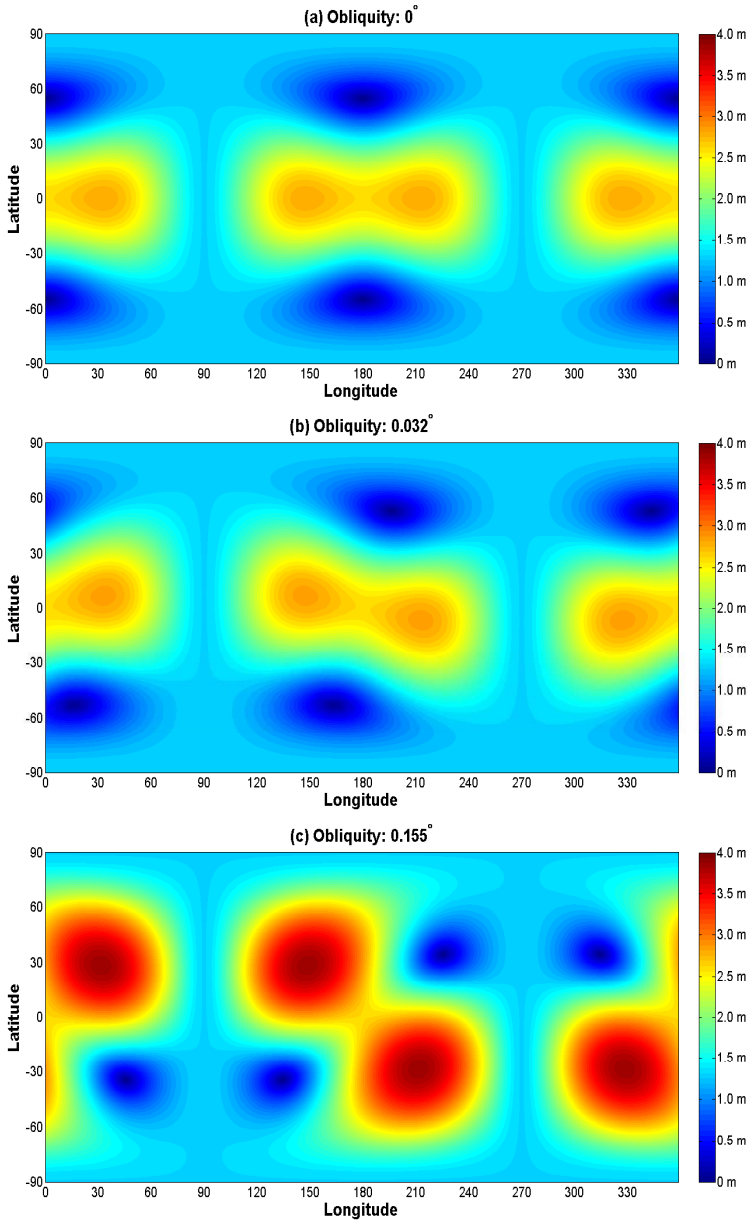


Figure 5.18: Maximum radial displacement (single amplitude) at the surface of Ganymede due to the acting diurnal tides for: a) obliquity $\epsilon = 0^\circ$, b) obliquity $\epsilon = 0.032^\circ$, and c) obliquity $\epsilon = 0.155^\circ$. In all cases, the interior of Ganymede is described by our reference model given in Table 5.2 and the argument of pericenter ϖ is assumed to be equal to 0° .

is mostly sensitive to the uncertainties in the thickness and rigidity of the ice-I shell, as can be observed from Figure 5.14. In addition, Figure 5.16 shows that the Love number h_2 is also sensitive to the poorly constrained density of the ocean, with its contribution being more important in the lower - and most plausible - range of values for the rigidity of the shell (i.e. $\mu_I = [1, 3.5]$ GPa), and for thinner shells. Other internal parameters have a small effect on its amplitude, with the density of the ice-I shell having the largest effect by introducing an uncertainty of a few percent.

The sensitivity of the gravitational perturbation Love number k_2 on the parameters that characterize the interior is a bit different. Like for h_2 , the Love number k_2 is mostly sensitive to the thickness and rigidity of the shell, but also to a larger extent to the density of the ocean (see Figures 5.15 and 5.16 for the preferred range of rigidities $\mu_I = [1, 3.5]$ GPa). The large dependence of k_2 on the density of the ocean is in agreement with the results obtained by e.g. Baland et al. [2014] for the case of Titan, which is aimed to provide a possible explanation for the large value of k_2 ($k_2 = 0.589 \pm 0.150$ and $k_2 = 0.637 \pm 0.224$) obtained from observations of the acceleration of the Cassini spacecraft during six fly-bys [Iess et al., 2012]. In the hypothetical case that such values would apply to the case of Ganymede as well, the results shown in Figures 5.15 and 5.16 would indicate that the Love number implies the presence of a dense ocean in combination with a preferably thin and not very rigid ice-I shell.

The introduction of a low-viscosity ductile ice-I layer adds one extra poorly constrained parameter to our analysis, i.e. the viscosity of the ductile part of the shell. As shown in Figures 5.14 and 5.15, the sensitivity of the Love numbers h_2 and k_2 on the large uncertainties in the viscosity of this layer is comparable to their sensitivity on the also poorly constrained rigidity. This effect is expected, as lowering the viscosity leads to a reduction in the effective rigidity of a layer (see e.g. Equation 50 of Jara-Oru e and Vermeersen [2011]). In addition, the introduction of a low-viscosity layer may lead to a phase-lag in the tidal response, which can be a few degrees if the ratio Γ_j (see Equation 5.12) of the dominating transient mode TS_1 of the viscoelastic response is in the range $\Gamma_j = [0.1, 10]$. Note, however, that the discussion presented here on the effect of viscoelasticity on the tidal response of Ganymede is based on our description of the rheology by use of the simple Maxwell model. Hence, the numerical results representing the sensitivity of the Love numbers on the rheology only apply to a Maxwell rheology and may be different if more complex - and perhaps more realistic - anelastic rheologies (Burgers, Andrade) are used in the modeling (see e.g. McCarthy and Castillo-Rogez [2013] for a discussion about rheological models for ice-I relevant to icy satellites).

Since the accuracy of measurements of the tidal Love number k_2 of Ganymede by the 3GM instrument is expected to be around 10^{-3} for both the real and imaginary parts [Parisi et al., 2014], the determination of k_2 would provide an unambiguous assessment about the presence or absence of a subsurface ocean in Ganymede's interior (recall that k_2 for oceanless models is expected to be smaller than 0.2 [Moore and Schubert, 2003] for ice-I viscosities larger than the reference viscosity at the melting temperature ($\sim 10^{13}$ Pa s), while our models always predict values larger than 0.3 in the presence of a subsurface ocean). The characterization of the geophysical properties of the shell and the ocean is, however, substantially more challenging as many configurations may be representative for the same Love number. For example, an assumed value of $k_2 = 0.48$ could

fit any shell thickness in the range $\sim [40, 130]$ km (derived from Figure 5.16) due to uncertainties in the ocean density, even if the rigidity of ice-I would be known to be equal to the reference value of 3.5 GPa. Measurements of the tidal Love number h_2 and the quantity $\Delta = 1 + k_2 - h_2$ [Wahr et al., 2006] may have the potential, if sufficiently accurate, to narrow down the possible range of values for the thickness of Ganymede's shell as h_2 is less sensitive to the uncertainties in the ocean density (see Figure 5.16). In addition, uncertainties due to the unknown rigidity of ice-I can be narrowed down by measurements of the amplitude of the longitudinal librations of the shell by GALA and/or imaging of the surface, as the shell librations are expected to be very sensitive to the rigidity of ice-I [Van Hoolst et al., 2013, Jara-Oru e and Vermeersen, 2014].

5.4. TIDAL AND NSR STRESSES: APPLICATION TO EUROPA

The content of this Section has been entirely taken from the article *Effects of low-viscous layers and a non-zero obliquity on surface stresses induced by diurnal tides and non-synchronous rotation: The case of Europa* [Jara-Oru e and Vermeersen, 2011] published in the journal the *Icarus*. Nevertheless, the discussion presented in this Section does not include Sections 2, 4 (including Appendix A) and 5 of Jara-Oru e and Vermeersen [2011], as a detailed description of the modeling presented in those Sections has been already discussed in Section 4.2, Chapter 3 and Section 4.4 of this thesis, respectively. As a result, the content in this Section has been kept as in the original publication, thereby implying that the notation and interior models used for the generation of results in this Section may differ from the ones that apply to other Sections of this thesis.

5.4.1. ABSTRACT

In this study we present a semi-analytical Maxwell-viscoelastic model of the variable tidal stress field acting on Europa's surface. In our analysis, we take into account surface stresses induced by the small eccentricity of Europa's orbit, the non-zero obliquity of Europa's spin axis - both acting on a diurnal 3.55-days timescale - and the reorientation of the ice shell as a result of non-synchronous rotation (NSR). We assume that Europa's putative ocean is covered by an ice shell, which we subdivide in a low-viscous and warm lower ice layer (asthenosphere, viscosity $10^{12} - 10^{17}$ Pa-s), and a high-viscous and cold upper ice layer (lithosphere, viscosity 10^{21} Pa-s).

Viscoelastic relaxation influences surface stresses in two ways: (1) through viscoelastic relaxation in the lithosphere, and (2) through the viscoelastic tidal response of Europa's interior. The amount of relaxation in the lithosphere is proportional to the ratio between the period of the forcing mechanism and the Maxwell relaxation time of the high-viscous lithosphere. As a result, this effect is only relevant to surface stresses caused by the slow NSR mechanism. On the other hand, the importance of the viscoelastic response on surface stresses is proportional to the ratio between the relaxation time (τ_j) of a given viscoelastic mode j and the period of the forcing function. On a diurnal timescale the fast relaxation of transient modes related to the low viscosity of the asthenosphere can alter the magnitude and phase shift of the diurnal stress field at Europa's surface. The

effects are largest, up to 20% in magnitude and 7° in phase for ice rigidities lower than 3.487 GPa, when the value of τ_j corresponding to the aforementioned transient modes approaches the inverse of the average angular rate of Europa's orbit. On timescales relevant for NSR ($> 10^4$ years) the magnitude and phase shift of NSR surface stresses can be affected by viscoelastic relaxation of the ice/shell boundary. This effect, however, becomes only important when the behavior of the lithosphere w.r.t. NSR approaches the fluid limit, i.e. for strong relaxation in the lithosphere. The combination of NSR and diurnal stresses for different amounts of viscoelastic relaxation of NSR stresses in the lithosphere leads to a large variety of global stress fields that can explain the formation of the large diversity of lineament morphologies observed on Europa's surface. Variation of the amount of relaxation in the lithosphere is likely due to changes in the spin rate of Europa and/or the rheological properties of the surface.

In addition, we show that a small obliquity (< 1 degree) can have a considerable effect on Europa's diurnal stress field. A non-zero obliquity breaks the symmetric distribution of stress patterns with respect to the equator, thereby affecting the magnitude and orientation of the principal stresses at the surface. As expected, increasing the value of Europa's obliquity leads to larger diurnal stresses at the surface, especially when Europa is located 90° away from the nodes formed by the intersection of its orbital and equatorial planes.

5.4.2. INTRODUCTION

The determination of Europa's second-degree gravitational coefficients J_2 and C_{22} from the Doppler shift of Galileo's radio signal during four close flybys has allowed us to have a better understanding about the internal structure of this peculiar icy moon. Under the assumption of hydrostatic equilibrium, the measured values for J_2 and C_{22} imply a differentiated interior consisting of at least three material layers: a Fe or Fe-FeS metallic core, a silicate mantle and a 80 – 170 km thick H_2O layer [Anderson et al., 1998, Sohl et al., 2002, Schubert et al., 2009]. Due to the similar densities of liquid water and solid ice, it is not possible to determine unambiguously from the gravity data whether Europa's H_2O shell is subdivided into a global liquid ocean and an overlying ice shell [Anderson et al., 1998, Sohl et al., 2002]. However, the existence of a global subsurface ocean below Europa's ice shell is essentially confirmed by the detection of an induced magnetic field by Galileo's magnetometer [Khurana et al., 1998, Kivelson et al., 2000, Zimmer et al., 2000, Hand and Chyba, 2007, Schilling et al., 2007], and by the existence of a complex network of intersecting cracks, bands and ridges on Europa's surface [e.g. Geissler et al., 1998, Greeley et al., 1998, Hoppa et al., 1999b,c, Pappalardo et al., 1999, Kattenhorn and Hurford, 2009]. Europa's liquid ocean would be in direct contact with the underlying silicates, as the pressure at the rock-water interface is too low for the formation of high-pressure ice phases [e.g. Sotin and Tobie, 2004]. The currently undetected, but plausible, existence of hydrothermal seafloor systems would then allow for a mechanism to supply energy and nutrients to Europa's ocean [Hand et al., 2009], increasing the habitability potential of this Jovian moon.

The formation of tectonic features (cracks, bands and ridges) has been attributed to various sources of stresses acting at different timescales. On a 3.55-days timescale, stresses at the icy surface are induced by the diurnal tides induced by the non-zero

eccentricity of Europa's orbit [Greenberg et al., 1998, Hoppa et al., 1999b,c, Greenberg et al., 2003, Harada and Kurita, 2006, Wahr et al., 2009], the non-zero obliquity of Europa's spin axis [Bills, 2005, Hurford et al., 2009, Rhoden et al., 2010, 2011], and physical librations of a decoupled shell [Van Hoolst et al., 2008, Rhoden et al., 2010]. Diurnal stresses have been mainly used to model the formation of cycloidal features [Hoppa et al., 1999b, Hurford et al., 2007, 2009, Rhoden et al., 2010] and strike-slip faults [Hoppa et al., 1999c, Preblich et al., 2007, Rhoden et al., 2011] on Europa's surface. On a much longer timescale, stresses may be induced by true polar wander (TPW) of the spin axis with respect to the icy surface [Ojakangas and Stevenson, 1989a, Leith and McKinnon, 1996, Matsuyama and Nimmo, 2008, Schenk et al., 2008] and/or by non-synchronous rotation (NSR) of a decoupled shell [Leith and McKinnon, 1996, Greenberg et al., 1998, Kattenhorn, 2002, Greenberg et al., 2003, Hurford et al., 2007, Harada and Kurita, 2007, Wahr et al., 2009]. These slow stressing mechanisms lead to large (\sim MPa) stresses, which have been used to model the formation of global-scale surface features [Leith and McKinnon, 1996, Geissler et al., 1998, Greenberg et al., 1998, Schenk et al., 2008]. In addition, large isotropic stresses (up to \sim 10 MPa) can result from thickening of the ice shell [Nimmo, 2004].

Diurnal stresses acting on Europa's surface have been usually computed by means of the thin shell approximation [Leith and McKinnon, 1996, Greenberg et al., 1998, Hoppa et al., 1999b, Hurford et al., 2007, 2009, Rhoden et al., 2010, 2011]. In this method, which is based on the work of Melosh [1980], Europa is assumed to be a thin elastic icy shell floating on a global liquid ocean [Hurford et al., 2007]. A more realistic model by Harada and Kurita [2006] analyzes the influence of a differentiated internal structure on the surface diurnal stress, focusing on the relation between the magnitude of surface stresses and the thickness of the material layers. Harada and Kurita [2006] show that surface diurnal stresses only depend on the thickness of the ice shell, hence supporting the assumption made by the thin shell approximation regarding the effect of the deep interior. The methods discussed above inherently assume that Europa's ice shell behaves elastically when forced by diurnal tides. However, as suggested by thermal models [e.g. Hussmann et al., 2002, Tobie et al., 2003] and impact crater models [Schenk, 2002], the lower portion of Europa's ice shell most probably behaves in a viscoelastic way under the influence of diurnal tides. Recent modeling by Wahr et al. [2009] includes the effect of viscoelasticity on surface diurnal stresses, thereby offering a potential method to study the effect of such a layer. However, the discussion in Wahr et al. [2009] only focus on cases for which Europa's interior behaves nearly elastically with respect to diurnal tides.

Europa's decoupled ice shell can experience slow non-synchronous rotation as a result of the acting tidal torque and lateral thickness variations in the shell [Greenberg and Weidenschilling, 1984, Ojakangas and Stevenson, 1989b, Bills et al., 2009]. If existing, NSR would be a slow periodic process with a period ($>$ 11,000 years) comparable to the characteristic Maxwell relaxation time ($\tau = \text{viscosity/rigidity}$) of the lithospheric shell (see Section 5.4). Hence, viscoelastic relaxation in the lithospheric shell is expected to have an important influence on the magnitude and orientation of NSR stresses at Europa's surface. Nevertheless, NSR stresses acting on Europa's surface have been often computed through application of the thin shell approximation to determine the elastic stress fields induced by the current tidal bulge and by the original tidal bulge [Leith

and McKinnon, 1996, Greenberg et al., 1998, Hurford et al., 2007]. The rotation angle between the two elastic stress fields, usually referred to as the accumulated degrees of NSR, defines the amount of NSR stress that accumulates in the shell [e.g. Greenberg et al., 1998]. More realistic models of surface NSR stresses by Harada and Kurita [2007] and Wahr et al. [2009] have focused on the determination of the stress directly from the Maxwell viscoelastic equations of motion and the acting NSR tidal potential. This kind of modeling has two main advantages with respect to the simpler thin shell approximation: 1) it includes viscoelastic relaxation effects into the computation of NSR stresses, and 2) it allows to relate the obtained stress field to the rheological properties of the interior. Both aforementioned studies obtain similar results for the relation between the simulated NSR stress and the rheological properties of the icy shell. However, both studies take a different approach to analyze the effect of viscoelastic relaxation on surface NSR stresses. The work by Harada and Kurita [2007] constrains the magnitude of diurnal and NSR stresses to be comparable, as previously suggested by Greenberg et al. [1998]. As a result, Harada and Kurita [2007] implicitly assume that NSR stresses are severely affected by viscoelastic relaxation in the lithospheric shell. This assumption inherently leads to a westward shift of 45 degrees in the surface distribution of the NSR stress field; the same as the one predicted in Greenberg et al. [1998]. On the other hand, the work by Wahr et al. [2009] takes into consideration that NSR stresses could be larger in magnitude than diurnal stresses. Therefore, the westward shift of the NSR stress field does not necessarily have to be equal to 45 degrees. This conclusion has a large effect on the determination of the time elapsed since the formation of a surface feature [Wahr et al., 2009], especially if the relaxation state of the NSR stress field changes with time.

Although the studies by Harada and Kurita [2007] and Wahr et al. [2009] already discussed the influence of viscoelasticity on surface stresses, their treatment is mostly focused on NSR stresses. Viscoelastic effects on diurnal stresses have often been neglected by considering quasi-elastic interior models. However, thermal models of Europa's ice shell have often assumed that the lower convective portion of the ice (asthenosphere) has a Newtonian viscosity in the range $1.0 \cdot 10^{13}$ Pa·s to $1.0 \cdot 10^{15}$ Pa·s [e.g. Hussmann et al., 2002, Sotin and Tobie, 2004, Nimmo and Manga, 2009]. In this range, not only tidal heat dissipation becomes largest but also the viscoelastic effect on diurnal stresses. As a result, we aim to extend the determination of diurnal stresses to interior models with a 2-layered ice shell, in which the Maxwell time of the lower icy sublayer is smaller or comparable to the orbital period, as suggested by thermal modeling. In addition we will take into account the effect of a non-zero obliquity on diurnal stresses from a viscoelastic perspective. Regarding NSR stress modeling, we will discuss the effect of the viscosity of the lower ice layer as a function of the amount of relaxation. In addition, we allow NSR stresses to be larger, comparable and smaller than diurnal stresses in order to infer the possible relation between the resulting NSR-diurnal stress field and the observed features.

The viscoelastic modeling of tidal stresses on Europa's surface is based on three aspects: determination of the tidal forcing (Section 4.2), assumptions on Europa's internal configuration (Section 5.4.3) and determination of Europa's viscoelastic response to tidal forces (Chapter 3). In Section 4.2, we have presented analytical expressions for the diurnal and NSR tidal potential, in which we include the effect of a non-zero obliquity. In

Section 5.4.3, we define our reference 5-layer model of Europa's interior, which only applies to the discussion in this Section of the thesis. In Chapter 3, we have discussed an alternative method to determine the tidal Love numbers of Maxwell viscoelastic planets with an internal ocean. This method, which is derived from normal mode techniques applied to postglacial rebound and true polar wander on Earth, subdivides the non-elastic response into several relaxation modes, each of them characterized by an specific relaxation time. In Section 4.4, we used the tools presented in Sections 4.2 and 5.4.3 and Chapter 3 to develop an analytical representation of diurnal and NSR stresses acting on Europa's surface. In Section 5.4.4, we analyze the relation between diurnal/NSR stresses and the physical properties of the interior. We show there that the magnitude of diurnal stresses mainly depends on the presence of an ocean and the rigidity of ice-I, while the spatial distribution of the stress patterns at the surface primarily depends on the obliquity of the Europa's spin axis and the viscosity and thickness of the asthenosphere. On the other hand, NSR stresses are most influenced by the rheological properties of the lithosphere and the unknown frequency of the non-synchronous motion of the ice shell. Finally, in Section 5.4.5 we combine the results obtained in Section 5.4.4 for diurnal and NSR stresses. We suggest that time variations in the relative importance of NSR stresses with respect to diurnal stresses could theoretically lead to the wide variety of lineament morphologies observed on Europa's icy surface.

5.4.3. THE INTERIOR OF EUROPA

The materials composing the interior of Europa and other planetary satellites do not respond in a perfectly elastic way to the acting tidal forces neither at diurnal timescales nor at timescales relevant to NSR. Part of the interior's response is delayed with respect to the onset time of the tidal forcing as a result of viscous relaxation effects. Therefore, the interior of a planetary satellite will most probably behave as a viscoelastic body rather than as a purely elastic or fluid body [e.g. [Tobie et al., 2005](#)]. In this paper, the Maxwell viscoelastic model has been adopted to describe the rheological behavior of Europa's interior. An important parameter in the definition of the Maxwell model is the ratio between the viscosity η and the rigidity μ of the material under deformation. This ratio, the so-called Maxwell relaxation time $\tau_M = \eta/\mu$, gives an indication of the time at which the material shows a transition from elastic behavior to viscous behavior. At short-term timescales, i.e. $t \ll \tau_M$, the Maxwell model describes the interior as an elastic body, whereas at long-term timescales, i.e. $t \gg \tau_M$, the interior is described as a fluid body [[Sabadini and Vermeersen, 2004](#)].

The internal structure of Europa has been assumed to consist of five homogeneous and incompressible spherical layers: a fluid metallic core of Fe and/or FeS, a large silicate mantle, a liquid ocean, a warm low-viscous ice-I layer and a cold high-viscous ice-I layer on top. The radius r and density ρ of each of these concentric spherical layers needs to be such that the complete model of Europa's interior satisfies the conditions on average density ($\rho_{av} = 2989 \text{ kg m}^{-3}$) and normalized mean moment of inertia ($\frac{I}{MR^2} = 0.346$) [[Anderson et al., 1998](#)]. The methodology used in this paper to model the layered structure of Europa's interior follows the approach outlined in [Sohl et al. \[2002\]](#) and [Harada and Kurita \[2006\]](#).

Table 5.6: Reference 5-layer model of Europa's interior.

Layer	Outer Radius [km]	Density [kg m ⁻³]	Rigidity [GPa]	Viscosity [Pa s]
Lithosphere	1562	937.0	3.487	$1.0 \cdot 10^{21}$
Asthenosphere	1557	937.0	3.487	$1.0 \cdot 10^{14}$
Ocean	1532	1000.0	0	0
Silicate Mantle	1432	3453.6	65.000	$1.0 \cdot 10^{19}$
Core	600	5565.8	0	0

Although the entire ice shell is assumed to have a constant density ρ and rigidity μ , we subdivide the ice shell in two layers with different viscosities η . The introduced viscosity contrast leads to the existence of two ice layers with different mechanical and thermal properties (viscosity is a function of temperature). The subdivision of the ice shell in two layers is consistent with thermal models dealing with stagnant lid convection in the ice shell [e.g. Hussmann et al., 2002, Tobie et al., 2003] and with the morphology of impact craters on Europa's surface [Schenk, 2002].

In this paper, we will make use of various models of Europa's interior to analyze the relation between tidal stresses at the surface and the parameters defining the interior. To reduce the number of plausible models, we do not change the size of the core (600 km), the thickness of the H₂O layer (130 km), the thickness of the lithosphere (5 km), the densities of ice and liquid water (937 kg m⁻³ and 1000 kg m⁻³, respectively), the rigidity of the silicate mantle (65 GPa), and the viscosities of the mantle and the lithosphere ($1.0 \cdot 10^{19}$ Pa s and $1.0 \cdot 10^{21}$ Pa s, respectively). We vary the total thickness of the ice shell from 5 km to 130 km (no ocean), the rigidity of ice-I from 1 GPa to 10 GPa, and the viscosity of the asthenosphere from $1.0 \cdot 10^{12}$ Pa s to $1.0 \cdot 10^{17}$ Pa s. However, we will limit the graphical representation of spatial and temporal variations of surface stresses to our standard model of Europa's interior, which is defined by the physical parameters listed

Table 5.7: Tidal response of the reference model of Europa's interior to diurnal tidal forces.

Mode	τ_j [s]	Γ_j [-]	\mathbf{h}_2^e or \mathbf{h}_{2j}^v [-]	\mathbf{l}_2^2 or \mathbf{l}_{2j}^v [-]
elastic	–	–	$1.15100 \cdot 10^0$	$3.07996 \cdot 10^{-1}$
C ₀	$7.02026 \cdot 10^{10}$	$1.43745 \cdot 10^6$	$5.17509 \cdot 10^{-2}$	$1.40296 \cdot 10^{-2}$
M ₃	$9.15741 \cdot 10^9$	$1.87504 \cdot 10^5$	$7.16925 \cdot 10^{-1}$	$1.94722 \cdot 10^{-1}$
M ₂	$9.75577 \cdot 10^{10}$	$1.99756 \cdot 10^6$	$1.38050 \cdot 10^{-3}$	$2.35200 \cdot 10^{-4}$
M ₀	$2.91957 \cdot 10^{11}$	$5.97802 \cdot 10^6$	$3.69559 \cdot 10^{-2}$	$1.00498 \cdot 10^{-2}$
T ₁	$1.73366 \cdot 10^5$	$3.54978 \cdot 10^0$	$7.19132 \cdot 10^{-5}$	$6.00107 \cdot 10^{-3}$
T ₂	$3.07948 \cdot 10^4$	$6.30543 \cdot 10^{-1}$	$8.49611 \cdot 10^{-2}$	$2.26471 \cdot 10^{-2}$

Table 5.8: Tidal response of the reference model of Europa's interior to NSR forces. (a) The core-mode C_0 and the mantle-mode M_3 vanish from the NSR response, since we assumed that the synchronously locked rocky interior behaves as a fluid with respect to NSR forces. (b) Corresponds to the minimum period of NSR, i.e. $T_{ns} = 12,000$ years ($\Delta \approx 0.1$).

Mode ^a	τ_j [yr.]	γ_j^b [-]	\mathbf{h}_2^e or \mathbf{h}_{2j}^v [-]	\mathbf{l}_2^e or \mathbf{l}_{2j}^v [-]
elastic	–	–	$1.85155 \cdot 10^0$	$4.95366 \cdot 10^{-1}$
M_2	$9.24992 \cdot 10^3$	$9.68650 \cdot 10^0$	$3.60537 \cdot 10^{-2}$	$9.80448 \cdot 10^{-3}$
M_0	$3.09117 \cdot 10^3$	$3.23707 \cdot 10^0$	$1.80231 \cdot 10^{-3}$	$3.07295 \cdot 10^{-4}$
T_1	$5.49324 \cdot 10^{-3}$	$5.75251 \cdot 10^{-6}$	$1.16432 \cdot 10^{-4}$	$9.28203 \cdot 10^{-3}$
T_2	$9.84029 \cdot 10^{-4}$	$1.03047 \cdot 10^{-6}$	$1.53522 \cdot 10^{-1}$	$4.09211 \cdot 10^{-2}$

in Table 5.6.

Since the reference interior model of Europa described in Table 5.6 is defined in a slightly different way relative to the reference model introduced in Table 2.8, the tidal response of Europa to diurnal tidal forces will differ from the one presented earlier in Table 5.1. As such, the relevant tidal response at diurnal frequency for the interior model defined by the parameters depicted in Table 5.6 is shown in Table 5.7.

Furthermore, the tidal response relevant for NSR is shown in Table 5.8. As briefly mentioned in Section 4.4.3, the different set of tidal Love numbers results from our assumption to keep the rocky interior synchronously locked while the ice shell experiences NSR. As the rocky mantle remains tidally locked, the stresses induced by the formation of the mantle's bulge had sufficient time to relax completely and, therefore, the response of the rocky interior to the NSR forcing function can be described as being purely fluid. From a modeling perspective, we can describe this physical behavior by decreasing the rigidity of the mantle μ to values relevant for near-fluid materials, i.e. $\mu \approx 0$ [Wahr et al., 2009].

5.4.4. RESULTS

The diurnal and NSR stress fields acting on Europa's surface are important factors in the study of the formation and evolution of tectonic features on Europa's surface. Stress fields on planetary surfaces are commonly expressed in location-dependent coordinates defined by the so-called principal axes. These axes are aligned in such a way that the planes normal to them are not affected by shear stresses [Ranalli, 1995]. The normal stresses working along the principal axes are defined as the principal stresses. The derivation of principal stresses and axes is a typical eigenvalue problem applied to the diurnal stress tensor (Equations 4.50 to 4.58) and/or NSR stress tensor (Equations 4.61 to 4.69), where the principal stresses are given by the eigenvalues and the principal axes by the corresponding eigenvectors. The resulting diurnal stress field acting at the surface of the reference model of Europa's interior is graphically presented in Figure 5.19 at four different positions along Europa's orbit. As expected, the diurnal stress field closely follows the

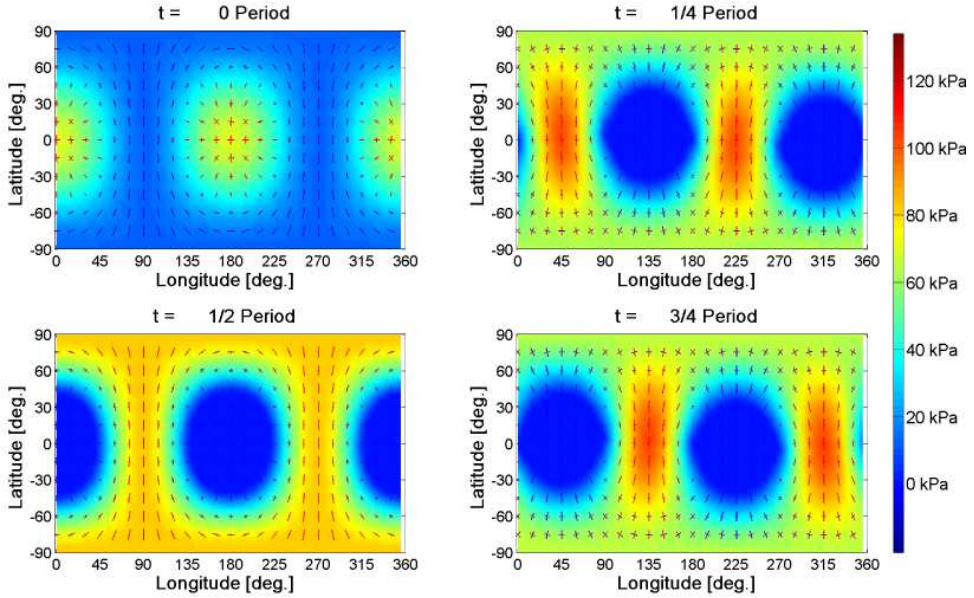


Figure 5.19: Diurnal stress field at the surface of the reference model of Europa's interior (Table 5.6) for an eccentricity $e = 0.0094$ and an obliquity $\varepsilon = 0.1^\circ$. The stress patterns are given at four different positions on Europa's orbit around Jupiter. The colored bars represent the principal components of the surface stress, with red indicating tension and blue indicating compression. The background color indicates the amplitude of the largest tensile principal component of the surface stress and is set to 0 kPa (blue color) if both components are compressive.

radial displacement field, showing tension where Europa's figure stretches (red lines in Figure 5.19) and compression where Europa's figure squeezes (blue lines in Figure 5.19). This result is rather expected because diurnal stresses acting on Europa's surface are always elastically stored in the lithosphere, i.e. $\Lambda \ll 0.1$ (see Figure 4.1).

Although the largest part of diurnal stresses is caused by the eccentricity, we cannot neglect the effect of a small non-zero obliquity. As can be observed from Figure 5.19, a small obliquity of 0.1° already breaks the symmetric distribution of stress patterns with respect to the equator. This effect is enhanced for larger values for the obliquity, as is clearly shown by Figure 5.20 for a hypothetical obliquity of 0.5° . The rupture of the symmetry with respect to the equator leads to latitudinal shifts of the tensile and compressive bulges, thereby yielding changes in the orientation and magnitude of the diurnal stress patterns (see Figure 5.20). In our example, increasing the obliquity from 0.1° to 0.5° leads, on average, to $\sim 9\%$ larger stresses at Europa's surface, whereas the effect on the spatial distribution is clearly visible from Figures 5.19 and 5.20. At mid-latitudes, where the influence of a non-zero obliquity is largest, diurnal stresses can locally become as much as $\sim 50\%$ larger after increasing the value of the obliquity from 0.1° to 0.5° .

Diurnal stresses at the surface of Europa depend on the rheological and structural properties of the interior through the tidal Love numbers h_2 and l_2 . From all physi-

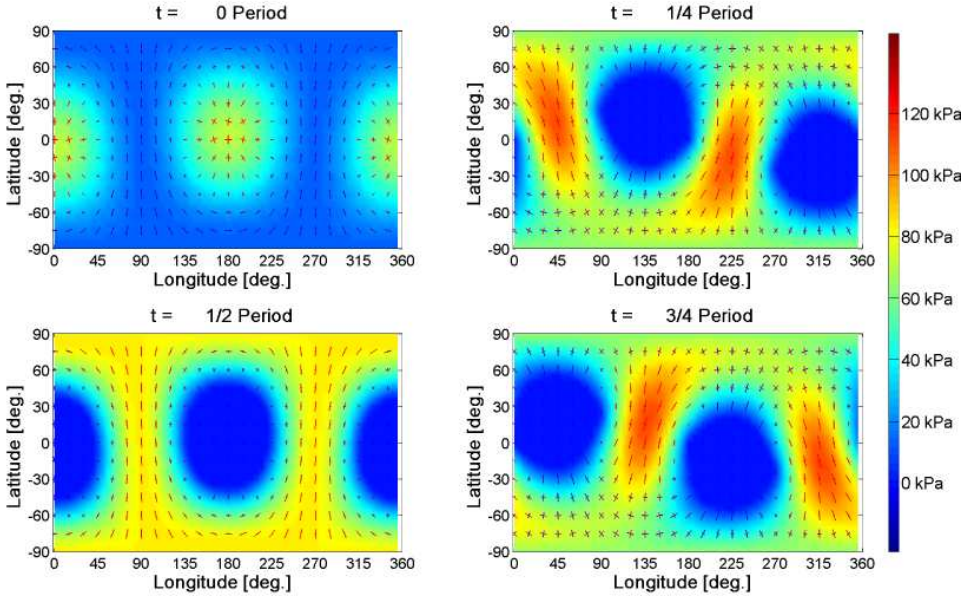


Figure 5.20: Diurnal stress field at the surface of the reference model of Europa's interior (Table 5.6) for an eccentricity $e = 0.0094$ and an obliquity $\varepsilon = 0.5^\circ$. The stress patterns are given at four different positions on Europa's orbit around Jupiter. The colored bars represent the principal components of the surface stress, with red indicating tension and blue indicating compression. The background color indicates the amplitude of the largest tensile principal component of the surface stress and is set to 0 kPa (blue color) if both components are compressive.

cal parameters of the interior, the largest effect on the tidal response, deformations and stresses is caused by the existence or non-existence of a subsurface ocean below the ice shell. As shown in Figure 5.21, diurnal stresses are usually much larger (more than one order of magnitude) when a subsurface ocean is present below the ice shell. However, as shown by the left panel of Figure 5.21, diurnal stresses may become even larger if an extremely low-viscous asthenosphere (i.e. $\eta_{ast} = 1.0 \times 10^{12}$ Pa s) extends down to the upper boundary of the silicate mantle. This peculiar behavior is caused by a decrease in the relaxation time of the strong transient modes T_1 and T_2 towards values comparable to the inverse of Europa's mean motion (keep in mind that the relaxation time of the transient modes T_1 and T_2 does not necessarily need to be comparable to the Maxwell time of the asthenosphere). Since also the modal strengths of T_1 and T_2 become larger than the elastic Love numbers, the diurnal stress field at the surface will be characterized by a large longitudinal phase shift which can exceed 40 degrees.

The influence of a subsurface ocean on the surface diurnal stresses is by far the largest, but certainly not the only one. As shown by Figure 5.21, the magnitude of surface diurnal stresses is roughly directly proportional to the elastic rigidity of the lithospheric shell, especially for models with a thin ice shell (less than 10 km) and/or an effectively elastic asthenosphere (curves for $\eta_{ast} = 1.0 \times 10^{16}$ Pa s). However, deviations

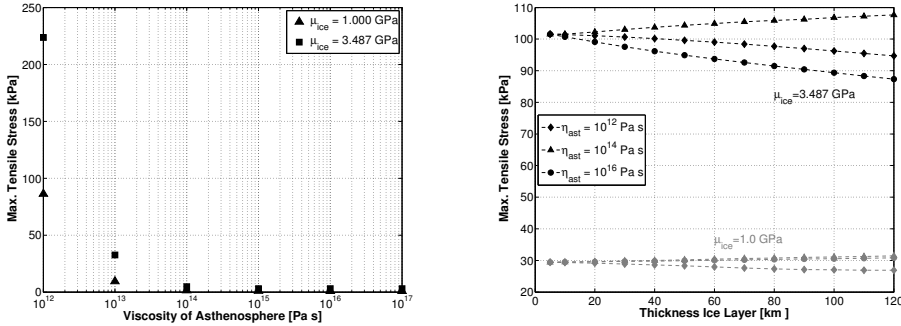


Figure 5.21: Magnitude of the largest diurnal tensile stresses acting on Europa's surface as a function of the properties of the ice-I shell. In all cases, the eccentricity is set at $e = 0.0094$ and the obliquity at $\varepsilon = 0.1^\circ$. (Left:) Magnitude of largest tensile stresses as a function of the viscosity of the ductile part of the ice-I shell for interior models without a subsurface ocean. The squares correspond to an ice rigidity of $\mu_{ice} = 3.487$ GPa and the triangles to an ice rigidity of $\mu_{ice} = 1$ GPa. (Right:) Magnitude of largest tensile stresses as a function of the rigidity and thickness of the ice-I shell, as well as the viscosity of the ductile part of the shell, for interior models with a subsurface ocean with its bottom at 130 km depth. The black solid curves correspond to an ice rigidity of $\mu_{ice} = 3.5$ GPa and the gray solid curves to an ice rigidity of $\mu_{ice} = 1$ GPa.

from direct proportionality are clearly observable in Figure 5.21 for interior models with a lower value for the viscosity of the asthenosphere (curves for $\eta_{ast} = 1.0 \times 10^{12}$ Pa s and $\eta_{ast} = 1.0 \times 10^{14}$ Pa s in Figure 5.21). This statement applies the most to interior models with a value for the viscosity for which the Maxwell relaxation time of the asthenosphere approaches the inverse of Europa's mean motion (curves for $\eta_{ast} = 1.0 \times 10^{14}$ Pa s in Figure 5.21).

The combined effect of the asthenosphere's viscosity and thickness also leads to a westward shift in the surface distribution of the surface stress patterns. The amount of phase shift depends on the ratio Γ_j of the dominant relaxation mode T_2 , and is therefore strongest when the relaxation time of T_2 is comparable to the inverse of Europa's mean angular velocity. This effect is illustrated in Figure 5.22, where we observe that phase shifts up to 7° are plausible for interior models with a thick ice shell and highly dissipative asthenosphere (i.e. $\eta_{ast} = 1.0 \times 10^{14}$ Pa s). The value of the phase shift, however, does not indicate the actual longitudinal shift of the stress patterns at Europa's surface. Instead, it denotes the time delay of the shell's response expressed as a difference in true anomaly. Due to eccentricity of Europa's orbit, the actual westward shift of the surface patterns will oscillate around the value of the phase shift during one orbital revolution. Figure 5.22 also shows that the phase shift becomes negligibly small as the behavior asthenosphere becomes nearly elastic ($\eta_{ast} \geq 10^{16}$ Pa s) or nearly fluid ($\eta_{ast} \leq 10^{13}$ Pa s). As a result, we can conclude that viscoelasticity only influences the diurnal stress field if the characteristic Maxwell time of the asthenosphere does not deviate by more than approximately one order of magnitude from the inverse mean motion $1/n$.

The diurnal stress field resulting from our modeling closely resembles the results published in previous studies [Greenberg et al., 1998, Harada and Kurita, 2006, Wahr et al., 2009]. However, some differences arise from the Maxwell viscoelastic treatment of

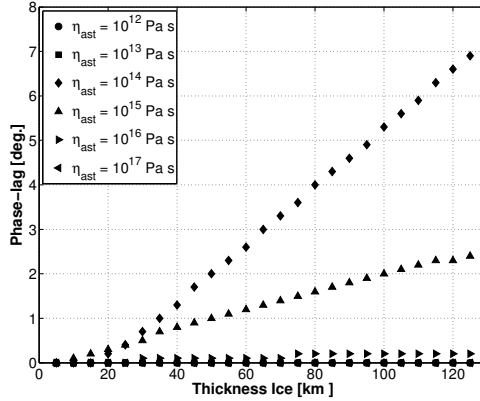


Figure 5.22: Phase shift of diurnal stress field as a function of the thickness of the entire ice layer and the viscosity of the asthenosphere. In all cases, the bottom of the ocean is set at 130 km from the surface, the rigidity of ice at $\mu_{ice} = 3.487$ GPa, the eccentricity at $e = 0.0094$ and the obliquity at $\varepsilon = 0^\circ$.

the interior's rheology, the non-zero obliquity, incompressibility and the use of different interior models. As partially shown in Figure 5.21, the viscoelastic representation of the tidal response leads to variations up to 20% in the magnitude of diurnal stresses. As mentioned above, viscoelasticity might also shift the entire stress field in westward direction, especially if the relaxation time of the strong transient mode T_2 is comparable to the inverse of Europa's mean motion. These typical viscoelastic effects are not observed in the surface stress modeling by Greenberg et al. [1998] and Harada and Kurita [2006], as they assume a perfectly elastic tidal response; neither in the modeling by Wahr et al. [2009], as they only explicitly show cases for which viscoelasticity becomes unimportant. In addition, our modeling of the obliquity's effect on surface diurnal stresses resembles the modeling by Rhoden et al. [2010] for nearly elastic bodies. Obviously, some differences arise from our viscoelastic treatment.

In contrast to diurnal stresses, NSR stresses at the surface of Europa might experience severe relaxation effects depending on the rheological properties of the lithosphere. The relaxation state of NSR stresses at Europa's surface depends on the dimensionless parameter Δ , which is proportional to the ratio between the period of NSR and the Maxwell relaxation time of the lithosphere (see Equation 4.70). As shown by Figure 4.2, viscoelastic relaxation starts to affect the magnitude and spatial distribution of NSR stresses for $\Delta > 0.1$ and becomes more severe as Δ increases. At $\Delta = 100$, viscoelastic relaxation already reduces the magnitude of NSR stresses by two orders of magnitude and shifts the entire stress field by nearly 45 degrees in westward direction.

In the particular case of our reference model of Europa's interior, the Maxwell relaxation time of the lithosphere is equal to about 9100 years and hence $\Delta = 0.1$ would correspond to a period of NSR approximately equal to 11500 years. This value for T_{ns} is slightly smaller than the assumed minimum value for T_{ns} (12000 years, see Table 4.1), meaning that the NSR stress field at the surface of our reference model will always show signs of viscoelastic relaxation. The effects of viscoelastic relaxation are clearly visible in

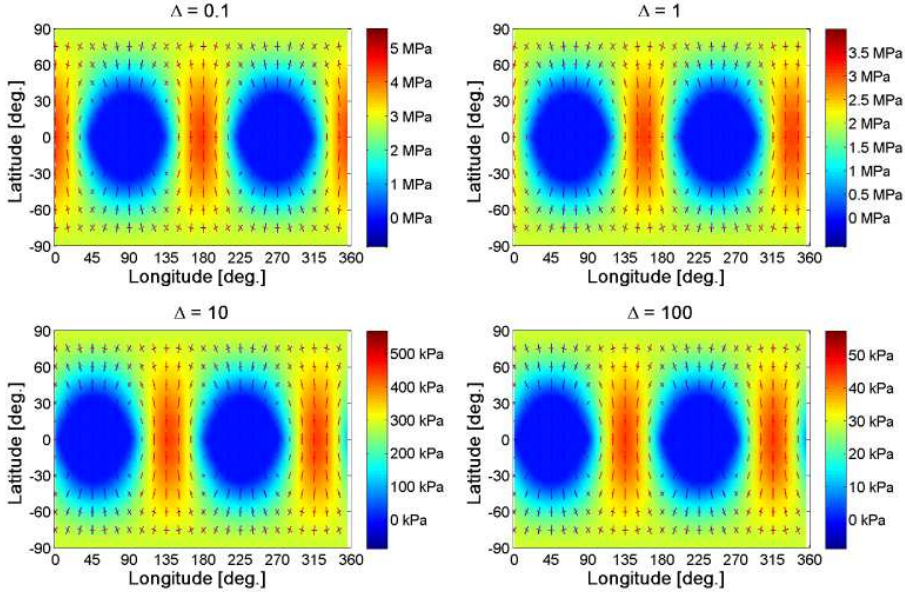


Figure 5.23: NSR stress field at the surface of the reference model of Europa's interior as a function of the ratio $\Delta = \frac{\mu/\eta}{2\Omega_{ns}}$. For the rheological properties of the reference model of Europa's interior, $\Delta = 0.1$ corresponds to $T_{ns} = 11,419$ years, $\Delta = 1$ to $T_{ns} = 114,188$ years, $\Delta = 10$ to $T_{ns} \approx 1.14$ million years and $\Delta = 100$ to $T_{ns} \approx 11.4$ million years. The colored bars represent the principal components of the surface stress, with red indicating tension and blue indicating compression. The background color indicates the amplitude of the largest tensile principal component of the surface stress and is set to 0 kPa (blue color) if both components are compressive.

Figure 5.23, where the NSR stress field at Europa's surface is depicted for $\Delta = 0.1, 1, 10$ and 100. There, we clearly observe that an increasing Δ leads to a gradual decrease of the magnitude of NSR stresses and a gradual shift of the entire stress field in westward direction. For $\Delta = 100$, in accordance with our theoretical expectations, the magnitude of NSR stresses becomes nearly two orders of magnitude smaller than for $\Delta = 0.1$ and the entire stress field is shifted by approximately 45 degrees in westward direction.

Furthermore, as shown in Figure 5.24, the magnitude of the largest NSR stresses at the surface does not depend on the thickness of the ice shell for our reference model of Europa's interior ($\eta_{ast} = 10^{14}$ Pa s). However, the situation is different for other models of Europa's interior, especially if the viscosity of the ductile lower part of the shell is increased towards values larger than or equal to 1.0×10^{16} Pa s. In this so-called high-viscous range, the magnitude of the largest NSR stresses will strongly depend on the thickness and viscosity of the ductile portion of the shell (see Figure 5.24). The strong dependence on the properties of the asthenosphere is caused by the relaxation of the ocean/ice boundary, represented by the buoyancy mode M_2 . In the high-viscous range (i.e. $\eta_{ast} \geq 10^{16}$ Pa s), this relaxation mode is characterized by having the slowest relaxation of all induced modes and by having a notoriously large tangential modal strength $l_{2,j}$. As a result, the effect of the buoyancy mode M_2 on NSR stresses is negligibly small

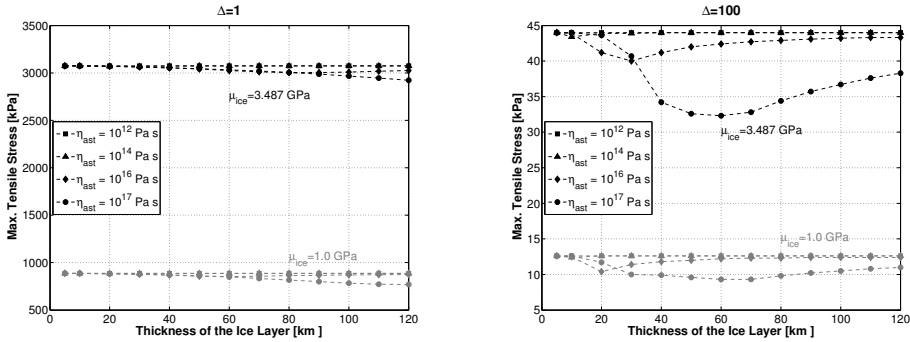


Figure 5.24: Magnitude of largest NSR tensile stresses at Europa's surface as a function of the ice thickness, ice rigidity and viscosity of the ductile lower part of the ice-I shell. In both cases, the black solid lines correspond to a rigidity of $\mu_{ice} = 3.487$ GPa for the ice shell and the gray dotted lines to a rigidity of $\mu_{ice} = 1$ GPa. (Left:) $\Delta = 1$. (Right:) $\Delta = 100$.

for values of Δ corresponding to elastic storage of stresses or even moderate relaxation (i.e. $\Delta < 1$). The effect of M_2 on NSR stresses clearly increases as relaxation in the icy lithosphere becomes more severe, leading to the large deviations observed in the right panel of Figure 5.24 for $\Delta = 100$. In our modeling, the relaxation mode M_2 can become sufficiently strong for $\eta_{ast} \geq 10^{17}$ Pa s and $\Delta \geq 100$ to shift the entire NSR stress field by more than 45° in westward direction, altering the usual orientation of the NSR stress patterns.

Although viscoelastic relaxation severely reduces the magnitude of NSR stresses, the NSR stress field remains larger than the ever-acting diurnal stress field for $\Delta < 43$ (i.e. $T_{ns} < 4.9$ million years in the case of our reference model). That means that NSR stresses will dominate the state of stresses at Europa's surface if the lithosphere is viscous enough to prevent strong viscoelastic relaxation or if NSR is sufficiently fast to reduce the value of the ratio Δ . In other cases, the state of stresses at Europa's surface will be dominated by the diurnal stress field.

5.4.5. DISCUSSION AND CONCLUSIONS

The main goal for modeling tidal stresses at Europa's surface is to study the origin and formation of the observed tectonic features. These features are thought to have formed as a result of tensile failure of Europa's icy surface [Greenberg et al., 1998]. Tensile failure most likely initiates when the acting tensile stresses exceed the tensile strength of the surface ice. Estimates of the poorly known tensile strength of ice-I at conditions relevant to Europa range from 40 kPa to several MPa, depending on porosity and contamination of the surface ice [Hoppa et al., 1999b, Schulson, 2001, Lee et al., 2005]. In this paper, we have dealt with the modeling of diurnal and NSR stresses acting at Europa's surface. Diurnal stresses are often related to the origin and formation of multi-arc cycloidal features on Europa's surface, whereas NSR stresses are often required to explain the formation of long arcuate lineaments [e.g. Wahr et al., 2009].

As shown by Figure 5.21, diurnal stresses at the surface of oceanless models of Europa's interior are usually much smaller than the plausible values for the tensile strength of ice (40 kPa to several MPa). Failure of the icy surface due to solely diurnal stresses, as suggested by the existence of numerous cycloidal lineaments on Europa's surface, would therefore require the existence of a subsurface ocean. However, diurnal stresses might exceed the tensile strength of ice if the silicate mantle would be in direct contact with an extremely low-viscous asthenosphere (η_{ast} less than $\sim 10^{12}$ Pa s). The resulting surface stress field, although large in magnitude (> 100 kPa, see left panel of Figure 5.21), will considerably differ from the stress field at the surface of interior models with a subsurface ocean. The question remains whether the orientation of existing cycloids can be explained by the diurnal stress field at the surface of an oceanless Europa.

The presence of a subsurface ocean, on the other hand, does not inherently guarantee that the acting diurnal stresses can be large enough to cause failure of the icy surface. As shown in the right panel of Figure 5.21, diurnal stresses do not exceed the tensile strength of ice when the rigidity of the icy lithosphere is assumed to be as low as 1 GPa. However, due to our poor knowledge regarding the mechanical strength of Europa's surface ice, we cannot preclude the possibility that diurnal cracking would occur for such a low rigidity. On the other hand, the sole effect of diurnal stresses could lead to mechanical failure of a 10 GPa icy lithosphere, but only if the tensile strength of the surface ice is less than ~ 300 kPa. This condition suggests that the formation of cycloidal features as a response to diurnal tides would require the existence of a contaminated and porous upper lithosphere, as such values for the tensile strength of ice are too low to be representative for non-contaminated and non-porous ice [e.g. Lee et al., 2005]. In addition, as shown by Figure 5.20, a non-zero obliquity breaks the north-south symmetry of the diurnal stress field, allowing for an explanation for equator-crossing cycloidal features [Hurford et al., 2009].

If one takes into account that Europa's ice shell would rotate faster than synchronous, tensile stresses up to several MPa might be induced at the surface, depending on the rheological properties of the lithosphere and the rate of non-synchronous rotation. Since NSR is assumed to be a slow process ($> 10^4$ years), the magnitude of NSR stresses at Europa's surface can be severely reduced by viscoelastic relaxation. The amount of viscoelastic relaxation acting on NSR stresses is physically described by the parameter Δ , which is directly proportional to the ratio between the period of NSR and the Maxwell time of the lithosphere. As a result, slow NSR and low-values for the viscosity of the icy lithosphere would lead to an increase of the ratio Δ , enhancing viscoelastic relaxation of NSR stresses.

NSR stresses, if present, do not act alone on Europa's surface but superimpose upon the ever-acting diurnal stresses. Variations in the value of Δ , i.e. in the relaxation state of NSR stresses, can reduce or enhance the importance of NSR stresses relative to diurnal stresses and lead to changes in the spatial and temporal distribution of the combined stress field. Without the effect of viscoelastic relaxation (i.e. $\Delta < 0.1$), NSR stresses would be much larger than diurnal stresses (approximately a factor 42 in the case of our standard model as shown by Figures 5.19 and 5.23 for $\Delta = 0.1$). Hence, the spatial and temporal distribution of the NSR-diurnal stress patterns will hardly change on a diurnal scale. Increasing the effect of viscoelastic relaxation on NSR stresses towards $\Delta \approx 30$ gradu-

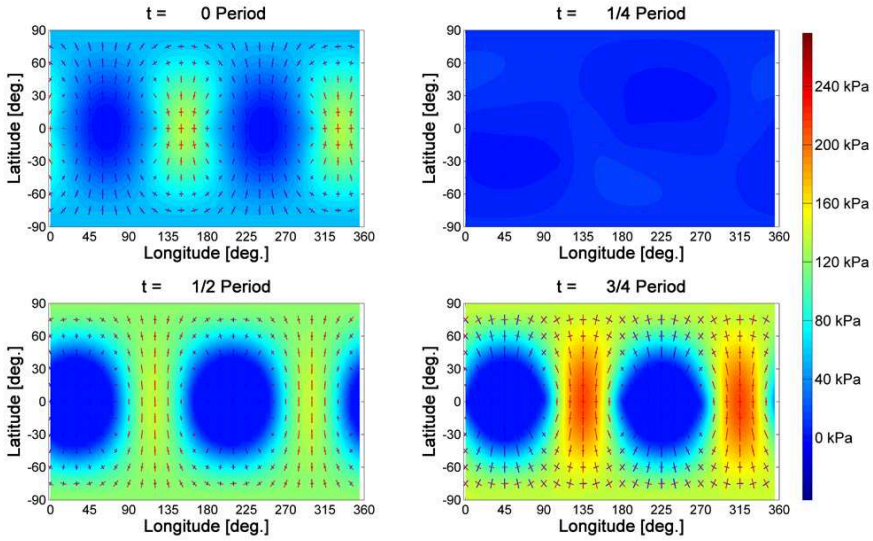


Figure 5.25: Combined diurnal-NSR stress field at the surface of our reference model of Europa for $\Delta = 40$, $e = 0.0094$ and $\varepsilon = 0.1^\circ$. The stress patterns are given at four different positions on Europa's orbit around Jupiter. The colored bars represent the principal components of the surface stress, with red indicating tension and blue indicating compression. The background color indicates the amplitude of the largest tensile principal component of the surface stress and is set to 0 kPa (blue color) if both components are compressive.

ally enhances the effect of diurnal stresses on the combined field. The combined NSR-diurnal stress field experiences periodic longitudinal oscillations on a diurnal timescale, which gradually become larger as Δ increases. When Δ becomes larger than ~ 30 (depending on the interior's model), longitudinal oscillations of the combined stress field can no longer be sustained by the strongly relaxed NSR stress field. The combined stress field would then become diurnal-like, as can be observed from Figure 5.25.

We can use the combined NSR-diurnal stress field to analyze the formation of the diverse lineament morphologies observed on Europa's surface. The formation of long arcuate lineaments requires either a slowly-changing stress field or unrealistically fast crack propagation speeds. The combined NSR-diurnal stress field remains nearly static as long as the NSR component clearly dominates the spatial-temporal distribution of the surface stress patterns. In our modeling, the NSR component keeps the combined stress field nearly static for values of Δ approximately smaller than 5 (equivalent to about 8 degrees of NSR). On the other hand, the formation of cycloidal features requires a highly-variable stress field and slow crack propagation speeds. The combined NSR-diurnal stress field becomes highly-variable (diurnal-like) for values of Δ larger than 30 (equivalent to about 2 degrees of NSR). An interesting characteristic of Europa's surface is that cycloidal features coexist with global arcuate lineaments, implying variations of the relaxation parameter Δ throughout the geological history of Europa's surface. Temporal variations of the relaxation parameter Δ can either be caused by secular variations in the rotation rate of Europa's ice shell, changes in the rheological properties of the sur-

face ice, or both of them. Changes in tidal heat dissipation with time, due to e.g. the time evolution of the orbit's eccentricity [Husmann and Spohn, 2004], could then lead to changes in the ice shell thickness distribution with time, affecting Europa's rotation rate (through the principal moments of inertia of the shell) and thereby the relaxation parameter Δ . Moreover, the same changes in tidal dissipation could also induce variations in the viscosity of the icy surface and Δ [Wahr et al., 2009]. Consequently, variations of the relaxation parameter Δ as a function of time would require the existence of a dynamic ice layer covering a subsurface ocean.

It is worth mentioning that the methodology presented in Chapters 3 and 4 implicitly assumes that Europa's interior behaves as an incompressible Maxwell body, while in fact all materials are known to be compressible. However, the effect of compressibility tidal deformations and stresses is known to be generally small (less than about 20% in magnitude [Sabadini and Vermeersen, 2004]). At the same time, we consider the assumption of linear rheology of more severe influence as the rheology of planetary ices is known to be best described by non-Newtonian rheological models [Durham et al., 1997, 2001, Goldsby and Kohlstedt, 2001]. The study of Europa's surface stress field from a non-Newtonian perspective requires numerical modeling and depends strongly on the poorly known properties of ice-I at European conditions. Nevertheless, the dependence of the effective viscosity on the stress (non-linear effect) is small compared to the dependence on the temperature [Showman and Han, 2004], as diffusion creep might be the dominating flow mechanism for all grain sizes [Moore, 2006]. By comparing our results with simulations from the viscoelastic SatStress software of Wahr et al. [2009], we obtain differences in magnitude up to $\sim 20\%$ for equivalent interior models; i.e. much less than the differences caused by the poorly constrained rigidity of ice (see Figure 5.21). We assign the obtained differences in magnitude to compressibility and partially to the fact that we treated Europa's inner structure as differentiated into a liquid metallic core and a rocky mantle, whereas Wahr et al. [2009] considered a single homogeneous core/mantle layer with a higher density than our silicate mantle. Although the effect of compressibility on the magnitude of surface tidal stresses is similar to e.g. the influence of a low-viscous asthenosphere, it is less important for our purposes as compressibility does not affect the orientation of the global stress patterns.

The purpose of this paper has been to determine the influence of a viscoelastic interior and a non-zero obliquity on diurnal and NSR stresses. We have shown that diurnal stresses at Europa's surface might experience the effects of viscoelastic relaxation of the asthenosphere, mainly in the form of a longitudinal shift of the surface stress patterns. However, the relevance of the viscoelastic effect is limited to interior models with a thick and highly dissipative asthenosphere. On timescales relevant for NSR ($> 10^4$ years) the magnitude and phase shift of NSR surface stresses can be affected by viscoelastic relaxation of the ice/shell boundary. This effect, however, becomes only important when NSR stresses experience strong viscoelastic relaxation in the lithospheric shell (i.e. $\Delta \sim 100$ or larger). The combination of NSR and diurnal stresses for different amounts of viscoelastic relaxation of NSR stresses in the lithosphere leads to a large variety of global stress fields that might explain the formation of the large diversity of lineament morphologies observed on Europa's surface.

In addition, we have shown that even a small obliquity breaks the symmetric dis-

tribution of surface stress patterns with respect to the equator. The effect of a small obliquity on the local magnitude and orientation of diurnal stress patterns is largest at mid-latitudes and when Europa is located 90° away from the nodes formed by the intersection of Europa's orbital and equatorial planes (see Figure 5.20). In those cases, local differences in magnitude up to more than 100% with respect to the eccentricity-only case are possible, even for very small obliquities ($< 0.25^\circ$). Diurnal stresses induced by the obliquity can offer an explanation for the existence of equator-crossing cycloids and the southern shift of the Wedges region, as suggested by [Hurford et al., 2009, Rhoden et al., 2010].

6

ROTATIONAL DYNAMICS OF ICY SATELLITES

6.1. INTRODUCTION

Both the spin rate and the orientation of the rotation axis with respect to the surface can experience variations as a result of redistribution of mass within a planetary body. These rotational variations have been proposed as a plausible explanation for the formation of some of the cracks observed on the surface of Jupiter's moon Europa [e.g. [Greenberg et al., 1998](#), [Hoppa et al., 2001](#), [Kattenhorn, 2002](#), [Greenberg et al., 2003](#), [Hurford et al., 2007](#), [Rhoden et al., 2010](#), [Rhoden and Hurford, 2013](#)] and for the current location of the active southern pole of Saturn's moon Enceladus [e.g. [Nimmo and Pappalardo, 2006](#), [Collins and Goodman, 2007](#), [Matsuyama and Nimmo, 2008](#)]. Furthermore, radar observations of Saturn's moon Titan made by the Cassini spacecraft suggest that Titan's upper ice shell rotates slightly faster than synchronous [[Stiles et al., 2008, 2010](#)]. In addition, future measurements of short-term periodic variations in the spin rate of several icy satellites (also called forced longitudinal librations) are expected to provide useful information about the properties of the subsurface ocean and the overlying ice shell [e.g. [Grasset et al., 2013](#)].

As mentioned in the Introduction to this thesis, it is the main objective of this research to analyze whether the previous claims can be supported by consistent dynamical models which take into account viscoelastic relaxation of the materials in the interior. As a consequence, in this Chapter, the analytical normal mode model that has been developed in Chapter 3 and applied to the determination of the tidal response of Europa and Ganymede in Chapters 4 and 5 is implemented into the description of the rotational dynamics of icy satellites in order to introduce the effect of viscoelastic deformation on the rotational response. The rotational dynamics are described through the linearized Liouville equations, which describe conservation of angular momentum for small changes in the spin rate and/or orientation of the spin axis. Hence, large excursions of the pole ($> 10^\circ$), such as the one supposedly expected for Enceladus [[Nimmo and Pappalardo,](#)

2006], are beyond the scope of the method presented in this Chapter.

Due to the likely presence of a subsurface ocean at shallow depth from the surface (see Chapter 2), the ice shell and the mantle are allowed to perform differential rotational variations as the tangential motion of these layers is mechanically decoupled (see Chapter 3). Nevertheless, the rotational motion of the shell and the mantle remains to some degree coupled as a result of the effect of gravitational and fluid pressure torques. Existing rotational models that are commonly used for the study of rotational variations on terrestrial planets, such as Munk and MacDonald [1960], Sabadini et al. [1982], Wu and Peltier [1984], Sabadini and Vermeersen [2004], have not been originally developed to handle differential rotation of internal layers and are, therefore, unable to provide a realistic description of the rotational dynamics of icy satellites with a global subsurface ocean. As a result, the structure of the differential rotation model presented in this Chapter will be largely inspired by rotation models developed for the study of the rotation of Earth's and/or Mars' fluid core and solid core [e.g. Sasao et al., 1980, Hinderer and Legros, 1989, Mathews et al., 1991, Dehant et al., 1993, Szeto and Xu, 1997, Greff-Lefftz et al., 2000, Van Hoolst and Dehant, 2002, Dehant and Mathews, 2007, Van Hoolst, 2007, Dumberry, 2009]; a dynamical case that shows more similarities with the differential rotation expected on icy satellites with an internal ocean.

The structure of this Chapter is as follows. First, the basic linearized Liouville equations for triaxial bodies are presented in Section 6.2. This is followed in Section 6.3 by the derivation of the necessary inertia increments as a result of readjustment of the equatorial and tidal bulges of the satellite. Finally, Section 6.4 provides an introduction to the structure of the differential rotation model developed for the study of rotational variations on icy satellites with a subsurface ocean. A detailed application of the model to the case of forced longitudinal librations is the subject of the next Chapter.

6.2. BASIC LINEARIZED ROTATIONAL DYNAMICS FOR TRIAXIAL BODIES

The rotational dynamics of planetary bodies, such as terrestrial planets and icy moons, has been classically studied by means of the so-called Liouville equation, which describes the change in the angular momentum \mathbf{H} of a planetary body as a result of external torques $\mathbf{\Gamma}$ acting on it, internal mass displacements and relative motion within the interior. The Liouville equation is a special case of the more general Euler dynamic equation for conservation of angular momentum, which is defined as

$$\frac{d\mathbf{H}(t)}{dt} + \boldsymbol{\omega}(t) \times \mathbf{H}(t) = \mathbf{\Gamma}(t), \quad (6.1)$$

where $\boldsymbol{\omega}$ is the angular velocity of a body-fixed frame (i.e. $\boldsymbol{\omega}$ is the angular velocity of the planetary body itself).

For geophysical applications, it is convenient to separate the angular momentum \mathbf{H} into a term that accounts for the contribution of changes in the inertia tensor \mathbf{I} of the planetary body as a result of redistribution of mass within the interior and a term that accounts for the contribution of the motion of geophysical fluids (i.e. subsurface ocean,

liquid core, atmosphere) relative to the body-fixed co-rotating reference frame. Then, the angular momentum \mathbf{H} can be written as

$$\mathbf{H}(t) = \mathbf{I}(t)\boldsymbol{\omega}(t) + \mathbf{h}(t), \quad (6.2)$$

where \mathbf{h} denotes the relative angular momentum due to relative motion of geophysical fluids, which is defined as

$$\mathbf{h}(t) = \iiint \rho(\mathbf{r})\mathbf{r} \times \mathbf{v} dV, \quad (6.3)$$

with \mathbf{r} and \mathbf{v} being the position and velocity of a volume element dV of density $\rho(\mathbf{r})$ relative to the co-rotating reference frame.

Then, substitution of Equation 6.2 into 6.1 leads to the Liouville equation:

$$\frac{d}{dt} [\mathbf{I}(t)\boldsymbol{\omega}(t) + \mathbf{h}(t)] + \boldsymbol{\omega}(t) \times [\mathbf{I}(t)\boldsymbol{\omega}(t) + \mathbf{h}(t)] = \boldsymbol{\Gamma}(t), \quad (6.4)$$

which is the basic expression applied to the study of the rotational variations experienced by planetary bodies such as the Earth [e.g. Munk and MacDonald, 1960, Sasao et al., 1980, Hinderer et al., 1982, Sabadini et al., 1982, Wu and Peltier, 1984, Moritz and Mueller, 1987, Dehant et al., 1993, Greff-Lefftz et al., 2000, Sabadini and Vermeersen, 2004, Gross, 2007], Mars [e.g. Zharkov and Molodensky, 1996, Defraigne et al., 2000, Van Hoolst and Dehant, 2002, Dehant et al., 2003, 2006, Van Hoolst, 2007] and icy moons [e.g. Tokano et al., 2011].

The Liouville equation defined by Equation 6.4 is non-linear by definition and, as such, numerical methods would be necessary to find the solutions for the variations in the rotation vector of the planetary body [e.g. Ricard et al., 1993]. However, for the cases relevant to this thesis, this expression can be substantially simplified by taking into consideration that the relative angular momentum \mathbf{h} , the changes in the inertia due to internal mass redistribution and the resulting deviations from the rotation axis usually remain small [e.g. Munk and MacDonald, 1960, Gross, 2007], thereby allowing for linearization of the full non-linear Liouville equation. Then, the inertia tensor \mathbf{I} can be defined as

$$\mathbf{I} = \begin{pmatrix} A + c_{xx} & c_{xy} & c_{xz} \\ c_{xy} & B + c_{yy} & c_{yz} \\ c_{xz} & c_{yz} & C + c_{zz} \end{pmatrix}, \quad (6.5)$$

where A and B are the principal equatorial moments of inertia of the entire planetary body, C is the principal polar moment of inertia¹ and the c_{ij} 's are the small inertia increments resulting from mass redistribution in the interior ($c_{ij} \ll A, B, C$). The axes of the body-fixed reference frame are defined in such a way that the z -axis initially coincides with the axis of rotation and the x -axis initially coincides with the tidal axis. In the perturbed state, the axes deviate slightly from their initial state and are then oriented in such a way that the relative angular momentum of the ice shell, to which the frame is attached, vanishes. In this frame, which is known as the Tisserand frame [Munk and

¹with $A < B < C$ for triaxial ellipsoidal planetary bodies such as the icy satellites of the outer planets.

MacDonald, 1960], the relative motion of other internal layers, such as the subsurface ocean, the silicate mantle and the core, would still lead to non-zero contributions to the relative angular momentum $\mathbf{h}(t)$. The perturbed instantaneous angular velocity vector $\boldsymbol{\omega}$ can then be defined as

$$\boldsymbol{\omega} = \begin{pmatrix} \omega_x \\ \omega_y \\ \omega_z \end{pmatrix} = \Omega \begin{pmatrix} m_x \\ m_y \\ 1 + m_z \end{pmatrix}, \quad (6.6)$$

where Ω is the mean spin rate of the planetary body. The small rotational deviations m_x and m_y describe the reorientation of the pole towards the direction of the x - and y -axes, respectively. The deviation m_z describes the changes in the spin rate (length of day variations). In all cases the m_i 's are considered to be much smaller than Ω .

Substitution of the definitions given by Equations 6.5 and 6.6 into the Liouville equation leads, after linearization in the small quantities m_i and c_{ij} , to the following system of equations for the whole icy satellite:

$$\frac{A}{(C-B)\Omega} \dot{m}_x + m_y = \frac{1}{(C-B)\Omega^2} (\Omega^2 c_{yz} - \Omega \dot{c}_{xz} + \Omega h_y - \dot{h}_x + \Gamma_x), \quad (6.7)$$

$$\frac{B}{(C-A)\Omega} \dot{m}_y - m_x = \frac{1}{(C-A)\Omega^2} (-\Omega^2 c_{xz} - \Omega \dot{c}_{yz} - \Omega h_x - \dot{h}_y + \Gamma_y), \quad (6.8)$$

$$\dot{m}_z = \frac{1}{C\Omega} (-\Omega \dot{c}_{zz} - \dot{h}_z + \Gamma_z). \quad (6.9)$$

An important property of the linearized Liouville equations, given by the system of Equations 6.7 to 6.9, is that the third equation decouples from the first two. As a result, polar motion and spin rate variations can be studied separately.

As a first approximation we assume that variations in the rotation of a planetary satellite are induced by the sole effect of mass displacements in the interior, thereby neglecting the contribution of relative motions ($h_i, \dot{h}_i = 0$), time variations of the inertia ($\dot{c}_{ij} = 0$) and external torques ($\Gamma_i = 0$). Then, Equations 6.7 to 6.9 can be written as

$$\frac{A}{(C-B)\Omega} \dot{m}_x + m_y = \frac{c_{yz}}{(C-B)}, \quad (6.10)$$

$$\frac{B}{(C-A)\Omega} \dot{m}_y - m_x = -\frac{c_{xz}}{(C-A)}, \quad (6.11)$$

$$m_z = -\frac{c_{zz}}{C}. \quad (6.12)$$

Equations 6.10 to 6.12 describe the rotational dynamics of a rigid planetary satellite. Therefore, these expressions do not account for the shift experienced by the equatorial and tidal bulges due to viscoelastic deformation. In other words, the reorientation of the pole towards the axis of maximum inertia (C) would imply that the position of the spin axis would not be perpendicular to the equatorial plane whenever the perturbing mass is not on the equator or the poles. The spin axis will then wobble around the axis of maximum inertia. The frequency σ_r of this wobble is given by the frequency of the free Eulerian precession, which in the case of triaxial bodies is defined as [Zharkov and

Molodensky, 1996, Tokano et al., 2011]

$$\sigma_r = \sqrt{\frac{C-B}{A} \frac{C-A}{B}} \Omega. \quad (6.13)$$

However, planetary satellites do not behave as rigid bodies as they experience elastic and/or viscoelastic deformation by tides and rotation. Elastic and/or viscoelastic material properties lead to the decrease of the frequency σ_r of the Chandler wobble, the decay of the wobble amplitude [e.g. Munk and MacDonald, 1960, Moritz and Mueller, 1987, Sabadini and Vermeersen, 2004] and the decrease of the libration amplitude [Van Hoolst et al., 2013, Jara-Oru e and Vermeersen, 2014]. The contribution of tidal and centrifugal deformation to the rotational dynamics is commonly introduced through the definition of the inertia increments, as will be discussed in Sections 6.3 and 6.4.

In addition, due to presence of a subsurface ocean at shallow depth, the relative angular momentum h_i due to relative motion of the ocean or other internal layers cannot be neglected in the case of icy moons like Europa. The role of the subsurface ocean on the rotational dynamics of icy satellites will be discussed in Section 6.4.

6.3. EFFECT OF DEFORMATION ON THE ROTATIONAL DYNAMICS OF TRIAXIAL BODIES

As has been briefly pointed out at the end of Section 6.2, the rotational variations experienced by a non-rigid planetary satellite are affected by the rotational and tidal deformation undergone by the interior of the satellite. The mass redistribution that accompanies this deformation leads to inertia increments and gives rise to an exterior gravitational potential V_2 , which can be defined as [e.g. Sabadini and Peltier, 1981, Mitrovica et al., 1994]

$$V_2 = \bar{V}_2 + \Delta V_2 = k_f \left(\frac{R_s^5}{r_o^5} \right) (\bar{V}_2^R + \bar{V}_2^T) + k_2(t) * \left(\frac{R_s^5}{r_o^5} \right) (\Delta V_2^R + \Delta V_2^T), \quad (6.14)$$

where we subdivided the perturbed gravitational potential (V_2), as well as the centrifugal (V_2^R) and tidal (V_2^T) potentials, into a constant component (\bar{V}_2 , \bar{V}_2^R and \bar{V}_2^T , respectively) and a time-variable component (ΔV_2 , ΔV_2^R and ΔV_2^T , respectively). Moreover, as introduced in Section 3.6, k_f is the secular Love number or fluid Love number related to the gravitational perturbation and $k_2(t)$ is the corresponding time-dependent Love number. Furthermore, R_s denotes the mean radius of the satellite, r_o is the radial distance of a point P on the satellite relative to the center of mass of the satellite, and the symbol $*$ indicates time convolution.

In this Section, we first provide a derivation of the expressions for the constant and time-dependent part of the centrifugal and tidal potentials acting on an icy satellite (subsections 6.3.1 and 6.3.2). In subsection 6.3.3, these expressions will be related to the inertia increments c_{ij} through the use of the defined exterior gravitational potential, which is given by Equation 6.14, and MacCullagh's formula, which expresses the gravitational potential near the boundary of a body slightly departing from spherical symmetry in terms of perturbations in the moments of inertia [Munk and MacDonald, 1960].

6.3.1. DEFINITION OF THE CENTRIFUGAL POTENTIAL FOR ROTATIONAL STUDIES

Here we provide a derivation of the expressions for the constant and time-dependent part of the centrifugal and tidal potentials acting on an icy satellite, as required for the definition of the inertia increments due to tidal and rotational deformation. Similar to the Liouville equation in the previous Section, the equations here are defined with respect to a rotating Cartesian reference frame attached to the surface of the satellite. By definition, this frame rotates with angular velocity $\boldsymbol{\omega} = [\omega_x, \omega_y, \omega_z]^T = n [m_x, m_y, 1 + m_z]^T$ relative to a frame fixed in space and initially coinciding with the rotating frame [Munk and MacDonald, 1960].

The centrifugal potential V^R acting on a rotating icy satellite is defined by

$$V^R = \frac{1}{2}\omega^2 l^2 = \frac{1}{2}\omega^2 (r_o^2 - r_o^2 \cos^2(\alpha)), \quad (6.15)$$

where ω is the magnitude of the angular velocity, r_o is the magnitude of the position vector of a point P in the interior or on the surface of an undeformed Europa, and l is the distance of point P perpendicular to the axis of rotation. The angle α is defined as the angular distance between the instantaneous axis of rotation and the position vector of point P , i.e.

$$\cos(\alpha) = \frac{\mathbf{r}_o \cdot \boldsymbol{\omega}}{r_o \omega} \quad (6.16)$$

Alternatively, the angle α can be conveniently expressed in terms of the Legendre polynomial $P_2(\cos \alpha)$ as follows

$$\cos^2(\alpha) = \frac{2}{3}P_2(\cos(\alpha)) + \frac{1}{3} \quad (6.17)$$

Substitution of Equation 6.17 into Equation 6.15 yields

$$V^R = V_0^R + V_2^R = \frac{1}{3}\omega^2 r_o^2 - \frac{1}{3}\omega^2 r_o^2 P_2(\cos(\alpha)), \quad (6.18)$$

in which the first term (V_0^R) represents the purely radial component of the centrifugal potential and the second term (V_2^R) describes the equatorial bulge. This second term can be expanded by using the definitions of the angle α given by Equations 6.16 and 6.17. The resulting expression becomes

$$V_2^R = -\frac{1}{2} \left(x_o^2 \omega_x^2 + y_o^2 \omega_y^2 + z_o^2 \omega_z^2 + 2x_o y_o \omega_x \omega_y + 2y_o z_o \omega_y \omega_z + 2x_o z_o \omega_x \omega_z \right) + \frac{1}{6} \omega^2 (x_o^2 + y_o^2 + z_o^2), \quad (6.19)$$

where x_o , y_o and z_o are the Cartesian components of the position vector \mathbf{r}_o .

Equation 6.19 can be further simplified by expressing the angular velocities ω_x , ω_y and ω_z in terms of the small rotational variations m_i . In the resulting expression for the

potential, we neglect all second and higher order terms in the rotational deviations m_i , such that the centrifugal potential of a synchronous satellite can be written as

$$\bar{V}_2^R = \frac{1}{6} n^2 \{x_o^2 + y_o^2 - 2z_o^2\}, \quad (6.20)$$

$$\Delta V_2^R = \frac{1}{3} n^2 \{m_z x_o^2 + m_z y_o^2 - 2m_z z_o^2 - 3m_x x_o z_o - 3m_y y_o z_o\}, \quad (6.21)$$

where \bar{V}_2^R and ΔV_2^R represent the constant and time-varying part of the centrifugal potential, respectively.

6.3.2. DEFINITION OF THE TIDAL POTENTIAL FOR ROTATIONAL STUDIES

In contrast to e.g. Earth or other terrestrial planets, the shape of most icy satellites is elongated in the direction pointing to the parent planet. This elongation, the so-called tidal bulge, is raised by the strong tidal forces exerted by the planet on the figure of the satellite. The tidal potential V_2^T exerted by a planet on a satellite located at a distance d is given by

$$V_2^T = n^2 r_o^2 \left(\frac{a}{d}\right)^3 \left(\frac{3}{2} \cos^2(\Psi) - \frac{1}{2}\right), \quad (6.22)$$

where a is the orbit's semi-major axis and Ψ is the angle between the position vector \mathbf{d} (position of the tide raising body with respect to the center of mass of the moon) and the previously defined position vector \mathbf{r}_o of a point P . Using well-known relations for right spherical triangles, the angle Ψ can be expressed as

$$\cos(\Psi) = \sin(\theta') \cos(\lambda'), \quad (6.23)$$

where λ' and θ' are the longitude and co-latitude of point P in a rotating reference frame in which the x' -axis points to the actual position of the tide raising body (i.e. coincides with \mathbf{d}) and the z' -axis coincides with the spin axis; thereby assuming that Europa's obliquity is negligibly small. This reference frame is not attached to Europa's surface and, as such, further derivations are necessary to express the coordinates $[(x', y', z')^T]$ in terms of the coordinates $[x_o, y_o, z_o]^T$ of the surface-fixed co-rotating reference frame defined in the previous Section. The two frames are related by

$$\begin{pmatrix} x' \\ y' \\ z' \end{pmatrix} = \mathbf{R}_z(\nu(t) - \phi(t)) \mathbf{R}_y(\gamma_y(t)) \mathbf{R}_x(\gamma_x(t)) \begin{pmatrix} x_o \\ y_o \\ z_o \end{pmatrix}, \quad (6.24)$$

where it can be observed that the $[x', y', z']^T$ -frame results from three subsequent right-handed rotations of the surface-fixed frame $[x_o, y_o, z_o]^T$: 1) about the x_o -axis by an angle $\gamma_x(t) = -m_y(t)$ (recall that m_y was defined positive towards the y_o -axis), 2) about the intermediate y_1 -axis by an angle $\gamma_y(t) = m_x(t)$, and 3) about the intermediate z_2 -axis by an angle $\nu(t) - \phi(t)$, which stands for the difference between the true anomaly $\nu(t)$ and the spin angle $\phi(t)$ at a time t . Using the definition of the z -component of the spin vector

ω , the latter can be defined as

$$\phi(t) = \int_0^t \omega_z dt = nt + n \int_0^t m_z(t) dt = M(t) + \gamma_z(t), \quad (6.25)$$

where $M(t)$ is the mean anomaly. Then, the argument $\nu(t) - \phi(t)$ of the rotation in the z -direction becomes $\nu(t) - M(t) - \gamma_z(t)$, where $\nu(t) - M(t)$ can be approximated as [Murray and Dermott, 1999]

$$\nu(t) - M(t) = 2e \sin(nt) + O(e^2). \quad (6.26)$$

Neglecting all second and higher order terms in the small eccentricity, $\nu(t) - \phi(t)$ can be written as $2e \sin(nt) - \gamma_z(t)$. Since both the eccentricity and $\gamma_z(t)$ are assumed to be small, all rotations in Equation 6.24 are over small angles. This property allows us to define the right-handed linearized rotation matrices \mathbf{R}_x , \mathbf{R}_y and \mathbf{R}_z as

$$\mathbf{R}_x = \begin{pmatrix} 1 & 0 & 0 \\ 0 & 1 & -m_y \\ 0 & m_y & 1 \end{pmatrix}, \quad (6.27)$$

$$\mathbf{R}_y = \begin{pmatrix} 1 & 0 & -m_x \\ 0 & 1 & 0 \\ m_x & 0 & 1 \end{pmatrix}, \quad (6.28)$$

$$\mathbf{R}_z = \begin{pmatrix} 1 & 2e \sin(nt) - \gamma_z(t) & 0 \\ -2e \sin(nt) + \gamma_z(t) & 1 & 0 \\ 0 & 0 & 1 \end{pmatrix}. \quad (6.29)$$

Then, Equation 6.24 can be written as

$$\begin{pmatrix} x' \\ y' \\ z' \end{pmatrix} = \begin{pmatrix} 1 & 2e \sin(nt) - \gamma_z(t) & -m_x(t) \\ -2e \sin(nt) + \gamma_z(t) & 1 & -m_y(t) \\ m_x(t) & m_y(t) & 1 \end{pmatrix} \begin{pmatrix} x_o \\ y_o \\ z_o \end{pmatrix}. \quad (6.30)$$

Using the coordinate transformation $x' = r_o \sin(\theta') \cos(\lambda')$ and Equation 6.30 allows us to define the angle Ψ in terms of the coordinates of the surface-fixed co-rotating frame. Equation 6.23 becomes

$$\cos(\Psi) = \frac{x'}{r_o} = \frac{x_o + (2e \sin(nt) - \gamma_z(t))y_o - m_x(t)z_o}{r_o}, \quad (6.31)$$

and consequently, $\cos^2(\Psi)$ can be written as

$$\cos^2(\Psi) = \frac{x_o^2 + 2(2e \sin(nt) - \gamma_z(t))x_o y_o - 2m_x(t)x_o z_o}{r_o^2}, \quad (6.32)$$

where all second order terms in the small eccentricity e , rotation angle γ_z and rotational variation m_x have been neglected. Substitution of Equation 6.32 into 6.22 yields the following expression for the tidal potential

$$V_2^T = n^2 r_o^2 \left(\frac{a}{d}\right)^3 \left(\frac{3}{2} \frac{x_o^2 + 2(2e \sin(nt) - \gamma_z(t))x_o y_o - 2m_x(t)x_o z_o}{r_o^2}\right)$$

$$-\frac{1}{2} \frac{x_o^2 + y_o^2 + z_o^2}{r_o^2} \Big), \quad (6.33)$$

where the ratio $(\frac{a}{d})^3$ can alternatively be written as [Murray and Dermott, 1999]

$$\left(\frac{a}{d}\right)^3 = 1 + 3e \cos(nt) + O(e^2). \quad (6.34)$$

Substitution of Equation 6.34 into Equation 6.33 then yields

$$V_2^T = n^2 \left(\frac{3}{2} [(1 + 3e \cos(nt))x_o^2 + 2(2e \sin(nt) - \gamma_z(t))x_o y_o - 2m_x(t)x_o z_o] - \frac{1}{2}(1 + 3e \cos(nt)) [x_o^2 + y_o^2 + z_o^2] \right), \quad (6.35)$$

where we again neglected all second and higher order terms in the small eccentricity and rotational variations. As a final step, similarly to the case of the centrifugal potential, the tidal potential is subdivided into a constant (\bar{V}_2^T) and time-varying part (ΔV_2^T), i.e.

$$\bar{V}_2^T = \frac{1}{2} n^2 \{2x_o^2 - y_o^2 - z_o^2\}, \quad (6.36)$$

$$\Delta V_2^T = \frac{3}{2} n^2 \{2e \cos(nt)x_o^2 - e \cos(nt)y_o^2 - e \cos(nt)z_o^2 + 2(2e \sin(nt) - \gamma_z(t))x_o y_o - 2m_x(t)x_o z_o\}. \quad (6.37)$$

6.3.3. INERTIA INCREMENTS

The deformation induced by the centrifugal and tidal potentials acting on the satellite causes mass displacements in the interior, which on their turn cause deviations in the inertia. To take into consideration the kind of physical process that leads to the changes in the satellite's moment of inertia, it is convenient to redefine the inertia deviations c_{ij} as

$$c_{ij} = c_{ij}^R + c_{ij}^T + c_{ij}^L, \quad (6.38)$$

where the superscripts R , T and L refer to the inertia variations induced by, respectively, the rotational deformation, tidal deformation and direct geodynamic forcing.

The purpose of this subsection is to relate the perturbed gravitational potential V_2 , defined by Equation 6.14, to the inertia deviations c_{ij} through the use of MacCullagh's formula, which expresses the gravitational potential near the boundary of a body slightly departing from spherical symmetry [Munk and MacDonald, 1960]. This expression is given by

$$V_2 = -\frac{G}{2r_o^5} \left[3\mathbf{r}_o^T \mathbf{I} \mathbf{r}_o - r_o^2 \text{tr}(\mathbf{I}) \right], \quad (6.39)$$

where the trace of the inertia tensor \mathbf{I} (Equation 6.5) is assumed to be constant², i.e.: $\text{tr}(\mathbf{I}) = A + B + C = 3\bar{I}$, with \bar{I} being the mean moment of inertia of the satellite. Substitution of Equation 6.5 and the definition of the trace into Equation 6.39 then leads to the

²The trace of the inertia tensor has been shown to be invariant under any deformation process whose potential does not include a spherical harmonic term of degree zero [Rochester and Smylie, 1974, Gross, 2003].

following expression for the perturbed potential

$$V_2 = -\frac{G}{2r_o^5} \left\{ 3(A + c_{xx}^{RT} - \bar{I})x_o^2 + 3(B + c_{yy}^{RT} - \bar{I})y_o^2 + 3(C + c_{zz}^{RT} - \bar{I})z_o^2 + 6c_{xy}^{RT}x_oy_o + 6c_{xz}^{RT}x_oz_o + 6c_{yz}^{RT}y_oz_o \right\}, \quad (6.40)$$

in which the superscript RT refers to the inertia perturbations caused by the combined rotational and tidal deformation experienced by the satellite.

As has been previously done for all potentials in this Section, the perturbed gravitational potential defined by Equation 6.40 can be conveniently decomposed into a constant component (\bar{V}_2) and a time-varying component (ΔV_2), which are defined as

$$\bar{V}_2 = -\frac{G}{2r_o^5} \left\{ 3(A - \bar{I})x_o^2 + 3(B - \bar{I})y_o^2 + 3(C - \bar{I})z_o^2 \right\}, \quad (6.41)$$

$$\Delta V_2 = -\frac{3G}{2r_o^5} \left\{ c_{xx}^{RT}x_o^2 + c_{yy}^{RT}y_o^2 + c_{zz}^{RT}z_o^2 + 2c_{xy}^{RT}x_oy_o + 2c_{xz}^{RT}x_oz_o + 2c_{yz}^{RT}y_oz_o \right\}. \quad (6.42)$$

Equations 6.14 and 6.40 are both representations of the same gravitational potential, and as such they can be used to express the principal moments of inertia and inertia increments in terms of the previously defined centrifugal and tidal potentials. Expressions for the principal moments of inertia A , B and C follow from substitution of the constant part of Equation 6.14 and Equations 6.20 and 6.36 into Equation 6.41, i.e.

$$A = \bar{I} - \frac{7}{9} \frac{R_s^5 n^2}{G} k_f, \quad (6.43)$$

$$B = \bar{I} + \frac{2}{9} \frac{R_s^5 n^2}{G} k_f, \quad (6.44)$$

$$C = \bar{I} + \frac{5}{9} \frac{R_s^5 n^2}{G} k_f, \quad (6.45)$$

where the mean moment of inertia \bar{I} is defined as

$$\bar{I} = \frac{8}{3} \pi \int_0^{R_s} \rho(r) r^4 dr. \quad (6.46)$$

In addition, Equations 6.43 to 6.45 can be combined in order to find equivalent expressions for the secular Love number k_f , i.e.

$$k_f = \frac{G(B - A)}{R_s^5 n^2} = \frac{3}{4} \frac{G(C - A)}{R_s^5 n^2} = 3 \frac{G(C - B)}{R_s^5 n^2}. \quad (6.47)$$

In a similar way, explicit expressions for the inertia increments c_{ij}^{RT} due to centrifugal and tidal deformation can be derived from substitution of the time-dependent part of Equation 6.14 and Equations 6.21 and 6.37 into Equation 6.42. The resulting expressions are listed below

$$c_{xx}^{RT} = -\frac{2}{9} \frac{R_s^5 n^2}{G} k_2(t) * [m_z(t) + 9e \cos(nt)], \quad (6.48)$$

$$c_{yy}^{RT} = -\frac{2}{9} \frac{R_s^5 n^2}{G} k_2(t) * \left[m_z(t) - \frac{9}{2} e \cos(nt) \right], \quad (6.49)$$

$$c_{zz}^{RT} = \frac{2}{9} \frac{R_s^5 n^2}{G} k_2(t) * \left[2m_z(t) + \frac{9}{2} e \cos(nt) \right], \quad (6.50)$$

$$c_{xy}^{RT} = -\frac{R_s^5 n^2}{G} k_2(t) * [2e \sin(nt) - \gamma_z(t)], \quad (6.51)$$

$$c_{xz}^{RT} = \frac{4}{3} \frac{R_s^5 n^2}{G} k_2(t) * m_x(t), \quad (6.52)$$

$$c_{yz}^{RT} = \frac{1}{3} \frac{R_s^5 n^2}{G} k_2(t) * m_y(t). \quad (6.53)$$

The expressions for the inertia increments given above, as well as the expressions for the principal moments of inertia, hold for a planetary body in which all internal layers experience the same rotational variations m_i . In the case of icy satellites, this scenario is applicable to cases in which a subsurface ocean is not present in the interior.

6.3.4. LIOUVILLE EQUATIONS IN THE OCEANLESS CASE

In the possible scenario that the interior of an icy satellite would not harbor an ocean, the rotational variations at the surface can be studied from the solutions of the linearized equation given by Equations 6.7 to 6.9 with the inertia increments given by Equations 6.48 to 6.53. In that case, the set of linearized Liouville equations would become

$$\frac{1}{n(C-B)} \left[A + (C-A) \frac{k_2(t)}{k_f} \right] * \dot{m}_x + \left[1 - \frac{k_2(t)}{k_f} \right] * m_y = \phi_y(t), \quad (6.54)$$

$$\frac{1}{n(C-A)} \left[B + (C-B) \frac{k_2(t)}{k_f} \right] * \dot{m}_y - \left[1 - \frac{k_2(t)}{k_f} \right] * m_x = -\phi_x(t), \quad (6.55)$$

$$\frac{1}{C} \left[C + \frac{4}{9}(B-A) \frac{k_2(t)}{k_f} \right] * \dot{m}_z - e n \frac{B-A}{C} \frac{k_2(t)}{k_f} * \sin(nt) = \dot{\phi}_z(t), \quad (6.56)$$

where the secular Love number k_f is defined by one of the expressions given by Equation 6.47 and the excitation functions ϕ_x , ϕ_y and ϕ_z are defined by

$$\phi_x(t) = \frac{1}{n^2(C-A)} \left(n^2 c_{xz}^L + n \dot{c}_{yz}^L + n h_x + \dot{h}_y - \Gamma_y \right), \quad (6.57)$$

$$\phi_y(t) = \frac{1}{n^2(C-B)} \left(n^2 c_{yz}^L - n \dot{c}_{xz}^L + n h_y - \dot{h}_x + \Gamma_x \right), \quad (6.58)$$

$$\phi_z(t) = \frac{1}{nC} \left(-n c_{zz}^L - h_z + \int_0^t \Gamma_z dt' \right). \quad (6.59)$$

As can be seen from Equations 6.54 to 6.56, the viscoelastic description of the linearized Liouville equations contains several time-convolution operations that complicate the structure of the equations in the time domain. It is therefore convenient to transform the equations to the frequency domain using either the Laplace or the Fourier transform. Here we opt for the use of the former, mainly because the Love numbers have

already been defined in the Laplace domain (see Chapter 3). The resulting expressions are shown below

$$\frac{s}{n(C-B)} \left[A + (C-A) \frac{\tilde{k}_2(s)}{k_f} \right] \tilde{m}_x + \left[1 - \frac{\tilde{k}_2(s)}{k_f} \right] \tilde{m}_y = \tilde{\phi}_y(s), \quad (6.60)$$

$$\frac{s}{n(C-A)} \left[B + (C-B) \frac{\tilde{k}_2(s)}{k_f} \right] \tilde{m}_y - \left[1 - \frac{\tilde{k}_2(s)}{k_f} \right] \tilde{m}_x = -\tilde{\phi}_x(s), \quad (6.61)$$

$$\frac{s}{C} \left[C + \frac{4}{9}(B-A) \frac{\tilde{k}_2(s)}{k_f} \right] \tilde{m}_z - e n \frac{B-A}{C} \frac{\tilde{k}_2(s)}{k_f} \frac{n}{n^2 + s^2} = s\tilde{\phi}_z(s), \quad (6.62)$$

In contrast to the case of a biaxial planetary body, the asymmetry in the equatorial components of the linearized Liouville equations does not allow to combine Equations 6.60 and 6.61 into a single complex expression, such as in [e.g. Sabadini and Vermeersen, 2004] for the case of Earth. As a result, the methodology applied in e.g. Sabadini and Vermeersen [2004] to find the rotational eigenmodes of a viscoelastic planetary body cannot be directly used for the case of a rotating triaxial icy satellite. Therefore, it is necessary to rewrite Equations 6.60 and 6.61 as a system of differential equations, i.e.

$$\tilde{\mathbf{R}}_{xy} \tilde{\mathbf{m}}_{xy} = \tilde{\boldsymbol{\phi}}_{xy}, \quad (6.63)$$

where $\tilde{\mathbf{m}}_{xy} = [\tilde{m}_x, \tilde{m}_y]^T$, $\tilde{\boldsymbol{\phi}}_{xy} = [\tilde{\phi}_x, \tilde{\phi}_y]^T$ and $\tilde{\mathbf{R}}_{xy}$ is defined as

$$\tilde{\mathbf{R}}_{xy} = \begin{pmatrix} 1 - \frac{\tilde{k}_2(s)}{k_f} & -\frac{s}{n(C-A)} \left[B + (C-B) \frac{\tilde{k}_2(s)}{k_f} \right] \\ \frac{s}{n(C-B)} \left[A + (C-A) \frac{\tilde{k}_2(s)}{k_f} \right] & 1 - \frac{\tilde{k}_2(s)}{k_f} \end{pmatrix}. \quad (6.64)$$

The rotational eigenmodes are then given by the values of s for which the determinant of the matrix $\tilde{\mathbf{R}}_{xy}$ is equal to zero; i.e the solutions of:

$$\left(1 - \frac{\tilde{k}_2(s)}{k_f} \right)^2 + \frac{s^2}{\sigma_r^2} \left(1 + \frac{C-B}{B} \frac{\tilde{k}_2(s)}{k_f} \right) \left(1 + \frac{C-A}{A} \frac{\tilde{k}_2(s)}{k_f} \right) = 0, \quad (6.65)$$

with σ_r being the frequency of the free Eulerian precession given by Equation 6.13.

Through the use of an algebraic software package such as MAPLE, the polynomial resulting from the expansion of the determinant given by Equation 6.65 after substitution of the definition of the viscoelastic tidal Love number $\tilde{k}_2(s)$ (Equation 3.86) can be conveniently rearranged as

$$\frac{K_r s^2 \prod_{j=1}^M (s - a_j) \prod_{j=1}^M (s - b_j)}{\sigma_r^2 \prod_{j=1}^M (s - s_j)^2} = 0, \quad (6.66)$$

where the a_j 's and b_j 's are the complex rotational eigenmodes associated with every relaxation mode M (in most cases b_j is the complex conjugate of a_j). Moreover, K_r is a constant defined by

$$K_r = 1 + \left(\frac{C^2}{AB} - \frac{\sigma_r^2}{n^2} - 1 \right) \frac{k_e}{k_f} + \frac{\sigma_r^2}{n^2} \left(\frac{k_e}{k_f} \right)^2, \quad (6.67)$$

Table 6.1: Reference 4-layer model of Europa's interior without a subsurface ocean.

Layer	Outer Radius [km]	Density [kg m ⁻³]	Rigidity [GPa]	Viscosity [Pa s]
Metallic Core	600	5409.6	0	0
Silicate Mantle	1432	3481.3	65.0	1.0 × 10 ¹⁹
Ductile Ice-I Layer	1557	937.0	3.5	1.0 × 10 ¹⁴
Ice-I Crust	1562	937.0	3.5	1.0 × 10 ²¹

with k_e being the elastic tidal Love number defined by Equation 3.87.

Using the reduced expression for the determinant given by Equation 6.66, the inverse of the rotation matrix $\tilde{\mathbf{R}}_{xy}$ defined by Equation 6.64 (recall that $\tilde{\mathbf{m}}_{xy} = \tilde{\mathbf{R}}_{xy}^{-1} \tilde{\boldsymbol{\phi}}_{xy}$) can then be written as

$$\tilde{\mathbf{R}}_{xy}^{-1} = \frac{\sigma_r^2}{K_r s^2} \frac{\prod_{j=1}^M (s - s_j)^2}{\prod_{j=1}^M (s - a_j) \prod_{j=1}^M (s - b_j)} \times \left(\begin{array}{cc} 1 - \frac{\tilde{k}_2(s)}{k_f} & \frac{s}{n(C-A)} \left[B + (C-B) \frac{\tilde{k}_2(s)}{k_f} \right] \\ -\frac{s}{n(C-B)} \left[A + (C-A) \frac{\tilde{k}_2(s)}{k_f} \right] & 1 - \frac{\tilde{k}_2(s)}{k_f} \end{array} \right), \quad (6.68)$$

where every element (i, k) of the inverse rotation matrix $\tilde{\mathbf{R}}_{xy}^{-1}$ can, alternatively, be expressed as a partial fraction expansion with the aid of MAPLE, i.e.

$$\tilde{\mathbf{R}}_{xy}^{-1}(i, k) = \frac{A_{0,ik}}{s} + \frac{B_{0,ik}}{s} + \sum_{j=1}^M \left(\frac{A_{j,ik}}{s - a_j} \right) + \sum_{j=1}^M \left(\frac{B_{j,ik}}{s - b_j} \right), \quad (6.69)$$

where $A_{0,ik}$ and $B_{0,ik}$ give the strength of the secular term. In a similar way, the residues $A_{j,ik}$ and $B_{j,ik}$ give the strength of the rotational modes a_j and b_j , respectively. The strength of the rotational modes is important to analyze which relaxation modes from the response contribute the most to the rotational variations at the surface.

APPLICATION TO AN OCEANLESS EUROPA

Equation 6.65 can be used to determine the rotational eigenmodes of an oceanless interior model of Europa. Based on the description and constraints provided in Chapter 2, such a model can be defined by the parameters depicted in Table 6.1, where the numerical values of the rheological parameters have been chosen to match the ones that define the reference interior model shown in Table 2.8. The corresponding tidal response at the surface (i.e. inverse relaxation times and Love numbers) is then determined through application of the conventional normal mode methodology (described in some detail in Section 3.2) to the defined oceanless interior model. Thereafter, the expression for the Love number $\tilde{k}_2(s)$ is substituted into Equation 6.65, thereby leading to the rotational eigenmodes $s = a_j$ and $s = b_j$, as shown in Equation 6.66. Both the tidal response (from a normal mode perspective) and the rotational eigenmodes are listed in Table 6.2.

As can be observed from the structure of the response presented in Table 6.2, the absence of a subsurface ocean leads to the appearance of an additional pair of weak and fast-relaxing transient modes in the response (T_3 and T_4). These modes are triggered at the mantle-ice interface because both the mantle and the lower part of the ice-I shell, which are in direct contact due to the absence of an internal ocean, are rheologically characterized by different values for the Maxwell time. In addition, the pair of transient modes triggered at the viscosity contrast within the ice-I shell (i.e. T_1 and T_2) are characterized by significantly larger relaxation times than in the case of a similar interior model but with a subsurface ocean (see e.g. Table 5.1). Therefore, these modes will not contribute to the tidal response at diurnal frequency, despite their modal strength. Furthermore, like in the case of the response of models with a subsurface ocean, the strongest mode in the response is the buoyancy mode M_0 triggered at the top of the mantle.

Regarding the rotational response, it can be observed from Table 6.2 that the vast majority of relaxation modes are associated with a pair of complex-valued rotational eigenmodes, in which the eigenmodes b_j are the complex conjugates of the eigenmodes a_j . The only exceptions are the weak transient modes T_3 and T_4 , which are characterized by a pair of real-valued rotational eigenmodes with nearly similar inverse relaxation times. From the perspective of rotational dynamics, real-valued eigenmodes as well as the real part of complex-valued rotational eigenmodes represent the inverse relaxation time of the modes. The imaginary part of complex-valued rotational eigenmodes, on the other hand, gives the frequency of the accompanying wobble. To analyze which relaxation modes are characterized by potentially large wobbles, the rotational response of the reference oceanless model of Europa needs first to be expressed in the form $\tilde{\mathbf{m}}_{xy} = \tilde{\mathbf{R}}_{xy}^{-1} \tilde{\boldsymbol{\phi}}_{xy}$ (with the aid of MAPLE) in order to determine the residues $A_{j,ik}$ and $B_{j,ik}$ that denote the strength of the rotational eigenmodes (see Equation 6.69). Inspection of the resulting values for the residues shows that the only modes with a significant strength are the transient mode T_1 and especially the mantle mode M_0 . This result is not unexpected as both T_1 and M_0 are the strongest modes in the tidal response as well (see Table 6.2).

Based on the numerical results presented in the last column of Table 6.2, it can be observed that the strong M_0 -mode is the only relaxation mode in the tidal response for

Table 6.2: Tidal and rotational response of the reference oceanless model of Europa's interior. The elastic part of the response has not been included. Each of the transient modes T_3 and T_4 are characterized by two almost equal real-valued rotational eigenmodes.

Mode	\mathbf{s}_j [kyr ⁻¹]	$\mathbf{k}_{2,j}$ [-]	\mathbf{a}_j (\mathbf{b}_j) [kyr ⁻¹]
C_0	-4.11788×10^{-1}	4.52107×10^{-2}	$-6.00383 \times 10^{-1} \pm 1.14827 \times 10^{-3} \mathbf{i}$
M_0	-3.46177×10^0	7.40571×10^{-1}	$-3.16956 \times 10^1 \pm 6.21347 \times 10^2 \mathbf{i}$
S_0	-1.08538×10^{-1}	1.01609×10^{-2}	$-1.34769 \times 10^{-1} \pm 1.04496 \times 10^{-4} \mathbf{i}$
T_1	-1.36589×10^2	2.11614×10^{-1}	$-1.09164 \times 10^2 \pm 4.68216 \times 10^0 \mathbf{i}$
T_2	-6.51516×10^3	1.65573×10^{-2}	$-6.51431 \times 10^3 \pm 1.02049 \times 10^1 \mathbf{i}$
T_3	-1.08181×10^6	1.07324×10^{-5}	$-1.08181 \times 10^{6(2\times)}$
T_4	-1.10062×10^6	6.62139×10^{-5}	$-1.10062 \times 10^{6(2\times)}$

which the imaginary part of its rotational eigenmode a_j (or b_j) is larger than the corresponding real part. This is consistent with studies on the rotational response of terrestrial planets [see e.g. Sabadini and Vermeersen, 2004]. From a physical point of view, the relatively large imaginary part of this eigenmode defines the frequency of the Chandler wobble of the analyzed oceanless model of Europa's interior. According to the numerical values listed in Table 6.2, the frequency of the Chandler wobble is equal to 621.347 kyr^{-1} , implying that the period of the wobble is approximately 10.1 years. This is slightly longer than the ~ 9.7 years period corresponding to the free Eulerian precession ($\sigma_r = 648.059 \text{ kyr}^{-1}$), with the difference being caused by the fact that Europa's interior does not behave as a rigid body due to its viscoelastic properties.

All the remaining wobbles, even the one associated with the strong T_1 -mode, are characterized by longer periods (> 1000 years) that exceed the timescale of the corresponding rotational relaxation times. In any case, the presence of wobbles as part of the actual rotational behavior of Europa would depend on geophysical excitations processes that are able to prevent the decay of the wobble amplitude as a result of viscoelastic relaxation in Europa's interior.

6.4. ROLE OF THE SUBSURFACE OCEAN: DIFFERENTIAL ROTATION

As hinted in Section 6.2, the presence of internal fluid layers such as a subsurface ocean or a fluid metallic core requires the introduction of relative motion into the description of the rotational dynamics in order to determine the rotational variations at the surface of an icy satellite. Based on previous studies on the rotational motion in Earth's fluid core [e.g. Hough, 1895, Poincaré, 1910, Sasao et al., 1980, Mathews et al., 1991], the relative rotational motion of fluid layers in the interior of icy satellites is considered to satisfy the conditions of a Poincaré flow. This flow is characterized by consisting of a dominant uniform vorticity flow and a residual flow needed to make the flow tangential to the boundaries [e.g. Sasao et al., 1980, Mathews et al., 1991]. Mathematically, the relative velocity field \mathbf{v}^f of a rotating fluid layer can then be expressed as [e.g. Sasao et al., 1980]

$$\mathbf{v}^f = \Delta\boldsymbol{\omega}^f \times \mathbf{r} + \mathbf{v}^{ir}, \quad (6.70)$$

where $\Delta\boldsymbol{\omega}^f$ is the differential angular velocity between the fluid layer and the ice-I shell (i.e. $\Delta\boldsymbol{\omega}^f = \boldsymbol{\omega}^f - \boldsymbol{\omega}$, with $\boldsymbol{\omega}^f$ being the angular velocity of the fluid layer), \mathbf{r} is the position vector and \mathbf{v}^{ir} is the residual velocity field. The latter consists of terms of the order $\epsilon r |\Delta\boldsymbol{\omega}^f|$ (with ϵ being the flattening of the solid boundaries around the fluid cavity) and the contribution from deformational motions, which are characterized to be even smaller [Sasao et al., 1980, Mathews et al., 1991]. As such, the residual term \mathbf{v}^{ir} is usually neglected from the definition of the fluid flow as it is much smaller than the term $\Delta\boldsymbol{\omega}^f \times \mathbf{r}$ [Sasao et al., 1980, Mathews et al., 1991]. However, this assumption may not apply if the flattenings of the two solid boundaries of the fluid layer are very different [e.g. Dehant et al., 1993].

In addition, the presence of a subsurface ocean in the interior of icy satellites is

thought to decouple the rotational motion of the upper ice-I shell from the motion of material layers located deeper in the interior (e.g. mantle and core) because mechanical quantities cannot be propagated through fluid layers (see Section 3.3). Although mechanically decoupled by the presence of an ocean, the rotational motion of the ice-I shell and the deep interior cannot be fully decoupled due to the effect of gravitational, pressure, electromagnetic and viscous torques acting on the layers under consideration [Wahr, 1981, Mathews et al., 1991, Szeto and Xu, 1997, Dehant and Mathews, 2007]. In order to take into account differential rotation of the deeper layers such as the silicate mantle relative to the ice-I shell, their corresponding angular velocity ($\boldsymbol{\omega}^m$ for e.g. the mantle) is considered to deviate slightly from the one of the ice-I shell by the differential angular velocity $\Delta\boldsymbol{\omega}^m$ (i.e. $\boldsymbol{\omega}^m = \boldsymbol{\omega} + \Delta\boldsymbol{\omega}^m$), such that the relative velocity field of the mantle (\mathbf{v}^m) becomes

$$\mathbf{v}^m = \Delta\boldsymbol{\omega}^m \times \mathbf{r}. \quad (6.71)$$

As a next step, the relative angular momentum $\mathbf{h}(t)$ due to differential rotation of internal layers is determined through the use of Equation 6.3 and the provided definitions for the relative velocity of internal layers (Equations 6.70 and 6.71). Since the introduced velocity fields are either completely defined or dominated by a rotational term, the contribution from relative motion of an internal layer l to the relative angular momentum can be expressed as [e.g. Sasao et al., 1980, Dehant et al., 1993, Van Hoolst and Dehant, 2002, Dehant and Mathews, 2007, Van Hoolst, 2007]

$$\mathbf{h}^l(t) = \mathbf{I}^l \Delta\boldsymbol{\omega}^l, \quad (6.72)$$

where \mathbf{I}^l and $\Delta\boldsymbol{\omega}^l$ are the inertia tensor and differential angular velocity of an internal layer l , respectively. Similar to the case of the entire planetary body, the inertia tensor \mathbf{I}^l can be defined as

$$\mathbf{I}^l = \begin{pmatrix} A^l + c_{xx}^l & c_{xy}^l & c_{xz}^l \\ c_{xy}^l & B^l + c_{yy}^l & c_{yz}^l \\ c_{xz}^l & c_{yz}^l & C^l + c_{zz}^l \end{pmatrix}, \quad (6.73)$$

where A^l , B^l and C^l are the principal moments of inertia of the layer, and the c_{ij}^l 's are the small inertia increments that result from mass redistribution within the layer.

Similarly, the differential angular velocity $\Delta\boldsymbol{\omega}^l$ can be written in terms of the small rotational variations m_x^l , m_y^l and m_z^l , i.e.

$$\Delta\boldsymbol{\omega}^l = \boldsymbol{\omega}^l - \boldsymbol{\omega} = n \begin{pmatrix} m_x^l \\ m_y^l \\ m_z^l \end{pmatrix}. \quad (6.74)$$

Then, taking into account the internal structure of icy satellites, the relative angular momentum $\mathbf{h}(t)$ can be written as

$$\mathbf{h}(t) = \mathbf{I}^w \Delta\boldsymbol{\omega}^w + \mathbf{I}^m \Delta\boldsymbol{\omega}^m + \mathbf{I}^c \Delta\boldsymbol{\omega}^c, \quad (6.75)$$

where the superscripts w , m and c refer to the subsurface ocean, the silicate mantle (and HP-ice mantle in the case of e.g. Ganymede or Titan) and the core, respectively. This expression can be linearized by using the expressions given by Equations 6.73 and 6.74 for the inertia tensor and differential angular velocity of each involved layer. After neglecting all second order terms (or higher) in the small rotational variations and inertia increments, the relative angular momentum $\mathbf{h}(t)$ can be written as

$$\mathbf{h}(t) = n \left\{ \begin{pmatrix} A^w m_x^w \\ B^w m_y^w \\ C^w m_z^w \end{pmatrix} + \begin{pmatrix} A^m m_x^m \\ B^m m_y^m \\ C^m m_z^m \end{pmatrix} + \begin{pmatrix} A^c m_x^c \\ B^c m_y^c \\ C^c m_z^c \end{pmatrix} \right\}. \quad (6.76)$$

Including the expressions for the relative angular momentum $\mathbf{h}(t)$, the linearized Liouville equations, which are given by Equations 6.7 to 6.9, can be written in the following way:

$$\begin{aligned} \Gamma_x = nA\dot{m}_x + n^2(C-B)m_y + n(A^w\dot{m}_x^w + A^m\dot{m}_x^m + A^c\dot{m}_x^c) \\ - n^2(B^w m_y^w + B^m m_y^m + B^c m_y^c) - n^2 c_{yz} + n\dot{c}_{xz}, \end{aligned} \quad (6.77)$$

$$\begin{aligned} \Gamma_y = nB\dot{m}_y - n^2(C-A)m_x + n(B^w\dot{m}_y^w + B^m\dot{m}_y^m + B^c\dot{m}_y^c) \\ + n^2(A^w m_x^w + A^m m_x^m + A^c m_x^c) + n^2 c_{xz} + n\dot{c}_{yz}, \end{aligned} \quad (6.78)$$

$$\Gamma_z = nC\dot{m}_z + n(C^w\dot{m}_z^w + C^m\dot{m}_z^m + C^c\dot{m}_z^c) + n\dot{c}_{zz}. \quad (6.79)$$

6.4.1. THE COUPLED LIOUVILLE EQUATIONS

As a consequence of the introduction of differential rotation into the description of the rotational dynamics, the set of linearized Liouville equations (Equations 6.77 to 6.79) becomes an underdetermined system of equations. Hence, in order to solve for the additional unknowns in the equations (i.e. the differential rotational variations m_j^l), it is necessary to consider the evolution of the angular momentum of each of the layers performing differential rotation by defining separate Liouville equations for each of these layers. In the case of Europa, the required system of equations to study the rotational variations consists of four sets of equations: one describing the evolution of angular momentum of the whole satellite (\mathbf{H}) and the remaining three describing the change of rate of the angular momentum of the subsurface ocean (\mathbf{H}^w), silicate (and HP-ice) mantle (\mathbf{H}^m) and fluid core (\mathbf{H}^c), respectively. In the previously defined surface-fixed reference frame, this system of equations can be expressed as [e.g. Mathews et al., 1991, Dehant et al., 1993, Greff-Lefftz et al., 2000, Dumberry, 2009]:

$$\frac{d\mathbf{H}}{dt} + \boldsymbol{\omega} \times \mathbf{H} = \boldsymbol{\Gamma}, \quad (6.80)$$

$$\frac{d\mathbf{H}^w}{dt} + \boldsymbol{\omega} \times \mathbf{H}^w = \boldsymbol{\Gamma}^w, \quad (6.81)$$

$$\frac{d\mathbf{H}^m}{dt} + \boldsymbol{\omega} \times \mathbf{H}^m = \boldsymbol{\Gamma}^m, \quad (6.82)$$

$$\frac{d\mathbf{H}^c}{dt} + \boldsymbol{\omega} \times \mathbf{H}^c = \boldsymbol{\Gamma}^c, \quad (6.83)$$

where $\mathbf{\Gamma}$ is the torque acting on the entire satellite and $\mathbf{\Gamma}^w$, $\mathbf{\Gamma}^m$ and $\mathbf{\Gamma}^c$ are the torques acting on the ocean, mantle and core, respectively. Unlike the torque on the entire satellite, the torques acting on separate layers do not only take into account the effect of external torques but also the contribution of internal coupling torques between layers [e.g. Mathews et al., 1991, Dehant et al., 1993, Szeto and Xu, 1997, Greff-Lefftz et al., 2000, Dehant and Mathews, 2007, Dumberry, 2009].

Alternatively, a Liouville equation describing the evolution of the angular momentum of the ice-I shell (\mathbf{H}^s) can be used instead of the one associated with the angular momentum of the entire satellite (i.e. Equation 6.80). This approach is commonly applied to the study of the rotational variations at the surface of icy satellites [e.g. Karatekin et al., 2008, Van Hoolst et al., 2008, 2009, Baland and Van Hoolst, 2010, Rambaux et al., 2011, Baland et al., 2012], mainly because the outer ice-I shell is relatively thin when compared to the radius of the satellite and hence it can be regarded as a thin shell floating on a global ocean. The relevant Liouville equation for the shell is defined by

$$\frac{d\mathbf{H}^s}{dt} + \boldsymbol{\omega} \times \mathbf{H}^s = \mathbf{\Gamma}^s, \quad (6.84)$$

where $\mathbf{\Gamma}^s$ denotes the total torque acting on the shell due to both external forcing and internal coupling.

The Liouville equations associated with the rotation of internal fluid layers, i.e. Equations 6.81 and 6.83, can be further simplified under the assumption that the flow within a layer can be described by a uniform vorticity Poincaré flow (see Equation 6.70). In that case, the angular momentum equations for the subsurface ocean and fluid core can be written as (see Sasao et al. [1980] and Mathews et al. [1991] for a detailed discussion)

$$\frac{d\mathbf{H}^w}{dt} - \Delta\boldsymbol{\omega}^w \times \mathbf{H}^w = 0, \quad (6.85)$$

$$\frac{d\mathbf{H}^c}{dt} - \Delta\boldsymbol{\omega}^c \times \mathbf{H}^c = 0, \quad (6.86)$$

such that the set of the vectorial Liouville equations relevant for the study of the rotational variations experienced by icy satellites is given by Equations 6.84, 6.85, 6.82 and 6.86, i.e.

$$\begin{aligned} \frac{d\mathbf{H}^s}{dt} + \boldsymbol{\omega} \times \mathbf{H}^s &= \mathbf{\Gamma}^s, \\ \frac{d\mathbf{H}^w}{dt} - \Delta\boldsymbol{\omega}^w \times \mathbf{H}^w &= 0, \\ \frac{d\mathbf{H}^m}{dt} + \boldsymbol{\omega} \times \mathbf{H}^m &= \mathbf{\Gamma}^m, \\ \frac{d\mathbf{H}^c}{dt} - \Delta\boldsymbol{\omega}^c \times \mathbf{H}^c &= 0. \end{aligned}$$

In a similar way as for the Liouville equation for the entire satellite (Equation 6.1), the coupled set of Liouville equations shown above can be linearized because rotational variations, differential rotational variations and inertia increments are expected to remain small. As a first step, explicit expressions for the angular momenta \mathbf{H}^s , \mathbf{H}^w , \mathbf{H}^m

and \mathbf{H}^c are derived using the definition of the inertia tensor (Equation 6.73) and angular velocity (Equation 6.74) of an internal layer. Then, the Cartesian components of \mathbf{H}^s , \mathbf{H}^w , \mathbf{H}^m and \mathbf{H}^c are given by

$$\mathbf{H}^s = \mathbf{I}^s \boldsymbol{\omega} = n \begin{pmatrix} A^s m_x + c_{xz}^s \\ B^s m_y + c_{yz}^s \\ C^s + C^s m_z + c_{zz}^s \end{pmatrix}, \quad (6.87)$$

$$\mathbf{H}^w = \mathbf{I}^w \boldsymbol{\omega} + \mathbf{h}^w = n \begin{pmatrix} A^w (m_x + m_x^w) + c_{xz}^w \\ B^w (m_y + m_y^w) + c_{yz}^w \\ C^w (1 + m_z + m_z^w) + c_{zz}^w \end{pmatrix}, \quad (6.88)$$

$$\mathbf{H}^m = \mathbf{I}^m \boldsymbol{\omega} + \mathbf{h}^m = n \begin{pmatrix} A^m (m_x + m_x^m) + c_{xz}^m \\ B^m (m_y + m_y^m) + c_{yz}^m \\ C^m (1 + m_z + m_z^m) + c_{zz}^m \end{pmatrix}, \quad (6.89)$$

$$\mathbf{H}^c = \mathbf{I}^c \boldsymbol{\omega} + \mathbf{h}^c = n \begin{pmatrix} A^c (m_x + m_x^c) + c_{xz}^c \\ B^c (m_y + m_y^c) + c_{yz}^c \\ C^c (1 + m_z + m_z^c) + c_{zz}^c \end{pmatrix}. \quad (6.90)$$

Substitution of Equations 6.87 to 6.90 into the set of Liouville equations given by Equations 6.84, 6.85, 6.82 and 6.86 leads then to the following linearized expressions for the coupled Liouville equations:

Ice-I shell

$$nA^s \dot{m}_x + n^2 (C^s - B^s) m_y - n^2 c_{yz}^s + n \dot{c}_{xz}^s = \Gamma_x^s, \quad (6.91)$$

$$nB^s \dot{m}_y - n^2 (C^s - A^s) m_x + n^2 c_{xz}^s + n \dot{c}_{yz}^s = \Gamma_y^s, \quad (6.92)$$

$$nC^s \dot{m}_z + n \dot{c}_{zz}^s = \Gamma_z^s. \quad (6.93)$$

Subsurface ocean

$$nA^w (\dot{m}_x + \dot{m}_x^w) - n^2 C^w m_y^w + n \dot{c}_{xz}^w = 0, \quad (6.94)$$

$$nB^w (\dot{m}_y + \dot{m}_y^w) + n^2 C^w m_x^w + n \dot{c}_{yz}^w = 0, \quad (6.95)$$

$$nC^w (\dot{m}_z + \dot{m}_z^w) + n \dot{c}_{zz}^w = 0. \quad (6.96)$$

Silicate mantle (includes HP-ice mantle and solid core, if present)

$$nA^m (\dot{m}_x + \dot{m}_x^m) + n^2 (C^m - B^m) m_y - n^2 B^m m_y^m - n^2 c_{yz}^m + n \dot{c}_{xz}^m = \Gamma_x^m, \quad (6.97)$$

$$nB^m (\dot{m}_y + \dot{m}_y^m) - n^2 (C^m - A^m) m_x + n^2 A^m m_x^m + n^2 c_{xz}^m + n \dot{c}_{yz}^m = \Gamma_y^m, \quad (6.98)$$

$$nC^m (\dot{m}_z + \dot{m}_z^m) + n \dot{c}_{zz}^m = \Gamma_z^m. \quad (6.99)$$

Fluid core (if present)

$$nA^c (\dot{m}_x + \dot{m}_x^c) - n^2 C^c m_y^c + n \dot{c}_{xz}^c = 0, \quad (6.100)$$

$$nB^c \left(\dot{m}_y + \dot{m}_y^c \right) + n^2 C^c m_x^c + n \dot{c}_{yz}^c = 0, \quad (6.101)$$

$$nC^c \left(\dot{m}_z + \dot{m}_z^c \right) + n \dot{c}_{zz}^c = 0. \quad (6.102)$$

The complete set given by Equations 6.91 to 6.102 provides the required framework to study the rotational variations experienced by icy satellites with a global internal ocean as a result of external torques and/or geophysical loading, where the Liouville equations associated with the subsurface ocean and silicate mantle (i.e. Equations 6.94 to 6.99) are equivalent to the ones used to study the rotational dynamics of a triaxial Mars with a fluid outer core and a solid inner core [Van Hoolst and Dehant, 2002, Van Hoolst, 2007]. Moreover, the same equations would reduce to the well-known complex expressions used to describe the rotational dynamics of the Earth's fluid outer core after assuming that the equatorial moments of inertia are equal to each other [e.g. Mathews et al., 1991, Dehant et al., 1993, Greff-Lefftz et al., 2000].

As in the case of the Liouville equations for an oceanless icy satellite (see Section 6.3.4), the contribution of deformation enters the description of the rotational dynamics through the inertia increments c_{ij}^s , c_{ij}^w , c_{ij}^m and c_{ij}^c . These terms, in contrast to the general case, are associated with the deformation of a material layer; thus requiring the definition of Love numbers at internal boundaries (see Section 3.6). The definition of inertia increments will be treated in Section 6.4.2. In addition, although the set of linearized Liouville equations given by Equations 6.91 to 6.102 seems to be uncoupled in terms of the rotational variations, they are coupled as a consequence of internal coupling torques between layers (i.e. gravitational, pressure, electromagnetic and viscous torques).

Full derivation of general expressions for the inertia increments and coupling torques required by the system of Equations 6.91 to 6.102 is beyond the scope of this thesis. However, a detailed derivation of inertia increments and internal coupling torques for the specific case of the forced longitudinal librations of Europa's shell will be provided in Sections 7.3.3 and 7.3.4.

6.4.2. INERTIA INCREMENTS

The interior of a synchronously rotating icy satellite in hydrostatic equilibrium is known to accommodate to the shape of a triaxial ellipsoid with principal axes $a > b > c$, as dictated by the acting rotational and tidal forces [Murray and Dermott, 1999]. The ellipsoidal distortion of the satellite's internal mass distribution leads to a permanent quadrupole gravitational field, which is commonly described by the principal moments of inertia A , B and C . Furthermore, the interior of the satellite experiences time-dependent deformations as a result of rotational variations and the acting diurnal tidal field, which lead to the inertia increments c_{ij} . In contrast to the case of the entire satellite, for which the elements of the inertia tensor can be derived from MacCullagh's equation (see Section 6.3.3), the principal moments of inertia (A^l , B^l and C^l) and the inertia increments (c_{ij}^l) of a layer due to rotational and tidal deformation need to be derived from their general definition, which is given by

$$A^l + c_{xx}^l = \iiint \rho(\mathbf{r}) (y^2 + z^2) dV^l, \quad (6.103)$$

$$B^l + c_{yy}^l = \iiint \rho(\mathbf{r}) (x^2 + z^2) dV^l, \quad (6.104)$$

$$C^l + c_{zz}^l = \iiint \rho(\mathbf{r}) (x^2 + y^2) dV^l, \quad (6.105)$$

$$c_{xy}^l = - \iiint \rho(\mathbf{r}) xy dV^l, \quad (6.106)$$

$$c_{xz}^l = - \iiint \rho(\mathbf{r}) xz dV^l, \quad (6.107)$$

$$c_{yz}^l = - \iiint \rho(\mathbf{r}) yz dV^l, \quad (6.108)$$

where x , y and z refer to the Cartesian coordinates of an infinitesimal volume dV^l in the deformed state, and $\rho(\mathbf{r})$ is the density at position $\mathbf{r} = x \hat{\mathbf{i}} + y \hat{\mathbf{j}} + z \hat{\mathbf{k}}$ inside the satellite. In spherical coordinates, Equations 6.103 to 6.108 can be written as

$$A^l + c_{xx}^l = \int_{r_o^b}^{r_o^t} \int_0^\pi \int_0^{2\pi} \left(\rho(r_o) r^4 \frac{\partial r}{\partial r_o} (\sin^3 \theta \sin^2 \phi + \sin \theta \cos^2 \theta) \right) dr_o d\theta d\phi, \quad (6.109)$$

$$B^l + c_{yy}^l = \int_{r_o^b}^{r_o^t} \int_0^\pi \int_0^{2\pi} \left(\rho(r_o) r^4 \frac{\partial r}{\partial r_o} (\sin^3 \theta \cos^2 \phi + \sin \theta \cos^2 \theta) \right) dr_o d\theta d\phi, \quad (6.110)$$

$$C^l + c_{zz}^l = \int_{r_o^b}^{r_o^t} \int_0^\pi \int_0^{2\pi} \left(\rho(r_o) r^4 \frac{\partial r}{\partial r_o} \sin^3 \theta \right) dr_o d\theta d\phi, \quad (6.111)$$

$$c_{xy}^l = - \int_{r_o^b}^{r_o^t} \int_0^\pi \int_0^{2\pi} \left(\rho(r_o) r^4 \frac{\partial r}{\partial r_o} \sin^3 \theta \sin \phi \cos \phi \right) dr_o d\theta d\phi, \quad (6.112)$$

$$c_{xz}^l = - \int_{r_o^b}^{r_o^t} \int_0^\pi \int_0^{2\pi} \left(\rho(r_o) r^4 \frac{\partial r}{\partial r_o} \sin^2 \theta \cos \theta \cos \phi \right) dr_o d\theta d\phi, \quad (6.113)$$

$$c_{yz}^l = - \int_{r_o^b}^{r_o^t} \int_0^\pi \int_0^{2\pi} \left(\rho(r_o) r^4 \frac{\partial r}{\partial r_o} \sin^2 \theta \cos \theta \sin \phi \right) dr_o d\theta d\phi, \quad (6.114)$$

where r and r_o are the radial distances in the deformed and the undeformed state, respectively; θ is the co-latitude; ϕ is the longitude; and the superscripts b and t refer to the lower and upper boundary of a layer, respectively. Taking into account the definition of the radial component of the deformation (Equation 3.83), the radial distance in the deformed state (r) can be defined in terms of Love numbers as [Hinderer and Legros, 1989, Dehant et al., 1993, Mitrovica et al., 1994, Greff-Lefftz et al., 2000]

$$r = r_o + h_{2,f}(r_o) \frac{\bar{V}_2}{g_0} + h_2(r_o, t) * \frac{\Delta V_2(t)}{g_0} + h_2^o(r_o, t) * \frac{\delta V_2^o}{g_0} + h_2^m(r_o, t) * \frac{\delta V_2^m}{g_0}, \quad (6.115)$$

where the second term on the right hand side of the equation refers to hydrostatic triaxial shape of the satellite; the third term refers to the experienced radial deformation as a result of diurnal tides and variations in the rotation of the body; the fourth term refers to the radial deformation as a result of the differential rotation of the subsurface ocean;

and the fifth term refers to the radial deformation as a result of the differential rotation of the mantle. As introduced in Chapter 3, the potentials \bar{V}_2 and $\Delta V_2(t)$ in Equation 6.115 are defined at the surface, whereas the differential rotation potentials δV_2^o and δV_2^m are defined at the ocean-ice interface and mantle-ocean interface, respectively.

In Chapter 7, a simplified version of Equation 6.115 is substituted into the Equations 6.109 to 6.111 in order to derive explicit expressions for the required principal moments of inertia and inertia increments for the case of forced longitudinal librations.

7

LONGITUDINAL LIBRATION OF EUROPA

In this Chapter the theoretical discussion about the rotational dynamics of icy satellites, which has been addressed in Chapter 6, is applied to study the longitudinal librations of Europa as a result of the gravitational torque exerted by Jupiter on the triaxial figure of Europa. The main purpose of this study is to relate the amplitude of the longitudinal libration of Europa's ice shell to the geophysical parameters that characterize the internal structure of Europa, thereby focusing on the parameters that characterize the outermost water layers (subsurface ocean and ice-I shell).

The content of this Chapter has been entirely taken from the article *The forced libration of Europa's deformable shell and its dependence on interior parameters* [Jara-Orué and Vermeersen, 2014]. Hence, the content in this Chapter may contain some topics that have been discussed in earlier Chapters of this thesis. Furthermore, the notation and interior models used for the generation of results in this Chapter only apply to the discussion presented in this Chapter.

7.1. ABSTRACT

One of the most important goals of future missions to the Jovian moon Europa will be to unambiguously determine the presence of an internal ocean and to characterize physical properties of the putative subsurface ocean and the overlying ice shell. In addition to magnetic, altimetry and gravity measurements, observations of Europa's librations are expected to contribute to the realization of such an important goal. The longitudinal libration of Europa's shell in the presence of a subsurface ocean has been previously studied assuming that Europa's internal solid layers behave rigidly. However, at the frequency of the acting diurnal tides and external gravitational torques, the response of Europa's interior is not rigid but rather viscoelastic. In this paper, we develop a differential libration model that takes into account the effect of diurnal deformation on the forced

longitudinal libration of Europa's internal solid layers. We apply our libration model to a rather large range of possible interior models of Europa to investigate the dependence of the shell libration amplitude on the geophysical parameters that characterize the interior of Europa, in particular the shell. From all analyzed interior parameters, we find that the poorly constrained rigidity of the shell has the largest effect on the libration amplitude. This result suggests thus that future libration observations could be very useful to constrain the value of this parameter for Europa. However, we also notice that the effect of the viscosity of a dissipating ice sublayer at the bottom of the shell (if present) on the libration amplitude of the shell would not allow for an unambiguous determination of the shell rigidity. Furthermore, the dependence of the shell libration amplitude on the shell thickness and density is rigidity-dependent and weak in comparison to the dependence on the rigidity. As a result, libration observations would not be able to provide any information on the thickness and/or density of the shell without previous determination of the rigidity.

7.2. INTRODUCTION

Several different observations made by Voyager and Galileo strongly suggest the existence of a subsurface ocean below Europa's ice shell. Among these observations, the strongest case is made by Galileo's detection of an induced magnetic field, which requires the existence of an electrically conductive layer at shallow depth, most probably a salty ocean [Khurana et al., 1998, Kivelson et al., 2000]. Furthermore, imaging of Europa's surface has revealed the presence of arcuate features, commonly known as cycloids, which are thought to have formed due to the effect of diurnal tidal stresses. Since diurnal stresses are expected to become large enough to crack the ice only if a subsurface ocean is present, the existence of these unique features on Europa's surface provides strong geological evidence for the presence of the internal ocean [Hoppa et al., 1999b, Lee et al., 2005, Hurford et al., 2007, Rhoden et al., 2010]. In addition, the existence of a subsurface ocean is strongly supported by theoretical models dealing with the thermal state and evolution of Europa's interior [e.g. Ojakangas and Stevenson, 1989b, Hussmann et al., 2002, Tobie et al., 2003, Hussmann and Spohn, 2004].

Despite the compelling evidence, the presence of a subsurface ocean has not yet been unambiguously determined. If present, both the ocean and the overlying ice shell will need to be characterized in order to assess the habitability potential of Europa's ocean. In order to reach this goal, several mission objectives have been proposed, such as the characterization of the magnetic field in the vicinity of Europa, the measurement of radial displacements and gravity perturbations as a result of the acting diurnal tides, and the determination of the amplitude of forced longitudinal librations [Van Hoolst et al., 2008, Baland and Van Hoolst, 2010]. Although the fulfillment of any of these mission objectives has the potential to confirm the existence of a subsurface ocean on an individual basis, the characterization of the thickness of both the ocean and the overlying ice shell would require an observation strategy that combines all of these objectives (see e.g. [Grasset et al., 2013] for the aimed strategy for JUICE's characterization of Ganymede's ocean and ice shell).

In this paper, we focus on studying the relation between the amplitude of Europa's

forced longitudinal libration at orbital frequency and the geophysical parameters that characterize Europa's ocean and ice shell. The forced libration at orbital frequency is defined as a small periodic variation in the spin rate of Europa driven by the gravitational torque exerted by Jupiter on the triaxial figure of the satellite. Although forced librations occur at different frequencies, we only consider here the main libration at orbital frequency because a) only short-periodic librations depend on the internal structure of the satellite, and b) the libration at orbital frequency is around two orders of magnitude larger than other short-periodic librations [Rambaux et al., 2011, Van Hoolst et al., 2013].

Due to the presence of an internal ocean, Europa's outer shell and deep solid interior may perform differential librations which are coupled to each other mainly through gravitational and pressure torques [Baland and Van Hoolst, 2010]. Considering that internal solid layers are rigid, previous models of Europa's differential libration infer that the amplitude of the shell libration decreases exponentially with increasing ice thickness [Van Hoolst et al., 2008, Baland and Van Hoolst, 2010, Rambaux et al., 2011]. For example, Baland and Van Hoolst [2010] estimate that the amplitude of the shell libration would range between 500 m (for a 100 km thick shell) and 40,000 m (for a 5 km shell). This range of values for the libration amplitude is substantially larger than the ~ 133 m predicted for the libration amplitude of an entirely rigid Europa [Comstock and Bills, 2003, Van Hoolst et al., 2008, Rambaux et al., 2011]. However, Europa's internal solid layers, in particular the ice shell, are not expected to behave rigidly but rather elastically in response to the acting diurnal tides and the librations themselves [Goldreich and Mitchell, 2010]. Using a thin shell approach, in which the shell behaves elastically and all internal layers below the shell are assumed to be fluid, Goldreich and Mitchell [2010] reach the conclusion that elastic effects would considerably diminish the amplitude of the shell libration to ~ 400 m (independent of the shell thickness). However, due to their assumptions regarding the internal configuration of Europa, the libration model of [Goldreich and Mitchell, 2010] neglects the effect of internal coupling between the shell and the solid interior below the ocean. A current differential libration model of Europa that treats both the ice shell and the deep interior as elastic layers is extensively described in Van Hoolst et al. [2013].

Treatment of the ice shell and silicate mantle as elastic material layers, or even as viscoelastic layers, has been common in studies concerning Europa's diurnal tidal response (i.e. Love numbers) and the corresponding deformations and stresses [e.g. Greenberg et al., 1998, Moore and Schubert, 2000, Wu et al., 2001, Tobie et al., 2005, Harada and Kunita, 2006, Wahr et al., 2009, Rhoden et al., 2010, Jara-Oru e and Vermeersen, 2011]. Here, we apply the viscoelastic Love number framework to include viscoelastic effects into the libration dynamics of Europa's shell and mantle. The importance of viscoelasticity on the response of a layer to tidal and libration forcing depends on the ratio Δ of the inverse Maxwell time τ_M of the layer ($\tau_M = \eta/\mu$, where η is the layer's viscosity and μ is its rigidity) to the orbital frequency or mean motion n ($n = 2.05 \cdot 10^{-5}$ rad/s for Europa), i.e. on the ratio $\Delta = \mu/(\eta n)$ [Sotin et al., 2009, Wahr et al., 2009, Jara-Oru e and Vermeersen, 2011]. If the Maxwell time of a layer is much larger than the orbital period (i.e. $\Delta \ll 1$), the material layer will behave effectively elastic in response to the applied tidal forcing. On the other hand, if the Maxwell time is much smaller than the orbital period (i.e. $\Delta \gg 1$), the layer will behave as a fluid. Viscoelastic effects are largest around $\Delta = 1$, which is a ratio expected for the bottom part of a convecting ice shell [e.g. Tobie et al., 2003, Sotin

et al., 2009].

The plan of this paper is as follows. In Section 7.3 we provide a detailed description of our developed libration model. We start in Section 7.3.1 by defining the general equations governing the libration dynamics of a differentiated interior representative for Europa's internal structure in the presence of an ocean. Thereafter, in Sections 7.3.2 to 7.3.5, we introduce viscoelastic deformation to the rotational dynamics by defining analytical expressions for the relevant inertia increments, internal coupling torques and acting external torques. Our complete libration model, which is summarized in Section 7.3.6, is then applied in Sections 7.4 and 7.5 to a range of plausible interior models of Europa in order to study the dependence of the amplitude of the shell libration on geophysical parameters such as the shell thickness, shell density, ocean density, ice rigidity and ice viscosity. Finally, in Section 7.6, we discuss our results and compare them with the findings of previous libration models, mainly the ones of Van Hoolst et al. [2013].

7.3. ROTATIONAL DYNAMICS

7.3.1. LONGITUDINAL LIBRATIONS

Europa's spin rate is not uniform but experiences small periodic variations, or longitudinal librations, largely caused by the time-dependent gravitational torque exerted by Jupiter on Europa's non-spherical (triaxial) shape. Depending on the internal structure of Europa, these rotational variations may or may not be the same throughout the interior. In our case, in which we consider the existence of a subsurface ocean between Europa's ice shell and rocky mantle, internal layers may perform differential rotational variations. However, this does not imply that the rotational variations experienced by a layer are decoupled from the ones experienced by other layers, because they remain coupled to each other through gravitational, pressure, viscous and electromagnetic torques [Van Hoolst et al., 2008, Baland and Van Hoolst, 2010]. Hence, the determination of the librations experienced by Europa's shell requires the simultaneous determination of the librations of other internal layers.

Since rotational variations and inertia increments are expected to be small, the modeling of longitudinal librations is based solely on the z -component of the linearized Liouville equations [e.g. Munk and MacDonald, 1960, Van Hoolst and Dehant, 2002, Sabadini and Vermeersen, 2004, Van Hoolst, 2007]. For a given material layer l , this component of the linearized Liouville equations can be expressed as [Van Hoolst, 2007]

$$C^l \Omega \dot{m}_z^l = -\dot{c}_{zz}^l \Omega + \Gamma_z^l, \quad (7.1)$$

where C^l is the principal axial moment of inertia of the layer, c_{zz}^l is the corresponding small inertia increment, Ω is the mean angular velocity of the body (equal to the mean motion n for synchronous natural satellites), m_z^l denotes the excited variations in the spin rate, and Γ_z^l is the sum of all external and internal torques acting on the layer. Furthermore, the dot on top of c_{zz}^l and m_z^l stands for their derivative with respect to time.

Although Equation 7.1 holds for both solid and fluid layers, a more convenient expression can be used for fluid layers when the flow within these layers is approximated as a uniform vorticity or Poincaré flow [Poincaré, 1910]. This Poincaré approximation has

been previously employed in the study of rotational dynamics of fluid layers to model the flow in Earth's fluid outer core [e.g. Mathews et al., 1991, Dehant et al., 1993, Greff-Lefftz et al., 2000] and in the putative subsurface oceans and assumed liquid cores of the Galilean satellites [Baland and Van Hoolst, 2010]. Based on the description given by Mathews et al. [1991], the relevant equation for fluid layers can then be expressed as

$$C^l \Omega \dot{m}_z^l = -\dot{c}_{zz}^l \Omega \quad (7.2)$$

The absence of a torque in the last equation shows that the rotation of internal fluid layers is decoupled from the libration dynamics of the adjacent solid layers. The same observation was made by Baland and Van Hoolst [2010], where they noticed that both internal and external pressure torques fully compensate the corresponding gravitational torques.

Since this is not the case for the solid layers (see eq. 7.1), we simplify our modeling by assuming a thin boundary layer at both the top and bottom part of the fluid which follows the rotational variations experienced by the adjacent solid layer [Van Hoolst et al., 2008, Baland and Van Hoolst, 2010, Van Hoolst et al., 2013]. These boundary layers share an ellipsoidal interface with the solid layer, but their fluid-fluid interface is assumed to be spherically symmetric. In this way the central part of the fluid layer becomes spherically symmetric and it will, therefore, not contribute to the total coupling torque exerted on each of the other layers. As a result, the rotational dynamics of the solid layers decouples from the librations experienced by the bulk of the fluid layers. The assumption introduced here allows us to reduce the system of equations we require to solve to:

$$C^s \Omega \dot{m}_z^s = -\dot{c}_{zz}^s \Omega + \Gamma_z^s, \quad (7.3)$$

$$C^m \Omega \dot{m}_z^m = -\dot{c}_{zz}^m \Omega + \Gamma_z^m, \quad (7.4)$$

where the superscripts s and m refer to the ice shell and the rocky mantle of Europa, respectively.

As mentioned before, the total axial torque on a layer (Γ_z^l) takes into consideration both the external gravitational torque exerted by Jupiter as well as internal coupling torques. As such, the torque can be more conveniently expressed as

$$\Gamma_z^l = \Gamma_{J,z}^l + \Gamma_{g,z}^l + \Gamma_{pJ,z}^l + \Gamma_{pg,z}^l, \quad (7.5)$$

where $\Gamma_{J,z}^l$ is the external torque by Jupiter, $\Gamma_{g,z}^l$ is the internal gravitational torque exerted by the misaligned material layers, $\Gamma_{pJ,z}^l$ is the torque exerted on the layer's boundaries by the fluid pressure induced by Jupiter's gravitational field, and $\Gamma_{pg,z}^l$ is the pressure torque due to the gravitational field of misaligned internal layers. Other internal coupling torques besides gravitational and pressure torques, such as viscous and electromagnetic torques, have not been taken into account as these torques are not expected to effectively couple internal layers at the timescale of the orbital motion [Baland and Van Hoolst, 2010]. Then, using the definition of the total axial torque given by Equation 7.5 we rewrite Equations 7.3 and 7.4 as

$$C^s \Omega \dot{m}_z^s + \dot{c}_{zz}^s \Omega = \Gamma_{J,z}^s + \Gamma_{g,z}^s + \Gamma_{pJ,z}^s + \Gamma_{pg,z}^s, \quad (7.6)$$

$$C^m \Omega \dot{m}_z^m + \dot{c}_{zz}^m \Omega = \Gamma_{J,z}^m + \Gamma_{g,z}^m + \Gamma_{pJ,z}^m + \Gamma_{pg,z}^m \quad (7.7)$$

Explicit analytical expressions for each of the terms in Equations 7.6 and 7.7 will be derived in the following Sections, in which we will pay special attention to the role of deformation.

7.3.2. INERTIA INCREMENTS

The interior of a synchronously rotating satellite in hydrostatic equilibrium is known to accommodate to the shape of a triaxial ellipsoid with principal axes $a > b > c$, as dictated by the acting rotational and tidal forces [Murray and Dermott, 1999]. The ellipsoidal distortion of the satellite's internal mass distribution leads to a permanent quadrupole gravitational field, which is commonly described by the principal moments of inertia A , B and C . On a diurnal timescale, which is the timescale we are interested in here, periodic variations of the spin rate (librations) and the presence of a diurnal tidal field lead to time-dependent deformations in the interior and hence to inertia increments.

Besides the principal moments of inertia, which will be required for the definition of the torques acting on internal layers, the only inertia increment relevant for the study of longitudinal librations is c_{zz} (see Equation 7.1). For an internal layer l , the principal moments of inertia and the inertia increment c_{zz} can be obtained from

$$A^l + c_{xx}^l = \iiint \rho(\mathbf{r}) (y^2 + z^2) dV^l, \quad (7.8)$$

$$B^l + c_{yy}^l = \iiint \rho(\mathbf{r}) (x^2 + z^2) dV^l, \quad (7.9)$$

$$C^l + c_{zz}^l = \iiint \rho(\mathbf{r}) (x^2 + y^2) dV^l, \quad (7.10)$$

where x , y and z refer to the Cartesian coordinates of an infinitesimal volume dV^l in the deformed state, and $\rho(\mathbf{r})$ is the density at position $\mathbf{r} = x \hat{\mathbf{i}} + y \hat{\mathbf{j}} + z \hat{\mathbf{k}}$ inside Europa. In spherical coordinates, Equations 7.8 to 7.10 can be written as

$$A^l + c_{xx}^l = \int_{r_o^b}^{r_o^t} \int_0^\pi \int_0^{2\pi} \left(\rho(r_o) (\sin^2 \theta \sin^2 \phi + \cos^2 \theta) \cdot r^4 \frac{\partial r}{\partial r_o} \sin \theta \right) dr_o d\theta d\phi, \quad (7.11)$$

$$B^l + c_{yy}^l = \int_{r_o^b}^{r_o^t} \int_0^\pi \int_0^{2\pi} \left(\rho(r_o) (\sin^2 \theta \cos^2 \phi + \cos^2 \theta) \cdot r^4 \frac{\partial r}{\partial r_o} \sin \theta \right) dr_o d\theta d\phi, \quad (7.12)$$

$$C^l + c_{zz}^l = \int_{r_o^b}^{r_o^t} \int_0^\pi \int_0^{2\pi} \left(\rho(r_o) r^4 \frac{\partial r}{\partial r_o} \sin^3 \theta \right) dr_o d\theta d\phi, \quad (7.13)$$

where r and r_o are the radial distances in, respectively, the deformed and the undeformed state; θ is the co-latitude; ϕ is the longitude; and the superscripts b and t refer

to the lower and upper boundary of a layer, respectively. Based on the definition of the tidal Love number h_2 , which accounts for the experienced radial displacement due to the acting rotational and tidal forces, we can express the disturbed radial distance r in terms of the undisturbed radial distance r_o as [e.g. Love, 1909, Mitrović et al., 1994]¹

$$r = r_o + h_f(r_o) \frac{\bar{V}_2(r_o)}{g_0} + h_2(r_o, t) * \frac{\Delta V_2(r_o, t)}{g_0}, \quad (7.14)$$

where the first two terms on the right-hand side of the equation refer to the hydrostatic triaxial shape of the satellite and the third term refers to the experienced radial deformation as a result of rotational variations and diurnal tides. In Equation 7.14, the Love number h_2 is time-dependent because we are considering viscoelastic deformation whereas h_f is the corresponding fluid Love number. These Love numbers are computed at every internal boundary using the normal mode approach based on the method presented in Jara-Orué and Vermeersen [2011]. Furthermore, g_0 is the surface gravity, the operator $*$ denotes time convolution, and \bar{V}_2 and ΔV_2 refer to, respectively, the constant and time-dependent part of the combined centrifugal and tidal potential acting on Europa. In a Cartesian frame attached to the surface of Europa, these potentials can be written as (see Section 6.3 for a derivation)

$$\bar{V}_2 = \frac{7}{6} n^2 x_o^2 - \frac{1}{3} n^2 y_o^2 - \frac{5}{6} n^2 z_o^2, \quad (7.15)$$

$$\begin{aligned} \Delta V_2 = n^2 & \left(\frac{1}{3} m_z^l + 3e \cos(nt) \right) x_o^2 + n^2 \left(\frac{1}{3} m_z^l - \frac{3}{2} e \cos(nt) \right) y_o^2 \\ & - n^2 \left(\frac{2}{3} m_z^l + \frac{3}{2} e \cos(nt) \right) z_o^2 - 3n^2 \left(\alpha_z^l - 2e \sin(nt) \right) x_o y_o \\ & - n^2 m_x^l x_o z_o - n^2 m_y^l y_o z_o, \end{aligned} \quad (7.16)$$

where the variables m_x^l , m_y^l and m_z^l refer to the time-dependent rotational deviations of an internal layer l (m_x^l and m_y^l describe polar motion), α_z^l refers to the angular deviation caused by m_z^l ($\alpha_z^l = \int n m_z^l dt$); e is the orbit's eccentricity ($e = 0.0094$); and x_o , y_o and z_o are the Cartesian coordinates, in the undeformed state, of an infinitesimal volume within the layer of interest.

The term $r^4 \frac{\partial r}{\partial r_o}$ in Equations 7.11 to 7.13 can alternatively be written as $\frac{1}{5} \frac{\partial r^5}{\partial r_o}$ in order to simplify the integration about the radial coordinate r_o . This implies that we need to find an expression for r^5 and its corresponding radial derivative using Equations 7.14 to 7.16. The resulting expression is lengthy but can be simplified by neglecting all second order and higher terms in eccentricity, rotational variations and n^2/g_0 ; all of them assumed to be negligibly small for our purposes. The simplified expression then reads:

$$\frac{\partial r^5}{\partial r_o} \approx 5r_o^4 - \frac{5}{6} \frac{n^2}{g_0} \left(5P_2^0(\cos\theta) - \frac{3}{2} P_2^2(\cos\theta) \cos(2\phi) \right) \frac{\partial (h_f(r_o) r_o^6)}{\partial r_o}$$

¹In contrast to the definition for the deformed radius given by Equation 6.115, the potentials in Equation 7.14 are defined at radial distance r_o and thus not at the surface. Therefore, the Love numbers in Equation 7.14 are equal to the Love numbers in Equation 6.115 but multiplied by the ratio $\left(\frac{R}{r_o}\right)^2$, with R being the surface radius.

$$\begin{aligned}
& -\frac{5n^2}{g_0} \left\{ \frac{2}{3} P_2^0(\cos\theta) m_z^l + \frac{1}{2} P_2^2(\cos\theta) \sin(2\phi) \alpha_z^l \right. \\
& - \frac{1}{3} P_2^1(\cos\theta) \left(\cos(\phi) m_x^l + \sin(\phi) m_y^l \right) \\
& + e \left[\frac{5}{2} \left(P_2^0(\cos\theta) - \frac{1}{2} P_2^2(\cos\theta) \cos(2\phi) \right) \cos(nt) \right. \\
& \left. \left. - P_2^2(\cos\theta) \sin(2\phi) \sin(nt) \right] \right\} * \frac{\partial(h_2(r_o, t) r_o^6)}{\partial r_o}, \tag{7.17}
\end{aligned}$$

where the associated Legendre polynomials $P_2^0(\cos\theta)$, $P_2^1(\cos\theta)$ and $P_2^2(\cos\theta)$ are given by

$$P_2^0(\cos\theta) = \frac{3}{2} \cos^2\theta - \frac{1}{2},$$

$$P_2^1(\cos\theta) = -3 \sin\theta \cos\theta,$$

$$P_2^2(\cos\theta) = 3 \sin^2\theta$$

Substitution of Equation 7.17 into Equations 7.11 to 7.13 and assuming that the density is constant within a layer (i.e. $\rho(r_o) = \rho^l$) leads to the following expressions for the axial moment of inertia C^l and the difference between the equatorial moments of inertia $B^l - A^l$:

$$C^l = I^l + \frac{4\pi}{9} \frac{n^2}{g_0} \rho^l \int_{r_o^b}^{r_o^t} \frac{\partial(h_f(r_o) r_o^6)}{\partial r_o} dr_o, \tag{7.18}$$

$$B^l - A^l = \frac{4\pi}{5} \frac{n^2}{g_0} \rho^l \int_{r_o^b}^{r_o^t} \frac{\partial(h_f(r_o) r_o^6)}{\partial r_o} dr_o, \tag{7.19}$$

where the mean moment of inertia I^l of the layer is defined by

$$I^l = \frac{8\pi}{3} \rho^l \int_{r_o^b}^{r_o^t} r_o^4 dr_o \tag{7.20}$$

In a similar way, the inertia increment c_{zz}^l can be written as

$$c_{zz}^l = \frac{4\pi}{5} \frac{n^2}{g_0} \rho^l \left(\frac{4}{9} m_z^l + e \cos(nt) \right) * \int_{r_o^b}^{r_o^t} \frac{\partial(h_2(r_o, t) r_o^6)}{\partial r_o} dr_o \tag{7.21}$$

This equation can be expressed in a more convenient way by using the definition of the inertia difference $B^l - A^l$ given by Equation 7.19. Hence

$$c_{zz}^l = (B^l - A^l) \left(\frac{4}{9} m_z^l + e \cos(nt) \right) * \psi^l(t), \tag{7.22}$$

where $\psi^l(t)$ is given by the ratio

$$\psi^l(t) = \left(\int_{r_o^b}^{r_o^t} \frac{\partial(h_2(r_o, t) r_o^6)}{\partial r_o} dr_o \right) \left(\int_{r_o^b}^{r_o^t} \frac{\partial(h_f(r_o) r_o^6)}{\partial r_o} dr_o \right)^{-1} \tag{7.23}$$

7.3.3. GRAVITATIONAL COUPLING

Gravitational coupling between two laterally homogeneous layers arises when the layers are not geometrically aligned. Since fluids adapt to the shape of their boundaries, a thin region at the bottom of the fluid is expected to take the orientation of the solid layer below it whereas a thin region at the top of the fluid will be aligned with the upper solid layer [Van Hoolst et al., 2008]. The rest of the fluid layer, which is located between these two boundary layers, is assumed to have spherical boundaries and hence it will not contribute to the coupling torques [Van Hoolst et al., 2008]. Taking the described orientation of fluid layers into consideration, we can define the gravitational torque on Europa's rocky mantle ($\Gamma_{g,z}^m$) by the misaligned ice shell and upper ocean as follows [Szeto and Xu, 1997]:

$$\Gamma_{g,z}^m = \iiint_{V^m} \left[\rho(\mathbf{r}) \mathbf{r} \times \nabla \Phi^g(\mathbf{r}) \right]_z dV, \quad (7.24)$$

where \mathbf{r} is the position vector - in the deformed state - of an infinitesimal volume dV located within the mantle and Φ^g is the gravitational potential per unit volume exerted by the misaligned layers on an infinitesimal mass at position \mathbf{r} within the mantle. Since the gravitational torque on the mantle is only due to layers located further away from the center of the moon, the relevant gravitational potential $\Phi^g = \Phi_O^g$ is defined as [Szeto and Xu, 1997]

$$\Phi_O^g(\mathbf{r}) = G \sum_{n=0}^{\infty} \sum_{m=-n}^n \left((-1)^m r^n P_n^m(\cos\theta) \exp(im\phi) \cdot \iint_{V^O} \rho(\mathbf{r}') \frac{1}{r'^{n+1}} P_n^{-m}(\cos\theta') \exp(-im\phi') dV' \right), \quad (7.25)$$

where r' , θ' and ϕ' refer to the spherical coordinates of an infinitesimal mass $\rho(\mathbf{r}') dV'$ located within the misaligned outer layers (represented by the volume V^O); n and m are the degree and order of the spherical harmonic expansion; the P_n^m are associated Legendre polynomials; and i is the imaginary unit.

The gravitational torque on the rocky mantle could also be caused by layers located closer to the center of the moon, e.g. by a misaligned solid inner core. In that hypothetical case, the gravitational potential exerted by these misaligned inner layers can be written as

$$\Phi_I^g(\mathbf{r}) = G \sum_{n=0}^{\infty} \sum_{m=-n}^n \left(\frac{(-1)^m}{r^{n+1}} P_n^{-m}(\cos\theta) \exp(-im\phi) \cdot \iiint_{V^I} \rho(\mathbf{r}'') r''^n P_n^m(\cos\theta'') \exp(im\phi'') dV'' \right), \quad (7.26)$$

where r'' , θ'' and ϕ'' are the spherical coordinates of an infinitesimal mass $\rho(\mathbf{r}'') dV''$ located within the misaligned inner layers. Since we consider that Europa's core is entirely fluid, the last equation is not relevant for the determination of the gravitational torque on the mantle. However, Equation 7.26 will be used later to derive explicit expressions for the gravitational and pressure torques on the outer shell.

From all components of the gravitational potential $\Phi_O^g(\mathbf{r})$ only the harmonic term of

degree and order 2 will contribute to the torque [Buffett, 1996, Baland and Van Hoolst, 2010]. Such an expression can be derived from Equation 7.25 using the method described in Szeto and Xu [1997] and the definition of the radial distance in the deformed state, given by Equation 7.14. The resulting expression can be written as

$$\Phi_{O;2,2}^g = \frac{2\pi}{15} Gr^2 \left\{ \xi_c^O \cos(2\phi) - \xi_d^O * \left[(2\alpha_z^s - 4e \sin(nt)) \sin(2\phi) - 3e \cos(nt) \cos(2\phi) \right] \right\} P_2^2(\cos\theta), \quad (7.27)$$

where the superscript O refers to the entire group of misaligned outer layers, and where ξ_c^O and ξ_d^O are defined by

$$\xi_c^O = \int_{r'_o} \rho(r'_o) \frac{\partial \beta(r'_o)}{\partial r'_o} dr'_o, \quad (7.28)$$

$$\xi_d^O = \int_{r'_o} \rho(r'_o) \frac{\partial \Delta \beta(r'_o, t)}{\partial r'_o} dr'_o, \quad (7.29)$$

in which r'_o refers to the radial distance of a mass element within the misaligned outer layer(s) in the undeformed state, and $\beta(r'_o)$ refers to the static equatorial flattening ($a(r'_o) - b(r'_o) / a(r'_o)$). Using the static part of Equation 7.14 to write the equatorial axes $a(r'_o)$ and $b(r'_o)$ at undeformed radial distance r'_o in terms of the fluid Love number h_f , we can express the equatorial flattening $\beta(r'_o)$ as

$$\beta(r_o) = \frac{3}{2} \frac{n^2}{g_0} h_f(r_o) r_o \quad (7.30)$$

In contrast to the equatorial flattening $\beta(r'_o)$, the variable $\Delta \beta(r'_o, t)$ in Equation 7.29 does not refer to any physical flattening but is only an auxiliary variable used to simplify the expressions developed in this paper. $\Delta \beta(r'_o, t)$ is therefore defined as

$$\Delta \beta(r_o, t) = \frac{3}{2} \frac{n^2}{g_0} h_2(r_o, t) r_o \quad (7.31)$$

The definitions given in Equations 7.28 to 7.31 allow us to express the gravitational torque $\Gamma_{g,z}^m$ on the mantle in terms of rotational variations and Love numbers. To derive such an expression we substitute Equations 7.14 and 7.27 into Equation 7.24, which after some analytical manipulation becomes

$$\Gamma_{g,z}^m = \frac{4}{5} \pi G (B^m - A^m) \xi_c^O \left\{ 2(\alpha_z^s - \alpha_z^m) - \left(\frac{\xi_d^O}{\xi_c^O} * 2\alpha_z^s - \psi^m * 2\alpha_z^m \right) + 4e \sin(nt) * \left(\frac{\xi_d^O}{\xi_c^O} - \psi^m \right) \right\} \quad (7.32)$$

From a physical perspective, the first term within curly brackets in Equation 7.32 stands for the rigid gravitational torque; the second term describes the torque due to viscoelastic adjustment induced by the experienced rotational variations; and the third

term describes the torque due to viscoelastic deformation induced by diurnal tides. The second term and third term, which introduce the effect of viscoelastic deformation on the coupling torque, consist of two contributions, namely: 1) the torque by the deformed component of the shell's shape on the hydrostatic (rigid) shape of the mantle, and 2) the torque by the hydrostatic shape of the shell on the deformed component of the mantle's shape.

Next we proceed to define the gravitational torque $\Gamma_{g,z}^s$ exerted on the shell by the misaligned interior (i.e. rocky mantle, upper fluid core and lower portion of the water ocean). This torque is defined by an alternative version of Equation 7.24 in which the integration volume dV , radial distance \mathbf{r} and density ρ refer to the outer shell and the gravitational potential $\Phi^g(\mathbf{r})$ is solely due to misaligned internal layers located closer to the center (Equation 7.26). As previously done for the potential exerted by the outer layers, we use the method described in Szeto and Xu [1997] to express the gravitational potential $\Phi^g(\mathbf{r})$ induced by the misaligned internal layers as

$$\Phi_{I;2,2}^g = \frac{1}{4} \frac{G}{r^3} (B^I - A^I) \left\{ \cos(2\phi) - \psi^I * \left[(2\alpha_z^m - 4e \sin(nt)) \sin(2\phi) - 3e \cos(nt) \cos(2\phi) \right] \right\} P_2^2(\cos\theta), \quad (7.33)$$

where the superscript I refers to the entire group of internal misaligned layers and where the ratio ψ^I is defined by

$$\psi^I = \left(\int_I \rho(r_o) \frac{\partial(h_2(r_o, t) r_o^6)}{\partial r_o} dr_o \right) \left(\int_I \rho(r_o) \frac{\partial(h_f(r_o) r_o^6)}{\partial r_o} dr_o \right)^{-1} \quad (7.34)$$

In a similar way as for the torque on the mantle, substitution of Equations 7.14 and 7.33 into Equation 7.24 leads to an expression for the gravitational torque on the shell in terms of rotational variations and Love numbers. Again, after some analytical manipulation, the torque can be written as

$$\Gamma_{g,z}^s = -\frac{4}{5} \pi G (B^I - A^I) \xi_c^s \left\{ 2(\alpha_z^s - \alpha_z^m) - \left(\frac{\xi_d^s}{\xi_c^s} * 2\alpha_z^s - \psi^I * 2\alpha_z^m \right) + 4e \sin(nt) * \left(\frac{\xi_d^s}{\xi_c^s} - \psi^I \right) \right\}, \quad (7.35)$$

where ξ_c^s and ξ_d^s are given by Equations 7.28 and 7.29 for the case in which the shell would be the only outer layer (i.e. $O = s$).

Before ending the discussion on gravitational coupling torques we assess the limiting cases of the basic viscoelastic equations for the gravitational torques, given by Equations 7.32 and 7.35, to compare our derived expressions to more commonly used expressions for the torques. On one side, if all solid material layers are assumed to be rigid, all variables depending on deformation will become equal to zero (i.e. $h_2(r_o, t)$, $\Delta\beta(r_o, t)$, ξ_d^s , ξ_d^O , ψ^m and ψ^I). Hence, as expected, the resulting expressions for the gravitational torques will coincide with the equations given in e.g. Van Hoolst et al. [2008] and Baland and Van Hoolst [2010] for the gravitational torque in the rigid case. On the other extreme, if the solid layers are assumed to behave as a fluid, the deformation Love number $h_2(r_o, t)$ will be equal to the fluid Love number $h_f(r_o)$ and hence the gravitational

torques will vanish, as expected for fluid layers. However, none of these two limiting cases is expected to be representative for the rheological behavior of Europa's ice shell and rocky mantle at orbital frequency. The effect of deformation on the magnitude of the gravitational torques - and other internal and external torques - is outlined in Section 7.4.

7.3.4. PRESSURE COUPLING

The fluid pressure acting on the boundaries of Europa's shell and rocky mantle leads to additional torques, which contribute to the coupling of the rotational motion of these layers. Although the fluid pressure depends on the fluid motion through Navier-Stokes equations, a simplification can be obtained by approximating the fluid flow as a uniform vorticity or Poincaré flow [e.g. Mathews et al., 1991, Dehant et al., 1993, Van Hoolst and Dehant, 2002]. In such a scenario, the fluid pressure p satisfies the condition [Dehant et al., 1993]

$$\nabla p = \rho_f (\nabla \Pi + \nabla \Phi^g + \nabla \Phi^c + \nabla W^e), \quad (7.36)$$

where ρ_f is the density of the fluid at the boundary, Π is called the inertial potential [e.g. Dehant et al., 1993], Φ^g is the gravitational potential, Φ^c is the centrifugal potential and W^e is the external gravitational potential.

In the following discussion we neglect the contribution of the inertial potential to the pressure torque, as this term is shown to be considerably smaller than the other terms for a fluid in Poincaré flow [Mathews et al., 1991]. In addition, the torque due to the centrifugal potential vanishes because the part of the liquid exerting pressure on the surface of a solid layer is assumed to be aligned with the layer. Then, the pressure torque on a solid layer l can be expressed as [e.g. Baland and Van Hoolst, 2010]

$$\begin{aligned} \Gamma_{p,z}^l = & \iint_{S_b} [\mathbf{r}_b \times \mathbf{n}_b]_z \rho_b [\nabla \Phi^g(\mathbf{r}_b) + \nabla W^e(\mathbf{r}_b)] dS \\ & - \iint_{S_t} [\mathbf{r}_t \times \mathbf{n}_t]_z \rho_t [\nabla \Phi^g(\mathbf{r}_t) + \nabla W^e(\mathbf{r}_t)] dS, \end{aligned} \quad (7.37)$$

where S_b and S_t are the bottom and top boundaries of solid layer l ; \mathbf{n} is the unit normal to these boundaries; and the subscripts b and t refer to the conditions at the bottom and top solid-fluid boundaries.

As a next step we proceed to express the surface integrals in Equation 7.37 as volume integrals through the use of Gauss' theorem. The integration volumes involved in this transformation are the previously defined boundary layers which share an elliptical interface with the adjacent solid layer and a spherical boundary with the remaining part of the fluid. Then, the pressure torque induced by the gravitational potential Φ^g (the part due to the external potential will be discussed in the next Section) can alternatively be written as

$$\Gamma_{p,g,z}^l = \iiint_{V_{fb}} [\rho_{fb} \mathbf{r} \times \nabla \Phi^g(\mathbf{r})]_z dV + \iiint_{V_{ft}} [\rho_{ft} \mathbf{r} \times \nabla \Phi^g(\mathbf{r})]_z dV, \quad (7.38)$$

where V_{fb} and V_{ft} refer to the fluid (integration) volumes located below and on top of the solid layer under consideration; and ρ_{fb} and ρ_{ft} are the corresponding fluid densities. Application of this equation to our general internal model of Europa leads then to

the following expressions for the required pressure torques acting on the rocky mantle and the ice shell:

$$\Gamma_{pg,z}^m = \iiint_{V_{c'}} \left[\rho_c \mathbf{r} \times \nabla \Phi_O^g(\mathbf{r}) \right]_z dV + \iiint_{V_{w'}} \left[\rho_w \mathbf{r} \times \nabla \Phi_O^g(\mathbf{r}) \right]_z dV, \quad (7.39)$$

$$\Gamma_{pg,z}^s = \iiint_{V_{w''}} \left[\rho_w \mathbf{r} \times \nabla \Phi_I^g(\mathbf{r}) \right]_z dV, \quad (7.40)$$

in which ρ_c and ρ_w refer to the density of the fluid core and the water ocean; and $V_{c'}$, $V_{w'}$ and $V_{w''}$ are the fluid integration volumes on top of the fluid core, bottom of the ocean and top of the ocean, respectively.

Substitution of Equations 7.14, 7.27 and 7.33 into Equations 7.39 and 7.40 leads then to the desired expressions for the fluid pressure torque on the mantle and ice shell, which after some analytical manipulation, can be written as

$$\Gamma_{pg,z}^m = \frac{32}{75} \pi^2 G (\rho_c \beta(r_{o,c}) r_{o,c}^5 - \rho_w \beta(r_{o,m}) r_{o,m}^5) \xi_c^O \left\{ 2(\alpha_z^s - \alpha_z^m) - \left(\frac{\xi_d^O}{\xi_c^O} * 2\alpha_z^s - \zeta^{m+} * 2\alpha_z^m \right) + 4e \sin(nt) * \left(\frac{\xi_d^O}{\xi_c^O} - \zeta^{m+} \right) \right\}, \quad (7.41)$$

and

$$\Gamma_{pg,z}^s = -\frac{4}{5} \pi G (B^I - A^I) \rho_w \beta(r_{o,w}) \left\{ 2(\alpha_z^s - \alpha_z^m) - \left(\frac{h_2(r_{o,w}, t)}{h_f(r_{o,w})} * 2\alpha_z^s - \psi^I * 2\alpha_z^m \right) + 4e \sin(nt) * \left(\frac{h_2(r_{o,w}, t)}{h_f(r_{o,w})} - \psi^I \right) \right\}, \quad (7.42)$$

where $r_{o,c}$, $r_{o,m}$ and $r_{o,w}$ are the undeformed (spherical) outer radii of the fluid core, rocky mantle and water ocean, respectively. In addition, the ratio ζ^{m+} is given by

$$\zeta^{m+} = \frac{\rho_c \Delta \beta(r_{o,c}) r_{o,c}^5 - \rho_w \Delta \beta(r_{o,m}) r_{o,m}^5}{\rho_c \beta(r_{o,c}) r_{o,c}^5 - \rho_w \beta(r_{o,m}) r_{o,m}^5} \quad (7.43)$$

In a similar way as for the gravitational torques, discussed in the previous Section, we observe from Equations 7.41 and 7.42 that the expressions for the pressure torques will reduce to the ones given in Baland and Van Hoolst [2010] if the layers behave as rigid bodies. Moreover, the pressure torques will vanish if the layers would behave as a fluid at the forcing frequency.

7.3.5. EXTERNAL TORQUES

A commonly used expression to denote the external gravitational torque $\Gamma_{J,z}^l$ of Jupiter on an internal layer l is given by [Van Hoolst et al., 2008, Baland and Van Hoolst, 2010, Rambaux et al., 2011]

$$\Gamma_{J,z}^l = \frac{3}{2} n^2 (B^l - A^l) \left(\frac{a_e}{d} \right)^3 \sin 2(f - nt - \alpha_z^l), \quad (7.44)$$

where a_e is the orbit's semi-major axis, d the planet-moon distance and f the true anomaly. Under the assumption of a small eccentricity and rotational variations, this expression for the external torque can be rewritten in a more convenient way using well-known series expansions for $(\frac{a_e}{d})^3$, $\cos(f)$ and $\sin(f)$ in terms of the eccentricity [e.g. Murray and Dermott, 1999]. Up to the first order in the small eccentricity, the resulting expression becomes

$$\Gamma_{J,z}^l = 3n^2 (B^l - A^l) (2e \sin(nt) - \alpha_z^l) \quad (7.45)$$

Nevertheless, Equations 7.44 and 7.45 only hold if the internal layers are considered to behave rigidly when forced by the gravitational potential of Jupiter. As that is not the case in our analysis, we need to redefine the external torque exerted by Jupiter in order to take into account the effect of deformations. We start this procedure by defining the external torque $\Gamma_{J,z}^l$ on a layer l as

$$\Gamma_{J,z}^l = \iiint_{V^l} \rho(\mathbf{r}) [\mathbf{r} \times \nabla W^J]_z dV, \quad (7.46)$$

where the position vector \mathbf{r} takes into account the effect of deformation. Moreover, the external gravitational potential W^J exerted by Jupiter can be defined as (see Section 6.3)

$$W^J = n^2 \left\{ x_o^2 - \frac{1}{2} y_o^2 - \frac{1}{2} z_o^2 + \frac{3}{2} \left((2x_o^2 - y_o^2 - z_o^2) e \cos(nt) - 2(\alpha_z - 2e \sin(nt)) x_o y_o \right) \right\} \quad (7.47)$$

Then, subsequent substitution of Equations 7.14 and 7.47 into Equation 7.46 leads to the following expressions for the external torque on the mantle and ice shell:

$$\Gamma_{J,z}^m = 3n^2 (B^m - A^m) (2e \sin(nt) - \alpha_z^m) * (1 - \psi^m), \quad (7.48)$$

$$\Gamma_{J,z}^s = 3n^2 (B^s - A^s) (2e \sin(nt) - \alpha_z^s) * (1 - \psi^s), \quad (7.49)$$

where the ratios ψ^m and ψ^s take the effect of deformation into account, in accordance with the definition given by Equation 7.23. Therefore, as expected, both expressions for the external torque would reduce to Equation 7.45 if the layers would behave in a rigid way.

Furthermore, as has been mentioned in the previous Section, the fluid pressure due to the external gravitational potential of Jupiter induces an additional torque on the boundaries of the mantle and the ice shell. Then, in accordance with the definition given by Equation 7.37, we can derive the following expressions for the pressure torque on the mantle and ice shell:

$$\Gamma_{pJ,z}^m = \frac{8}{5} \pi n^2 (2e \sin(nt) - \alpha_z^m) * \left\{ \rho_c \beta(r_{o,c}) r_{o,c}^5 \left(1 - \frac{h_2(r_{o,c}, t)}{h_f(r_{o,c})} \right) - \rho_w \beta(r_{o,m}) r_{o,m}^5 \left(1 - \frac{h_2(r_{o,m}, t)}{h_f(r_{o,m})} \right) \right\}, \quad (7.50)$$

$$\Gamma_{pJ,z}^s = \frac{8}{5} \pi n^2 \rho_w \beta(r_{o,w}) r_{o,w}^5 (2e \sin(nt) - \alpha_z^s) * \left(1 - \frac{h_2(r_{o,w}, t)}{h_f(r_{o,w})}\right) \quad (7.51)$$

Again, as for the previous expressions for internal and external torques, Equations 7.50 and 7.51 reduce to their rigid counterparts [e.g. Baland and Van Hoolst, 2010, Rambaux et al., 2011] if the solid layers are considered to behave as rigid bodies, whereas they would vanish if the layers would show a fluid-like behavior.

7.3.6. LIBRATION EQUATIONS FOR A MULTI-LAYERED EUROPA

In this Section we use the relevant expressions for the moments of inertia, inertia increments and torques derived in Sections 7.3.2 to 7.3.5 to rewrite the coupled system of angular momentum equations (Equations 7.6 and 7.7) in terms of the unknown libration angles α_z^s and α_z^m , i.e.

$$\left(C^m + \frac{4}{9}(B^m - A^m)\psi^m\right) * \ddot{\alpha}_z^m + 2\kappa_m^m * \alpha_z^m - 2\kappa_m^s * \alpha_z^s = 4e \left(\kappa_m^e + \frac{1}{4}n^2(B^m - A^m)\psi^m\right) * \sin(nt), \quad (7.52)$$

$$\left(C^s + \frac{4}{9}(B^s - A^s)\psi^s\right) * \ddot{\alpha}_z^s + 2\kappa_s^s * \alpha_z^s - 2\kappa_s^m * \alpha_z^m = 4e \left(\kappa_s^e + \frac{1}{4}n^2(B^s - A^s)\psi^s\right) * \sin(nt), \quad (7.53)$$

where the torque-related parameters κ_m^m , κ_m^s , κ_m^e , κ_s^m , κ_s^s and κ_s^e are defined as

$$\begin{aligned} \kappa_m^m &= (K_g^m + K_J^m)(1 - \psi^m) + (K_p^m + K_{pJ}^m)(1 - \zeta^{m+}), \\ \kappa_m^s &= (K_g^m + K_p^m) \left(1 - \frac{\xi_d^O}{\xi_c^O}\right), \\ \kappa_m^e &= K_J^m(1 - \psi^m) + K_{pJ}^m(1 - \zeta^{m+}) + K_g^m \left(\frac{\xi_d^O}{\xi_c^O} - \psi^m\right) \\ &\quad + K_p^m \left(\frac{\xi_d^O}{\xi_c^O} - \zeta^{m+}\right), \\ \kappa_s^m &= (K_g^s + K_p^s)(1 - \psi^I), \\ \kappa_s^s &= K_g^s \left(1 - \frac{\xi_d^s}{\xi_c^s}\right) + K_J^s(1 - \psi^s) + (K_p^s + K_{pJ}^s) \left(1 - \frac{h_2(r_{o,w}, t)}{h_f(r_{o,w})}\right), \\ \kappa_s^e &= K_J^s(1 - \psi^s) + K_{pJ}^s \left(1 - \frac{h_2(r_{o,w}, t)}{h_f(r_{o,w})}\right) - K_g^s \left(\frac{\xi_d^s}{\xi_c^s} - \psi^I\right) \\ &\quad - K_p^s \left(\frac{h_2(r_{o,w}, t)}{h_f(r_{o,w})} - \psi^I\right), \end{aligned}$$

with

$$K_g^m = \frac{4}{5} \pi G (B^m - A^m) \xi_c^O,$$

$$\begin{aligned}
K_p^m &= \frac{32}{75} \pi^2 G (\rho_c \beta(r_{o,c}) r_{o,c}^5 - \rho_w \beta(r_{o,m}) r_{o,m}^5) \xi_c^O, \\
K_J^m &= \frac{3}{2} n^2 (B^m - A^m), \\
K_{pJ}^m &= \frac{4}{5} \pi n^2 (\rho_c \beta(r_{o,c}) r_{o,c}^5 - \rho_w \beta(r_{o,m}) r_{o,m}^5), \\
K_g^s &= \frac{4}{5} \pi G (B^I - A^I) \xi_c^s, \\
K_p^s &= \frac{4}{5} \pi G (B^I - A^I) \rho_w \beta(r_{o,w}), \\
K_J^s &= \frac{3}{2} n^2 (B^s - A^s), \\
K_{pJ}^s &= \frac{4}{5} \pi n^2 \rho_w \beta(r_{o,w}) r_{o,w}^5
\end{aligned}$$

As can be seen from Equations 7.52 and 7.53, our viscoelastic description of the libration equations contains several time-convolution operations that complicate the structure of the equations in the time domain. It is therefore convenient to transform Equations 7.52 and 7.53 to the frequency domain using either the Laplace or the Fourier transform. In this paper we opt for the use of the Laplace transform as our internal and surface Love numbers are already defined in the Laplace domain [Sabadini and Vermeersen, 2004, Jara-Oru e and Vermeersen, 2011]. As we do not only solve for the forcing frequency we are interested in, our solution also includes the free librations of the involved layers as well as the effect of viscoelastic relaxation.

7.4. INTERIOR MODELS OF EUROPA AND LOVE NUMBERS

Our calculations will be performed on a set of interior models of Europa consisting of four concentric homogeneous material layers, namely: a fluid metallic core, a silicate mantle, a water ocean and an ice-I shell. Moreover, in order to be in agreement with previous studies on the thermal state of Europa's ice shell [e.g. Hussmann et al., 2002, Tobie et al., 2003] and on the morphology of impact craters [Schenk, 2002], we choose to subdivide the ice shell into two homogeneous sub-layers: 1) a low-viscous, ductile, convecting layer at the lower part of the shell (or asthenosphere); and 2) a thin, high-viscous, effectively elastic layer on top of it (or lithosphere). The rheological behavior of all internal solid layers is simulated using a Maxwell rheology.

As our purpose is to analyze the dependence of the shell libration amplitude on geophysical parameters characterizing Europa's ocean and the shell, we apply our libration model to a set of interior models covering a range of plausible values for the shell thickness, shell density (ρ_s), ocean density (ρ_w), ice rigidity (μ_s) and the viscosity of the lower part of the shell (η_s). The set of interior models used in this study is summarized in Table 7.1, in which the values corresponding to the density of both the mantle and the core are not shown because they depend on the parameters characterizing the ocean and the ice shell, as all our interior models need to satisfy the conditions on average density ($\bar{\rho} = 2989 \text{ kg/m}^3$) and normalized mean moment of inertia ($\frac{I}{MR^2} = 0.346$) [Anderson et al., 1998].

Table 7.1: Basic 5-layer model of Europa's interior used in the modeling of longitudinal librations. ⁽¹⁾ Constrained to be smaller or at most equal to the density of the ocean. ⁽²⁾ Constrained to be larger or at least equal to the shell density. ⁽³⁾ The density of the core and the mantle depends on the characterization of the ocean and the shell as the entire model satisfies the imposed conditions on average density and mean moment of inertia. Reference values for the variable interior parameters are: shell density $\rho_s = 950 \text{ kg}\cdot\text{m}^{-3}$, ocean density $\rho_w = 1000 \text{ kg}\cdot\text{m}^{-3}$, shell rigidity $\mu_s = 3.487 \text{ GPa}$ and asthenosphere viscosity $\eta_s = 1.0 \cdot 10^{17} \text{ Pa}\cdot\text{s}$.

Layer	Outer Radius (km)	Density ($\text{kg}\cdot\text{m}^{-3}$)	Rigidity (GPa)	Viscosity (Pa·s)
Lithosphere	1562	900 – 1000 ⁽¹⁾	1 – 10	$1.0 \cdot 10^{21}$
Asthenosphere	1557	900 – 1000 ⁽¹⁾	1 – 10	$1.0 \cdot 10^{12} - 1.0 \cdot 10^{17}$
Ocean	1462 – 1557	950 – 1150 ⁽²⁾	0	0
Silicate Mantle	1432	⁽³⁾	65	$1.0 \cdot 10^{19}$
Core	600	⁽³⁾	0	0

The Love numbers h_f and h_2 that characterize the hydrostatic and diurnal deformation at every internal layer boundary of our interior models are then determined by means of an adapted version of the viscoelastic normal-mode approach outlined in [Jara-Oru  and Vermeersen \[2011\]](#). Typical values for h_f and h_2 at the considered internal layer boundaries are shown in [Figures 7.1 and 7.2](#), respectively, for a limited range of interior models for which $\rho_s = 950 \text{ kg}\cdot\text{m}^{-3}$, $\rho_w = 1000 \text{ kg}\cdot\text{m}^{-3}$, $\mu_s = 3.487 \text{ GPa}$ and $\eta_s = 1.0 \cdot 10^{17} \text{ Pa}\cdot\text{s}$. In the following Sections, these interior models are going to be referred to as our reference models of Europa's interior. [Figures 7.1 and 7.2](#) clearly show that the amount of diurnal deformation (h_2) experienced at boundaries on top of the ocean is about two orders of magnitude larger than at the bottom of the ocean, whereas the hydrostatic deformation (h_f) remains within the same order of magnitude throughout the interior of Europa. The ratios describing the effect of the shell's deformation on the libration dynamics will be, hence, around two orders of magnitude larger than the ones corresponding to mantle (see [Table 7.2](#) for the numerical values corresponding to a representative interior model of Europa for which the Love numbers are defined in [Figures 7.1 and 7.2](#) at a shell thickness of 40 km). Using the numerical values presented in [Table 7.2](#), we can give a rough estimation of the effect of deformation on the libration dynamics of the shell and mantle, i.e.:

- Diurnal deformation experienced by the shell considerably reduces the magnitude of the external torques acting on the shell (see [Equations 7.49 and 7.51](#)). As a result, the amplitude of the forced libration of a deformable shell is expected to be smaller than in the case of a rigid shell. This statement is in agreement with the findings of [Goldreich and Mitchell \[2010\]](#).
- On the other hand, the much smaller diurnal deformation experienced by the mantle only has a slight effect on the magnitude of the acting external torques (see [Equations 7.48 and 7.50](#)). Therefore, the amplitude of the forced libration of a deformable mantle is expected to be similar to that of a rigid mantle.

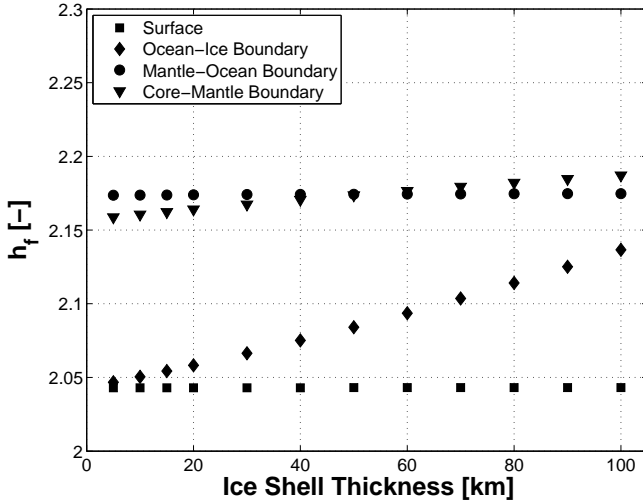


Figure 7.1: Fluid Love number h_f at internal layer boundaries and at the surface as a function of the total thickness of the ice shell. The Love numbers shown correspond to a set of interior models defined by the parameters listed in Table 7.1, and for which $\rho_s = 950 \text{ kg}\cdot\text{m}^{-3}$, $\rho_w = 1000 \text{ kg}\cdot\text{m}^{-3}$, $\mu_s = 3.487 \text{ GPa}$ and $\eta_s = 1.0 \cdot 10^{17} \text{ Pa}\cdot\text{s}$. The fluid Love number h_f at the core-mantle boundary has been multiplied by a factor 1/2.

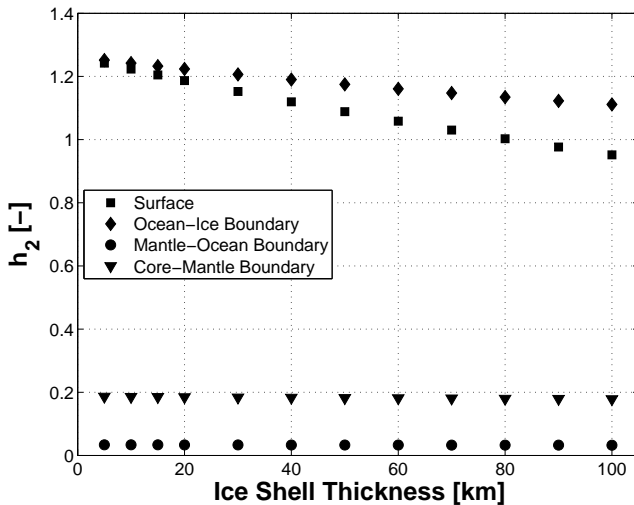


Figure 7.2: Tidal Love number h_2 at internal layer boundaries and at the surface as a function of the total thickness of the ice shell. The Love numbers shown correspond to a set of reference interior models defined by the parameters listed in Table 7.1, and for which $\rho_s = 950 \text{ kg}\cdot\text{m}^{-3}$, $\rho_w = 1000 \text{ kg}\cdot\text{m}^{-3}$, $\mu_s = 3.487 \text{ GPa}$ and $\eta_s = 1.0 \cdot 10^{17} \text{ Pa}\cdot\text{s}$.

Table 7.2: Ratios describing the effect of deformation on both internal and external torques. The numerical values correspond to an interior model for which the Love numbers are defined in Figures 7.1 and 7.2 at a shell thickness of 40 km.

Ratio	Relevant to	Value [-]
ψ^s	$\Gamma_{J,z}^s$	0.3781
ψ^m	$\Gamma_{g,z}^m, \Gamma_{J,z}^m$	0.0149
ψ^l	$\Gamma_{g,z}^s, \Gamma_{p,z}^s$	0.0155
ζ^{m+}	$\Gamma_{p,z}^m$	0.0135
$\frac{\xi_d^s}{\xi_c^s}$	$\Gamma_{g,z}^s$	-1.8979
$\frac{\xi_d^m}{\xi_c^m}$	$\Gamma_{g,z}^m, \Gamma_{p,z}^m$	0.5493
$\frac{h_2(r_{o,w}, t)}{h_f(r_{o,w})}$	$\Gamma_{p,z}^s, \Gamma_{pJ,z}^s$	0.5736
$\frac{h_2(r_{o,m}, t)}{h_f(r_{o,m})}$	$\Gamma_{p,z}^s, \Gamma_{pJ,z}^m$	0.0152
$\frac{h_2(r_{o,c}, t)}{h_f(r_{o,c})}$	$\Gamma_{p,z}^s, \Gamma_{pJ,z}^m$	0.0421

- The magnitude of internal torques is enhanced by the tidal deformation experienced by the shell (see Equations 7.32, 7.35, 7.41 and 7.42, keeping in mind that $2e$ is usually orders of magnitude larger than α_z^s and α_z^m even in the rigid case). Stronger internal coupling, which is mainly caused by the gravitational and pressure torques induced by the rigid mantle on the tidally deformed part of the shell, is expected to reduce the amplitude of the forced libration of the shell to values more common for the amplitude of the mantle libration. This effect on the libration of Europa's shell was neglected in Goldreich and Mitchell [2010].

7.5. RESULTS

Before we analyze the effect of deformation on surface librations, we shortly discuss the case in which internal solid layers behave as rigid bodies. In the rigid case, the tidal Love number h_2 is equal to zero at all considered internal boundaries and at the surface. Hence, Equations 7.52 and 7.53 reduce to their rigid counterparts (see e.g. the libration model described in [Baland and Van Hoolst, 2010]). Application of our libration model in the rigid limit to the interior models of Europa defined in Table 7.1 results in the square-shaped markers shown in Figure 7.3. There, we observe that the amplitude of the shell's rigid libration decreases exponentially from $\sim 18,000$ m for a 5 km shell to ~ 500 m for a 100 km shell. The large values for the rigid librations of thin shells are caused by a 1:1 resonance between the forcing frequency n and the natural libration frequency of the shell, which takes place at a shell thickness of ~ 2 km. For all analyzed values for the thickness of the shell, the amplitude of the shell's rigid librations considerably exceeds the values corresponding to the librations of a rigid mantle (about 87 – 95 m at the surface) and the libration of a rigid Europa without a subsurface ocean (~ 133 m). This large difference suggests that the libration of a rigid shell would be largely decoupled from the libration

of a rigid deep interior.

However, as shown in Figure 7.2, the response of Europa's internal solid layers to the acting diurnal forcing cannot be considered rigid but rather elastic. As briefly mentioned in Section 7.4 and shown in Figure 7.3, diurnal deformation induced on Europa's internal layers by e.g. tides and the librations themselves leads to a considerable decrease in the amplitude of the forced libration of Europa's shell relative to the case of a rigid shell. In the particular case of our reference models of Europa's interior, for which the libration amplitude is depicted by the star-shaped markers in Figures 7.3 to 7.7, the libration amplitude of the shell decreases by ~75% to ~99% if deformations are taken into account, with the largest amplitude reduction corresponding to the libration of very thin ice shells. The larger decrease in amplitude towards smaller values for the shell thickness is partially due to the effect of deformation on lowering the natural libration frequency of the shell. As a result, the resonance peak in the libration-thickness curve will be shifted towards smaller values for the thickness of the shell if deformation is taken into account.

The amount of deformation experienced by the shell, and hence the libration amplitude, depends on several geophysical parameters characterizing the interior, such as the rigidity, thickness and density of the shell, and to a lesser extent the density of the ocean and the rigidity of the silicate mantle. In order to analyze how uncertainties in

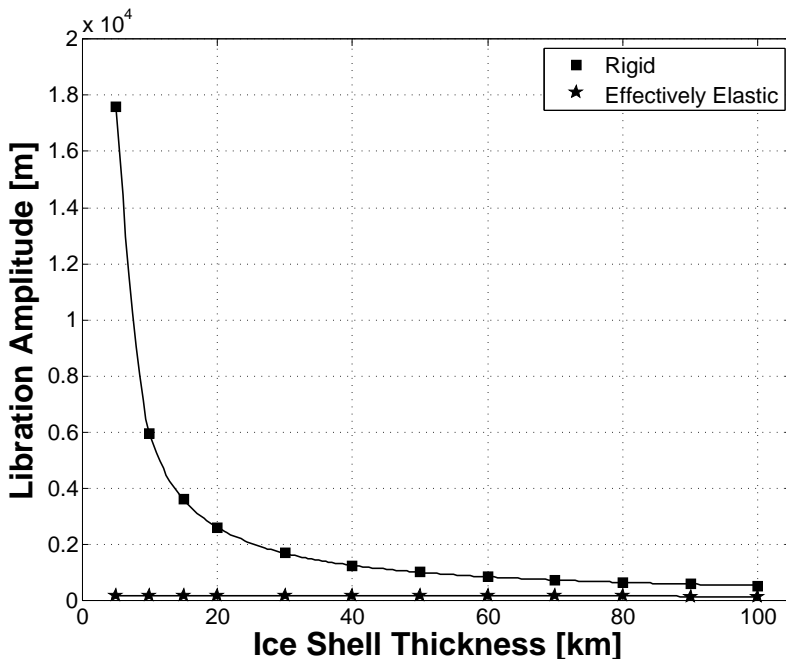


Figure 7.3: Amplitude of Europa's shell longitudinal libration at the equator as a function of the thickness of the entire ice-I layer for two different cases: (squares) shell and rocky interior behave as rigid bodies; and (stars) shell and rocky interior experience deformation. In both cases the geophysical parameters of the interior - except the rigidity and viscosity - are the same as for our reference models of Europa's interior.

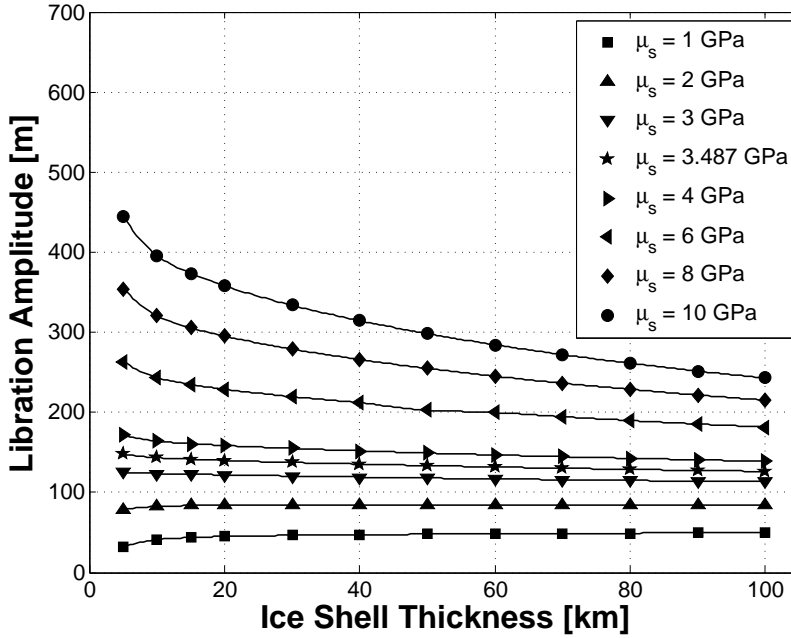


Figure 7.4: Amplitude of the longitudinal libration of Europa's ice shell at the equator as a function of the thickness of the entire ice-I layer for values of the rigidity of ice ranging from 1 GPa to 10 GPa. The densities of the shell and ocean are fixed at $950 \text{ kg}\cdot\text{m}^{-3}$ and $1000 \text{ kg}\cdot\text{m}^{-3}$, respectively.

one of these parameters may influence the amplitude of the forced libration of the shell, we apply our libration model to a set of interior models in which only the geophysical parameter we are interested in (i.e. either ρ_s , ρ_w or μ_s for the moment) and the shell thickness are considered to be variable. The remaining parameters are kept fixed to their reference values, which have been previously defined in Section 7.4. The dependence of the libration amplitude of the shell on the shell thickness is illustrated in Figures 7.4 to 7.7 for different values of μ_s , ρ_s and ρ_w .

As can be inferred from Figures 7.4 to 7.7, the geophysical parameter with the largest influence on the amplitude of the shell libration is its poorly constrained rigidity. This parameter is uncertain by roughly one order of magnitude, with values as low as 0.4 GPa [Nimmo and Schenk, 2006, Wahr et al., 2006] (for a porous ice shell) and as high as 10 GPa [e.g. Moore and Schubert, 2000] being previously assigned to it. This large uncertainty in the value of the rigidity leads to similar order of magnitude variations in the amplitude of the libration, as can be observed in Figure 7.4 for the range $\mu_s = 1 - 10$ GPa. In addition, the rigidity influences the dependence of the libration amplitude on the thickness of the shell. As can be inferred from Figure 7.4, the decreasing behavior of the libration amplitude with increasing shell thickness becomes less pronounced as the rigidity of the shell decreases (e.g. the libration of a 100 km thick shell is 32.1% smaller in amplitude than the libration of a 10 km shell if the rigidity is equal to 10 GPa, while it would be only

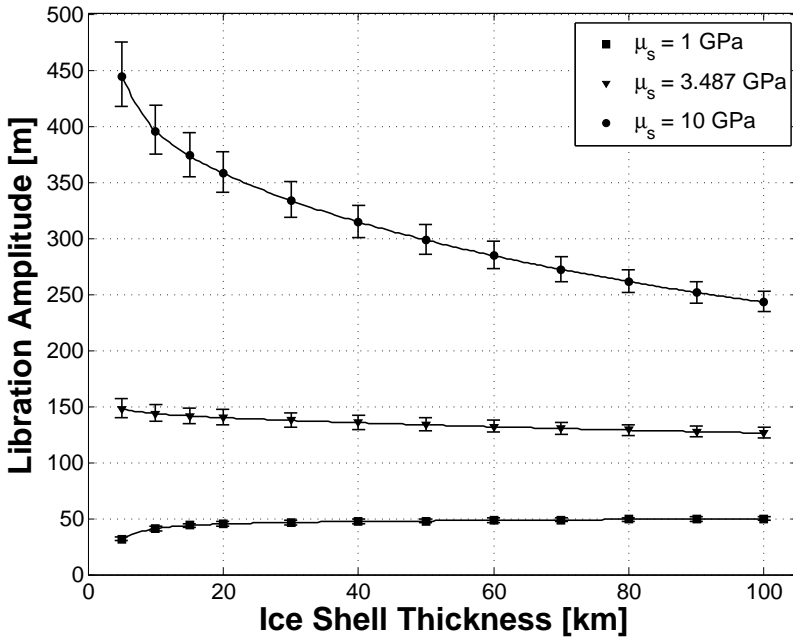


Figure 7.5: Amplitude of the longitudinal libration of Europa's ice shell at the equator as a function of the thickness of the ice-I layer for ice rigidities $\mu_s = 1$ GPa, 3.487 GPa and 10 GPa. The solid lines correspond to the reference value for the shell density ($\rho_s = 950 \text{ kg}\cdot\text{m}^{-3}$) and the error bars represent the effect of the introduced $\pm 50 \text{ kg}\cdot\text{m}^{-3}$ uncertainty in the density of the shell, with the upper bound corresponding to $\rho_s = 900 \text{ kg}\cdot\text{m}^{-3}$ and the lower bound to $\rho_s = 1000 \text{ kg}\cdot\text{m}^{-3}$. The density of the ocean is fixed at $1000 \text{ kg}\cdot\text{m}^{-3}$.

9.8% smaller if the rigidity would be equal to 3.487 GPa). For rigidities smaller than ~ 2 GPa, the libration amplitude does not longer decrease with increasing thickness but it increases towards a nearly constant value, as illustrated in Figure 7.4 for e.g. $\mu_s = 1$ GPa.

Furthermore, as shown by the size of the error bars in Figure 7.5, uncertainties in the density of the shell may also lead to significant variations in the amplitude of the shell libration. Taking into account that the upper bound of each error bar in Figure 7.5 corresponds to a density of $900 \text{ kg}\cdot\text{m}^{-3}$ and the lower bound to a density of $1000 \text{ kg}\cdot\text{m}^{-3}$, we can infer that the decrease of the libration amplitude with increasing density is slightly more pronounced for models with a large value for the rigidity of the shell (7.1 – 10.5% decrease in amplitude for $\mu_s = 10$ GPa against 5.8 – 8.2% decrease in amplitude for $\mu_s = 1$ GPa)². The dependence of the libration amplitude on the shell density is thus less sensitive to variations in the rigidity than the dependence on the shell thickness. Hence, the effect of uncertainties in the shell density on the libration amplitude may become as important as uncertainties in the shell thickness for low values for the shell rigidity, as

²In absolute sense, the uncertainty in the density leads to more pronounced variations in the libration amplitude for models with a high value for the rigidity of ice-I. This is expected as the libration amplitude strongly increases with increasing rigidity (see Figure 7.4).

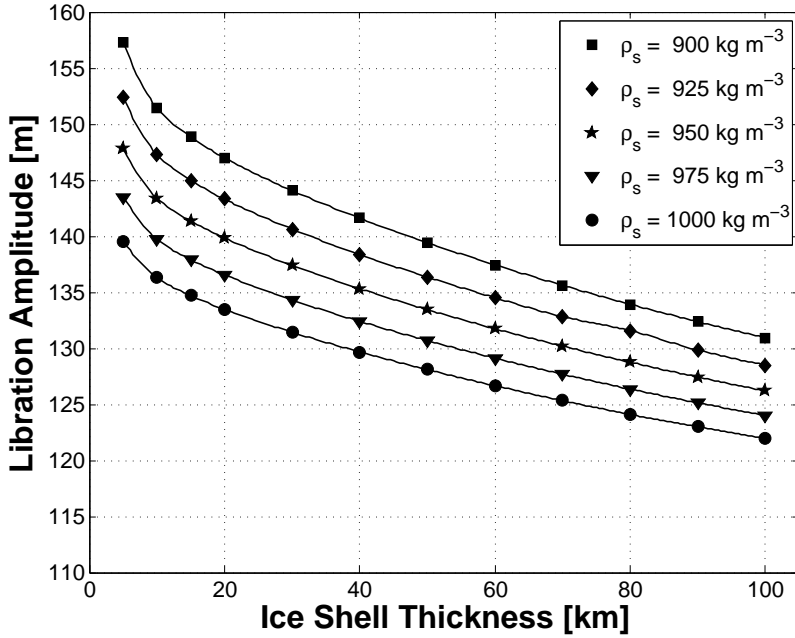


Figure 7.6: Amplitude of Europa’s shell longitudinal libration at the equator as a function of the thickness of the entire ice-I layer for values of the density of the shell ranging from 900 kg m^{-3} to 1000 kg m^{-3} . The density of the ocean is fixed at 1000 kg m^{-3} and the rigidity of the shell is taken to be 3.487 GPa .

shown in Figure 7.6 for $\mu_s = 3.487 \text{ GPa}$.

Other interior parameters, such as the ocean density and the rigidity of the silicate mantle, have a smaller effect on the amplitude of the shell libration. As an example, we show in Figure 7.7 that uncertainties in the density of the ocean ($\rho_w = 950\text{--}1150 \text{ kg m}^{-3}$) lead only to 3–5.4% variations in the amplitude of the shell libration if $\mu_s = 3.487 \text{ GPa}$. The induced variations in the libration amplitude are about 40–50% smaller in magnitude than the variations induced by uncertainties in either the shell thickness (8.1%) or the shell density (6.9–10%) for the same value of the rigidity.

So far in this paper we have focused our analysis on interior models of Europa for which the diurnal tidal response is effectively elastic. However, modeling of the thermal state of Europa’s shell [e.g. Hussmann et al., 2002, Tobie et al., 2003, Mitri and Showman, 2005, Moore, 2006, Nimmo and Manga, 2009, Sotin et al., 2009] and the morphology of impact craters [Schenk, 2002, Schenk and Turtle, 2009] suggests the existence of a warm, ductile and low-viscous ice-I asthenosphere covering at least the lower 50% of the icy shell. The viscosity of this layer would be nearly constant and its value would be close to the viscosity of ice-I near the melting point, i.e. between 10^{13} Pa s and 10^{15} Pa s depending on the grain size [Tobie et al., 2003]. Taking into account the defined range of values for the rigidity of ice, we see that the Maxwell time $\tau_M = \eta_s/\mu_s$ of this low-viscous layer could become smaller or comparable in magnitude to Europa’s orbital period T .

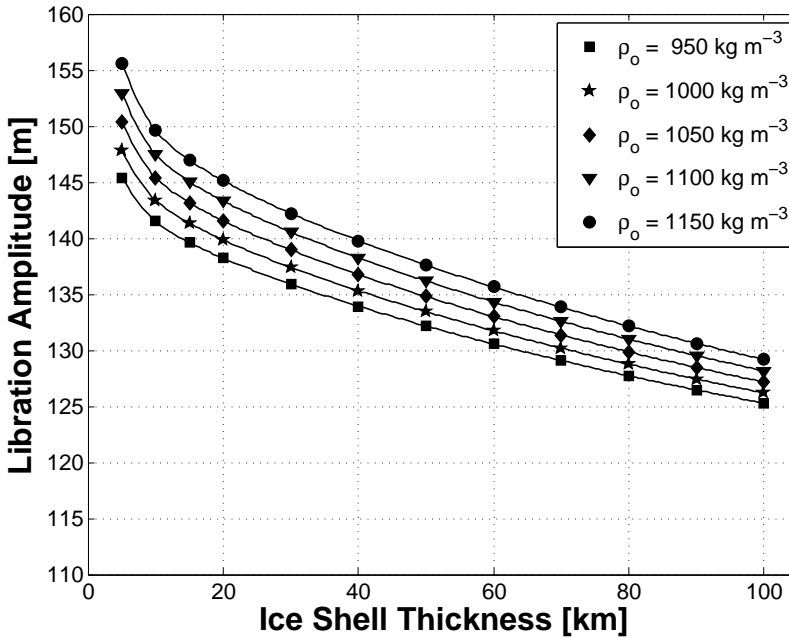


Figure 7.7: Amplitude of Europa's shell longitudinal libration at the equator as a function of the thickness of the entire ice-I layer for values of the density of the ocean ranging from $950 \text{ kg}\cdot\text{m}^{-3}$ to $1150 \text{ kg}\cdot\text{m}^{-3}$. The density of the shell is fixed at $950 \text{ kg}\cdot\text{m}^{-3}$ and the rigidity of the shell is taken to be 3.487 GPa .

The diurnal response of the interior will be then characterized by the presence of normal modes with a fast relaxation time τ_j : the so-called transient modes. As shown in e.g. [Jara-Oru  and Vermeersen \[2011\]](#), the strongest of these transient modes may introduce substantial viscoelastic relaxation in the diurnal response of Europa, especially if the ratio $2\pi\tau_j/T$ is close to 1.

Here we opt to analyze the effect of viscosity on the amplitude of the shell libration at three different values for the shell rigidity (1 GPa , 3.487 GPa and 10 GPa), as it has been previously shown that the unconstrained rigidity has the largest effect on the libration amplitude (see [Figures 7.4 and 7.5](#)). The other interior parameters, including the shell thickness, are then kept fixed to their reference values (see [Table 7.1](#)) and to an arbitrary value for the shell thickness (here we will perform our calculations on a 60 km thick shell). As shown in [Figure 7.8](#) for $\mu_s = 1 \text{ GPa}$, 3.487 GPa and 10 GPa , the amplitude of the shell libration decreases with decreasing viscosity in a way that clearly reflects the use of a Maxwell rheology. For large viscosities, the relaxation time of the strongest transient mode is much larger than the orbital period and hence the ratio $2\pi\tau_j/T$ is much larger than one. As a result, the entire shell behaves in an effectively elastic way and the libration amplitude will not differ significantly from the purely elastic case. For viscosities in the range $\sim 10^{13} - 10^{15} \text{ Pa}\cdot\text{s}$, the relaxation time of the strong transient mode is such that the ratio $2\pi\tau_j/T$ is close to one. In this viscosity range, substantial viscoelastic

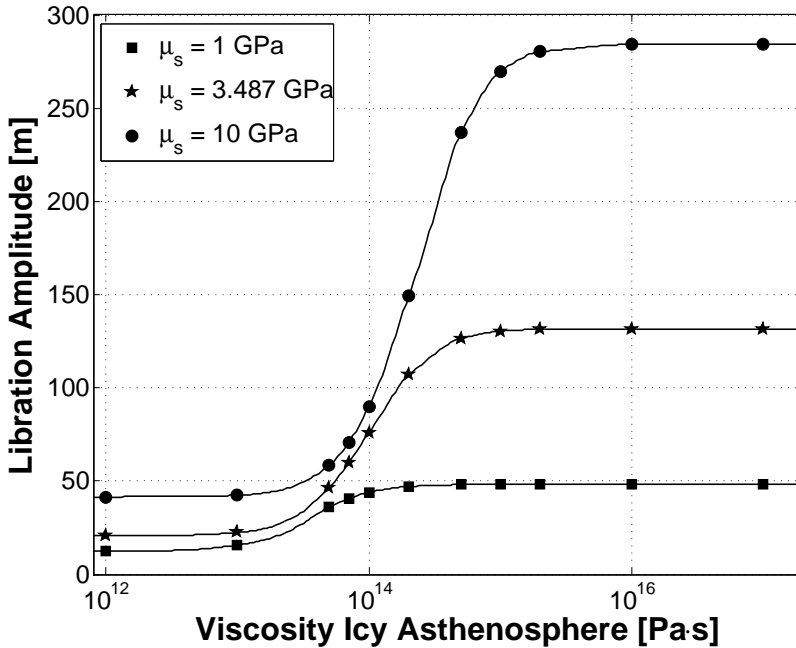


Figure 7.8: Amplitude of Europa's shell longitudinal libration at the equator as a function of the viscosity of the bottom part of the ice shell for a 60 km thick shell with $\mu_s = 1, 3.487$ or 10 GPa. Other interior parameters are defined by the reference values in Table 7.1.

relaxation takes place in the shell and the libration amplitude is strongly attenuated, as shown in Figure 7.8. For smaller viscosities, the bottom part of the shell shows a rather fluid behavior ($2\pi\tau_j/T$ much smaller than one) and hence the libration amplitude starts to converge to a constant value which is much lower than the one corresponding to the effectively elastic case. Furthermore, as can be observed from Figures 7.5 and 7.8, the range of possible values for the amplitude of the shell libration due to the unknown viscosity of the bottom part of the shell (for a fixed value for the rigidity) may be considerably larger than the range introduced by uncertainties in the thickness and/or density of the shell.

7.6. DISCUSSION AND CONCLUSIONS

In this paper we have analyzed the effect that deformation of Europa's internal solid layers has on the forced longitudinal libration of Europa's ice shell. Deformation of Europa's internal solid layers, which is primarily caused by the acting diurnal tides, leads to additional asymmetries in the mass distribution within a layer. As mentioned in Section 7.4, Jupiter's gravitational torque on these asymmetries (or diurnal bulge) counteracts the torque on the hydrostatic figure, thereby reducing the magnitude of the total ex-

ternal gravitational torque acting on a layer. In addition, internal coupling torques are enhanced by the additional torque induced on the diurnal bulge of the shell by the hydrostatic bulge of the silicate mantle (and vice versa). In the case of Europa's shell, which experiences more deformation than the mantle at diurnal timescales, the combination of weaker external forcing and enhanced internal coupling leads to a considerable decrease of its libration amplitude relative to the case of a rigid shell (see e.g. Figure 7.3). Our conclusions here are in agreement with the ones by [Van Hoolst et al. \[2013\]](#).

In Section 7.5 we have analyzed how the forced libration of Europa's shell depends on uncertainties in the value of geophysical parameters that describe the structural and rheological properties of internal layers, such as the thickness, density, rigidity and viscosity of the shell, the density of the ocean and the rigidity of the silicate mantle. From all investigated parameters, we have shown that the poorly constrained rigidity of the shell has the largest influence on the libration amplitude of Europa's shell. As can be observed in e.g. Figures 7.4 and 7.5, a one order uncertainty in the value of the rigidity of the shell leads to a similar order of magnitude uncertainty in the amplitude of the shell libration. This effect on the libration amplitude is much larger than the one introduced by uncertainties in the shell thickness and/or shell density, as can be clearly observed in Figure 7.5. In addition, as shown in Figure 7.8, the unknown viscosity of the lower part of Europa's shell introduces a significantly large uncertainty in the libration amplitude, that could be almost as large as the uncertainty introduced by the rigidity. Hence, we can state that the libration amplitude of Europa's shell is mostly sensitive to the poorly constrained rheological properties of the shell.

In agreement with [Van Hoolst et al. \[2013\]](#), we thus find that the libration amplitude of the shell does not depend in a simple way on parameters that characterize the internal structure of Europa. If we compare the results presented in [Van Hoolst et al. \[2013\]](#) to our results for effectively elastic models with shell rigidity of 3.487 GPa (curves with star-shaped markers in Figures 7.4 to 7.7), we notice that both studies reach the same conclusions, namely: 1) the libration amplitude weakly decreases with increasing shell thickness and 2) a slight decrease in the libration amplitude is observed for an increasing shell density. Furthermore, the obtained numerical values for the libration amplitude differ by less than 1% if both libration models would be applied to the same interior models of Europa (based on a benchmarking session). In addition, although both libration models treat Europa's core in a different way (we consider the core to be fluid whereas [Van Hoolst et al. \[2013\]](#) assume a solid core), no difference in the resulting libration amplitude has been observed. Therefore, as expected, we can state that the physical state of the core does not affect the libration amplitude of the shell.

Despite the agreements with the results shown in [Van Hoolst et al. \[2013\]](#) for a rigidity of 3.487 GPa, we should not forget that their conclusions on the dependence of the shell libration amplitude on the shell thickness and density are limited to the value chosen for the rigidity of the shell. As we have shown in Section 7.5, the libration amplitude does not always decrease with increasing shell thickness (Figure 7.4 clearly shows that the libration amplitude would increase with increasing shell thickness for rigidities smaller than ~ 2 GPa). Furthermore, the libration amplitude does not show a weak dependence on the shell thickness for large values for the rigidity of the shell, as also shown in Figure 7.4. In this sense, our libration model complements the one of [Van Hoolst et al. \[2013\]](#)

by taking into account a large range of values for the rigidity (and viscosity) of the shell.

On the other hand, our values for the libration of an effectively elastic shell on Europa are about three times smaller in amplitude than the ~ 400 m predicted by Goldreich and Mitchell [2010] for the same rigidity ($\mu_s = 3.487$ GPa). This difference can be largely explained by the different assumptions taken regarding the deformation of the rocky interior at the frequency of the tidal forcing. In our case, the response of the rocky interior at the tidal frequency is nearly rigid (small amount of deformation), whereas Goldreich and Mitchell [2010] assume a simplified fluid water interior for their modeling. Therefore, in our modeling, internal coupling between the shell and the rocky interior will tend to lower the amplitude of the shell libration towards values that are more representative for the libration of the interior, while this effect has been neglected in the model by Goldreich and Mitchell [2010]. Moreover, in contrast to Goldreich and Mitchell [2010], the libration of Europa's icy shell in our modeling slightly decreases with increasing thickness of the shell for the same rigidity (see Figure 7.4). The dependence of the libration amplitude on the thickness of the shell in our models is introduced by the tidal Love numbers h_2 at both the surface and the ocean-ice boundary (see Figure 7.2), whereas in Goldreich and Mitchell [2010] the Love numbers do not depend on the thickness of the shell.

As a final point, we would like to discuss the implications that our libration results have on the characterization of Europa's ocean and ice shell from future libration observations. First of all, unambiguous detection of a subsurface ocean from libration observations would only be possible if the uncertainty region of future measurements of the libration amplitude does not include the 131 m predicted for an oceanless model, as both oceanless models and several models with a subsurface ocean (see e.g. Figure 7.6) would satisfy the performed measurement of the libration amplitude. If the existence of an internal ocean would be confirmed, our results suggest that libration observations could be used to constrain the rigidity of the shell due to the strong dependence of the libration amplitude on this parameter (see Figure 7.4). Furthermore, as the dependence of the libration amplitude on the thickness and density of the shell is weak in comparison to the dependence on the rigidity, libration observations would not provide any useful information about the thickness and density of the shell without previous determination of the shell rigidity. Therefore, as illustrated in Grasset et al. [2013] for the case of Ganymede, the characterization of Europa's icy shell and subsurface ocean will require a combination of observation techniques able to measure the tidal Love numbers k_2 and h_2 , the induced magnetic field and the libration amplitude.

Moreover, as shown in Figure 7.8, the lower viscosity of a low-viscous sublayer at the bottom of the shell may interfere with the determination of the shell rigidity from libration observations. In such case, observation of a phase-lag in the forced libration of the shell could be useful to retrieve some information about the rheological properties of the lower part of Europa's shell. These general conclusions would also apply to different viscosity profiles and/or more realistic rheological models, although the numerical values will certainly differ.

8

CONCLUSIONS AND RECOMMENDATIONS

In this final Chapter, the conclusions that arose from the modeling and analysis presented in previous Chapters will be summarized. Furthermore, this Chapter will provide a discussion on recommendations for further research that could be built upon the modeling developed in this thesis, as well as recommendations on research topics that might enhance the work described in this thesis.

8.1. CONCLUSIONS

The main objective of this research concerns the development of a consistent framework to deduce the geophysical properties that characterize the subsurface ocean and ice-I shell of icy satellites from future measurements of the radial displacements and gravity perturbations induced by the acting diurnal tides, as well as from the longitudinal librations forced by the gravitational torque of the satellite's parent planet on the triaxial figure of the satellite (Section 1.2). To this end, we developed an analytical model to determine the tidal response of a viscoelastic icy satellite with an internal ocean (Chapters 2 to 4) and applied it for the calculation of tidal deformations and stresses at the surface of Ganymede¹ and Europa (Chapter 5). To be consistent with the modeling of the tidal response, we developed an analytical rotational model in which the contribution of deformations is expressed in terms of the determined tidal Love numbers (Chapter 6). This model is then applied to study the relation between longitudinal librations at the surface and the physical properties that characterize the internal structure of Europa (Chapter 7).

Although the model developed in this thesis may have been applied to any icy satellite with an internal ocean, the applications and discussions presented in this thesis have mainly focused on the study of the tidal response and rotational dynamics of Jupiter's

¹only tidal deformations

moon Europa (see Section 1.3). As a result, the conclusions in this Chapter will mostly address the case of Europa. This Chapter is subdivided in three parts: 1) Section 8.1.1 discusses the most relevant findings regarding the viscoelastic modeling of the tidal response of icy satellites, with a particular emphasis on the geophysical implications of the computed tidal Love numbers of Europa, 2) Section 8.1.2 summarizes the conclusions inferred from the modeling of the diurnal and NSR stresses at the surface of Europa, and 3) Section 8.1.3 presents a concise discussion on the geophysical implications of the modeled forced longitudinal librations of Europa's ice shell.

8.1.1. MODELING THE RESPONSE TO DIURNAL TIDES

In Chapters 3 and 4 we have presented an analytical method based on the normal mode technique to determine the time-dependent tidal Love numbers h_2 , l_2 and k_2 at the surface of a viscoelastic icy satellite with a global subsurface ocean. The developed method has been applied throughout Chapter 5 to various multilayer interior models of Europa and Ganymede; all of them built in accordance with the mean moment of inertia condition obtained from the measurement of the degree-2 gravity field under the assumption of hydrostatic equilibrium (Chapter 2). As such, it is important to remark that the results and conclusions achieved throughout this thesis only apply to icy satellites whose interior is in hydrostatic equilibrium and for which lateral heterogeneities in the internal structure can be neglected. Moreover, the results and conclusions in this thesis only apply to linear rheologies.

As pointed out in Chapter 5, the tidal Love numbers at the frequency of the acting diurnal tides are largely dominated by the elastic part of the response unless a low-viscosity and possibly convecting icy asthenosphere is present at the bottom of the ice-I shell. As a result, the amplitude of the radial deformation Love number h_2 (and the other Love numbers as well) is mostly sensitive to the uncertainties in the thickness and rigidity of the ice-I shell. Since the magnitude of the tidal Love numbers decreases with increasing thickness and/or increasing rigidity, the largest values for the Love number h_2 (i.e. $h_2 \sim 1.25$ for Europa and $h_2 \sim 1.5$ for Ganymede) are representative for interior models with a thin ice shell (i.e. about 10-30 km for Europa and 40-60 km for Ganymede) and a low value for the rigidity of ice (i.e. $\mu_I = 1$ GPa). On the other hand, the smallest values for the Love number h_2 (i.e. $h_2 \sim 0.65$ for Europa and $h_2 \sim 1.0$ for Ganymede) are representative for interior models with a thick shell (i.e. > 100 km for Europa and > 140 km for Ganymede) and a large value for the rigidity of ice (i.e. $\mu_I = 10$ GPa). For most values for the tidal Love number h_2 , however, many different combinations of thickness and rigidity are possible as the contribution of both parameters to the tidal response is difficult to separate (see Sections 5.1 and 5.3).

The sensitivity of the gravitational perturbation Love number k_2 at the frequency of the acting diurnal tides on the parameters that characterize the interior is a bit different. Like for h_2 , the Love number k_2 is mostly sensitive to the thickness and rigidity of the shell, but also to a large extent to the density of the internal ocean (see Sections 5.1 and 5.3). As shown in Section 5.1 for the case of Europa's tidal response, the magnitude of the tidal Love number k_2 can experience variations in the order 15–18% as a result of uncertainties in the density of the ocean. These variations are nearly of a similar order

as the ones induced by uncertainties in the thickness and/or rigidity of the ice-I shell on the magnitude of the k_2 tidal Love number at the surface. A similar uncertainty also applies to the case of Ganymede, as shown in Section 5.3. The large sensitivity of k_2 to uncertainties in the density of the ocean is in agreement with the results obtained by e.g. Baland et al. [2014] for the case of Titan, in which a possible explanation is given for the large value of k_2 ($k_2 = 0.589 \pm 0.150$ and $k_2 = 0.637 \pm 0.224$) obtained from observations of the acceleration of the Cassini spacecraft during six flybys (first value) and from a combination of radio-metric tracking and optical navigation data from Cassini, data from the Pioneer and Voyager Saturn encounters, and astronomical observations of Saturn and its satellites (second value) [Iess et al., 2012].

The presence of a low-viscosity ductile ice-I layer adds one extra poorly constrained parameter to our analysis, i.e. the viscosity of the ductile part of the shell. As shown in Sections 5.1 and 5.3, the sensitivity of the tidal Love numbers h_2 and k_2 to the large uncertainties in the viscosity of this layer is comparable to their sensitivity to the also poorly constrained rigidity. The effect of viscoelastic relaxation on the magnitude of the tidal Love numbers is largest for values for the viscosity of the icy asthenosphere close to the reference value at melting point ($\sim 10^{13}$ Pa s), as the behavior of the lower portion of the ice-I shell in response to the acting diurnal tides starts to approach the fluid limit. In addition, the introduction of a low-viscosity layer may lead to a phase lag in the tidal response, which can be a few degrees if a strong transient mode with a relaxation time comparable to the orbital period of the icy satellite is present in the viscoelastic response. Note, however, that the discussion presented here is based on our description of the rheology by application of the simple Maxwell model. Hence, the numerical results representing the sensitivity of the Love numbers on the rheology only apply to a Maxwell rheology and may be different if more complex - and perhaps more realistic - anelastic rheologies (Burgers, Andrade) are used in the modeling (see e.g. McCarthy and Castillo-Rogez [2013] for a discussion about rheological models for ice-I relevant to icy satellites).

Due to the complex dependence of the tidal Love numbers on the geophysical properties of the ice-I shell and ocean, it can be stated that future measurements of the tidal Love numbers h_2 and k_2 of either Europa or Ganymede will most likely not allow for the unambiguous determination of the shell thickness. As shown in Figure 5.9 for an hypothetical measurement of Europa's tidal Love numbers ($h_2 = 1.12 \pm 0.01$ and $k_2 = 0.23 \pm 0.0014$), the determination of h_2 and k_2 have the potential to provide a rather good constraint on the density of the ocean but would fail to constrain the thickness of the ice shell, mainly as a consequence of the poorly known rigidity and viscosity of the ice shell. Additional independent measurements, such as of the forced longitudinal librations (see Section 8.1.3) and observations by the ice-penetrating radar, would be then required to discriminate between the rheological properties of the shell and the thickness.

8.1.2. SURFACE STRESSES INDUCED BY DIURNAL AND NSR TIDES ON EUROPA

The main goal behind the modeling of tidal stresses at Europa's surface is to study the origin and formation of observed tectonic features, such as global lineaments and cy-

clouds. Irrespective of their morphology, these features are thought to have formed as a result of tensile failure of Europa's icy surface [Greenberg et al., 1998]; which is expected to occur when the acting tensile stresses exceed the tensile strength of the surface ice. As shown in Section 5.4.4, the magnitude of diurnal stresses at the surface of an oceanless Europa never becomes large enough to exceed the lower range of plausible values for the tensile strength of ice (~ 40 kPa). Failure of the icy surface due to solely diurnal stresses, as suggested by the existence of numerous cycloidal lineaments on Europa's surface, would therefore require the existence of a subsurface ocean. The presence of a subsurface ocean does not implicitly guarantee that the acting diurnal stresses can be large enough to cause tensile failure of the icy surface. As discussed in Section 5.4.4, the magnitude of diurnal stresses may only lead to mechanical failure if the tensile strength of the surface ice is less than ~ 300 kPa. This condition suggests that the formation of cycloidal features as a sole response to diurnal tides would require the existence of a contaminated and porous upper lithosphere, as such values for the tensile strength of ice are too low to be representative for non-contaminated and non-porous ice [e.g. Lee et al., 2005].

If one takes into account that a subsurface ocean decouples the rotational motion of Europa's ice shell from the motion of the deep interior (i.e. mantle and core), tensile stresses up to several MPa might be induced at the surface. As shown in Section 5.4.4, the exact magnitude of the induced stresses is largely dictated by the rheological properties of the icy lithosphere and the rate of non-synchronous rotation. Since NSR is assumed to be a relatively slow process ($> 10^4$ years), the magnitude of NSR stresses at Europa's surface can be severely attenuated by viscoelastic relaxation in the uppermost layer. The amount of viscoelastic relaxation acting on NSR stresses is physically described by the parameter Δ , which is directly proportional to the ratio between the period of NSR and the Maxwell time of the lithosphere (see Equation 4.70). As shown in e.g. Figure 5.23, an increase of the value of Δ from $\Delta = 0.1^2$ to $\Delta = 100$ leads to a decrease of the magnitude of the tensile stresses by around two orders of magnitude.

NSR stresses do not act independently on Europa's surface but are superimposed on the ever-acting diurnal stresses. Variations in the value of Δ , i.e. in the relaxation state of NSR stresses, can reduce or enhance the importance of NSR stresses relative to diurnal stresses and lead to changes in the spatial and temporal distribution of the combined stress field. Without the effect of viscoelastic relaxation (i.e. $\Delta < 0.1$), NSR stresses would be around two orders of magnitude larger than diurnal stresses. Hence, the spatial and temporal distribution of the combined stress field will be dominated by the static NSR stress field. On the other hand, as shown in some detail in Section 5.4.4, the increase of the effect of viscoelastic relaxation on NSR stresses with increasing Δ allows for the existence of combined stress fields with diurnal-like properties, especially for values of Δ larger than ~ 30 .

The combined NSR-diurnal stress field can be used to analyze the formation of the diverse lineament morphologies observed on Europa's surface. On one hand, the formation of long arcuate lineaments requires either a slowly-changing stress field or unrealistically fast crack propagation speeds. On the other hand, the formation of cycloidal features requires a highly-variable stress field and slow crack propagation speeds. An in-

²NSR stresses are stored elastically for this value of Δ

interesting characteristic of Europa's surface is that cycloidal features coexist with global arcuate lineaments, implying variations of the relaxation parameter Δ throughout the geological history of Europa's surface. As discussed in Section 5.4.5, temporal variations of the relaxation parameter Δ can either be caused by secular variations in the rotation rate of Europa's ice shell, temporal variations in the rheological properties of the surface ice, or both. Changes in tidal heat dissipation with time, due to e.g. the time evolution of the orbit's eccentricity [Husmann and Spohn, 2004], could then lead to changes in the ice shell thickness distribution with time, affecting Europa's rotation rate (through the principal moments of inertia of the shell) and thereby the relaxation parameter Δ . Moreover, the same changes in tidal dissipation could also induce variations in the viscosity of the icy surface and Δ [Wahr et al., 2009]. Consequently, it can be stated that variations of the relaxation parameter Δ as a function of time would require the existence of a dynamic ice layer covering a subsurface ocean.

In addition, we have shown in Section 5.4.4 that diurnal stresses at Europa's surface might experience the effects of viscoelastic relaxation of the asthenosphere, mainly in the form of a longitudinal shift of the surface stress patterns. However, the relevance of the viscoelastic effect is limited to interior models with a thick and highly dissipative asthenosphere. On timescales relevant for NSR ($> 10^4$ years) the magnitude and phase shift of NSR surface stresses can be affected by viscoelastic relaxation of the ice/shell boundary. This effect, however, becomes only important when the behavior of the lithosphere with respect to NSR approaches the fluid limit, i.e. for strong relaxation in the lithosphere (i.e. $\Delta \sim 100$ or larger).

Furthermore, we have shown in Section 5.4.4 that a small obliquity can have a considerable effect on Europa's diurnal stress field. A non-zero obliquity breaks the symmetric distribution of stress patterns with respect to the equator, thereby affecting the magnitude and orientation of the principal stresses at the surface. As expected, increasing the value of Europa's obliquity leads to larger diurnal stresses at the surface, especially when Europa is located 90° away from the nodes formed by the intersection of its orbital and equatorial planes.

8.1.3. LONGITUDINAL LIBRATIONS OF EUROPA'S ICE SHELL

Prior to Goldreich and Mitchell [2010], all differential rotational models dealing with the study of the forced longitudinal librations of Europa (and other icy satellites with a subsurface ocean) assumed that internal solid layers behave as rigid bodies at the timescale of the orbital motion of the satellite [see e.g. Van Hoolst et al., 2008, Baland and Van Hoolst, 2010, Rambaux et al., 2011]. Application of these early models to the libration of Europa's shell led to estimates for the amplitude of the forced libration ranging from ~ 500 m for a 100 km thick shell to $\sim 40,000$ m for a 5 km shell [Baland and Van Hoolst, 2010]. Irrespective of the thickness of the shell, the derived values were significantly larger than the value predicted for the forced libration of an entirely solid Europa (~ 133 m [Comstock and Bills, 2003, Van Hoolst et al., 2008, Rambaux et al., 2011]), thereby suggesting that the thickness of the ice shell could be constrained by measurements of the libration amplitude to within a few kilometers [Baland and Van Hoolst, 2010]. However, as noted by Goldreich and Mitchell [2010], these early results were very optimistic as the

used rotational models neglected the effect of elastic deformation in Europa's ice shell. Using a thin shell approach, in which the shell behaves elastically and all internal layers below the shell are assumed to be fluid, Goldreich and Mitchell [2010] suggest that elastic deformation of Europa's shell would considerably diminish the amplitude of the shell libration to ~ 400 m, irrespective of the thickness of the shell.

As mentioned in Section 1.2, the main purpose of this thesis is to develop a consistent rotational and tidal model to deduce the geophysical properties of Europa's upper layers (i.e. the internal ocean and the overlying ice-I shell) from future measurements of the radial displacements and gravity perturbations induced by the diurnal tides exerted by Jupiter on Europa, as well as from the longitudinal librations forced by Jupiter's gravitational torque on Europa's triaxial shape. However, as mentioned in the previous paragraph, existing approaches to determine the libration amplitude of Europa's shell are not compatible with the framework presented in Chapters 3 and 4 to model the viscoelastic response of an icy satellite to the acting tides. Hence, the key part of this thesis involved the introduction of the developed Love number framework into differential rotation models to study the effect of elastic and viscoelastic deformation on the libration dynamics of Europa's ice shell. The resulting rotation model, which is compatible with the model of Van Hoolst et al. [2013] in the elastic limit, is described in detail in Chapters 6 and 7.

Using the developed rotation model, we determined the amplitude of the shell libration of numerous models of Europa's interior in order to analyze the sensitivity of the computed libration to uncertainties in the value of geophysical parameters that describe the structural and rheological properties of the interior. As discussed in Section 7.6, the libration amplitude is most sensitive to the poorly constrained rigidity of the ice-I shell as the order of magnitude uncertainty in the value of the rigidity of the shell leads to a similar order of magnitude uncertainty in the amplitude of the shell libration (see Figure 7.4). This effect on the libration amplitude is much larger than the one introduced by uncertainties in the shell thickness and/or shell density (see Figure 7.5). Moreover, the dependence of the libration amplitude on the thickness of the ice shell follows different patterns depending on the assumed value for the rigidity of the ice-I shell. For values of the rigidity of ice-I (μ_I) larger than ~ 2 GPa, a range that includes the reference value $\mu_I \approx 3.5$ GPa obtained from laboratory experiments on several samples of natural and artificial ice, the amplitude of the forced libration of the shell decreases with increasing thickness of the shell. On the other hand, for rigidities smaller than ~ 2 GPa, the libration amplitude would decrease with increasing thickness of the shell.

In addition, as shown in Figure 7.8, the unknown viscosity of the lower ductile part of Europa's shell introduces a large uncertainty in the libration amplitude, that could be comparable to the uncertainty introduced by the rigidity, especially for the upper range of tested values for the rigidity of the ice-I shell. As a result, it can be stated that the amplitude of the forced libration of a deformable Europa with a subsurface ocean is mostly sensitive to the poorly constrained rheological properties of the ice-I shell, rather than the thickness of the ice shell.

As a final point, we would like to discuss the implications that our libration results have on the characterization of the geophysical properties of Europa's ocean and ice shell from future observations of the libration amplitude of Europa's shell. First of all, unam-

Table 8.1: Tidal Love numbers (h_2 and k_2) and libration amplitudes for the interior models of Europa that satisfied the hypothetical measurement $h_2 = 1.12 \pm 0.01$ and $k_2 = 0.23 \pm 0.0014$ shown in Figure 5.9. For all models the density of the ocean is $\rho_w = 1000 \text{ kgm}^{-3}$ and the density of the shell is $\rho_I = 937 \text{ kgm}^{-3}$. The symbols μ_I and η_{ast} refer to the rigidity of the ice-I shell and the viscosity of the asthenosphere, respectively.

Ice Thickness (km)	μ_I (GPa)	η_{ast} (Pa·s)	h_2 (-)	k_2 (-)	Libration Amplitude (m)
30	5.0	1.0E17	1.1114	0.2306	190.3
40	3.5	1.0E17	1.1174	0.2316	137.3
70	2.0	1.0E17	1.1101	0.2293	84.9
110	3.5	1.0E14	1.1169	0.2295	78.3
120	1.0	1.0E17	1.1156	0.2291	51.0

biguous detection of a subsurface ocean from libration observations would only be possible if the uncertainty region of future measurements of the libration amplitude does not include the ~ 131 m predicted for a deformable oceanless model, as both oceanless models and several models with a subsurface ocean would satisfy the performed measurement of the libration amplitude (see Section 7.5). If the presence of an internal ocean would be confirmed by other independent observations, the results presented in Chapter 7 strongly suggest that the measurement of the libration amplitude of Europa's shell has the potential to provide a reasonable constraint on the rigidity of the ice-I shell in combination with measurements of the tidal Love numbers h_2 and k_2 (see Section 8.1.1). For example, Table 8.1 shows that the interior models that satisfied the hypothetical measurement $h_2 = 1.12 \pm 0.01$ and $k_2 = 0.23 \pm 0.0014$ (see Figure 5.9) are characterized by a widespread range of values for the libration amplitude. As such, measurements of the libration amplitude with an accuracy in the order of several meters [see e.g. Baland and Van Hoolst, 2010] would be able to discriminate between the models in Table 8.1. However, the set of interior models analyzed is too sparse to support a strong conclusion regarding whether the ice shell thickness could be inferred from combined measurements of the libration amplitude and tidal Love numbers at the surface of Europa.

Moreover, as shown in Figure 7.8, the lower viscosity of a low-viscous sublayer at the bottom of the shell may interfere with the determination of the shell rigidity from libration observations. In such case, observation of a phase-lag in the forced libration of the shell could be useful to retrieve some information about the rheological properties of the lower part of Europa's shell. These general conclusions would also apply to different viscosity profiles and more complex rheological models, although the numerical values will certainly differ.

8.2. RECOMMENDATIONS

The research presented in this thesis has not only led to the numerous important results and conclusions discussed in the previous Section, but also to several questions and ideas that are recommended for further research. As shortly mentioned in Section 8.1.3, one important recommendation is to apply the modeling presented in this thesis

to determine the libration amplitude and tidal response (i.e. the tidal Love numbers h_2 and k_2 at orbital frequency) of a wide variety of interior models of Europa and Ganymede in order to assess whether the measurement of these physical parameters by future missions such as ESA's JUICE and NASA's Europa Multiple-Flyby Mission could constrain the thickness of the ice-I shell, as suggested in this thesis. Selected instruments that need to be involved in this assessment are [Grasset et al., 2013, Phillips and Pappalardo, 2014]:

1. laser altimeter, which is aimed to provide observations of the vertical deformation due to the acting diurnal tides (i.e. the Love number h_2) and of variations in the spin of the satellite (i.e. longitudinal librations);
2. radio science package, which is aimed to measure the low degrees of the gravity field as well as the gravitational perturbation due to the acting diurnal tides (i.e. the Love number k_2);
3. ice-penetrating radar, which is aimed to provide direct constraints on the material properties of the upper ~ 10 km of the ice shell and maybe even detect the transition depth to a global ocean if the shell is thinner than ~ 10 km;
4. magnetometer, which is aimed to measure the conductivity of the subsurface ocean, from which its depth and density may be retrieved;
5. cameras, which are aimed to provide images of control points (surface features) at the surface during the lifetime of the mission, from which rotational variations (e.g. forced longitudinal librations) can be retrieved.

Furthermore, it is recommended to extend the differential rotation model developed in Chapter 6 to study other interesting aspects of the rotational behavior of icy satellites, such as: librations at frequencies different from the orbital motion, the evolution of the spin's axis obliquity, non-synchronous rotation (NSR) and true polar wander (TPW). To this end, it is necessary to define explicit expressions for the inertia increments, coupling torques and external forces that are consistent with the Love number framework introduced in Chapter 3. The resulting extended differential rotational models can then be applied to a wide range of interior models of icy satellites in order to analyze whether future observations of these rotational variations, e.g. by the use of control-point measurements delivered by long-term imaging of the surface [see e.g. Thomas et al., 2016], can provide further insight into the internal stratification of icy satellites as well as some hints about their evolution.

In Chapter 7 we studied the longitudinal libration response of Europa from a purely Keplerian perspective. However, the purely Keplerian orbit of any icy satellite experiences perturbations caused by the gravitational interaction with other satellites, the Sun and the oblateness of the parent planet [Lainey et al., 2006, Rambaux et al., 2011]. These perturbations lead to a multi-frequency librational response that can be roughly separated into two groups of terms: 1) short-periodic terms with a period close to the orbital period, and 2) long-periodic terms caused primarily by the interaction with other celestial bodies. As shown in Chapter 7, the study of short-periodic libration terms is interesting from a geophysical perspective as the amplitude of these terms can be related to the properties of the ice shell and underlying ocean [see also Van Hoolst et al., 2013, Richard

et al., 2014, Thomas et al., 2016]. On the other hand, the study of long-periodic terms is necessary for the analysis of observations linked to the study of long-term secular variations of the rotation, such as NSR [see e.g. Rambaux et al., 2010, 2011]. The forcing model required for the introduction of a multi-frequency librational response into the rotational model presented in Chapter 7 could be based on the Fourier decomposition given in Rambaux et al. [2011].

Furthermore, as introduced in Section 1.1, non-synchronous rotation (NSR) of a floating ice shell has been often suggested as the most likely mechanism to explain the longitudinal migration of tectonic features on Europa's surface [Hurford et al., 2007, Rhoden et al., 2010, Rhoden and Hurford, 2013], as well as a source of large tensile stresses that could lead to the formation of a wide variety of lineaments on Europa's surface (see Section 8.1.2). Despite the geological evidence, the occurrence of NSR of Europa's shell is a debated topic from the viewpoint of rotational dynamics. Greenberg and Weidenschilling [1984] suggested that NSR of a decoupled ice shell in Europa may be driven by the tidal torque resulting from the non-perfectly elastic response of the satellite's interior to Jupiter's tides. However, Bills et al. [2009] and Goldreich and Mitchell [2010] have shown that this torque is not large enough to overcome the gravitational torque on Europa's permanent asymmetries. Still, as pointed out by Ojakangas and Stevenson [1989b], NSR may be driven by lateral variations in the ice shell thickness caused by tidal heating in a conductive shell. Within the scope of this debate, our differential rotation model can be extended to analyze whether lateral variations in thickness and/or composition may drive secular length-of-day (LOD) variations in the spin rate of Europa's ice shell. This extended version of our differential rotation model may also be applied to explain the observed faster than synchronous spin rate of Saturn's moon Titan [Stiles et al., 2008, 2010, Meriggiola and Iess, 2012], which is most likely driven by atmospheric forcing on a seasonal scale [Van Hoolst et al., 2013].

As an extension of the previous point, the extended differential rotation model can be applied to the study of the long-term secular drift of the rotation axis with respect to the surface or true polar wander (TPW). For the case of the icy satellites, TPW is a plausible physical mechanism that may be driven by lateral heterogeneities in the interior (e.g. lateral variations in the thickness and composition of the ice shell), surface loading (e.g. impacts and impact basins, mountains, convecting diapirs, etc). However, in contrast to NSR, the occurrence of TPW on Europa is not strongly supported by the morphology of global surface lineaments [Leith and McKinnon, 1996, Kattenhorn and Hurford, 2009, Rhoden et al., 2011], although the formation of circular surface features known as small-circle depressions (SCD's) has been hypothesized to be the result of a large ($\sim 80^\circ$) TPW event [Schenk et al., 2008, Matsuyama et al., 2014]. Evidences of large TPW excursions are stronger for Enceladus [Nimmo and Pappalardo, 2006, Collins and Goodman, 2007]. However, the differential rotational model developed in Chapter 6 would not be able to handle Enceladus' case because: 1) a basin is expected to be present below the active South Polar Region [see e.g. Tobie et al., 2008, Iess et al., 2014, Porco et al., 2014], thereby introducing lateral heterogeneities in the internal structure (recall that the normal mode method requires laterally homogeneous layers), and 2) the expected excursion of the spin axis ($\sim 90^\circ$) is too large to be analyzed with a linearized rotation model (this also holds for the suggested TPW event of Europa). Rotational models based on numerical

methods, most likely finite difference and finite volume methods, would then be necessary.

Besides the study of rotational dynamics and its correlation with observed features, the analytical model developed in Chapters 3 and 4 to determine the tidal response, deformations and stresses at the surface of icy satellites can be extended to include the determination of tidal heat dissipation in the interior of icy satellites [see e.g. [Tobie et al., 2005](#)]. The study of tidal dissipation in the interior of icy satellites, in combination with the modeling of heat transfer, is of key importance to gain understanding on the thermal evolution of the interior of icy satellites (e.g. the stability of subsurface oceans), as well as on the evolution of their orbits [see e.g. [Ojakangas and Stevenson, 1989b](#), [Husmann et al., 2002](#), [Tobie et al., 2003](#), [Husmann and Spohn, 2004](#), [Tobie et al., 2005](#), [Roberts and Nimmo, 2008](#), [Sotin et al., 2009](#), [Beuthe, 2013](#)]. Since tidal heat dissipation in the ice-I shell of icy satellites depends strongly on the rheological behavior of ice-I at the frequency of the orbital motion [see e.g. [Tobie et al., 2003, 2005](#)], the commonly used Maxwell viscoelastic model is not adequate for this purpose as it underestimates heat dissipation by neglecting the effect of anelastic attenuation [[McCarthy and Castillo-Rogez, 2013](#)]. As such, one of the major challenges in the modeling of tidal dissipation is the introduction of a rheological model that is able to incorporate the anelastic behavior of ice-I in the transient creep regime (e.g. extended Burgers, Andrade models) [[Castillo-Rogez et al., 2011](#), [McCarthy and Castillo-Rogez, 2013](#), [Shoji et al., 2013](#)]. Another important challenge is to validate the combined heat dissipation (and heat transfer model) with future observations of the heat flux at the surface of icy satellites and with astrometric measurements of the orbit of the satellites of the giant planets [see e.g. [Lainey and Tobie, 2005](#), for the case of heat dissipation on Io].

REFERENCES

- Z. Alterman, H. Jarosch, and C.L. Pekeris. Oscillations of the Earth. *Proceedings of the Royal Society of London. Series A, Mathematical and Physical Sciences (1934-1990)*, 252:80–95, 1959.
- J.D. Anderson and G. Schubert. Rhea's gravitational field and interior structure inferred from archival data files of the 2005 Cassini flyby. *Physics of the Earth and Planetary Interiors*, 178(3):176–182, 2010.
- J.D. Anderson, E.L. Lau, W.L. Sjogren, G. Schubert, and W.B. Moore. Gravitational constraints on the internal structure of Ganymede. *Nature*, 384(6609):541–543, 1996.
- J.D. Anderson, E.L. Lau, W.L. Sjogren, G. Schubert, and W.B. Moore. Gravitational evidence for an undifferentiated Callisto. *Nature*, 387(6630):264–266, 1997.
- J.D. Anderson, G. Schubert, R.A. Jacobson, E.L. Lau, W.B. Moore, and W.L. Sjogren. Europa's differentiated internal structure: Inferences from four Galileo encounters. *Science*, 281:2019–2022, 1998.
- J.D. Anderson, R.A. Jacobson, T.P. McElrath, W.B. Moore, G. Schubert, and P.C. Thomas. Shape, mean radius, gravity field, and interior structure of Callisto. *Icarus*, 153(1):157–161, 2001.
- B.A. Archinal, M.F. A'hearn, E. Bowell, A. Conrad, G.J. Consolmagno, R. Courtin, T. Fukushima, D. Hestroffer, J.L. Hilton, G.A. Krasinsky, et al. Report of the IAU working group on cartographic coordinates and rotational elements: 2009. *Celestial Mechanics and Dynamical Astronomy*, 109(2):101–135, 2011.
- R.M. Baland and T. Van Hoolst. Librations of the Galilean satellites: The influence of global internal liquid layers. *Icarus*, 209(2):651–664, 2010.
- R.M. Baland, M. Yseboodt, and T. Van Hoolst. Obliquity of the Galilean satellites: The influence of a global internal liquid layer. *Icarus*, 220(2):435–448, 2012.
- R.M. Baland, G. Tobie, A. Lefèvre, and T. Van Hoolst. Titan's internal structure inferred from its gravity field, shape, and rotation state. *Icarus*, 237:29–41, 2014.
- A.C. Barr and R.T. Pappalardo. Onset of convection in the icy Galilean satellites: Influence of rheology. *Journal of Geophysical Research: Planets (1991–2012)*, 110(E12), 2005.
- A.C. Barr and A.P. Showman. Heat transfer in Europa's icy shell. In R.T. Pappalardo, W.B. McKinnon, and K. Khurana, editors, *Europa*, pages 405–430. Arizona Press Space Science Series, 2009.

- C. Béghin, C. Sotin, and M. Hamelin. Titan's native ocean revealed beneath some 45km of ice by a Schumann-like resonance. *Comptes Rendus Geoscience*, 342(6):425–433, 2010.
- C. Béghin, O. Randriamboarison, M. Hamelin, E. Karkoschka, C. Sotin, R.C. Whitten, J.-J. Berthelier, R. Grard, and F. Simões. Analytic theory of Titan's Schumann resonance: Constraints on ionospheric conductivity and buried water ocean. *Icarus*, 218(2):1028–1042, 2012.
- M. Beuthe. Spatial patterns of tidal heating. *Icarus*, 223(1):308–329, 2013.
- M. Beuthe. Tides on Europa: the membrane paradigm. *Icarus*, 248:109–134, 2015.
- B.G. Bills. Free and forced obliquities of the Galilean satellites of Jupiter. *Icarus*, 175(1): 233–247, 2005.
- B.G. Bills and F. Nimmo. Forced obliquity and moments of inertia of Titan. *Icarus*, 196 (1):293–297, 2008.
- B.G. Bills, F. Nimmo, O. Karatekin, T. Van Hoolst, N. Rambaux, B. Levrard, and J. Laskar. Rotational dynamics of Europa. In R.T. Pappalardo, W.B. McKinnon, and K. Khurana, editors, *Europa*, pages 119–134. Arizona Press Space Science Series, 2009.
- M.T. Bland, A.P. Showman, and G. Tobie. The orbital–thermal evolution and global expansion of Ganymede. *Icarus*, 200(1):207–221, 2009.
- B.A. Buffett. Gravitational oscillations in the length of day. *Geophysical Research Letters*, 23(17):2279–2282, 1996.
- J.C. Castillo-Rogez, M. Efroimsky, and V. Lainey. The tidal history of Iapetus: Spin dynamics in the light of a refined dissipation model. *Journal of Geophysical Research: Planets*, 116(E09008), 2011.
- M. Chaplin. Water structure and science, 2015. URL http://www1.lsbu.ac.uk/water/water_structure_science.html. Last accessed, October 2015.
- M.A. Chinnery. The static deformation of an Earth with a fluid core: A physical approach. *Geophysical Journal of the Royal Astronomical Society*, 42:461–475, 1975.
- M. Choukroun and O. Grasset. Thermodynamic model for water and high-pressure ices up to 2.2 GPa and down to the metastable domain. *The Journal of Chemical Physics*, 127(12):124506, 2007.
- C.F. Chyba and C.B. Phillips. Europa as an abode of life. *Origins of Life and Evolution of the Biosphere*, 32(1):47–67, 2002.
- K. Clark, J. Boldt, R. Greeley, K. Hand, I. Jun, R. Lock, R. Pappalardo, T. Van Houten, and T. Yan. Return to Europa: Overview of the Jupiter Europa orbiter mission. *Advances in Space Research*, 48(4):629–650, 2011.

- D.M. Cole and G.D. Durell. The cyclic loading of saline ice. *Philosophical Magazine A*, 72(1):209–229, 1995.
- G.C. Collins and J.C. Goodman. Enceladus' south polar sea. *Icarus*, 189(1):72–82, 2007.
- R.L. Comstock and B.G. Bills. A solar system survey of forced librations in longitude. *Journal of Geophysical Research*, 108(E9):5100, 2003.
- P. Defraigne, O. Viron, V. Dehant, T. Van Hoolst, and F. Hourdin. Mars rotation variations induced by atmosphere and ice caps. *Journal of Geophysical Research: Planets (1991–2012)*, 105(E10):24563–24570, 2000.
- V. Dehant and P.M. Mathews. Earth rotation variations. In T.A. Herring, editor, *Treatise on Geophysics*, vol. 3, pages 295–349. Elsevier, 2007.
- V. Dehant, J. Hinderer, H. Legros, and M. Lefftz. Analytical approach to the computation of the Earth, the outer core and the inner core rotational motions. *Physics of the Earth and Planetary Interiors*, 76(3):259–282, 1993.
- V. Dehant, T. Van Hoolst, O. de Viron, M. Greff-Lefftz, H. Legros, and P. Defraigne. Can a solid inner core of Mars be detected from observations of polar motion and nutation of Mars? *Journal of Geophysical Research: Planets (1991–2012)*, 108(E12), 2003.
- V. Dehant, O. De Viron, O. Karatekin, and T. Van Hoolst. Excitation of Mars polar motion. *Astronomy & Astrophysics*, 446(1):345–355, 2006.
- F. Deschamps and C. Sotin. Thermal convection in the outer shell of large icy satellites. *Journal of Geophysical Research: Planets*, 106(E3):5107–5121, 2001.
- M. Dumberry. Influence of elastic deformations on the inner core wobble. *Geophysical Journal International*, 178(1):57–64, 2009.
- W.B. Durham, S.H. Kirby, and L.A. Stern. Creep of water ices at planetary conditions: A compilation. *Journal of Geophysical Research*, 102:16–293, 1997.
- W.B. Durham, L.A. Stern, and S.H. Kirby. Rheology of ice I at low stress and elevated confining pressure. *Journal of Geophysical Research*, 106(B6):11031–11042, 2001.
- ESA. CDF study report: assessment of a Europa penetrator mission as part of NASA Clipper mission, CLEP. Technical Report CDF–154(E), ESTEC Concurrent Design Facility, 2015.
- H.J. Fischer and T. Spohn. Thermal-orbital histories of viscoelastic models of Io (J1). *Icarus*, 83(1):39–65, 1990.
- P.H. Gammon, H. Kieft, and M.J. Clouter. Elastic constants of ice samples by Brillouin spectroscopy. *The Journal of Physical Chemistry*, 87(21):4025–4029, 1983.
- P.E. Geissler, R. Greenberg, G. Hoppa, A. McEwen, R. Tufts, C. Phillips, B. Clark, M. Ockert-Bell, P. Helfenstein, J. Burns, et al. Evolution of Lineaments on Europa: Clues from Galileo Multispectral Imaging Observations* 1. *Icarus*, 135(1):107–126, 1998.

- D. Gleeson, Z. Crawford, A.C. Barr, M.C. Mullen, R.T. Pappalardo, L.M. Prockter, M.M. Stempel, and J. Wahr. Wavy and cycloidal lineament formation on Europa from combined diurnal and nonsynchronous stresses. In *36th Lunar and Planetary Science Conference*, volume XXXVI, 2005. Abstract 2364.
- P. Goldreich and S. Peale. Spin-orbit coupling in the solar system. *The Astronomical Journal*, 71(6):425–438, 1966.
- P.M. Goldreich and J.L. Mitchell. Elastic ice shells of synchronous moons: Implications for cracks on Europa and non-synchronous rotation of Titan. *Icarus*, 209:631–638, 2010.
- D.L. Goldsby and D.L. Kohlstedt. Superplastic deformation of ice: Experimental observations. *Journal of Geophysical Research*, 106(B6):11017–11030, 2001.
- O. Grasset, M.K. Dougherty, A. Coustenis, E.J. Bunce, C. Erd, D. Titov, M. Blanc, A. Coates, P. Drossart, L.N. Fletcher, H. Hussmann, R. Jaumann, N. Krupp, J.-P. Lebreton, O. Prieto-Ballesteros, P. Tortora, F. Tosi, and T. Van Hoolst. JUperiter ICy moons Explorer (JUICE): An ESA mission to orbit Ganymede and to characterise the Jupiter system. *Planetary and Space Science*, 78:1–21, 2013.
- R. Greeley, R. Sullivan, J. Klemaszewski, K. Homan, J.W. Head, et al. Europa: Initial Galileo Geological Observations* 1. *Icarus*, 135(1):4–24, 1998.
- R. Greenberg and S.J. Weidenschilling. How fast do Galilean satellites spin? *Icarus*, 58: 186–196, 1984.
- R. Greenberg, P. Geissler, G. Hoppa, B.R. Tufts, D.D. Durda, R. Pappalardo, J.W. Head, R. Greeley, R. Sullivan, and M.H. Carr. Tectonic processes on Europa: Tidal stresses, mechanical response, and visible features. *Icarus*, 135:64–78, 1998.
- R. Greenberg, G.V. Hoppa, B.R. Tufts, P. Geissler, J. Riley, and S. Kadel. Chaos on Europa. *Icarus*, 141(2):263–286, 1999.
- R. Greenberg, G.V. Hoppa, G. Bart, and T. Hurford. Tidal stress patterns on Europa's crust. *Celestial Mechanics and Dynamical Astronomy*, 87:171–188, 2003.
- M. Greff-Lefftz and H. Legros. Some remarks about the degree-one deformation of the Earth. *Geophysical Journal International*, 131(3):699–723, 1997.
- M. Greff-Lefftz, H. Legros, and V. Dehant. Influence of the inner core viscosity on the rotational eigenmodes of the Earth. *Physics of the Earth and Planetary Interiors*, 122: 187–204, 2000.
- R.S. Gross. CHAMP, mass displacements, and the Earth's rotation. In C. Reigber, H. Lühr, and P. Schwintzer, editors, *First CHAMP mission results for gravity magnetic and atmospheric studies*, pages 174–179. Springer-Verlag, 2003.
- R.S. Gross. Earth rotation variations - long period. In T.A. Herring, editor, *Treatise on Geophysics*, vol. 3, pages 239–294. Elsevier, 2007.

- N.P. Hammond and A.C. Barr. Formation of Ganymede's grooved terrain by convection-driven resurfacing. *Icarus*, 227:206–209, 2014.
- K.P. Hand and R.W. Carlson. Europa's surface color suggests an ocean rich with sodium chloride. *Geophysical Research Letters*, 42(9):3174–3178, 2015.
- K.P. Hand and C.F. Chyba. Empirical constraints on the salinity of the european ocean and implications for a thin ice shell. *Icarus*, 189(2):424–438, 2007.
- K.P. Hand, C.F. Chyba, J.C. Priscu, R.W. Carlson, and K.H. Nealson. Astrobiology and the potential of life on Europa. In R.T. Pappalardo, W.B. McKinnon, and K. Khurana, editors, *Europa*, pages 589–629. Arizona Press Space Science Series, 2009.
- Y. Harada and K. Kurita. The dependence of surface tidal stress on the internal structure of Europa: The possibility of cracking of the icy shell. *Planetary and Space Science*, 54: 170–180, 2006.
- Y. Harada and K. Kurita. Effect of non-synchronous rotation on surface stress upon Europa: Constraints on surface rheology. *Geophysical Research Letters*, 34(11):L11204, 2007.
- S.A. Hauck, J.M. Aurnou, and A.J. Dombard. Sulfur's impact on core evolution and magnetic field generation on Ganymede. *Journal of Geophysical Research: Planets (1991–2012)*, 111(E9), 2006.
- W.A. Heiskanen and H. Moritz. Physical geodesy, 1984.
- M.B. Helgerud, W.F. Waite, S.H. Kirby, and A. Nur. Elastic wave speeds and moduli in polycrystalline ice Ih, sI methane hydrate, and sII methane-ethane hydrate. *Journal of Geophysical Research: Solid Earth*, 114(B2), 2009.
- J. Hinderer and H. Legros. Elasto-gravitational deformation, relative gravity changes and Earth dynamics. *Geophysical Journal International*, 97(3):481–495, 1989.
- J. Hinderer, H. Legros, and M. Amalvict. A search for Chandler and nearly diurnal free wobbles using Liouville equations. *Geophysical Journal International*, 71(2):303–332, 1982.
- G. Hoppa, R. Greenberg, P. Geissler, B.R. Tufts, J. Plassmann, and D.D. Durda. Rotation of Europa: Constraints from terminator and limb positions. *Icarus*, 137(2):341–347, 1999a.
- G. Hoppa, B. Tufts, R. Greenberg, and P. Geissler. Formation of cycloidal features on Europa. *Science*, 285(5435):1899–1902, 1999b.
- G. Hoppa, B.R. Tufts, R. Greenberg, and P. Geissler. Strike-slip faults on Europa: Global shear patterns driven by tidal stress. *Icarus*, 141(2):287–298, 1999c.
- G.V. Hoppa, B.R. Tufts, R. Greenberg, T.A. Hurford, D.P. O'Brien, and P.E. Geissler. Europa's rate of rotation derived from the tectonic sequence in the Astypalaea region. *Icarus*, 153(1):208–213, 2001.

- S.S. Hough. The oscillations of a rotating ellipsoidal shell containing fluid. *Philosophical Transactions of the Royal Society of London. A*, 186:469–506, 1895.
- C.J.A. Howett, J.R. Spencer, J. Pearl, and M. Segura. High heat flow from Enceladus' south polar region measured using 10–600 cm- 1 Cassini/CIRS data. *Journal of Geophysical Research: Planets (1991–2012)*, 116(E3):E03003, 2011.
- W.B. Hubbard. *Planetary Interiors*. Van Nostrand Reinhold Company Inc., 1984.
- T.A. Hurford, A.R. Sarid, and R. Greenberg. Cycloidal cracks on Europa: Improved modeling and non-synchronous rotation implications. *Icarus*, 186(1):218–233, 2007.
- T.A. Hurford, A.R. Sarid, R. Greenberg, and B.G. Bills. The influence of obliquity on european cycloid formation. *Icarus*, 202(1):197–215, 2009.
- H. Hussmann and T. Spohn. Thermal-orbital evolution of Io and Europa. *Icarus*, 171(2): 391–410, 2004.
- H. Hussmann, T. Spohn, and K. Wiczerkowski. Thermal equilibrium states of Europa's ice shell: Implications for internal ocean thickness and surface heat flow. *Icarus*, 156: 143–151, 2002.
- L. Iess, N.J. Rappaport, P. Tortora, J. Lunine, J.W. Armstrong, S.W. Asmar, L. Somenzi, and F. Zingoni. Gravity field and interior of Rhea from Cassini data analysis. *Icarus*, 190(2): 585–593, 2007.
- L. Iess, N.J. Rappaport, R.A. Jacobson, P. Racioppa, D.J. Stevenson, P. Tortora, J.W. Armstrong, and S.W. Asmar. Gravity field, shape, and moment of inertia of Titan. *Science*, 327(5971):1367–1369, 2010.
- L. Iess, R.A. Jacobson, M. Ducci, D.J. Stevenson, J.I. Lunine, J.W. Armstrong, S.W. Asmar, P. Racioppa, N.J. Rappaport, and P. Tortora. The tides of Titan. *Science*, 337(6093): 457–459, 2012.
- L. Iess, D.J. Stevenson, M. Parisi, D. Hemingway, R.A. Jacobson, J.I. Lunine, F. Nimmo, J.W. Armstrong, S.W. Asmar, M. Ducci, et al. The gravity field and interior structure of Enceladus. *Science*, 344(6179):78–80, 2014.
- H.M. Jara-Orué and B.L.A. Vermeersen. Effects of low-viscous layers and a non-zero obliquity on surface stresses induced by diurnal tides and non-synchronous rotation: The case of Europa. *Icarus*, 215(1):417–438, 2011.
- H.M. Jara-Orué and B.L.A. Vermeersen. The forced libration of Europa's deformable shell and its dependence on interior parameters. *Icarus*, 229:31–44, 2014.
- H.M. Jara-Orué and B.L.A. Vermeersen. Tides on Jupiter moon Ganymede and their relation to its internal structure. *Netherlands Journal of Geosciences*, 95(2):191–201, 2016.
- O. Karatekin, T. Van Hoolst, and T. Tokano. Effect of internal gravitational coupling on Titan's non-synchronous rotation. *Geophysical Research Letters*, 35:L16202, 2008.

- S.A. Kattenhorn. Nonsynchronous rotation evidence and fracture history in the Bright Plains region, Europa. *Icarus*, 157(2):490–506, 2002.
- S.A. Kattenhorn and T. Hurford. Tectonics of Europa. In R.T. Pappalardo, W.B. McKinnon, and K. Khurana, editors, *Europa*, pages 199–236. Arizona Press Space Science Series, 2009.
- W.M. Kaula. Tidal dissipation by solid friction and the resulting orbital evolution. *Review of Geophysics and Space Physics*, 2:661–685, 1964.
- K.K. Khurana, M.G. Kivelson, D.J. Stevenson, G. Schubert, C.T. Russell, R.J. Walker, and C. Polansky. Induced magnetic fields as evidence for subsurface oceans in Europa and Callisto. *Nature*, 395:777–780, 1998. ISSN 0028-0836.
- R.L. Kirk and D.J. Stevenson. Thermal evolution of a differentiated Ganymede and implications for surface features. *Icarus*, 69(1):91–134, 1987.
- M.G. Kivelson, K.K. Khurana, C.T. Russell, R.J. Walker, J. Warnecke, F.V. Coroniti, C. Polansky, D.J. Southwood, and G. Schubert. Discovery of Ganymede’s magnetic field by the Galileo spacecraft. *Nature*, 384(6609):537–541, 1996.
- M.G. Kivelson, K.K. Khurana, C.T. Russell, M. Volwerk, R.J. Walker, and C. Zimmer. Galileo magnetometer measurements: A stronger case for a subsurface ocean at Europa. *Science*, 289(5483):1340–1343, 2000.
- M.G. Kivelson, K.K. Khurana, and M. Volwerk. The permanent and inductive magnetic moments of Ganymede. *Icarus*, 157(2):507–522, 2002.
- O.L. Kuskov and V.A. Kronrod. Internal structure of Europa and Callisto. *Icarus*, 177(2):550–569, 2005.
- V. Lainey and G. Tobie. New constraints on Io’s and Jupiter’s tidal dissipation. *Icarus*, 179(2):485–489, 2005.
- V. Lainey, L. Duriez, and A. Vienne. Synthetic representation of the Galilean satellites’ orbital motions from L1 ephemerides. *Astronomy & Astrophysics*, 456(2):783–788, 2006.
- S. Lee, R.T. Pappalardo, and N.C. Makris. Mechanics of tidally driven fractures in Europa’s ice shell. *Icarus*, 177(2):367–379, 2005.
- A.C. Leith and W.B. McKinnon. Is There Evidence for Polar Wander on Europa? *Icarus*, 120(2):387–398, 1996.
- R.D. Lorenz, B.W. Stiles, R.L. Kirk, M.D. Allison, P.P. del Marmo, L. Iess, J.I. Lunine, S.J. Ostro, and S. Hensley. Titan’s rotation reveals an internal ocean and changing zonal winds. *Science*, 319(5870):1649–1651, 2008.
- A.E.H. Love. The yielding of the Earth to disturbing forces. *Proceedings of the Royal Society of London. Series A*, 82(551):73–88, 1909.
- A.E.H. Love. *Some Problems of Geodynamics*. Cambridge University Press, 1911.

- P.M. Mathews, B.A. Buffett, T.A. Herring, and I.I. Shapiro. Forced nutations of the Earth: Influence of inner core dynamics 1. Theory. *Journal of Geophysical research*, 96(B5): 8219–8242, 1991.
- I. Matsuyama and F. Nimmo. Tectonic patterns on reoriented and despun planetary bodies. *Icarus*, 195(1):459–473, 2008. ISSN 0019-1035.
- I. Matsuyama, F. Nimmo, and J.X. Mitrovica. Planetary reorientation. *Annual Review of Earth and Planetary Sciences*, 42:605–634, 2014.
- C. McCarthy and J.C. Castillo-Rogez. Planetary ices attenuation properties. In M.S. Gudipati and J.C. Castillo-Rogez, editors, *The Science of Solar System Ices*, pages 183–225. Springer, 2013.
- A.J. McConnell. *Application of tensor analysis*. Dover Publications New York, 1957.
- W.B. McKinnon. On convection in ice I shells of outer Solar System bodies, with detailed application to Callisto. *Icarus*, 183(2):435–450, 2006.
- W.B. McKinnon. Effect of Enceladus's rapid synchronous spin on interpretation of Cassini gravity. *Geophysical Research Letters*, 42(7):2137–2143, 2015.
- H.J. Melosh. Tectonic patterns on a tidally distorted planet. *Icarus*, 43(3):334–337, 1980.
- R. Meriggiola and L. Iess. A new rotational model of Titan from Cassini SAR data. In *European Planetary Science Congress 2012, Abstracts*, volume 7, pages EPSC2012–593, 2012.
- G. Mitri and A.P. Showman. Convective-conductive transitions and sensitivity of a convecting ice shell to perturbations in heat flux and tidal-heating rate: Implications for Europa. *Icarus*, 177(2):447–460, 2005.
- G. Mitri, R. Meriggiola, A. Hayes, A. Lefevre, G. Tobie, A. Genova, J.I. Lunine, and H. Zebker. Shape, topography, gravity anomalies and tidal deformation of Titan. *Icarus*, 236:169–177, 2014.
- J.X. Mitrovica and G.A. Milne. Glaciation-induced perturbations in the Earth's rotation: A new appraisal. *Journal of Geophysical Research: Solid Earth*, 103(B1):985–1005, 1998.
- J.X. Mitrovica, J.L. Davis, P.M. Mathews, and I.I. Shapiro. Determination of tidal h Love number parameters in the diurnal band using an extensive VLBI data set. *Geophysical Research Letters*, 21(8):705–708, 1994.
- W.B. Moore. Tidal heating and convection in Io. *Journal of Geophysical Research: Planets (1991–2012)*, 108(E8), 2003.
- W.B. Moore. Thermal equilibrium in Europa's ice shell. *Icarus*, 180(1):141–146, 2006.
- W.B. Moore and H. Hussmann. Europa's silicate interior. In R.T. Pappalardo, W.B. McKinnon, and K. Khurana, editors, *Europa*, pages 369–380. Arizona Press Space Science Series, 2009.

- W.B. Moore and G. Schubert. The tidal response of Europa. *Icarus*, 147:317–319, 2000.
- W.B. Moore and G. Schubert. The tidal response of Ganymede and Callisto with and without liquid water oceans. *Icarus*, 166(1):223–226, 2003.
- H. Moritz and I. Mueller. *Earth rotation: theory and observation*. Ungar, 1987.
- W.H. Munk and G.J.F. MacDonald. *The Rotation of the Earth: a geophysical discussion*. Cambridge University Press, 1960.
- C.D. Murray and S.F. Dermott. *Solar System dynamics*. Cambridge University Press, 1999.
- K. Nagel, D. Breuer, and T. Spohn. A model for the interior structure, evolution, and differentiation of Callisto. *Icarus*, 169(2):402–412, 2004.
- NASA. JPL Solar System Dynamics: Planetary Satellite Physical Parameters, 2014. URL http://ssd.jpl.nasa.gov/?sat_phys_par. Last accessed, May 2014.
- F. Nimmo. Stresses generated in cooling viscoelastic ice shells: Application to Europa. *Journal of Geophysical Research*, 109:E12001, 2004.
- F. Nimmo and M. Manga. Geodynamics of Europa's icy shell. In R.T. Pappalardo, W.B. McKinnon, and K. Khurana, editors, *Europa*, pages 119–134. Arizona Press Space Science Series, 2009.
- F. Nimmo and R.T. Pappalardo. Diapir-induced reorientation of Saturn's moon Enceladus. *Nature*, 441(7093):614–616, 2006.
- F. Nimmo and P. Schenk. Normal faulting on Europa: Implications for ice shell properties. *Journal of Structural Geology*, 28(12):2194–2203, 2006.
- F. Nimmo, B.G. Bills, and P.C. Thomas. Geophysical implications of the long-wavelength topography of the Saturnian satellites. *Journal of Geophysical Research: Planets (1991–2012)*, 116(E11):E11001, 2011.
- D.P. O'Brien, P. Geissler, and R. Greenberg. A melt-through model for chaos formation on Europa. *Icarus*, 156(1):152–161, 2002.
- G.W. Ojakangas and D.J. Stevenson. Polar wander of an ice shell on Europa. *Icarus*, 81(2):242–270, 1989a.
- G.W. Ojakangas and D.J. Stevenson. Thermal state of an ice shell on Europa. *Icarus*, 81(2):220–241, 1989b.
- C. O'Neill and F. Nimmo. The role of episodic overturn in generating the surface geology and heat flow on Enceladus. *Nature Geoscience*, 3(2):88–91, 2010.
- R.T. Pappalardo, M.J.S. Belton, H.H. Breneman, M.H. Carr, C.R. Chapman, G.C. Collins, T. Denk, S. Fagents, P.E. Geissler, B. Giese, R. Greeley, R. Greenberg, J.W. Head, P. Helfenstein, G. Hoppa, S.D. Kadel, K.P. Klaasen, J.E. Klemaszewski, K. Magee, A.S. McEwen, J.M. Moore, G. Neukum, C.B. Phillips, L.M. Prockter, G. Schubert, D.A.

- Senske, R.J. Sullivan, B.R. Tufts, E.P. Turtle, R. Wagner, and K.K. Williams. Does Europa have a subsurface ocean? Evaluation of the geological evidence. *Journal of Geophysical Research: Planets*, 104:24015–24055, 1999.
- M. Parisi, L. Iess, and S. Finocchiaro. The gravity fields of Ganymede, Callisto and Europa: how well can JUICE do? In *Geophysical Research Abstracts*, volume 16, pages EGU2014–11758, 2014.
- W.R. Peltier. The impulse response of a Maxwell Earth. *Reviews of Geophysics*, 12(4): 649–669, 1974.
- C.B. Phillips and R.T. Pappalardo. Europa Clipper Mission Concept: Exploring Jupiter's Ocean Moon. *Eos, Transactions American Geophysical Union*, 95(20):165–167, 2014.
- H. Poincaré. Sur la précession des corps déformables. *Bulletin Astronomique, Serie I*, 27: 321–356, 1910.
- C. Porco, D. DiNino, and F. Nimmo. How the geysers, tidal stresses, and thermal emission across the south polar terrain of Enceladus are related. *The Astronomical Journal*, 148 (3):45, 2014.
- C.C. Porco, P. Helfenstein, P.C. Thomas, A.P. Ingersoll, J. Wisdom, R. West, G. Neukum, T. Denk, R. Wagner, T. Roatsch, S. Kieffer, E. Turtle, A. McEwen, T.V. Johnson, J. Rathbun, J. Veverka, D. Wilson, J. Perry, J. Spitale, A. Brahic, J.A. Burns, A.D. DelGenio, L. Dones, C.D. Murray, and S. Squyres. Cassini observes the active south pole of Enceladus. *Science*, 311(5766):1393–1401, 2006.
- F. Postberg, S. Kempf, J. Schmidt, N. Brilliantov, A. Beinsen, B. Abel, U. Buck, and R. Srama. Sodium salts in E-ring ice grains from an ocean below the surface of Enceladus. *Nature*, 459(7250):1098–1101, 2009.
- F. Postberg, J. Schmidt, J. Hillier, S. Kempf, and R. Srama. A salt-water reservoir as the source of a compositionally stratified plume on Enceladus. *Nature*, 474(7353):620–622, 2011.
- B. Preblich, R. Greenberg, J. Riley, and D. O'Brien. Tidally driven strike-slip displacement on Europa: Viscoelastic modeling. *Planetary and Space Science*, 55:1225–1245, 2007.
- N. Rambaux, J.C. Castillo-Rogez, J.G. Williams, and Ö. Karatekin. Librational response of Enceladus. *Geophysical Research Letters*, 37(4):L04202, 2010.
- N. Rambaux, T. Van Hoolst, and Ö. Karatekin. Librational response of Europa, Ganymede, and Callisto with an ocean for a non-Keplerian orbit. *Astronomy & Astrophysics*, 527:A118, 2011.
- G. Ranalli. *Rheology of the Earth, second edition*. Chapman and Hall, 1995.
- N.J. Rappaport, L. Iess, J. Wahr, J.I. Lunine, J.W. Armstrong, S.W. Asmar, P. Tortora, M. Di Benedetto, and P. Racioppa. Can Cassini detect a subsurface ocean in Titan from gravity measurements? *Icarus*, 194(2):711–720, 2008.

- A. Rhoden, T.A. Hurford, H. Jara-Orue, and B.L. Vermeersen. Cycloid formation in Europa's viscoelastic ice shell. In *AGU Fall Meeting Abstracts*, volume 1, page 1842, 2013.
- A.R. Rhoden and T.A. Hurford. Lineament azimuths on Europa: Implications for obliquity and non-synchronous rotation. *Icarus*, 226(1):841–859, 2013.
- A.R. Rhoden, B. Militzer, E.M. Huff, T.A. Hurford, M. Manga, and M.A. Richards. Constraints on Europa's rotational dynamics from modeling of tidally-driven fractures. *Icarus*, 210(2):770–784, 2010.
- A.R. Rhoden, T.A. Hurford, and M. Manga. Strike-slip fault patterns on Europa: Obliquity or polar wander? *Icarus*, 211(1):636–647, 2011.
- A.R. Rhoden, G. Wurman, E.M. Huff, M. Manga, and T.A. Hurford. Shell tectonics: A mechanical model for strike-slip displacement on Europa. *Icarus*, 218(1):297–307, 2012.
- Y. Ricard, G. Spada, and R. Sabadini. Polar wandering of a dynamic Earth. *Geophysical Journal International*, 113(2):284–298, 1993.
- A. Richard, N. Rambaux, and B. Charnay. Librational response of a deformed 3-layer Titan perturbed by non-Keplerian orbit and atmospheric couplings. *Planetary and Space Science*, 93:22–34, 2014.
- J.H. Roberts and F. Nimmo. Tidal heating and the long-term stability of a subsurface ocean on Enceladus. *Icarus*, 194(2):675–689, 2008.
- G. Robuchon, G. Choblet, G. Tobie, O. Čadež, C. Sotin, and O. Grasset. Coupling of thermal evolution and despinning of early Iapetus. *Icarus*, 207(2):959–971, 2010.
- M.G. Rochester and D.E. Smylie. On changes in the trace of the Earth's inertia tensor. *Journal of Geophysical Research*, 79(32):4948–4951, 1974.
- J. Ruiz and R. Tejero. Heat flow, lenticulae spacing, and possibility of convection in the ice shell of Europa. *Icarus*, 162(2):362–373, 2003.
- R. Sabadini and W.R. Peltier. Pleistocene deglaciation and the Earth's rotation: implications for mantle viscosity. *Geophysical Journal International*, 66(3):553–578, 1981.
- R. Sabadini and B. Vermeersen. *Global dynamics of the Earth: applications of normal mode relaxation theory to Solid-Earth geophysics*. Kluwer Academic Publishers, 2004.
- R. Sabadini, D.A. Yuen, and E. Boschi. Polar wandering and the forced responses of a rotating, multilayered, viscoelastic planet. *Journal of Geophysical Research: Solid Earth*, 87(B4):2885–2903, 1982.
- M. Saito. Some problems of static deformation of the Earth. *Journal of Physics of the Earth*, 22(1):123–140, 1974.
- T. Sasao, S. Okubo, and M. Saito. A simple theory on the dynamical effects of a stratified fluid core upon nutational motion of the Earth. In *Nutation and the Earth's Rotation*, pages 165–183. Springer, 1980.

- J. Saur, S. Duling, L. Roth, X. Jia, D.F. Strobel, P.D. Feldman, U.R. Christensen, K.D. Retherford, M.A. McGrath, F. Musacchio, et al. The search for a subsurface ocean in Ganymede with Hubble Space Telescope observations of its auroral ovals. *Journal of Geophysical Research: Space Physics*, 120, 2015. doi:10.1002/2014JA020778.
- P.M. Schenk. Thickness constraints on the icy shells of the Galilean satellites from a comparison of crater shapes. *Nature*, 417:419–421, 2002.
- P.M. Schenk and E.P. Turtle. Europa's impact craters: probes of the icy shell. In R.T. Pappalardo, W.B. McKinnon, and K. Khurana, editors, *Europa*, pages 181–198. Arizona Press Space Science Series, 2009.
- P.M. Schenk, I. Matsuyama, and F. Nimmo. True polar wander on Europa from global-scale small-circle depressions. *Nature*, 453(7193):368–371, 2008.
- N. Schilling, F.M. Neubauer, and J. Saur. Time-varying interaction of Europa with the jovian magnetosphere: Constraints on the conductivity of Europa's subsurface ocean. *Icarus*, 192(1):41–55, 2007.
- M. Schmeltz, E. Rignot, and D. MacAyeal. Tidal flexure along ice-sheet margins: comparison of InSAR with an elastic-plate model. *Annals of Glaciology*, 34(1):202–208, 2002.
- B.E. Schmidt, D.D. Blankenship, G.W. Patterson, and P.M. Schenk. Active formation of chaos terrain over shallow subsurface water on Europa. *Nature*, 479(7374):502–505, 2011.
- G. Schubert, F. Sohl, and H. Hussmann. Interior of Europa. In R.T. Pappalardo, W.B. McKinnon, and K. Khurana, editors, *Europa*, pages 353–367. Arizona Press Space Science Series, 2009.
- E.M. Schulson. Brittle failure of ice. *Engineering Fracture Mechanics*, 68(17-18):1839–1887, 2001.
- P.K. Seidelmann, B.A. Archinal, M.F. A'hearn, A. Conrad, G.J. Consolmagno, D. Hestroffer, J.L. Hilton, G.A. Krasinsky, G. Neumann, J. Oberst, et al. Report of the IAU/IAG Working Group on cartographic coordinates and rotational elements: 2006. *Celestial Mechanics and Dynamical Astronomy*, 98(3):155–180, 2007.
- L.E. Senft and S.T. Stewart. Modeling the morphological diversity of impact craters on icy satellites. *Icarus*, 214(1):67–81, 2011.
- D. Shoji, H. Hussmann, K. Kurita, and F. Sohl. Ice rheology and tidal heating of Enceladus. *Icarus*, 226(1):10–19, 2013.
- A.P. Showman and L. Han. Numerical simulations of convection in Europa's ice shell: Implications for surface features. *Journal of Geophysical Research: Planets*, 109(E01010), 2004.
- A.P. Showman, D.J. Stevenson, and R. Malhotra. Coupled orbital and thermal evolution of Ganymede. *Icarus*, 129(2):367–383, 1997.

- F. Sohl, T. Spohn, D. Breuer, and K. Nagel. Implications from Galileo observations on the interior structure and chemistry of the Galilean satellites. *Icarus*, 157:104–119, 2002.
- F. Sohl, A. Solomonidou, F.W. Wagner, A. Coustenis, H. Hussmann, and D. Schulze-Makuch. Structural and tidal models of Titan and inferences on cryovolcanism. *Journal of Geophysical Research: Planets*, 119(5):1013–1036, 2014.
- C. Sotin and G. Tobie. Internal structure and dynamics of the large icy satellites. *Comptes Rendus-Physique*, 5:769–780, 2004.
- C. Sotin, J.W. Head, and G. Tobie. Europa: Tidal heating of upwelling thermal plumes and the origin of lenticulae and chaos melting. *Geophysical Research Letters*, 29(8): 74–1, 2002.
- C. Sotin, G. Tobie, J. Wahr, and W.B. McKinnon. Tides and tidal heating on Europa. In R.T. Pappalardo, W.B. McKinnon, and K. Khurana, editors, *Europa*, pages 85–117. Arizona Press Space Science Series, 2009.
- G. Spada, R. Sabadini, D.A. Yuen, and Y. Ricard. Effects on post-glacial rebound from the hard rheology in the transition zone. *Geophysical Journal International*, 109(3): 683–700, 1992.
- J.R. Spencer and F. Nimmo. Enceladus: An active ice world in the Saturn system. *Annual Review of Earth and Planetary Sciences*, 41(1):693–717, 2013.
- J.R. Spencer, J.C. Pearl, M. Segura, F.M. Flasar, A. Mamoutkine, P. Romani, B.J. Buratti, A.R. Hendrix, L.J. Spilker, and R.M.C. Lopes. Cassini encounters Enceladus: Background and the discovery of a south polar hot spot. *science*, 311(5766):1401–1405, 2006.
- J.R. Spencer, A.C. Barr, L.W. Esposito, P. Helfenstein, A.P. Ingersoll, R. Jaumann, C.P. McKay, F. Nimmo, and J.H. Waite. Enceladus: An active cryovolcanic satellite. In *Saturn from Cassini-Huygens*, pages 683–724. Springer, 2009.
- T. Spohn and G. Schubert. Oceans in the icy Galilean satellites of Jupiter? *Icarus*, 161(2): 456–467, 2003.
- B.W. Stiles, R.L. Kirk, R.D. Lorenz, S. Hensley, E. Lee, S.J. Ostro, M.D. Allison, P.S. Callahan, Y. Gim, L. Iess, P. Perci del Marmo, G. Hamilton, W.T.K. Johnson, R.D. West, and the Cassini RADAR Team. Determining Titan's spin state from Cassini RADAR images. *The Astronomical Journal*, 135(5):1669, 2008.
- B.W. Stiles, R.L. Kirk, R.D. Lorenz, S. Hensley, E. Lee, S.J. Ostro, M.D. Allison, P.S. Callahan, Y. Gim, L. Iess, P. Perci del Marmo, G. Hamilton, W.T.K. Johnson, R.D. West, and the Cassini RADAR Team. Erratum: "Determining Titan's spin state from Cassini RADAR images". *The Astronomical Journal*, 139(1):311, 2010.
- A.M.K. Szeto and S. Xu. Gravitational coupling in a triaxial ellipsoidal Earth. *Journal of Geophysical Research*, 102(B12):27651–27657, 1997.

- N. Thomas, T. Spohn, J.-P. Barriot, W. Benz, G. Beutler, U. Christensen, V. Dehant, C. Fallnich, D. Giardini, O. Groussin, et al. The BepiColombo Laser Altimeter (BELA): concept and baseline design. *Planetary and Space Science*, 55(10):1398–1413, 2007.
- P.C. Thomas, R. Tajeddine, M.S. Tiscareno, J.A. Burns, J. Joseph, T.J. Loredo, P. Helfenstein, and C. Porco. Enceladus's measured physical libration requires a global subsurface ocean. *Icarus*, 264:37–47, 2016.
- G. Tobie, G. Choblet, and C. Sotin. Tidally heated convection: Constraints on Europa's ice shell thickness. *Journal of Geophysical Research*, 108(E11):5124, 2003.
- G. Tobie, A. Mocquet, and C. Sotin. Tidal dissipation within large icy satellites: Applications to Europa and Titan. *Icarus*, 177(2):534–549, 2005.
- G. Tobie, O. Čadek, and C. Sotin. Solid tidal friction above a liquid water reservoir as the origin of the south pole hotspot on Enceladus. *Icarus*, 196(2):642–652, 2008.
- T. Tokano, T. Van Hoolst, and O. Karatekin. Polar motion of Titan forced by the atmosphere. *Journal of Geophysical Research: Planets (1991–2012)*, 116(E5), 2011.
- D.L. Turcotte and G. Schubert. *Geodynamics*. Cambridge University Press, 2014.
- T. Van Hoolst. The rotation of the terrestrial planets. In T. Spohn, editor, *Treatise on Geophysics*, vol. 10, pages 123–164. Elsevier, 2007.
- T. Van Hoolst and V. Dehant. Influence of triaxiality and second-order terms in flattenings on the rotation of terrestrial planets: I. Formalism and rotational normal modes. *Physics of the Earth and Planetary Interiors*, 134(1):17–33, 2002.
- T. Van Hoolst, N. Rambaux, O. Karatekin, V. Dehant, and A. Rivoldini. The librations, shape, and icy shell of Europa. *Icarus*, 195(1):386–399, 2008.
- T. Van Hoolst, N. Rambaux, O. Karatekin, and R.-M. Baland. The effect of gravitational and pressure torques on Titan's length-of-day variations. *Icarus*, 200(1):256–264, 2009.
- T. Van Hoolst, R.M. Baland, and A. Trinh. On the librations and tides of large icy satellites. *Icarus*, 226:299–315, 2013.
- S. Vance and J. Goodman. Oceanography of an ice-covered moon. In R.T. Pappalardo, W.B. McKinnon, and K. Khurana, editors, *Europa*, pages 459–482. Arizona Press Space Science Series, 2009.
- S. Vance, M. Bouffard, M. Choukroun, and C. Sotin. Ganymede's internal structure including thermodynamics of magnesium sulfate oceans in contact with ice. *Planetary and Space Science*, 96:62–70, 2014.
- D.G. Vaughan. Tidal flexure at ice shelf margins. *Journal of Geophysical Research: Solid Earth*, 100(B4):6213–6224, 1995.
- L.L.A. Vermeersen, R. Sabadini, and G. Spada. Analytical visco-elastic relaxation models. *Geophysical Research Letters*, 23(7):697–700, 1996.

- J. Wahr, M.T. Zuber, D.E. Smith, and J.I. Lunine. Tides on Europa, and the thickness of Europa's icy shell. *Journal of Geophysical Research*, 111(E12):E12005, 2006.
- J. Wahr, Z.A. Selvens, M.C.E. Mullen, A.C. Barr, G.C. Collins, M.M. Selvens, and R.T. Pappalardo. Modeling stresses on satellites due to nonsynchronous rotation and orbital eccentricity using gravitational potential theory. *Icarus*, 200(1):188–206, 2009.
- J.M. Wahr. A normal mode expansion for the forced response of a rotating Earth. *Geophysical Journal International*, 64(3):651–675, 1981.
- J.H. Waite Jr, W.S. Lewis, B.A. Magee, J.I. Lunine, W.B. McKinnon, C.R. Glein, O. Mouis, D.T. Young, T. Brockwell, J. Westlake, M.-J. Nguyen, B.D. Teolis, H.D. Niemann, R.L. McNutt Jr, M. Perry, and W.-H. Ip. Liquid water on Enceladus from observations of ammonia and ^{40}Ar in the plume. *Nature*, 460(7254):487–490, 2009.
- P. Wu and W.R. Peltier. Viscous gravitational relaxation. *Geophysical Journal of the Royal Astronomical Society*, 70:435–485, 1982.
- P. Wu and W.R. Peltier. Pleistocene deglaciation and the Earth's rotation: a new analysis. *Geophysical Journal International*, 76(3):753–791, 1984.
- X. Wu, Y. Bar-Sever, W.M. Folkner, J.G. Williams, and J.F. Zumberge. Probing Europa's hidden ocean from tidal effects on orbital dynamics. *Geophysical Research Letters*, 28(11):2245–2248, 2001.
- D.A. Yuen and W.R. Peltier. Normal modes of the viscoelastic Earth. *Geophysical Journal International*, 69(2):495–526, 1982.
- D.A. Yuen, R. Sabadini, P. Gasperini, and E. Boschi. On transient rheology and glacial isostasy. *Journal of Geophysical Research: Solid Earth*, 91(B11):11420–11438, 1986.
- V.N. Zharkov and S.M. Molodensky. On the Chandler wobble of Mars. *Planetary and Space Science*, 44(11):1457–1462, 1996.
- C. Zimmer, K.K. Khurana, and M.G. Kivelson. Subsurface oceans on Europa and Callisto: Constraints from Galileo magnetometer observations. *Icarus*, 147(2):329–347, 2000.
- M.Y. Zolotov. An oceanic composition on early and today's Enceladus. *Geophysical Research Letters*, 34(23):L23203, 2007.
- M.Y. Zolotov and J.S. Kargel. On the chemical composition of Europa's icy shell, ocean, and underlying rocks. In R.T. Pappalardo, W.B. McKinnon, and K. Khurana, editors, *Europa*, pages 431–457. Arizona Press Space Science Series, 2009.

ACKNOWLEDGEMENTS

It was the year 2009, while finishing my Master of Science thesis, that the idea of pursuing a career in the field of planetary sciences entered my skeptical mind. As usual, I started to look outwards, often neglecting the possibilities that were offered by a research group that had the ambition of becoming an important player in planetary research. It was not until my thesis supervisor, Bert Vermeersen, showed me an accepted research proposal to study the rotational variations of icy satellites with shallow low-viscosity zones that the tide started to change. Some months later, in 2010, I started my PhD research on the aforementioned topic, thereby becoming the first PhD student of the Astrodynamics and Satellite Missions group who dealt with a topic in planetary sciences. This was the start of an unforgettable and exciting journey that in the end, and rather unexpectedly, has taken more than six years. Although the outcome of this journey is what fills most of the pages of this dissertation, it is nearly impossible to describe the traversed path in simple words. Here I would like to emphasize on the human factor, i.e. the people who made this journey possible and those who shared the path with me during the last six years.

First of all, I would like to thank my daily supervisor and promotor Bert Vermeersen, who not only believed in my research capabilities but also gave me the freedom to design and follow my own research path throughout these years. I learned a lot from your guidance and expertise, and your comments were always a source of valuable input to improve my work as a researcher, even when it seemed that I was no longer listening. Furthermore, I would like to thank Boudewijn Ambrosius and Pieter Visser for giving me the feeling of being a valuable member of this group, even after fulfillment of my contract.

Being the first of the group working fully on planetary sciences meant often to look outside the expertise of the Astrodynamics and Satellite Missions group in order to discuss my research methodology and simulation results. Here I would like to thank i.a. Tim van Hoolst, Mikael Beuthe, Nicolas Rambaux, Frank Sohl, Hauke Hussmann, Gabriel Tobie and Alyssa Rhoden for the numerous insightful discussions about the tidal and rotational dynamics of icy moons, mostly during the EPSC conferences I attended throughout these years. This dissertation would have been very different without your input.

Needless to say, my colleagues at the Astrodynamics and Satellite Missions group have been of great significance during my time as a PhD researcher, both from an academic viewpoint as well as from a social perspective. As such, I would like to thank Ejo, Erwin, Ron, Eelco, Jose, Wouter, Joao, Daphne, Loïc, Marc, Wim and Dominic for all the helpful advice as well as the diverse range of interesting conversations (i.e. including the ESC). Two of you, however, made such an impact on my journey that a special thanks would not be misplaced. Firstly, I would like to thank Wouter for a myriad of reasons that are impossible to fully describe in a few lines. Secondly, I would like to thank Erwin for all the fun moments. I mean, you even created a verb based on my name (not that I

should be too proud of that, by the way).

One of the best experiences of being a PhD student is to share the challenging journey with other similar-minded people. As such, I would like to thank all the PhD-students who were part of the Astrodynamics and Satellite Missions group throughout the last six years; you all helped to create a nice international working environment within the group. Special thanks go to my officemates at room 9.09 over the years - Luuk, Bart and Haiyang - for the nice conversations, both work related as well as non-work related. Further, I would like to thank Tatiana for sharing the Latin American spirit within the group and Svenja for all the tasteful self-made cakes (you kind of spoiled us). Obviously I cannot forget to thank the people from the Space Systems Engineering group for all the good moments inside and outside the faculty.

Finally, I would like to thank my family for all your support, patience and understanding. Very often I was so extremely consumed by the work I was doing that it was very challenging to communicate with each other. Your support has been of great value, especially in difficult times.

Hermes Miguel Jara Orué
Delft, October 2016

CURRICULUM VITÆ

Hermes Miguel JARA ORUÉ

30-08-1980 Born in Arequipa, Perú.

EDUCATION

1992–2001 Secondary Education
C.E.P. San José SJ, Arequipa, Perú (1992–1996)
Johan de Witt College (VWO), The Hague, The Netherlands (1998–2001)

2002–2006 Bachelor of Science in Aerospace Engineering
Delft University of Technology

2006–2009 Master of Science in Aerospace Engineering (cum laude)
Delft University of Technology

2010–2016 PhD. Aerospace Engineering
Delft University of Technology
Thesis: Rotational Dynamics of Icy Satellites
Promotor: Prof. dr. L.L.A. Vermeersen
Prof. dr.ir. P.N.A.M. Visser

LIST OF PUBLICATIONS

JOURNAL ARTICLES

3. **H.M. Jara Orué** and B.L.A. Vermeersen, *Tides on Jupiter moon Ganymede and their relation to its internal structure*, Netherlands Journal of Geosciences, **95(2)**, 191–201 (2016).
2. **H.M. Jara Orué** and B.L.A. Vermeersen, *The forced libration of Europa's deformable shell and its dependence on interior parameters*, Icarus **229**, 31–44 (2014).
1. **H.M. Jara Orué** and B.L.A. Vermeersen, *Effects of low-viscous layers and a non-zero obliquity on surface stresses induced by diurnal tides and non-synchronous rotation: The case of Europa*, Icarus **215(1)**, 417–438 (2011).

SELECTED CONFERENCE CONTRIBUTIONS

11. B.L.A. Vermeersen, L.R. Maas, S. van Oers, A. Rabitti and **H.M. Jara Orué**, *Tidal-induced internal ocean waves as an explanation for Enceladus' tiger stripe pattern and hotspot activity*, AGU Fall Meeting Abstracts **1**, AGU Fall Meeting (2014).
10. A.R. Rhoden, T.A. Hurford, **H.M. Jara Orué** and L.L.A. Vermeersen, *Cycloid formation in Europa's viscoelastic shell*, AGU Fall Meeting Abstracts **1**, AGU Fall Meeting (2013).
9. B.L. Vermeersen, L.R. Maas, S. van Oers, A. Rabitti and **H.M. Jara Orué**, *Tidal-induced ocean dynamics as cause of Enceladus' tiger stripe pattern*, AGU Fall Meeting Abstracts **1**, AGU Fall Meeting (2013).
8. A.R. Rhoden, T.A. Hurford, **H.M. Jara Orué** and L.L.A. Vermeersen, *Cracking Europa's rotation history with tidally-driven fractures*, Geological Society of America Abstracts **45(7)**, The Geological Society of America Annual Meeting (2013).
7. **H.M. Jara Orué** and L.L.A. Vermeersen, *Effect of (visco)elastic deformation on the longitudinal libration of Europa's shell*, EPSC Abstracts **8**, European Planetary Sciences Conference (2013).
6. **H.M. Jara Orué** and L.L.A. Vermeersen, *Rotational dynamics of a viscoelastic Europa*, EPSC Abstracts **7**, European Planetary Sciences Conference (2012).
5. **H.M. Jara Orué** and L.L.A. Vermeersen, *Reorientation of the rotation axis of triaxial viscoelastic moons: Europa and Titan*, EPSC Abstracts **6**, EPSC-DPS Joint Meeting (2011).
4. **H.M. Jara Orué** and L.L.A. Vermeersen, *Effect of obliquity on viscoelastic deformation and stresses at Europa's surface*, Geophysical Research Abstracts **13**, EGU General Assembly (2011).
3. **H.M. Jara Orué** and L.L.A. Vermeersen, *Surface stress patterns and the possibility of a subsurface ocean on Europa*, EPSC Abstracts **5**, European Planetary Sciences Conference (2010).

2. L.L.A. Vermeersen and **H.M. Jara Orué**, *State of Stresses at the Icy Surface of Europa: A Strong Case for the Existence of a Subsurface Ocean*, Geophysical Research Abstracts **12**, EGU General Assembly (2010).
1. **H.M. Jara Orué** and L.L.A. Vermeersen, *Application of normal-modes formalism to the determination of tidal deformations and stresses at the surface of Europa*, EPSC Abstracts **4**, European Planetary Sciences Conference (2009).